NASA Technical Paper 2834

October 1988

# Aerodynamics in Ground Effect and Predicted Landing Ground Roll of a Fighter Configuration With a Secondary-Nozzle Thrust Reverser



Daniel W. Banks

NASA

NASA
Technical
Paper
2834

1988

# Aerodynamics in Ground Effect and Predicted Landing Ground Roll of a Fighter Configuration With a Secondary-Nozzle Thrust Reverser

Daniel W. Banks
*Langley Research Center*
*Hampton, Virginia*

National Aeronautics
and Space Administration

**Scientific and Technical
Information Division**

## Summary

An experimental investigation of the in-ground-effect aerodynamic characteristics and predicted landing-ground-roll performance of a wing-canard fighter configuration with a secondary-nozzle thrust reverser has been completed. These tests were conducted in the Langley 14- by 22-Foot Subsonic Wind Tunnel with a model equipped with a pneumatic jet for thrust simulation of nozzle pressure ratios up to 4.0. The model was tested in the landing roll-out configuration at approximately wheel touchdown height for decreasing dynamic pressures from 50 to 10 psf. Landing-ground-roll predictions of the configuration were calculated from the wind-tunnel results.

The results from this investigation indicated the secondary-nozzle thrust reverser is a viable concept, although it appears to suffer from some of the same disadvantages as conventional thrust reversers. However, the secondary-nozzle thrust reverser has some unique advantages, including integration with a high-lift system, short delay times, potentially reduced rudder deterioration, and reduced possibility of reingestion and foreign-object damage.

## Introduction

The design of contemporary high-performance jet-powered aircraft has been directed toward high-speed-cruising flight, maneuvering, and acceleration. These design goals generally lead to aircraft configurations which exhibit much better takeoff performance than landing performance. Because of their high thrust-to-weight ratios these aircraft can take advantage of good acceleration to become airborne in as little as 1000 ft. However, because of a limited high-lift capability, they must approach and land at relatively high speeds and generally require 2500 to 3000 ft of ground roll with maximum wheel braking after touchdown. If these aircraft could take advantage of their high thrust both to reduce their approach velocity through increased lift and to improve deceleration after touchdown by using thrust reversers, they could greatly improve their approach and landing performance without compromising their high-speed-cruise and maneuver design.

The need for aircraft capable of short takeoff and landing (STOL) operations has led to research on both thrust reversers and high-lift systems such as mechanical flaps, thrust vectoring, and thrust-induced lift. One problem area in the use of thrust reversers is the relatively long time required to increase engine thrust from low approach thrust levels to the high thrust levels needed to produce effective reverse thrust. One solution to this problem has been the development of multifunction nozzles which can partially spoil thrust during the landing approach to give the proper low levels of net thrust needed for glide-path control while allowing the engines to be set at high thrust levels. Then the only delay from touchdown to full reverse thrust is the time for mechanical devices to vector the thrust forward (about 1 sec). This could greatly reduce landing ground rolls, particularly under those conditions when wheel braking would be ineffective. If a configuration could use some or all of the thrust to improve high-lift capability rather than just to spoil excess thrust, then approach velocities could also be reduced, a result leading to further reductions in landing ground roll. The addition of complex multifunction nozzles and high-lift systems, however, can add significantly to the gross weight of an aircraft, and a desire to minimize this weight penalty has led to the idea of combining the high-lift, thrust-spoiling, and reverse-thrust functions into one nozzle concept.

Such a nozzle configuration has emerged out of a research program at the NASA Langley Research Center (LaRC) investigating various types of spanwise-blowing (SWB) high-lift concepts (ref. 1) and thrust-reverser concepts (ref. 2). One of the SWB concepts that appears promising, underwing spanwise blowing, diverts exhaust flow out the side of the engine nacelle through a secondary nozzle such that the spanwise jet mixes with the free-stream flow, turns downstream, and is deflected down by the trailing-edge flap. This concept produces high lift in a manner similar to an externally blown flap (EBF) without requiring wing-pylon-mounted engines exhausting directly onto the flap system. The investigation showed that significant levels of lift (approximately 20 percent of total configuration lift) could be generated if a large portion of the exhaust flow was diverted approximately parallel to the flap hinge line by the secondary nozzle (refs. 1 and 3). This concept, shown on a wing-canard fighter model in figures 1 and 2, uses a series of vanes to provide flow turning through the secondary nozzle, called a cascade, located on the underwing-mounted engines.

A promising thrust-spoiling and thrust-reversing concept which was also developed at LaRC is the rotating-vane thrust reverser described in reference 2. This nozzle is located upstream of the main nozzle throat and consists of a set of movable vanes to provide thrust vectoring from 45° aft to 45° forward (or reverse thrust). Thus, during approach, with the main nozzle blocked and the engine set to military or maximum dry power, the vanes are moved to provide the low level of net thrust needed for glide-path control while spoiling the majority of the high thrust produced by the engine operating at high power. Upon touchdown the vanes are rotated forward rapidly to give full reverse thrust.

The idea emerged that the rotating-vane nozzle concept could provide both spanwise blowing and reverse thrust if it were mounted horizontally like the cascade nozzle (ref. 4). This idea is appealing not only because a powered high-lift concept is integrated with a thrust-reverser concept, but also because the thrust-reverser plume is directed horizontally instead of vertically. The flow does not impinge on the ground plane, thereby reducing the problem of reingestion of exhaust gases, adverse aerodynamic effects, and the possiblity of foreign-object damage (FOD). In addition, the reversed flow blowing under the wing suggests the possibility of down loads (suckdown) which can increase braking forces to reduce ground roll further.

The only thrust reverser presently used on a fighter configuration is the bucket-type reverser (e.g., on the Panavia Tornado, ref. 5). These reversers deploy a turning "bucket" just aft of the exhaust nozzle to turn the flow forward. Normally the thrust vector is close to the longitudinal axis, although most reversers of this type "splay" or turn the flow somewhat to the side to avoid reingestion and loss of rudder control at high velocities. This splay angle is usually kept as small as possible so performance does not decrease below acceptable levels. A rule of thumb for good thrust-reverser performance is that the thrust reverser should obtain reverse-thrust levels of at least 50 percent of maximum dry thrust.

The bucket-type reverser is fairly simple in design and activation, and it has its advantages and disadvantages. Disadvantages of this design include a relatively long deployment time after touchdown (approximately 2 sec), a loss of directional stability (which was eventually improved on the Tornado) coupled with a decrease in rudder power, a reingestion velocity of approximately 40 knots, and yawing-moment asymmetries.

A conceptual advanced configuration employing secondary nozzles for both underwing spanwise blowing and thrust reversing is shown in figure 3. The configuration is also shown with a blown high-lift canard, which proved to be a powerful pitch-trim device for this configuration (ref. 6). The buildup of the longitudinal aerodynamics for such a configuration is shown in figure 4. At an approach angle of attack of 14°, the configuration could generate a trimmed lift coefficient of nearly 1.5 while maintaining a nominal 3° glide slope. The approach aerodynamics presented in figure 4 display a margin of available pitching moment for pitch control above that required for trim. Unloading the canard to obtain pitch trim results in a nearly equal increase in lift on the wing behind the canard. Because of this increase, the trimmed lift coefficient is much the same as the untrimmed lift coefficient depicted in figure 4. Upon touchdown, without reducing thrust, the secondary nozzles could rotate forward and provide reverse thrust.

An investigation to determine experimentally the validity of such a thrust-reverser concept and to determine parametrically the effects of blowing angle, thrust (i.e., nozzle pressure ratio), sideslip angle, and flap deflection was conducted in the Langley 14- by 22-Foot Subsonic Tunnel. In addition, predicted performance benefits in terms of landing ground roll for a hypothetical full-scale configuration were calculated from the wind-tunnel results.

## Symbols

All data have been reduced to coefficient form. Longitudinal data are presented in the stability-axis system, and lateral-directional data are presented in the body-axis system. The in-ground-effect data were all obtained at an angle of attack of 0°; therefore the body axis and wind-tunnel stability axis are collocated for these data. The moment reference center (MRC) for these data was located at F.S. 80.53, B.L. 0, and W.L. 0 (fig. 1(b)). The symbol used in computer-generated figures, where different, is given in parentheses after the usual symbol.

| | | |
|---|---|---|
| $A$ | | aspect ratio, $b^2/S$ |
| $a$ | | acceleration, ft/sec$^2$ |
| $b$ | | span, ft |
| $C_A$ | | axial-force coefficient, $F_A/q_\infty S$ |
| $C_D$ | | drag coefficient, $C_A \cos\alpha + C_N \sin\alpha$ |
| $C_L$ | | lift coefficient, $C_N \cos\alpha - C_A \sin\alpha$ |
| $C_l$ | | rolling-moment coefficient, $M_X/q_\infty S b$ |
| $C_m$ | | pitching-moment coefficient, $M_Y/q_\infty S \bar{c}$ |
| $C_N$ | | normal-force coefficient, $F_N/q_\infty S$ |
| $C_n$ | | yawing-moment coefficient, $M_Z/q_\infty S b$ |
| $C_Y$ | $(Cy)$ | side-force coefficient, $F_Y/q_\infty S$ |
| $c$ | | local chord, in |
| $\bar{c}$ | | wing mean aerodynamic chord, ft |

| | |
|---|---|
| $D$ | drag, lbf |
| $F$ | force, lbf |
| $F_A$ | axial force, lbf |
| $F_N$ | normal force, lbf |
| $F_x$ | braking force, lbf |
| $F_Y$ | side force, lbf |
| $g$ | gravitational constant, 32.2 ft/sec$^2$ |
| $h$ | height above tunnel floor (measured from MRC), ft |
| $L$ | lift, lbf |
| $M_X$ | rolling moment, ft-lbf |
| $M_Y$ | pitching moment, ft-lbf |
| $M_Z$ | yawing moment, ft-lbf |
| $m$ | mass, slug |
| NPR | nozzle pressure ratio, $p_{t,j}/p_\infty$ |
| $p_{t,j}$ | nozzle total pressure, psf |
| $p_\infty$ | free-stream static pressure, psf |
| $q$ | dynamic pressure, psf |
| $q_\infty$ | free-stream dynamic pressure, psf |
| $S$ | wing planform area, ft$^2$ |
| $t$ | time, sec |
| $t/c$ | local wing thickness ratio |
| $V$ | velocity, knots |
| $V_g$ | ground velocity, knots |
| $x$ | distance, ft |
| $x_g$ | total ground roll distance, ft |
| $W$ | weight, lbf |
| $\alpha$ | angle of attack, deg |
| $\beta$ | sideslip angle, deg |
| $\gamma$ | flight-path angle, deg |
| $\Delta$ | difference between coefficient data |
| $\delta_f$ | flap deflection angle, deg |
| $\Lambda_c$ | cascade vector angle, deg |
| $\mu$ | braking-friction coefficient |

Subscripts:

| | |
|---|---|
| app | approach condition |
| $f$ | final condition |
| $j$ | index of summation |
| $l$ | landing condition |
| $n$ | final index of summation |
| net | total or net |

Abbreviations:

| | |
|---|---|
| B.L. | butt line, in. |
| F.S. | fuselage station, in. |
| W.L. | waterline, in. |

## Model Description and Test Conditions

The model (shown in fig. 1) tested in the Langley 14- by 22-Foot Subsonic Tunnel was a general research, swept wing-canard fighter configuration modified to accommodate the necessary features to investigate underwing spanwise blowing (refs. 1 and 3). Details of the model geometry are presented in table I. To test the secondary nozzles as thrust-reverser devices it was necessary to modify the cascades to allow forward as well as aft blowing angles. The features of the model included underwing engine nacelles, a nearly full-span slotted flap, and two-dimensional convergent-divergent (2-D C-D) vectoring primary nozzles. Although the primary nozzle could be set at either 0° or 45°, it was unvectored (0°) for this investigation. The exhaust area of the secondary cascade nozzles was 60 percent of the primary nozzle, and vector angles of 0°, −30°, and −45° measured perpendicular to the longitudinal axis were investigated in the landing mode (i.e., the primary nozzle was blocked and unvectored during this current investigation). Negative angles refer to reverse thrust, with the nozzles angled forward. The configuration with a vector angle of 0° was not a thrust-reverser configuration but was investigated to note any adverse effects that would be generated as the powered cascade nozzles were rotated forward to their reverse-thrust configuration from their aft approach configuration. The canard incidence angle was set at 0° relative to the longitudinal axis and was not varied during these tests. With the method described in reference 7, boundary-layer transition was fixed at 5 percent of the local chord on the wing and canard and at 1 in. aft of the nose.

The exhaust flow was simulated with high-pressure air fed to the model plenum through a NASA air sting. The effects of mechanical bridging of the balance as well as of pressure and momentum

(mass-flow) tares were included in the corrections to the balance outputs.

Other model instrumentation included an internally mounted accelerometer, for measuring angle of attack, and pressure transducers for measuring nozzle and piping pressures to calculate pressure ratios and mass flows.

## Test Conditions

The model was tested at an angle of attack of 0° at a height-to-span ratio $h/b$ of 0.21 (height-to-chord ratio of 0.53). The free-stream dynamic pressure $q_\infty$ was varied from 50 to 10 psf to simulate slowing during the landing ground roll. The tunnel floor boundary layer was removed at the beginning of the test section with a boundary-layer suction system. The secondary nozzles were run at nozzle pressure ratios of 2.0, 3.0, and 4.0. A nozzle pressure ratio (NPR) of 3.0 is considered a nominal engine setting (full dry thrust) and NPR's of 2.0 and 4.0 were tested to bracket the nominal value. Sideslip angles of 5° and 10° were tested in addition to 0° to simulate crosswind conditions. Only force and moment data were obtained during this investigation (no pressure or flow visualization data). Table II summarizes the configurations and conditions tested.

The model was tested statically ($q_\infty = 0$ and NPR $\geq 1.0$, see table III) out of ground effect prior to the wind-on in-ground-effect runs. This was done in order to balance the flow, left and right, because of any misalignment of the cascades or any imbalance in the internal flow. Since it was not possible to perfectly balance the flow, minor misalignments and imbalances still existed for some conditions.

## Presentation of Results

The dynamic pressure was varied for each configuration and condition to simulate the aircraft slowing down during roll-out, and the data are presented in coefficient form plotted against free-stream dynamic pressure $q_\infty$ to reflect these conditions. The power was set by nozzle pressure ratio (NPR) which, unlike thrust coefficient, is nearly constant as dynamic pressure is varied at relatively low speed and high power settings. Since the coefficients are nondimensionalized by dynamic pressure, a constant force or moment in coefficient form would be characterized as varying hyperbolically with free-stream dynamic pressure (increasing with decreasing free-stream dynamic pressure), with the axes as asymptotes. For example, total drag is dominated by direct-thrust effects during thrust-reverser operations; therefore, its coefficient should vary nearly hyperbolically with free-stream dynamic pressure. Other characteristics are dominated by aerodynamic and thrust-induced effects, so their coefficients would not be expected to vary hyperbolically with free-stream dynamic pressure.

All the data from this investigation are presented as follows, although not every part of each figure is specifically discussed in the analysis:



## Discussion of Experimental Results

Drag (the sum of aerodynamic forces and reverse thrust and equal to resultant axial force since the aircraft is at $\alpha = 0°$) is of primary importance in the determination of the performance of a thrust reverser. However, the effect of the thrust-reverser flow on the other aerodynamic characteristics of the vehicle can be extremely important because of attendant performance gains or losses. For example, positive lift would decrease the effective normal force on the main landing gear and reduce braking effectiveness, whereas negative lift would have the opposite effect. Additionally, there may be large changes in the lateral-directional characteristics of the vehicle in ground contact. For example, large yawing moments and inadequate nose-wheel control on a wet or icy runway could create a situation in which an aircraft could depart the runway at high speed.

### Effects of Cascade Vector Angle

The effects of cascade vector angle on longitudinal and lateral-directional aerodynamics are presented in figure 5. As would be expected, in all cases deflecting the cascade vector angle farther forward ($\Lambda_c = -30°$ and $-45°$) results in an increase in drag because of the larger component of thrust in the axial direction. As mentioned, the drag coefficients increase hyperbolically with decreasing free-stream dynamic

pressure, while the actual levels of drag ($C_D q_\infty S$) for $\Lambda_c = -30°$ and $-45°$ remain nearly constant as the free-stream dynamic pressure decreases. This is because the dominant force is due to direct thrust. Although nothing unexpected is seen in the drag coefficient behavior for $\Lambda_c = -30°$ and $-45°$, when $\Lambda_c = 0°$ (blowing perpendicular to the body under the wing) the spanwise-blowing flow induces loads that are probably not due to direct thrust, since the direct-thrust component should cancel out. For example, when the flaps are undeflected and $\Lambda_c = 0°$ (figs. 5(a) to 5(i)), $C_D$ increases slightly as the free-stream dynamic pressure is reduced since little or no net thrust is present. However, when $\Lambda_c = 0°$ and $\delta_f = 26°$ (figs. 5(j) to 5(m)), $C_D$ decreases with reducing free-stream dynamic pressure, starting near zero and becoming negative, an indication of positive thrust. This is accompanied by a reduction in lift and a resultant increase in pitching moment, an indication that the flap downwash may be pulling the jet slightly aft and creating a suction on the underside of the flap. The model was tested with $q_\infty = 0$, out of ground effect, to ensure there was no major misalignment of the cascade nozzles. Since the $\Lambda_c = 0°$ condition would be transient (in going from the approach to the landing configuration) and would occur only at relatively high dynamic pressures (at the beginning of the ground roll), this jet effect does not appear to be a major operational concern.

The magnitudes of lift and pitching moment are different for $\Lambda_c = -30°$ and $-45°$ because of different levels of direct thrust, but they show similar trends, an indication that the thrust-induced effects do not change significantly with cascade deflection between $\Lambda_c = -30°$ and $-45°$. The jet is located behind and slightly below moment center; therefore the direct-thrust effects would induce a nose-down pitching moment. The geometry of the flow is much different for $\Lambda_c = 0°$ compared with that for either $\Lambda_c = -30°$ or $\Lambda_c = -45°$. For $\Lambda_c = 0°$, the jet blows directly along the underside of the wing and it therefore has much different aerodynamic characteristics. Although the flow fields for both $\Lambda_c = -30°$ and $\Lambda_c = -45°$ are dominated by direct-thrust effects, the flow field for $\Lambda_c = 0°$ is dominated by thrust-induced effects. As free-stream dynamic pressure is reduced there is a small reduction and a subsequent increase in lift for $\Lambda_c = -30°$ and $-45°$; for $\Lambda_c = 0°$ there is a constant reduction of $C_L$ as free-stream dynamic pressure decreases. Except for the level of lift lost this trend is similar for all conditions (figs. 5(a) to 5(m)), including the cases with flaps deflected ($\delta_f = 26°$). The lift loss is due to the jet creating a low-pressure region under the wing often referred to as suckdown. The major differences between thrust-induced effects and direct-thrust effects include more suckdown, nose-up pitching moment, and comparatively little drag change. For $\Lambda_c = 0°$ most of the $C_D$ changes are due to thrust-induced effects. The thrust-induced pitching-moment characteristics, for the most part, are what would be expected with thrust-induced lift (positive or negative) being generated behind the moment reference center.

In general, increasing the cascade vector angle from $\Lambda_c = 0°$ to $-30°$ has some effect on the lateral-directional characteristics. However, increasing from $\Lambda_c = -30°$ to $-45°$ generally causes few additional effects. There are many exceptions to these generalities, mainly because of asymmetries in the flow field. Ideally, the geometric symmetry of the model should produce a symmetric flow field and there should be no effect on lateral-directional characteristics from any model or flow condition except for sideslip angle. However, this is not the case and asymmetries are present in the data. Many of these asymmetries can be accounted for by the presence of slight differences in thrust (cascade vector angle or NPR) from one side to the other. These asymmetries show up as small changes in side force $C_Y$ and yawing moment $C_n$ which get larger as free-stream dynamic pressure is decreased, and since they are dominated by direct thrust they should vary nearly hyperbolically. Other asymmetries cannot be attributed to variations in direct thrust. These asymmetries tend to show up as changes in rolling moment $C_l$, changes in side force $C_Y$ without a corresponding change in yawing moment $C_n$ due to the moment arm, or changes in yawing moment without a change in side force. The causes of these asymmetries are sometimes difficult to locate and are most likely due to thrust-induced effects and uneven flow attachment to the model surfaces. These types of asymmetries also tend to show up as large deviations from a trend and usually occur only for a specific set of conditions.

### Effects of Nozzle Pressure Ratio

The effects of nozzle pressure ratio on the longitudinal and lateral-directional aerodynamics are presented in figure 6. As would be expected, for either $\Lambda_c = -30°$ or $\Lambda_c = -45°$ an increase in nozzle pressure ratio results in a significant increase in $C_D$ for all dynamic pressures. In every case for which $\Lambda_c = -30°$ or $-45°$ (figs. 6(a), 6(b), 6(d), 6(e), 6(g), 6(h), 6(j), and 6(k)) the trends for both $C_L$ and $C_m$ are different for NPR = 2.0 than those for NPR = 3.0 and NPR = 4.0. The plume of a nozzle operating at NPR = 3.0 is more completely developed than that of a nozzle at NPR = 2.0, but it does not develop much more in going to NPR = 4.0 from NPR = 3.0. This results because at NPR = 2.0 the

nozzle is just choked (should be choked at NPR = 1.9) and probably has local regions where the flow is subcritical (below choked condition). At NPR $\geq$ 3.0 the entire nozzle exit is most likely choked and the plume is probably overexpanded. This difference in the plume could cause the configuration operating at NPR = 2.0 to have different thrust-induced effects than those for the nozzle operating at NPR $\geq$ 3.0. For $\Lambda_c = 0°$ (figs. 6(c), 6(f), 6(i), and 6(l)) a change in NPR has nearly no effect on $C_D$, although it has a marked effect on $C_L$ and $C_m$. As discussed previously, the jet is blowing directly under the wing perpendicular to the longitudinal axis, so the major effect is expected to be a lift loss (suckdown) and no significant force in the axial direction. The lift loss is greatest for higher NPR's and lower free-stream dynamic pressures. At lower free-stream dynamic pressures the curves tend to converge ($\Delta C_l \approx 0$). With $\Lambda_c = -30°$ and $-45°$ significant suckdown is also experienced, although it is generally not quite as strong nor as dependent on NPR as that for $\Lambda_c = 0°$, apparently because less flow is interacting with the wing. The reverse-thrust cases ($\Lambda_c = -30°$ and $-45°$) also experience less of an effect on lift loss at lower free-stream dynamic pressures because of changing NPR. This occurs because at higher NPR's and lower free-stream dynamic pressures the jet travels well beyond the wing before it decays sufficiently to be turned outboard by the free stream. At higher free-stream dynamic pressures and lower NPR's the flow is more likely to be turned outboard by the free stream earlier and therefore interacts with a larger portion of the wing.

The effect of NPR on the lateral-directional aerodynamics is in general to magnify, with increasing NPR, any asymmetries present because of thrust level or thrust vector, although there are many exceptions which do not follow any obvious pattern. For example, for $\Lambda_c = -45°$ and $\delta_f = 0°$ (fig. 6(a)) $C_l \approx 0$ at both NPR = 2.0 and NPR = 4.0 between $q_\infty = 50$ and 20 psf, but $C_l \approx -0.02$ at NPR = 3.0 for $q_\infty = 50$ psf. All three power settings (NPR = 2.0, 3.0, and 4.0) result in $C_l$ collapsing to about 0.01 ($\Delta C_l \approx 0$) at $q_\infty = 10$ psf. Side force is also significantly different for NPR = 3.0 than it is for NPR = 2.0 or 4.0. It is unexpected that both the high and the low NPR's would show similar trends and that the intermediate NPR would show such an anomaly. The most likely hypothesis for such a phenomenon is that with the lower power setting the jet flow on both wings is attached, at the higher setting the flow on both is completely detached, and at the intermediate setting the flow on one wing is attached and not on the other. For $\delta_f = 26°$ with $\Lambda_c = -45°$ (fig. 6(j)) the same anomaly is not present at NPR = 3.0 and there is a lower level of asymmetry, probably because of inhibiting flow entrainment under the wings.

### Effects of Flap Deflection

The effects of flap deflection on longitudinal and lateral-directional aerodynamic characteristics are presented in figure 7. In general the effect of flap deflection on drag is very small (slightly more drag, $\Delta C_D \leq 0.05$, with flaps deflected) for $\Lambda_c = -30°$ and $-45°$. For $\Lambda_c = 0°$ (figs. 7(j) to 7(m)), however, the flap effect on drag is significant. With the flaps retracted ($\delta_f = 0°$) and $\Lambda_c = 0°$ the drag level for all NPR's is fairly constant ($C_D = 0.1$), but with the flaps deflected ($\delta_f = 26°$) $C_D \leq 0$ (thrust) for every NPR, with increasingly larger negative values as free-stream dynamic pressure decreases. The effect is nearly identical for every NPR.

In general the effect of flap deflection on the longitudinal aerodynamics for $\Lambda_c = -30°$ or $-45°$ results from the reduction or elimination of the flow entrainment caused by the jet, in addition to the classic effects of the flap itself without the jet. The increases in $C_D$, $C_L$, and negative $C_m$ with the flaps deflected can be predominantly explained as the effect of a flap alone, without the presence of the jet. The lift levels for $\Lambda_c = -30°$ and $-45°$ are also increased with flaps extended. (With the flaps deflected the lift is generally positive, and it is negative with the flaps retracted.) This effect would be expected from the flaps alone (without the thrust-reverser flow), with the recognition that with the flaps deflected, flow entrainment, which is at least partially responsible for the suckdown effect, is inhibited. In general the pitching-moment changes can be attributed to the changes of the wing lift vector, which is behind the moment reference center.

The effect of flap deflection on the lateral-directional characteristics is small in many cases, but it does lessen many severe asymmetries as previously observed. For example, when $\Lambda_c = 0°$ (figs. 7(j) to 7(m)) with the flaps undeflected, the configurations generate large yawing moments and side forces that are reduced with flap deflection in all cases except NPR = 2.0 (fig. 7(m)), for which the forces and moments are in the opposite directions. Again this is most likely a result of inhibited flow entrainment under the wings.

### Effects of Sideslip Angle

The effects of sideslip angle on the longitudinal and lateral-directional aerodynamic characteristics are presented in figure 8. The effect of sideslip angle on the longitudinal characteristics is minor or insignificant; however, it is significant for the lateral-directional characteristics, as expected. For every

case an increase in sideslip angle creates an increase in negative side force, which is expected without the presence of the jet effects. The corresponding yawing-moment changes are relatively small, but since this model had a large amount of side area well forward of the moment reference center, this would be expected to partially counteract the dominant effect of the tail. Rolling-moment changes with sideslip angle, which are fairly significant, can be partially explained by the 50° leading-edge sweep. The upwind wing on a swept-wing aircraft in a sideslip has its effective sweep angle reduced by the sideslip angle, and this reduction increases the normal free-stream component and therefore increases its lift (dihedral effect). The opposite effect is experienced by the downwind wing. Another factor is the effect of the jet in a sideslip and its effect on the wing, and these effects are also expected to be different for the upwind and downwind wings. The jet on the leeward side would experience lower resistance (lower effective dynamic pressure) than that on the windward side. This lower resistance would promote more flow entrainment on the leeward side than on the windward side. Sideslip would also cause the windward jet to decay faster since it would be experiencing more resistance. In general, at higher free-stream dynamic pressure the effects of sideslip angle are as expected. That is, a sideslip angle usually generates a side force in the direction of the sideslip (i.e., nose left, positive sideslip angle $\beta$, generates a side force to the left), a restoring yawing moment (i.e., nose left generates a yawing moment to the right), and a rolling moment away from the relative wind (i.e., nose left generates a rolling moment to the left (dihedral effect)). Since each of these effects have different results and each is present to some degree, it is not always possible to know which phenomenon is dominant. Because at lower free-stream dynamic pressures the jet-induced aerodynamic loads are dominant over the free-stream-induced aerodynamic loads, it would not be surprising that more unusual changes in lateral-directional characteristics are observed at lower free-stream dynamic pressures than at higher ones.

In general, most of the effects of sideslip are as mentioned. One exception to this generality is the case of apparent flow attachment. These flow-attachment asymmetries normally show up in rolling moment. One probable example of such a flow-attachment problem is shown in the rolling-moment characteristics for $\Lambda_c = -30°$ and $\delta_f = 26°$ (fig. 8(l)). Between $q_\infty = 50$ and 30 psf the rolling-moment coefficient remains nearly constant and the effect of sideslip ($\beta = 10°$) is in the direction expected. At $\beta = 10°$ and $q_\infty = 20$ psf, $C_l \approx -0.037$, whereas at $\beta = 0°$ and $q_\infty = 20$ psf, $C_l \approx -0.008$. At $q_\infty = 10$ psf, both curves ($\beta = 0°$ and 10°) converge ($\Delta C_l \approx 0$).

## Prediction of Landing Ground Roll

Landing ground roll was predicted with the method described in the appendix. It is assumed that a thrust reverser was installed on a conceptual full-scale configuration of the wind-tunnel model (i.e., model data scaled up). The following assumptions were also made: (1) the aircraft incorporated a high-lift system with the same secondary nozzles; (2) a 1-sec delay time was used to rotate the nozzles from the approach condition to the thrust-reverser condition; (3) the braking-friction coefficient varied with forward velocity at a magnitude typically produced by an antiskid braking system on this class of aircraft (fig. 9); (4) the braking system had a 2-sec time delay; and (5) the thrust reverser was deployed down to a slow taxi speed ($V_f \approx 5$ knots).

Figure 10 presents the predicted landing ground roll $x_g$ as a function of approach lift coefficient $C_{L,\text{app}}$ for typical dry, wet, and icy (assumed no wheel braking available) runway conditions. The calculations in each figure are based on an average wing loading $W/S$ of 40.0 psf, a landing weight of 20 000 lb, the throttle at full military power (NPR = 3.0), and the typical delay times mentioned previously. Aerodynamic characteristics ($C_D$ and $C_L$) with the thrust reverser operating were obtained from the wind-tunnel data. With a dry runway condition the differences with cascade vector angle and flap deflection are minimal. This is because wheel braking is very effective under these conditions. When braking effectiveness is diminished (wet and icy conditions), the $\Lambda_c = -45°$ reverser dominates. This is because it provides more thrust reversing (higher $C_D$), but less suckdown, as the brakes become ineffective. In all cases the flaps being deflected or retracted ($\delta_f = 26°$ or 0°) has little impact on reduction of the landing ground roll at a constant approach lift coefficient. Increasing the approach lift coefficient (i.e., reducing touchdown velocity) from 0.8 to 2.5 reduces the landing ground roll approximately 50 percent. The variations in ground roll noticeable at lower approach lift coefficients are due to the delay times (modeled as step functions) for reverser deployment and brake actuation becoming more influential (i.e., more or less ground roll prior to reverser deployment or brake actuation).

## Summary of Results

There are many things to be considered when evaluating a thrust reverser. A rule of thumb for evaluation is that if a thrust reverser can obtain

reverse-thrust levels in excess of 50 percent of maximum dry power, it may be a viable concept.

Stability and control considerations must also be taken into account when performance is evaluated, and things such as reingestion and the probability of foreign-object damage are important. (Tests have shown that normally the velocity at which foreign-object damage becomes a problem is less than that for reingestion (ref. 6).)

The thrust reverser evaluated in this investigation has not been used on a test aircraft, but its characteristics can be predicted from wind-tunnel results. Deployment time would be quick if the engines are at high power during the approach, as would be the case if the associated high-lift system is used, so some reverse thrust would be available as soon as the vector angle is forward of perpendicular ($\Lambda_c < 0°$). Although no flow visualization was done during this investigation, with the flow blowing in the geometry tested and not striking the ground plane, reingestion should be minimized and the possibility of foreign-object damage should be very small. A thrust reverser of this type would be able to deploy routinely down to taxi speed, whereas a bucket-type thrust reverser would only be deployed at such low speeds in emergencies. This concept, however, appears to suffer from some of the same disadvantages as the bucket-type thrust reverser, namely a loss of directional stability and yawing-moment asymmetries. In addition, it suffers from rolling-moment asymmetries and other possible flow-attachment problems. (Early bucket-type thrust reversers, such as those discussed in ref. 6, also suffered from this but were eventually corrected.) However, the thrust reverser investigated herein may have the additional advantage of some modest suckdown, which would increase the braking effectiveness, and it could use differential vector angles to contol yaw. The thrust-reverser flow is nowhere near the rudder, so it is improbable that rudder effectiveness would be degraded by its use. The thrust reverser with $\Lambda_c = -45°$ would be able to turn up to 71 percent of the flow, and with $\Lambda_c = -30°$ the reverser could turn up to 50 percent of the flow. These values would be reduced somewhat when turning losses are considered.

## Conclusions

An experimental investigation on the viability of a thrust-reverser concept employing dual-function secondary nozzles has been completed, and the following conclusions summarize the results:

1. The secondary cascade nozzles (cascade vector angle $\Lambda_c = -45°$ and $-30°$) are capable of generating a sufficient and nearly constant level of reverse thrust from free-stream dynamic pressures of 50 to 10 psf.

2. Longitudinal interactions for $\Lambda_c = -45°$ and $-30°$ include modest suckdown with some nose-up pitching moment without flaps deflected. With flaps deflected (26°) some positive lift is generated and is accompanied by a nose-down pitching moment. With $\Lambda_c = 0°$, which would be a transient condition between the approach cascade vector angles and the thrust-reversing cascade vector angles, the major longitudinal interactions are an increase in suckdown compared with $\Lambda_c = -30°$ and $-45°$ at lower free-stream dynamic pressures, a slight decrease in drag becoming negative (thrust) with flaps deflected (26°) at lower free-stream dynamic pressures, and a slight decrease in drag becoming negative with flaps deflected.

3. Lateral-directional interactions, which include asymmetries in yawing moment, rolling moment, and side force, are experienced in many cases. An apparent flow-attachment asymmetry may create potential stability and control problems, although these are reduced with the flaps deflected (26°).

4. This thrust reverser on a fighter type configuration could be capable of reducing the landing ground roll so that it would be on the order of the length of the takeoff ground run, even under adverse runway conditions where braking effectiveness would be decreased (for wet runway) or negligible (for icy runway).

NASA Langley Research Center
Hampton, VA 23665-5225
August 10, 1988

# Appendix

## Prediction of Landing Ground Roll

Landing ground roll can be predicted from the wind-tunnel results. In cases wherein the forces acting on the aircraft can be considered uniform, a closed-form approximation yields an accurate solution (ref. 8). However, many other cases exist wherein such an approximation is not sufficient. If detailed data, such as those from a wind tunnel, are available, an accurate prediction may still be made.

The known boundary conditions are the initial touchdown velocity $V_l$ and the final velocity $V_f$ (which is usually close to zero). What is then needed is the rate of change of the velocity, or deceleration, during the landing roll-out as a function of distance:

$$F = ma \tag{1}$$

and

$$\frac{F}{m} = \frac{dV}{dt} \tag{2}$$

Then, after multiplication by $V$,

$$V\frac{F}{m} = V\frac{dV}{dt} = \frac{1}{2}\frac{d(V^2)}{dt} \tag{3}$$

If equation (3) is considered over a finite but short period of time, then

$$\frac{F}{m}\frac{\Delta x}{\Delta t} = \frac{1}{2}\frac{\Delta(V^2)}{\Delta t} \tag{4}$$

and thus,

$$\Delta x = \frac{1}{2}\frac{m}{F}\Delta(V^2) \tag{5}$$

In order to calculate the landing-ground-roll distance $x_g$, it is necessary to sum small increments $\Delta x$ such that $V^2$ and $F$ can be treated as continuous and linear during the interval. A mean value of each can then be obtained for the interval and an approximation for the landing ground roll can be determined; thus,

$$x_g \approx \frac{m}{2}\sum_{j=1}^{n}\frac{\overline{V_j^2}}{\overline{F_j}} \tag{6}$$

which may also be written as

$$x_g \approx \frac{m}{2}\sum_{j=1}^{n}\frac{V_j^2 + V_{j+1}^2}{F_j + F_{j+1}} \tag{7}$$

where $j = 1$ corresponds to $V = V_l$ and $j = n$ corresponds to $V = V_f$. The acceleration $a$ at any instant can be computed by

$$a = \frac{\text{Net forces in } X\text{-direction}}{m} \tag{8}$$

There are three major forces acting on the aircraft: aerodynamic drag, friction from the tires and brakes, and drag from auxiliary devices including thrust reversers, drag chutes, and arresting wires. If the net drag is measured (scaled from the model test), then only the braking effectiveness is left to be calculated. Braking force (in the $X$-direction) is usually expressed as:

$$F_x = \mu F_N \tag{9}$$

where $\mu$ is the braking coefficient and $F_N$ is the normal force acting on the wheels. Then,

$$F = (D_{\text{net}} + \mu F_N) \tag{10}$$

The braking coefficient $\mu$ varies nonlinearly with velocity but is relatively linear over an interval in which $a$ is linear, and it can therefore be averaged over each increment. The total net normal force $F_{N,\text{net}}$ is the weight of the aircraft less any lift (or plus lift if it is a down load):

$$F_{N,\text{net}} = W - L \tag{11}$$

Then,

$$F = [D_{\text{net}} + \mu(W - L)] \tag{12}$$

Combining the terms and using coefficient notation for drag ($D = C_D qS$) and lift ($L = C_L qS$) yields

$$x_g \approx \frac{m}{2} \sum_{j=1}^{n} \frac{V_j^2 + V_{j+1}^2}{[C_D qS + \mu(mg - C_L qS)]_j + [C_D qS + \mu(mg - C_L qS)]_{j+1}} \tag{13}$$

where $j = 1$ corresponds to $V = V_1$, $j = n$ corresponds to $V = V_f$, and

$$\left.\begin{aligned} q &= \frac{1}{2}\rho V^2 \\ W &= mg \end{aligned}\right\} \tag{14}$$

With the aid of a computer, many small intervals can be calculated to obtain an accurate numerical solution.

This summation approximation must take intervals small enough so that all the forces and moments acting on the aircraft may be treated as being continuous and linear over the interval. It is also necessary to have fairly detailed aerodynamic data, including the interaction of the thrust reverser with the aircraft. The aerodynamic characteristics that most affect the landing performance are drag and lift. Pitching moment can affect the normal force on the main landing gear, and since the main wheels are normally the only ones with brakes, $C_m$ can change the ultimate braking effectiveness, but this change is usually insignificant. Many other factors also affect the ground roll. The touchdown velocity (based on wing load and approach lift coefficient) is of paramount importance, since it determines the initial landing velocity. The runway condition (dry, wet, or icy) affects the braking coefficient and therefore the braking effectiveness. Inertia and mechanical actuation time cause unavoidable delays in the thrust-reverser deployment, while reingestion and foreign-object damage make it impractical to operate the thrust reverser below some specified minimum velocity (typically well above the taxi speed of these aircraft). In order to get the maximum possible benefit from the thrust reverser, reverse thrust should be maintained for as long as possible; power may be reduced or the mechanism may be scheduled to provide only partial reverse thrust to avoid reingestion and foreign-object damage at low speeds.

## References


1. Paulson, John W., Jr.; Quinto, P. Frank; and Banks, Daniel W.: *Investigation of Trailing-Edge-Flap Spanwise-Blowing Concepts on an Advanced Fighter Configuration.* NASA TP-2250, 1984.
2. Banks, Daniel W.; Quinto, P. Frank; and Paulson, John W., Jr.: *Thrust Induced Effects on Low-Speed Aerodynamics of Fighter Aircraft.* NASA TM-83277, 1982.
3. Banks, Daniel W.; and Paulson, John W., Jr.: *Low-Speed Aerodynamic Characteristics of a Wing-Canard Configuration With Underwing Spanwise Blowing on the Trailing-Edge Flap System.* NASA TM-89020, 1987.
4. Banks, Daniel W.; and Paulson, John W., Jr.: Approach and Landing Technologies for STOL Fighter Configurations. *J. Aircr.*, vol. 22, no. 4, Apr. 1985, pp. 277–282.
5. Eagles, John David: Development of the Tornado Thrust Reverser. 1981 Report to the Aerospace Profession, *Tech. Reviews,* vol. 16, no. 2, Soc. Exp. Test Pilots, 1981, pp. 65–79.
6. Paulson, J. W., Jr.; Gatlin, G. M.; Quinto, P. F.; and Banks, D. W.: Trimming Advanced Fighters for STOL Approaches. *J. Aircr.*, vol. 20, no. 11, Nov. 1983, pp. 957–962.
7. Braslow, Albert L.; and Knox, Eugene C.: *Simplified Method for Determination of Critical Height of Distributed Roughness Particles for Boundary-Layer Transition at Mach Numbers From 0 to 5.* NACA TN 4363 1958.
8. Perkins, Courtland D.; and Hage, Robert E.: *Airplane Performance Stability and Control.* John Wiley & Sons, Inc., c.1949.

Table I. Basic Model Geometry

| | |
|---|---|
| **Body:** | |
| Length, in. | 91.20 |
| Width, in. | 7.20 |
| **Wing:** | |
| $A$ | 2.79 |
| $S$, ft$^2$ | 5.73 |
| $b$, in. | 48.0 |
| $\bar{c}$, in. | 19.11 |
| $c$ at root, in. | 27.86 |
| $c$ at tip, in. | 6.52 |
| Leading-edge sweep, deg | 50 |
| Trailing-edge sweep, deg | 27.86 |
| Moment center (F.S.), in. | 80.53 |
| **Airfoil:** | |
| Section | 6 percent aft cambered |
| $t/c$ at root | 0.06 |
| $t/c$ at tip | 0.06 |
| Twist at tip, deg | −6 |
| **Wing flaps:** | |
| $b$, in. | 6.34 |
| $c$ (inboard, B.L. 7.0), in. | 5.61 |
| $c$ (outboard, B.L. 19.68), in. | 2.88 |
| Hinge line | 0.726$c$ |
| **Nacelle:** | |
| Length, in. | 24.56 |
| Width, in. | 3.9 |
| **Nozzle exit:** | |
| Width, in. | 2.57 |
| Height, in. | 0.74 |
| F.S., in. | 101.79 |
| B.L., in. | 5.04 |
| W.L., in. | 8.26 |
| **Canard:** | |
| $A$ (exposed) | 2.76 |
| $S$ (exposed), ft$^2$ | 1.01 |
| $b/2$ (exposed), in. | 10.04 |
| $c$ at root (B.L. 3.6), in. | 11.71 |
| $c$ at tip, in. | 2.82 |
| **Canard airfoil:** | |
| Section root | NACA 65A004 (modified) |
| Section tip | NACA 65A003 (modified) |
| $t/c$ at root | 0.04 |
| $t/c$ at tip | 0.03 |
| Twist, deg | 0 |

Table II. Configurations and Conditions Tested

| $\Lambda_c$, deg | NPR | $\delta_f$, deg | $\beta$, deg |
|---|---|---|---|
| −45 | 2.0 | 0 | 0 |
| ↓ | 2.0 | ↓ | 5 |
| | 2.0 | | 10 |
| | 3.0 | | 0 |
| | 3.0 | | 5 |
| | 3.0 | | 10 |
| | 4.0 | | 0 |
| | 4.0 | | 5 |
| | 4.0 | | 10 |
| −30 | 2.0 | | 0 |
| ↓ | 2.0 | | 5 |
| | 2.0 | | 10 |
| | 3.0 | | 0 |
| | 3.0 | | 5 |
| | 3.0 | | 10 |
| | 4.0 | | 0 |
| | 4.0 | | 5 |
| | 4.0 | | 10 |
| 0 | 2.0 | | 0 |
| ↓ | 2.0 | | 5 |
| | 2.0 | | 10 |
| | 3.0 | | 0 |
| | 3.0 | | 5 |
| | 3.0 | | 10 |
| | 4.0 | | 0 |
| | 4.0 | | 5 |
| | 4.0 | | 10 |
| −45 | 2.0 | 26 | 0 |
| ↓ | 2.0 | ↓ | 10 |
| | 3.0 | | 0 |
| | 3.0 | | 10 |
| | 4.0 | | 0 |
| | 4.0 | | 10 |
| −30 | 2.0 | | 0 |
| ↓ | 3.0 | | 0 |
| | 3.0 | | 10 |
| | 4.0 | | 0 |
| 0 | 2.0 | | 0 |
| ↓ | 3.0 | | 0 |
| | 3.0 | | 10 |
| | 4.0 | | 0 |

Table III. Static Forces and Moments Out of Ground Effect

$[\alpha = 0°;\ \beta = 0°;\ q_\infty = 0$ psf$]$

(a) $\delta_f = 0°$

| NPR | $F_N$, lbf | $F_A$, lbf | $F_Y$, lbf | $M_Y$, in-lbf | $M_Z$, in-lbf | $M_X$, in-lbf |
|---|---|---|---|---|---|---|
| | | | $\Lambda_c = -45°$ | | | |
| 1.0000 | 0.057373 | 0.14802 | −1.9993 | −1.0492 | −1.9932 | 0.068969 |
| 1.1289 | −.80834 | 17.013 | −.69958 | −26.036 | 2.3230 | 2.1079 |
| 2.1560 | −1.5236 | 38.715 | −1.7661 | −67.820 | 21.690 | 5.1688 |
| 3.2606 | −2.1892 | 57.191 | −3.0521 | −90.616 | 46.350 | 11.140 |
| 4.3838 | −1.7456 | 76.144 | −5.2088 | −133.09 | 81.908 | 19.518 |
| 5.4559 | −3.2746 | 93.858 | −7.4118 | −153.94 | 102.67 | 27.872 |
| 2.7079 | −1.8794 | 47.118 | −3.4912 | −64.202 | 47.492 | 13.565 |
| 1.0000 | −.028396 | .20757 | −.39460 | −.70884 | −5.4187 | .26364 |
| | | | $\Lambda_c = -30°$ | | | |
| 1.1387 | 0.093060 | 11.105 | −0.46024 | 3.1215 | 12.630 | 2.3348 |
| 2.2120 | −.87239 | 26.728 | −1.5202 | −19.495 | 34.832 | 8.0238 |
| 3.3265 | −2.2164 | 39.539 | −3.5134 | −27.254 | 62.700 | 12.181 |
| 4.3379 | −2.1409 | 51.609 | −5.2861 | −30.924 | 88.645 | 19.903 |
| 5.4380 | −.45552 | 65.308 | −7.5781 | −97.340 | 122.25 | 31.073 |
| 2.8969 | −1.5148 | 34.603 | −3.6378 | −9.2669 | 62.279 | 14.544 |
| 1.0000 | .11827 | −.52040 | .34022 | 5.5603 | 3.4104 | −2.2958 |
| | | | $\Lambda_c = 0°$ | | | |
| 1.1917 | 1.1759 | 0.36780 | −1.8003 | 34.806 | −4.6385 | 4.9409 |
| 2.1770 | .29311 | .79412 | −3.1823 | 63.347 | 11.045 | 14.040 |
| 3.2906 | −.018311 | 1.2311 | −5.3227 | 82.261 | 28.633 | 20.282 |
| 4.4720 | −.36795 | 2.3334 | −7.5193 | 125.22 | 56.917 | 31.514 |
| 5.5249 | .81176 | 3.8981 | −9.7502 | 133.06 | 73.339 | 40.079 |
| 2.8914 | .16277 | 1.3361 | −5.4073 | 84.594 | 29.659 | 24.115 |
| 1.0000 | −.31421 | .46021 | −.81232 | −8.6191 | −16.911 | −.080594 |

Table III. Concluded

$[\alpha = 0°;\ \beta = 0°;\ q_\infty = 0$ psf$]$

(b) $\delta_f = 26°$

| NPR | $F_N$, lbf | $F_A$, lbf | $F_Y$, lbf | $M_Y$, in-lbf | $M_Z$, in-lbf | $M_X$, in-lbf |
|---|---|---|---|---|---|---|
| | | | $\Lambda_c = -45°$ | | | |
| 1.0000 | 0.57933 | −0.063583 | 0.15124 | 9.1716 | 1.9557 | −0.78783 |
| 1.1176 | −1.0291 | 14.931 | −.51859 | −23.439 | 19.719 | 1.9260 |
| 2.1984 | −3.6059 | 37.735 | −2.5542 | −68.624 | 47.747 | 6.3610 |
| 3.3190 | −4.2856 | 55.791 | −4.1955 | −116.34 | 74.594 | 11.181 |
| 4.4435 | −5.1594 | 74.258 | −6.6511 | −143.48 | 104.75 | 19.940 |
| 5.5303 | −7.3268 | 91.140 | −8.2883 | −169.10 | 147.01 | 23.673 |
| 2.7511 | −3.5620 | 46.296 | −3.2434 | −75.043 | 63.735 | 8.9008 |
| 1.0000 | −.15916 | −.30356 | .32756 | 6.0737 | 3.3886 | −3.7476 |
| | | | $\Lambda_c = -30°$ | | | |
| 1.0000 | −0.99806 | −0.10064 | 0.32392 | −12.594 | −0.84348 | −0.68504 |
| 1.0925 | −1.8610 | 10.216 | −1.0448 | −18.378 | 14.154 | 3.3695 |
| 2.3871 | −3.7883 | 28.208 | −3.0008 | −42.738 | 46.934 | 11.209 |
| 3.3388 | −4.6394 | 39.283 | −4.5246 | −67.955 | 71.189 | 14.161 |
| 4.2869 | −6.3720 | 49.736 | −6.5835 | −91.478 | 102.47 | 19.604 |
| 4.5131 | −7.4604 | 52.393 | −7.0728 | −90.190 | 97.217 | 25.265 |
| 5.5165 | −7.8282 | 63.832 | −9.0363 | −124.22 | 121.31 | 27.842 |
| 2.8637 | −5.9856 | 33.889 | −4.4213 | −61.780 | 56.000 | 13.568 |
| 1.0000 | −1.1808 | −.45330 | .20714 | −13.061 | .86302 | −1.8610 |
| | | | $\Lambda_c = 0°$ | | | |
| 1.0000 | −0.24067 | 0.093829 | −0.095262 | −4.1841 | −1.7917 | 0.27011 |
| 1.1419 | −1.2915 | −.15891 | −1.4585 | 10.561 | 9.7534 | 6.2030 |
| 2.2748 | −1.4623 | −.32783 | −3.0817 | 60.448 | 22.453 | 17.331 |
| 3.2845 | −3.5729 | .041899 | −4.7256 | 61.862 | 44.819 | 19.907 |
| 4.4349 | −4.5160 | .24298 | −6.2409 | 92.381 | 67.385 | 27.291 |
| 5.6843 | −3.8645 | .33329 | −8.5659 | 102.87 | 80.924 | 23.120 |
| 2.7088 | −2.5607 | −.17818 | −3.6597 | 50.005 | 34.049 | 15.893 |
| 1.0000 | .17178 | −.19587 | −.21122 | 5.1648 | −2.0404 | −.50112 |

L-88-106

(a) Model in wind tunnel.

Figure 1. Wing-canard fighter model as tested in Langley 14- by 22-Foot Subsonic Tunnel.

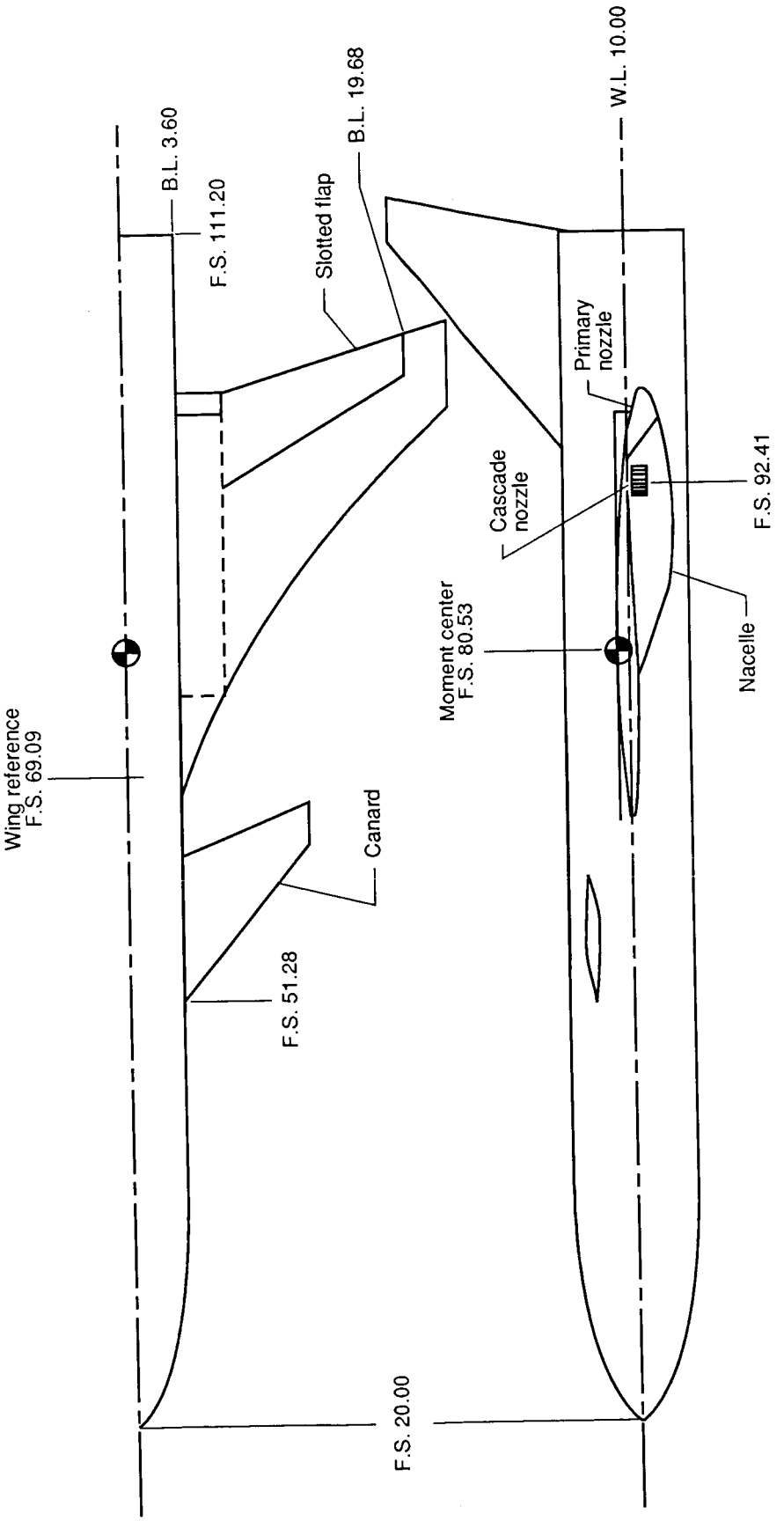


(b) Geometry. All dimensions are in inches.

Figure 1. Concluded.

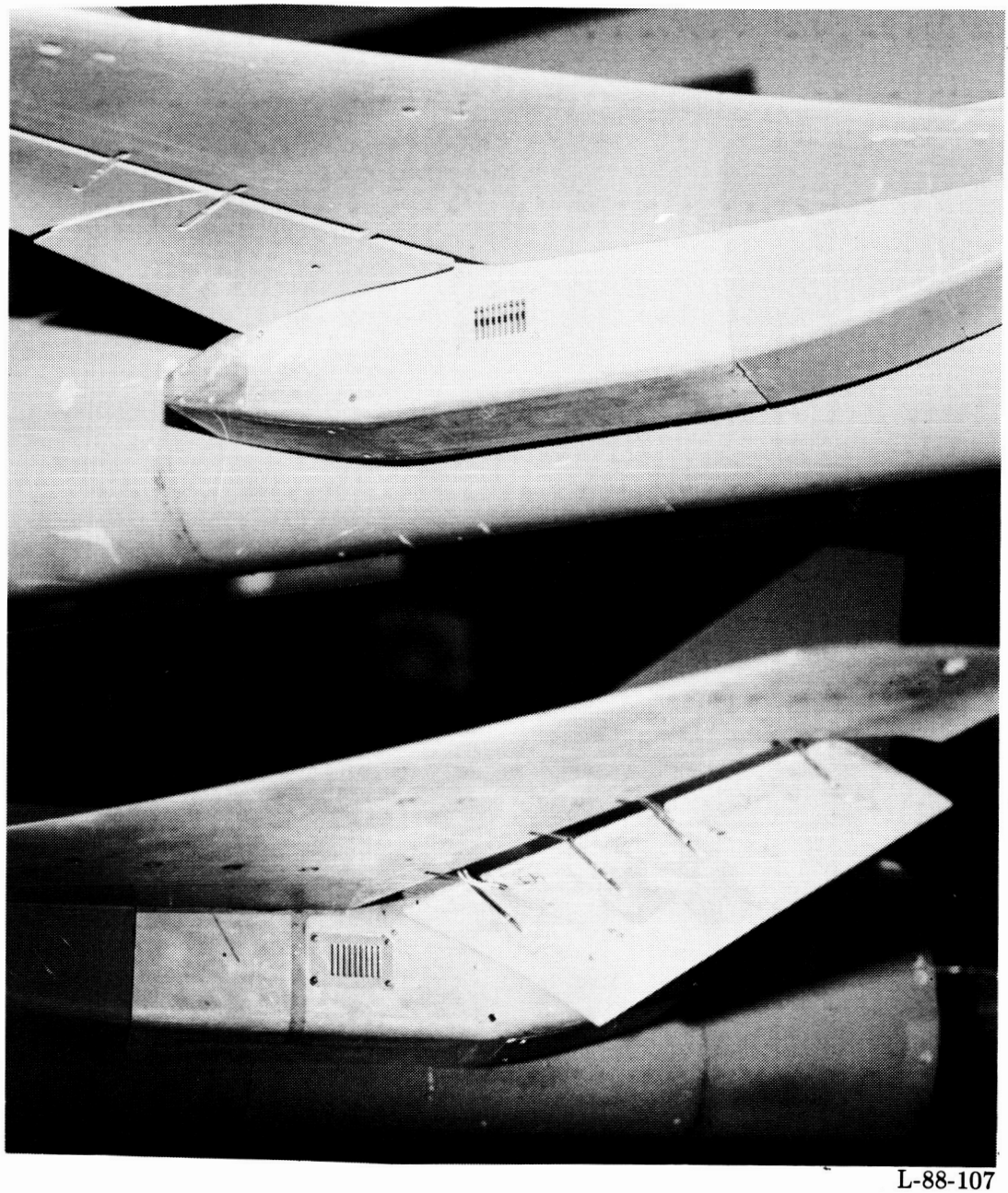

L-88-107

(a) Wind-tunnel model.

Figure 2. Cascade nozzles installed on wing-canard fighter model.

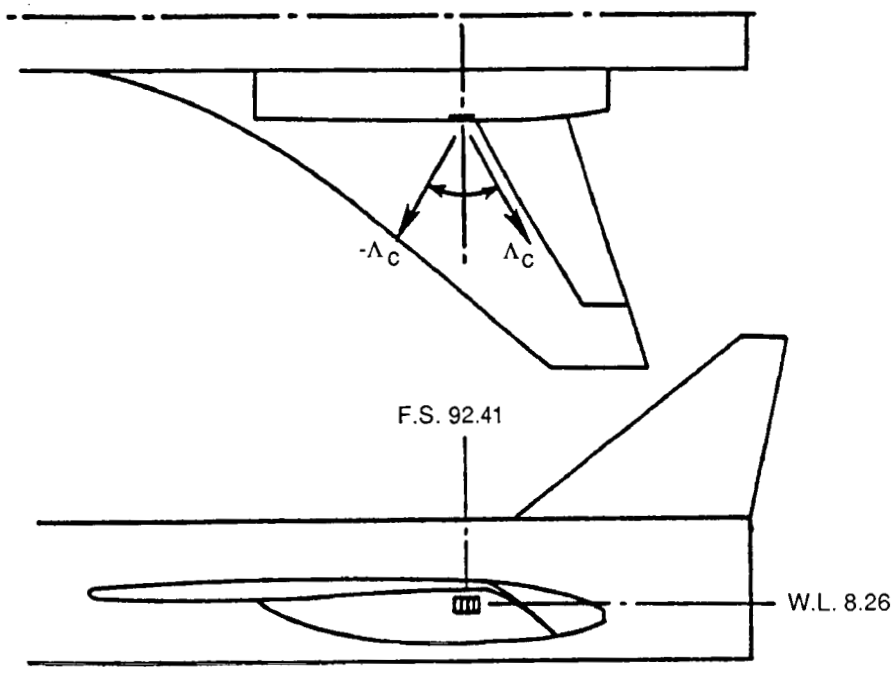


Basic cascade nozzle

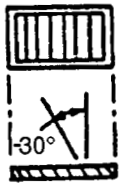


(b) Geometry.

**Figure 2. Concluded.**

L-88-108

(a) Model of configuration.

Figure 3. Conceptual configuration with high-lift blown canard.

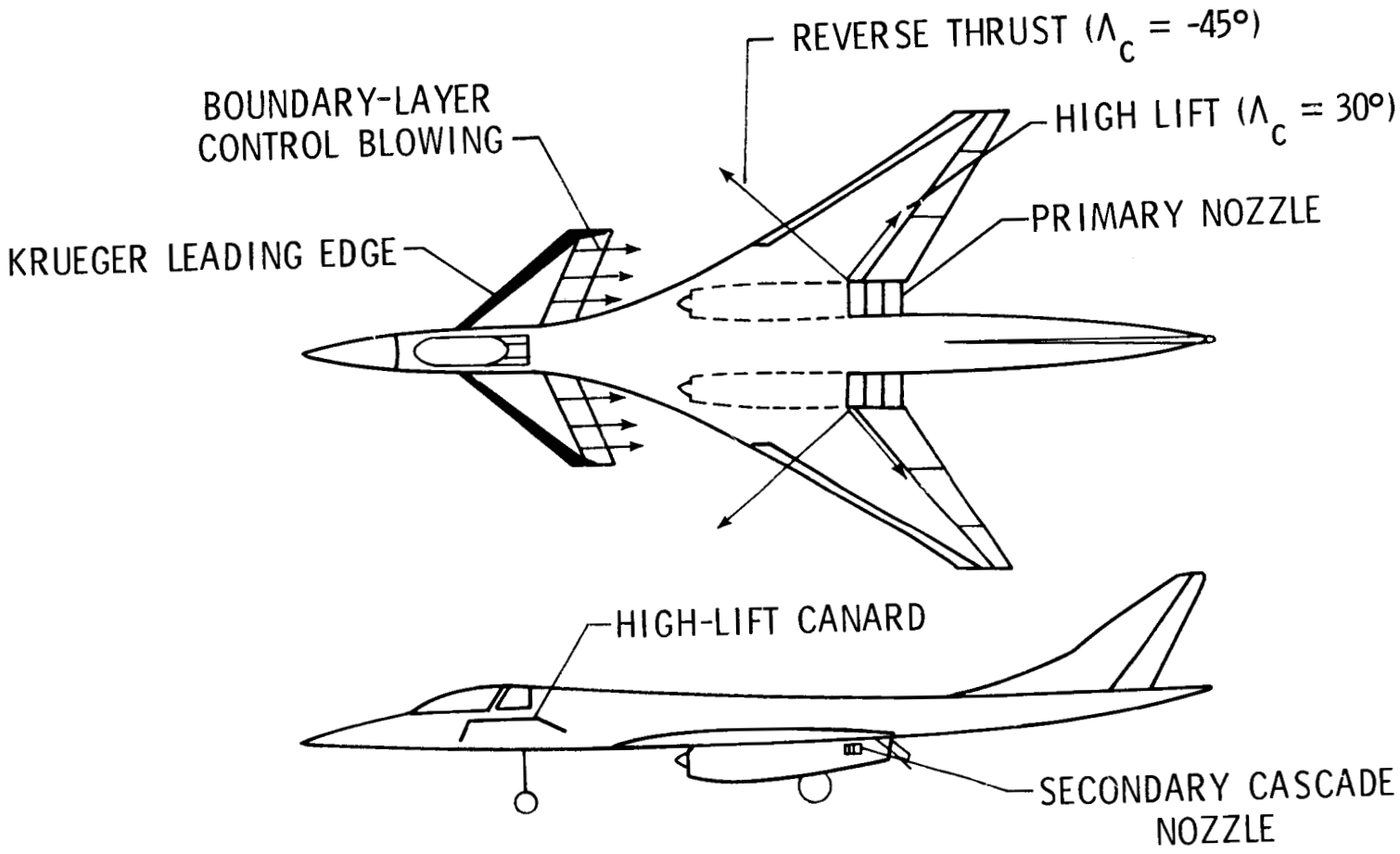


(b) Geometry with secondary cascade nozzles.

Figure 3. Concluded.

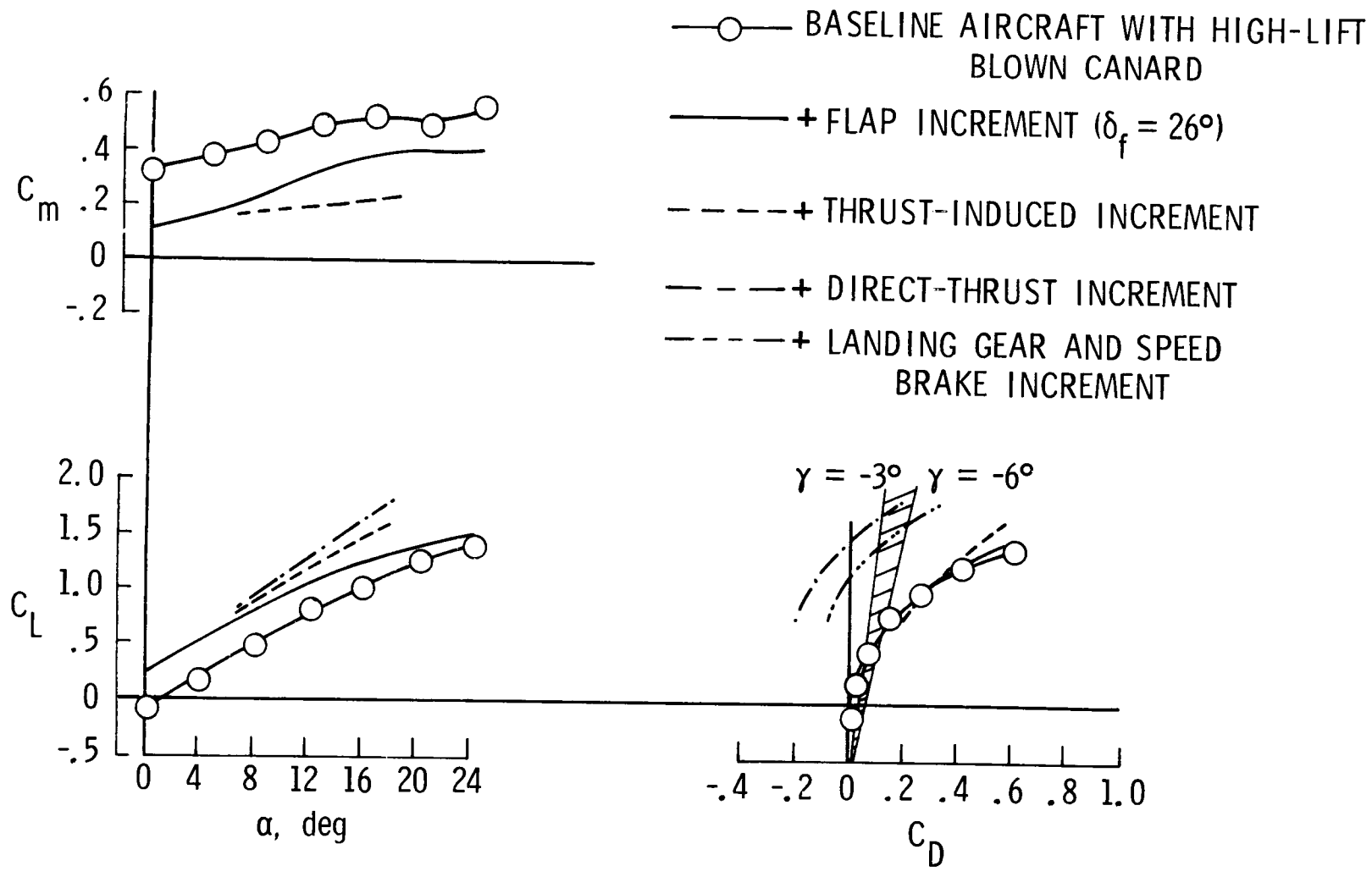


Figure 4. Buildup of longitudinal aerodynamics of conceptual configuration.

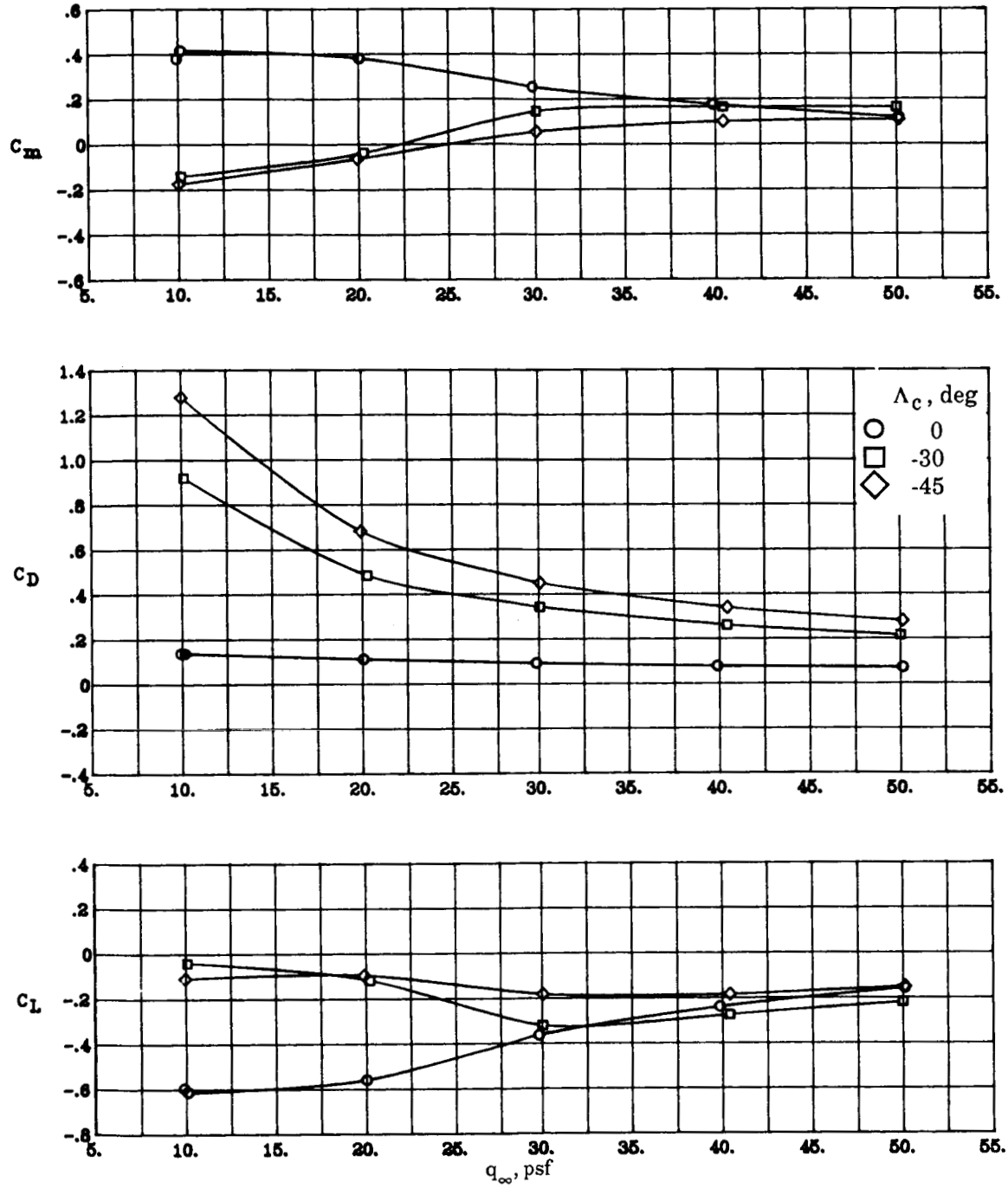


(a) NPR = 4.0; $\beta = 0°$; $\delta_f = 0°$.

Figure 5. Effects of cascade vector angle on aerodynamic characteristics.

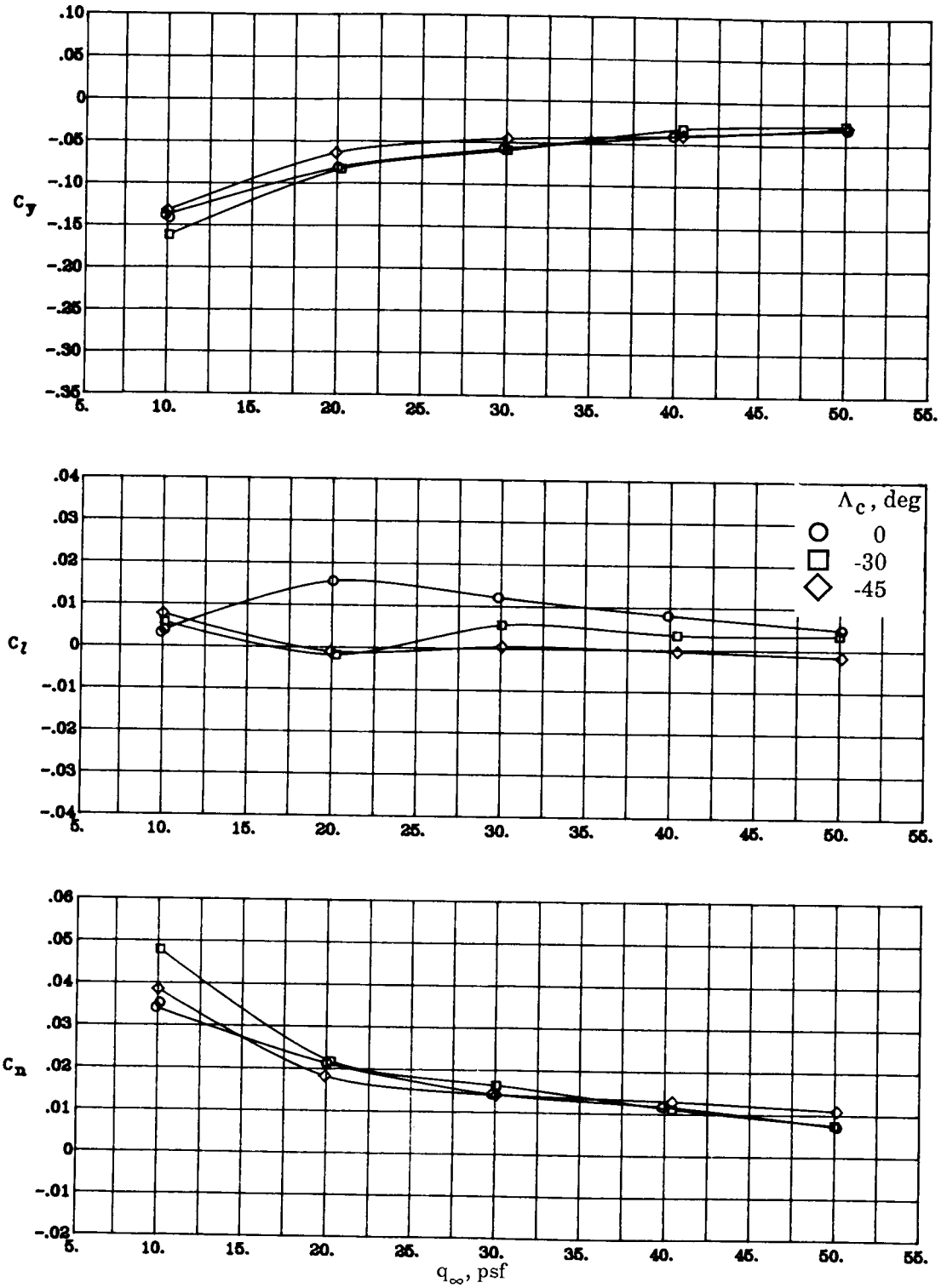


(a) Concluded.

Figure 5. Continued.

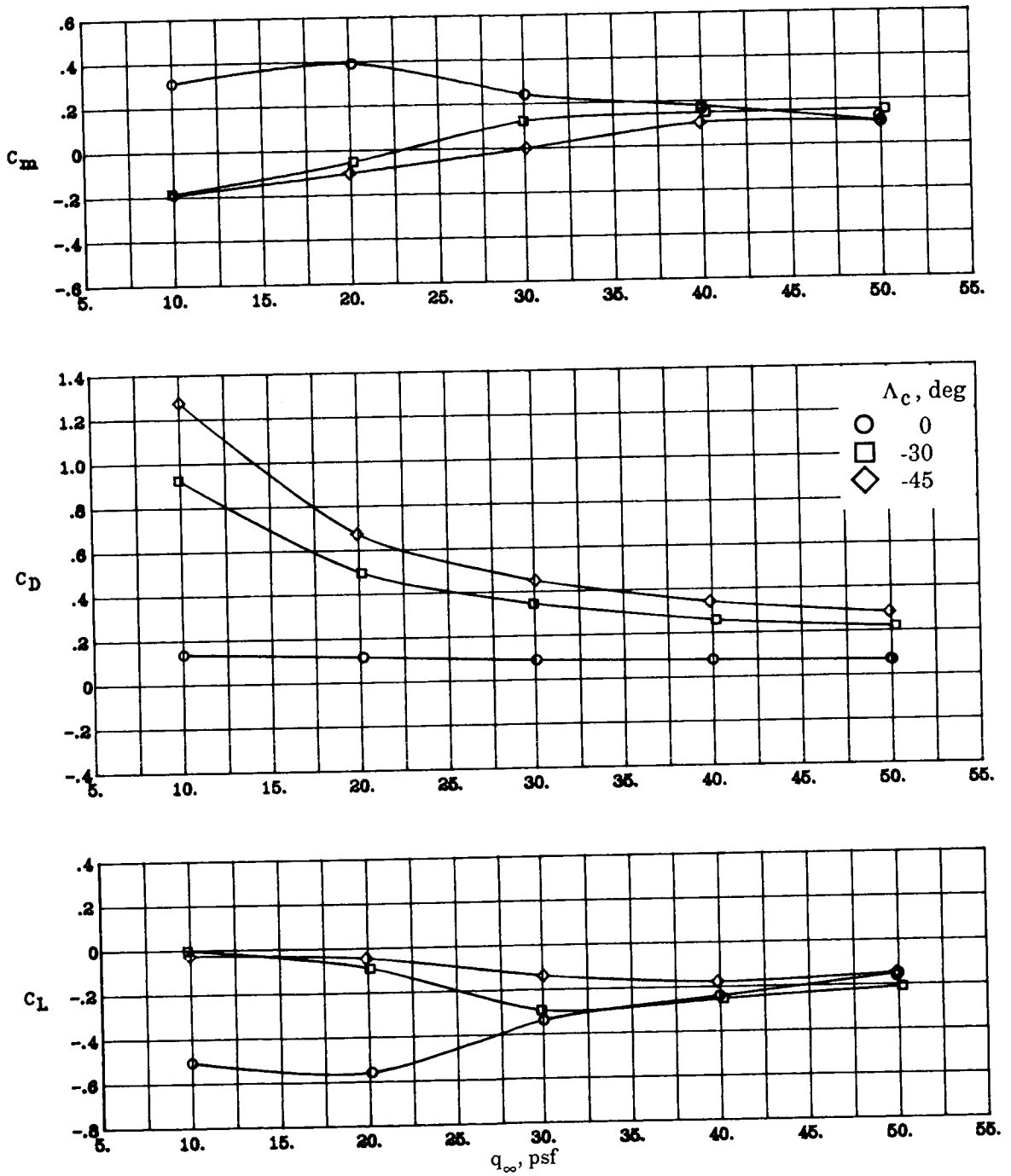


(b) NPR = 4.0; $\beta = 5°$; $\delta_f = 0°$.

Figure 5. Continued.

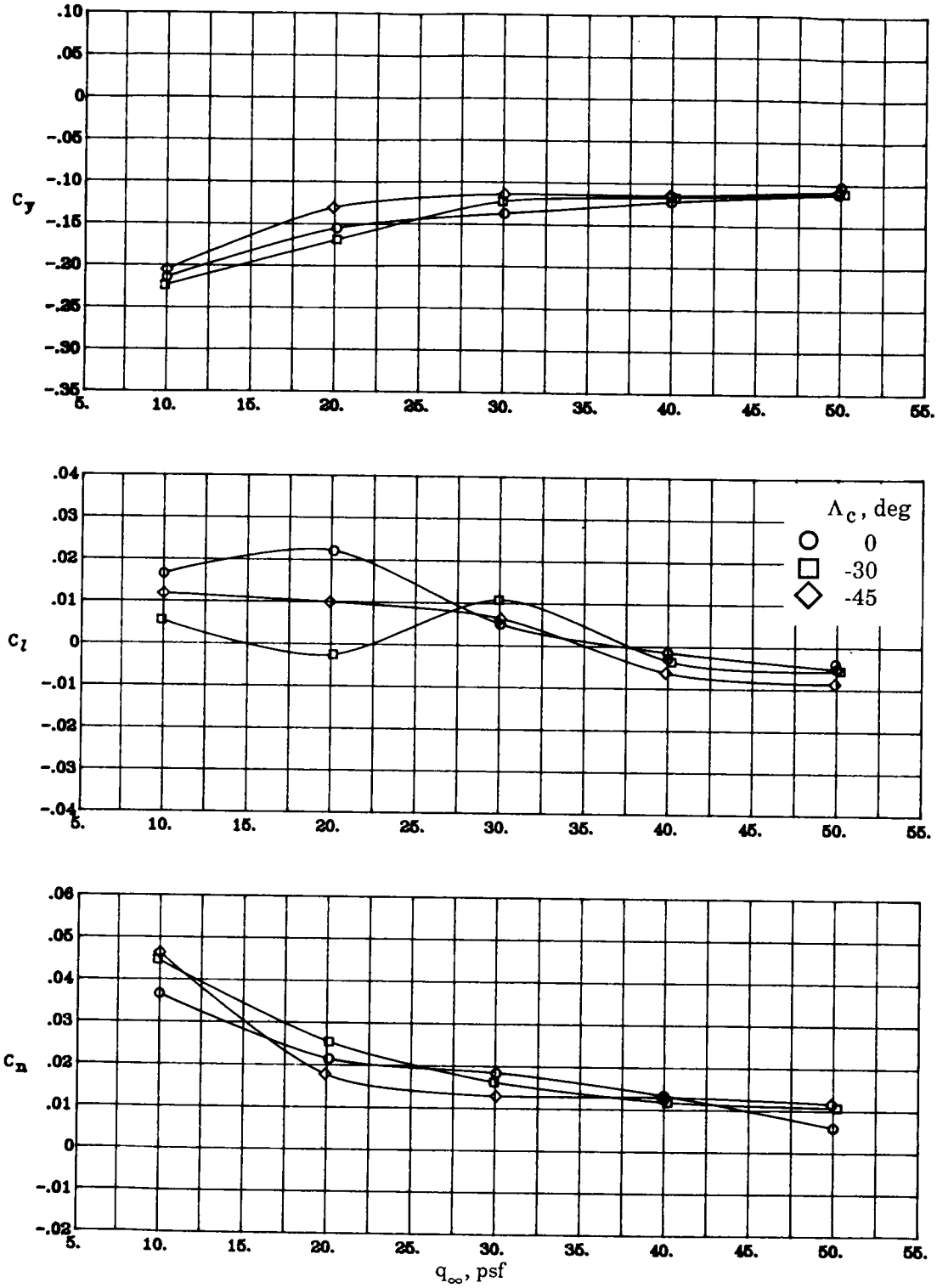


(b) Concluded.

Figure 5. Continued.

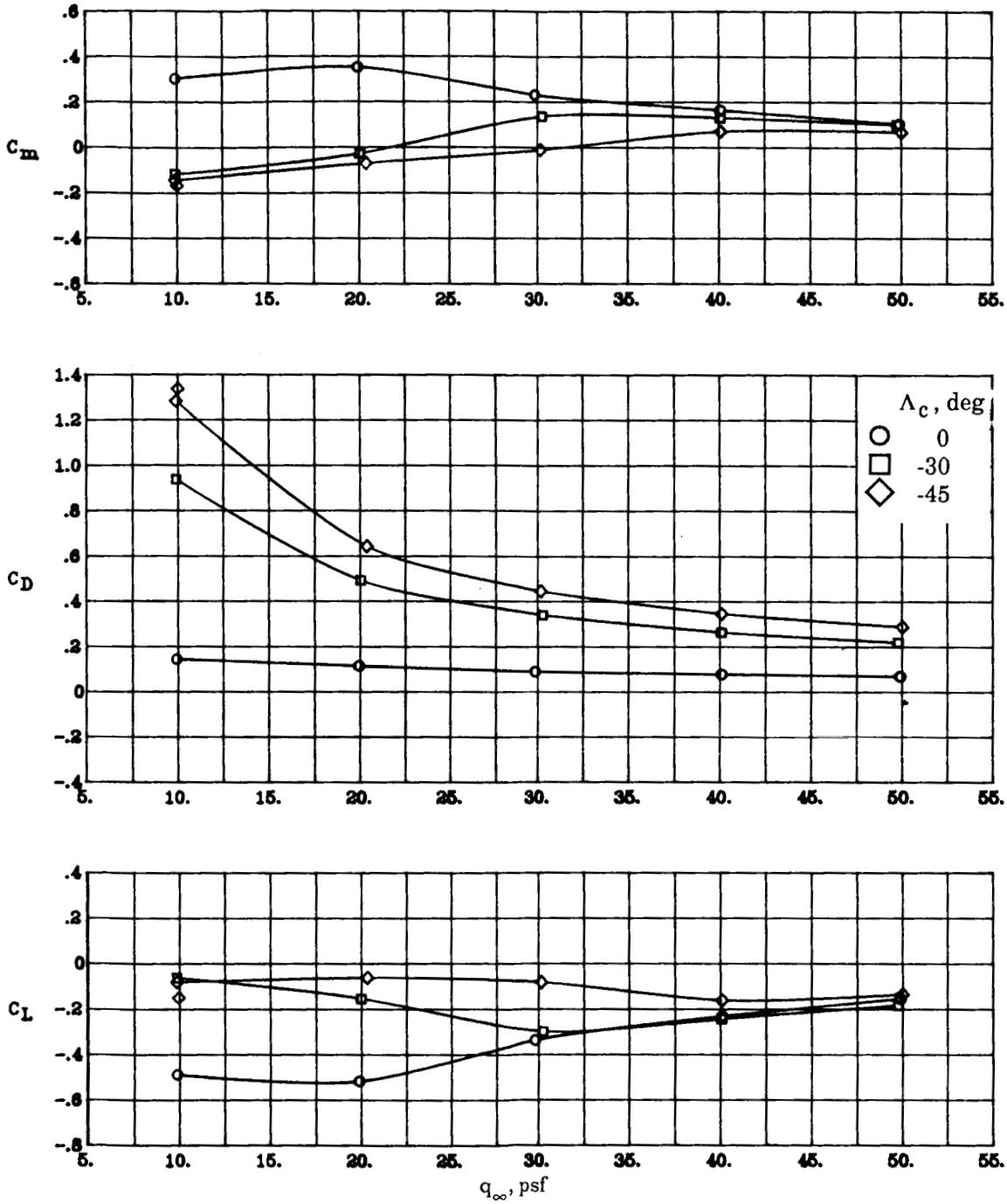


(c) NPR = 4.0; $\beta = 10°$; $\delta_f = 0°$.

Figure 5. Continued.

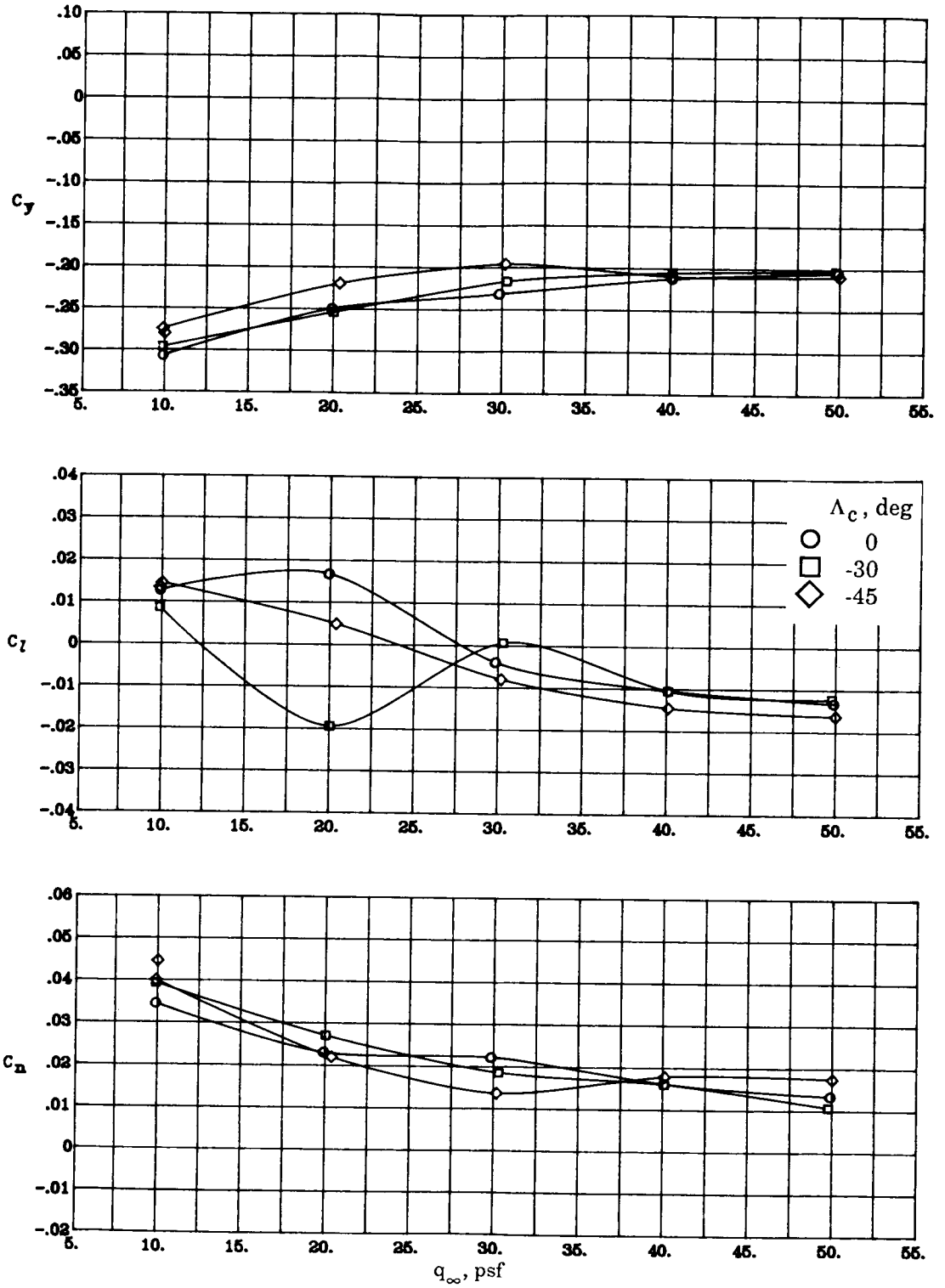


(c) Concluded.

Figure 5. Continued.

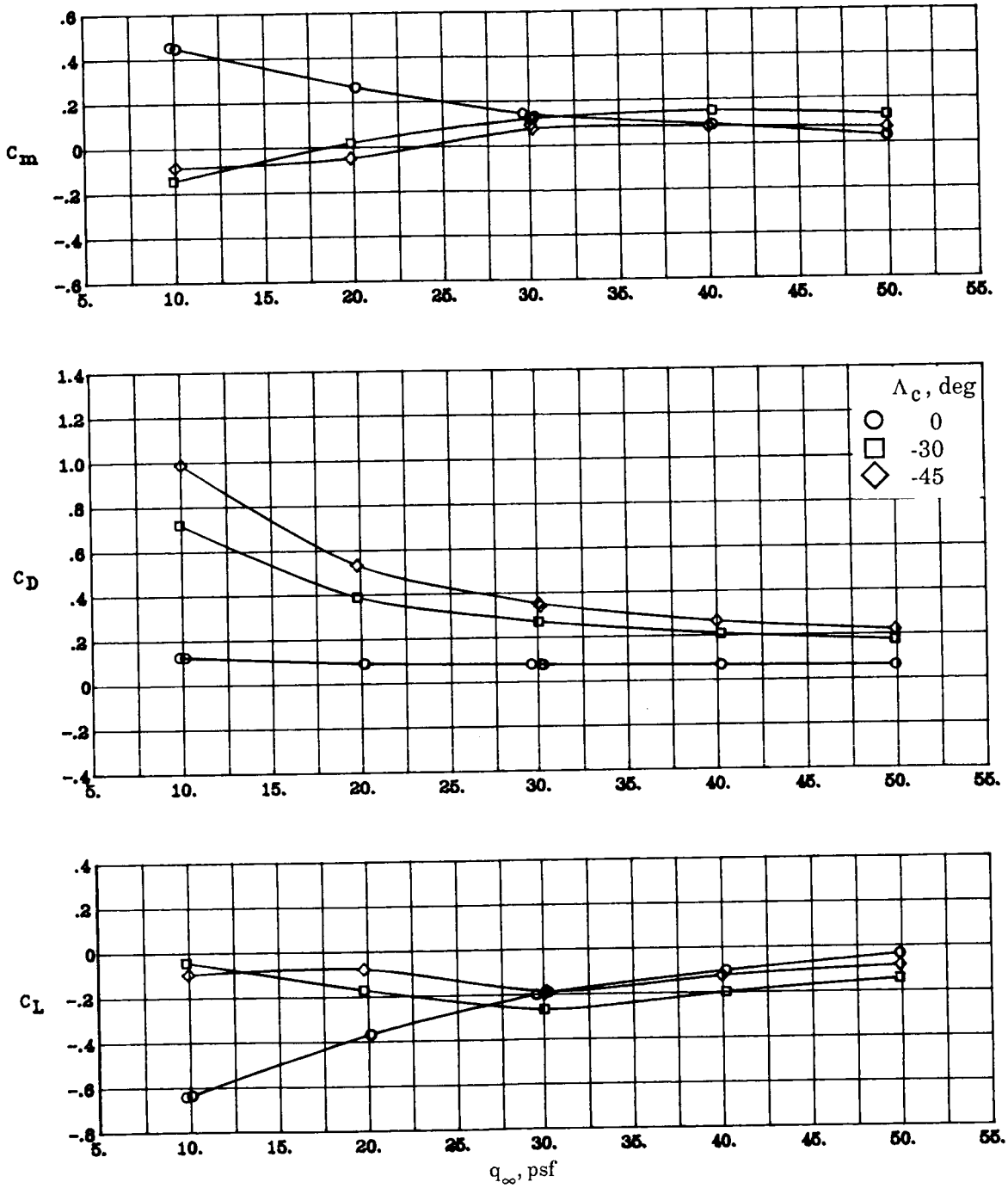


(d) NPR = 3.0; $\beta = 0°$; $\delta_f = 0°$.

Figure 5. Continued.

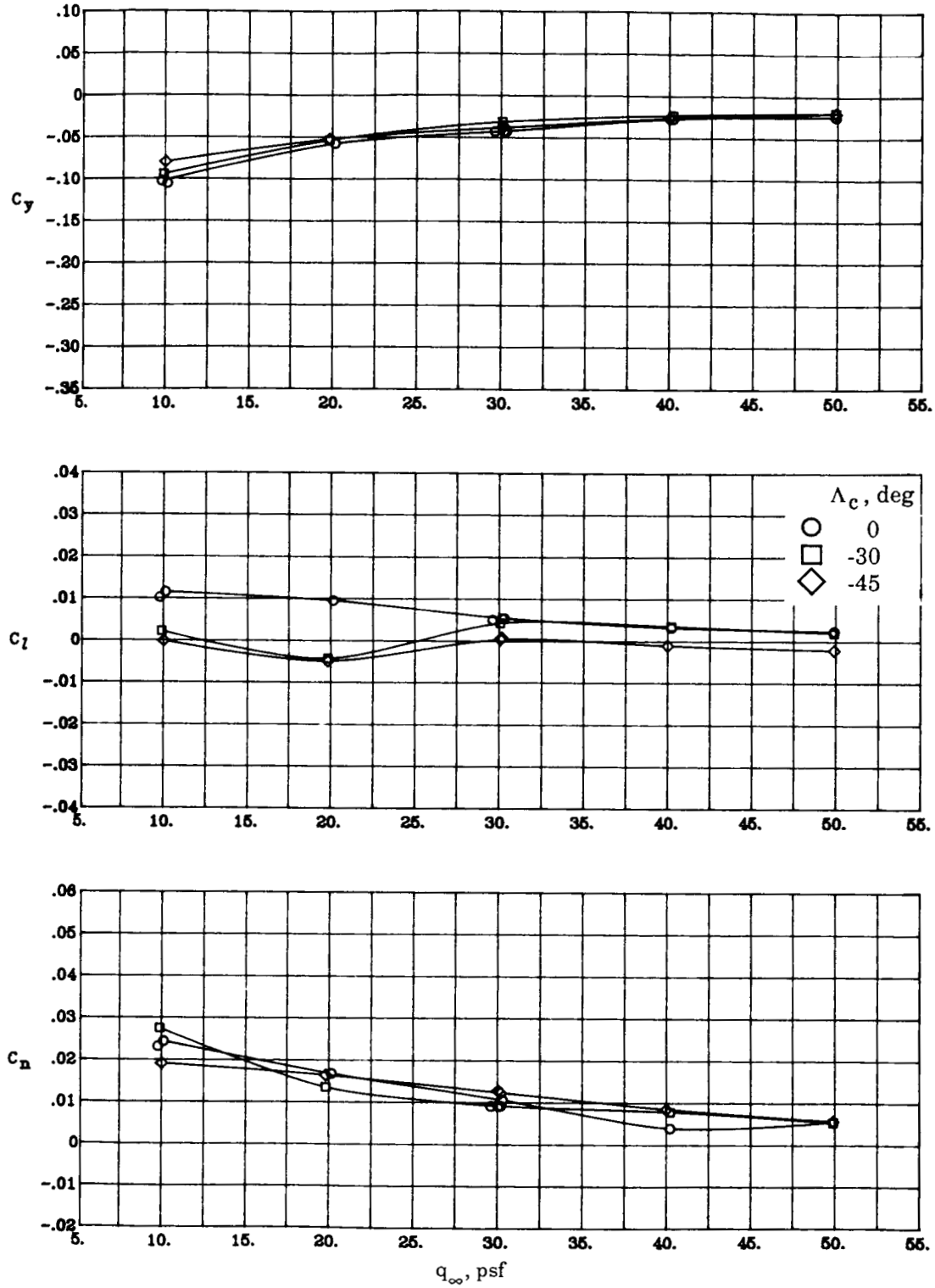


(d) Concluded.

Figure 5. Continued.

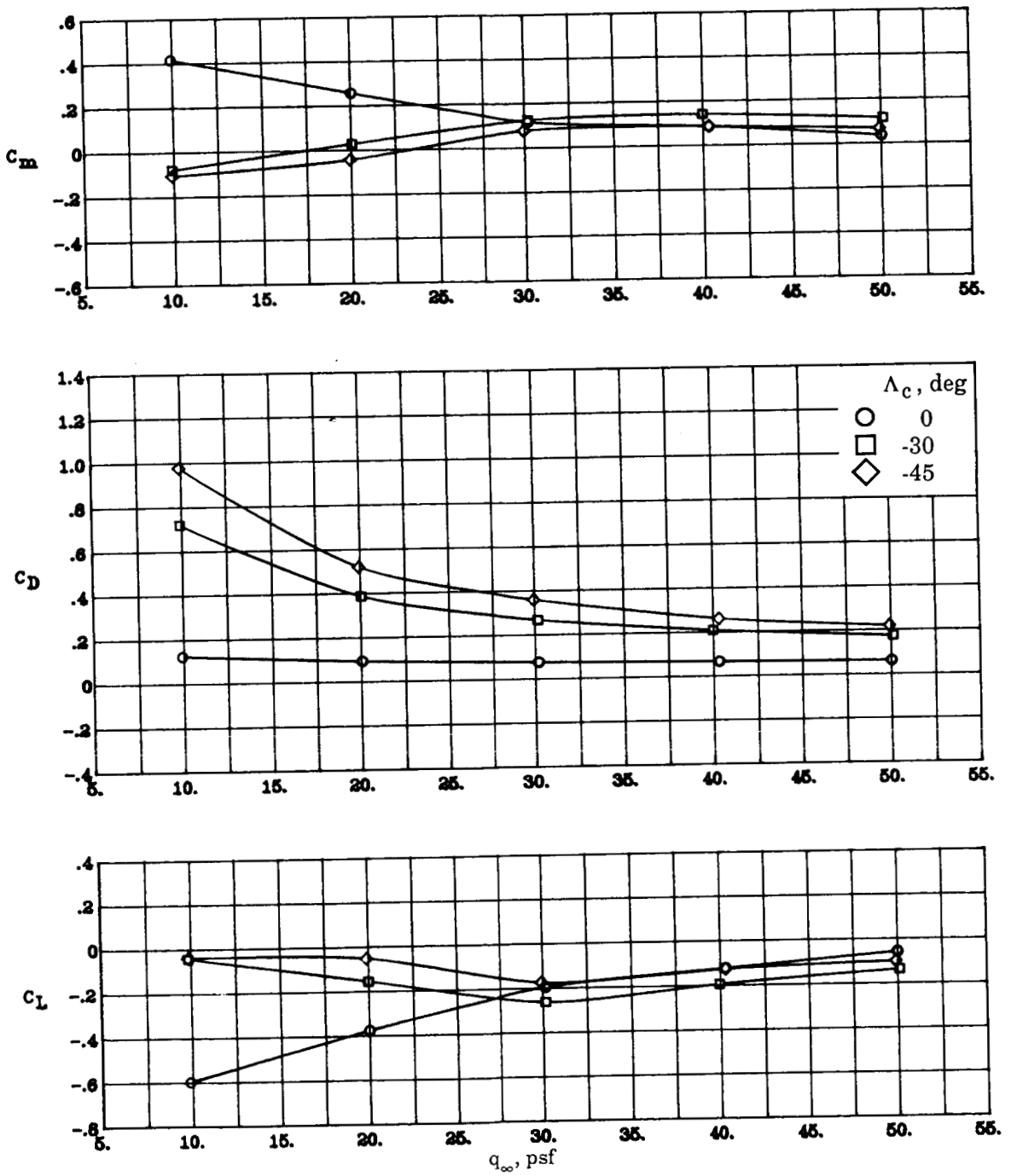


(e) NPR = 3.0; $\beta = 5°$; $\delta_f = 0°$.

Figure 5. Continued.

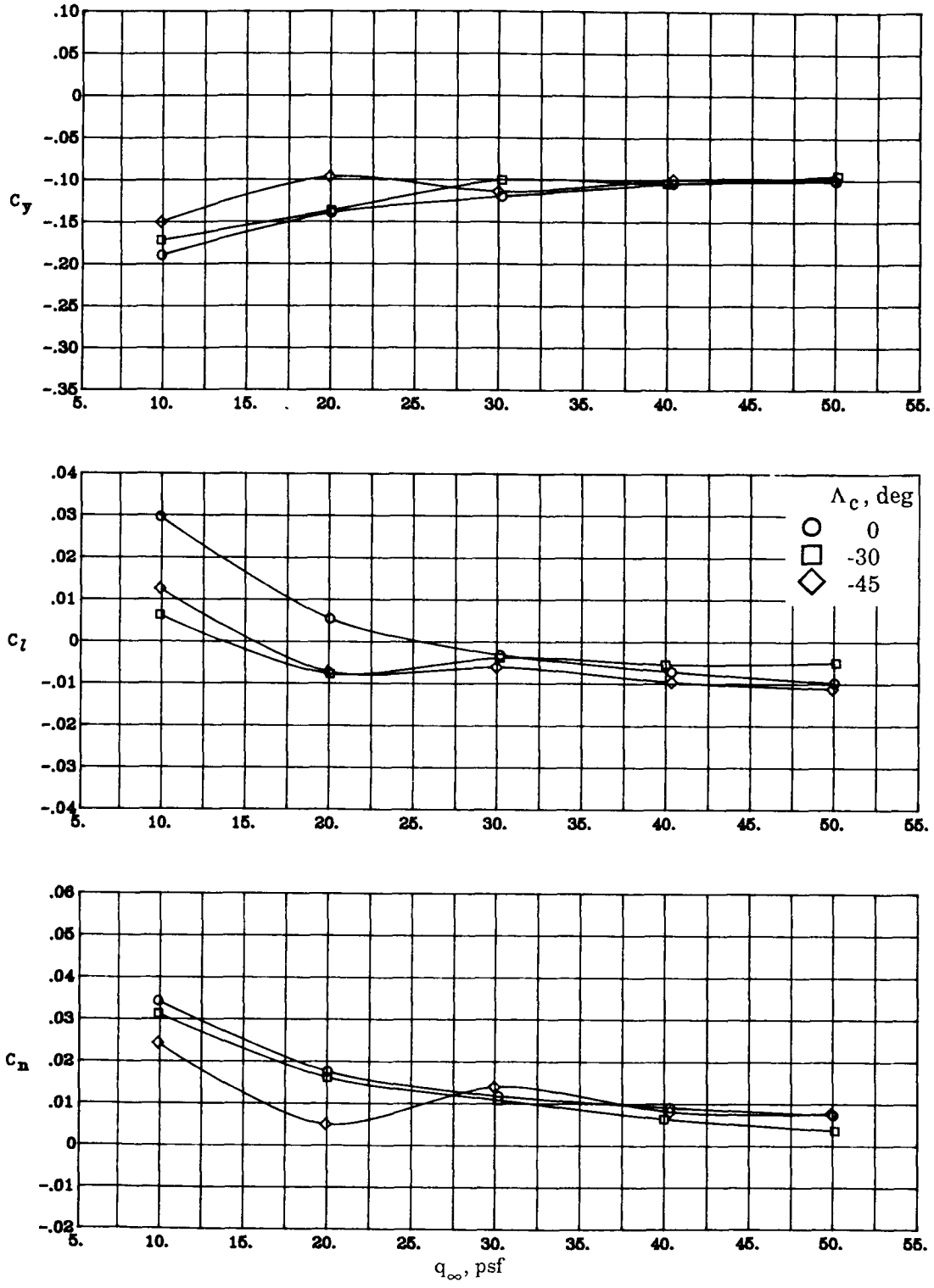


(e) Concluded.

Figure 5. Continued.

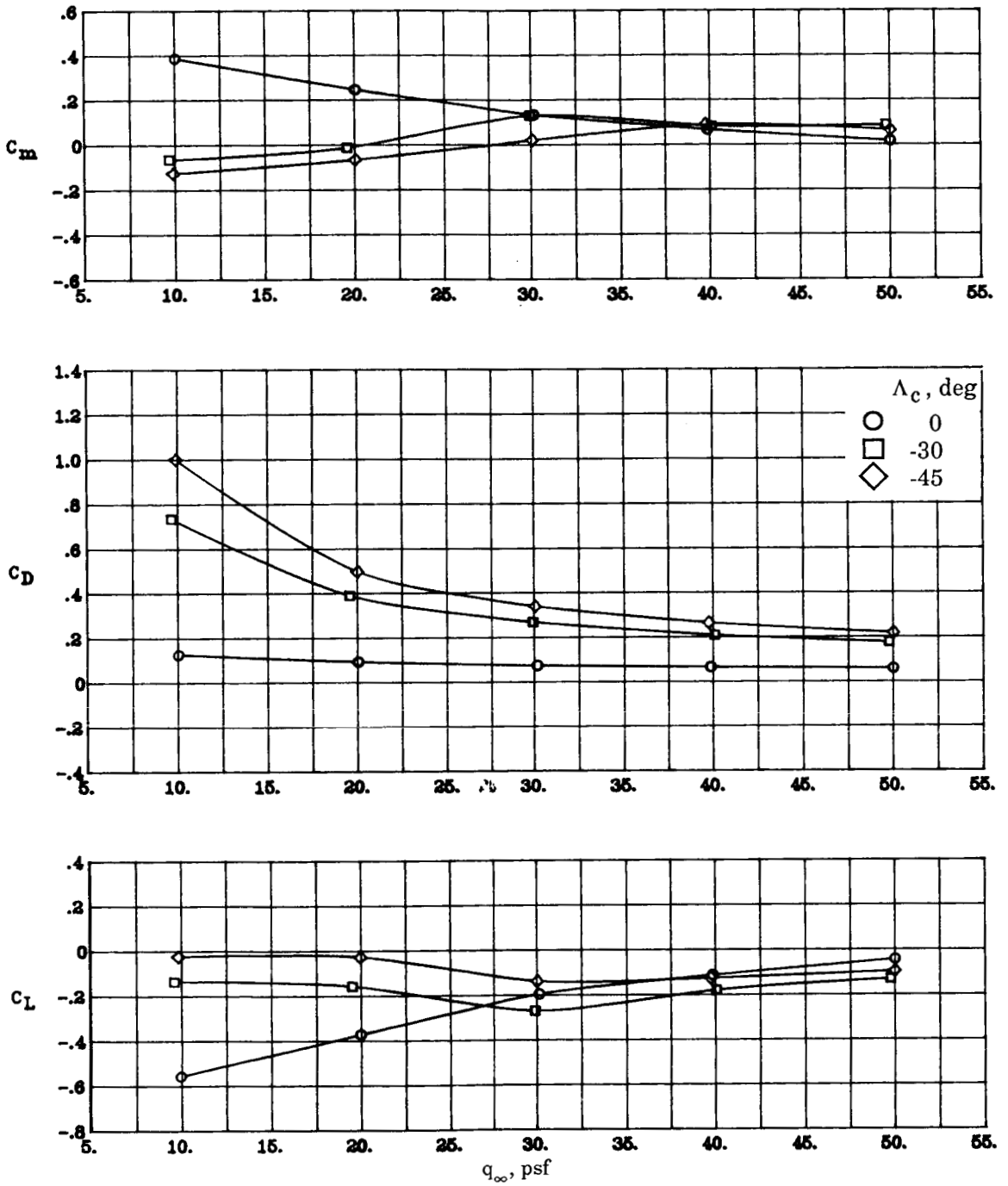


(f) NPR = 3.0; $\beta = 10°$; $\delta_f = 0°$.

Figure 5. Continued.

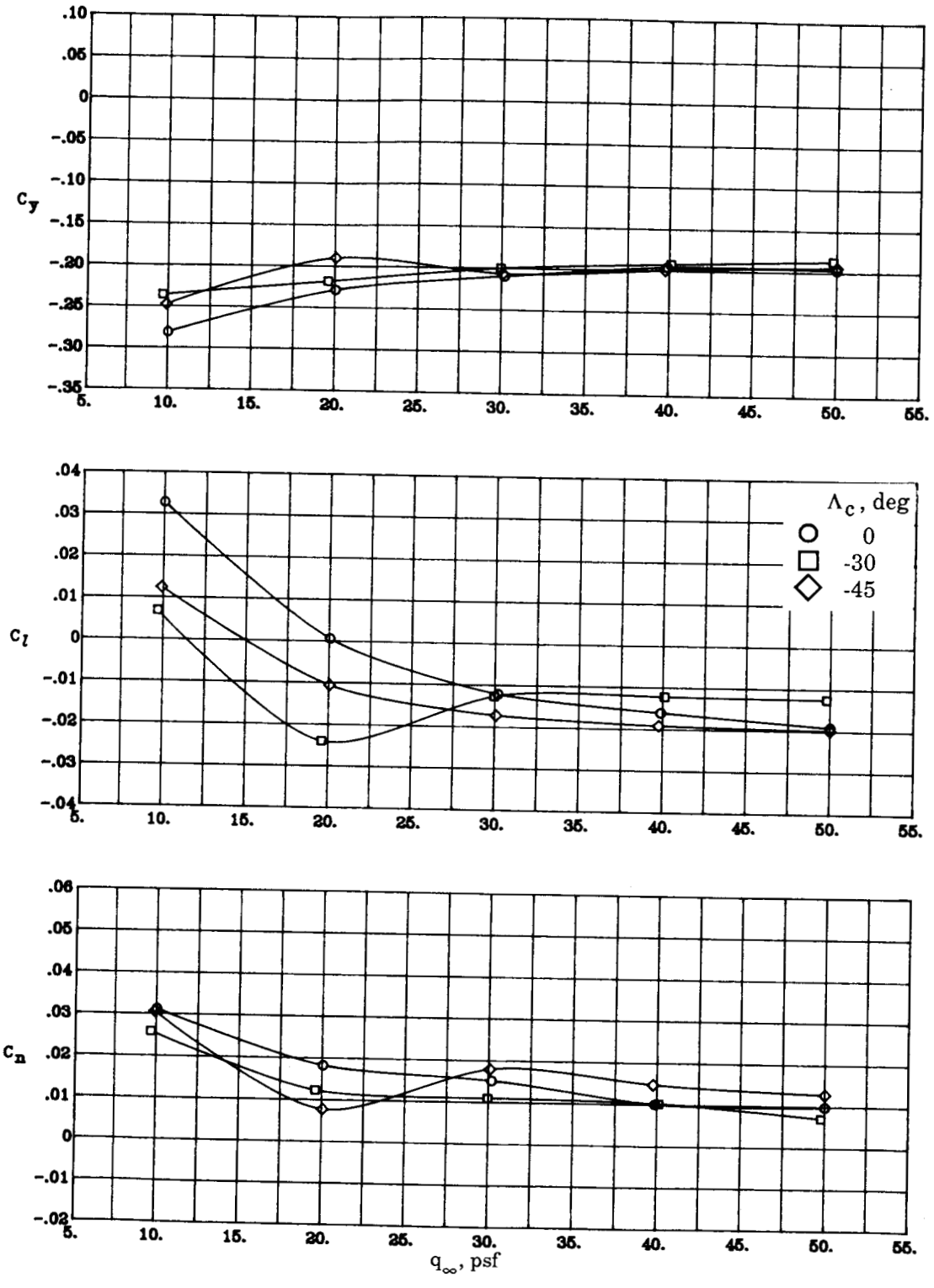


(f) Concluded.

Figure 5. Continued.

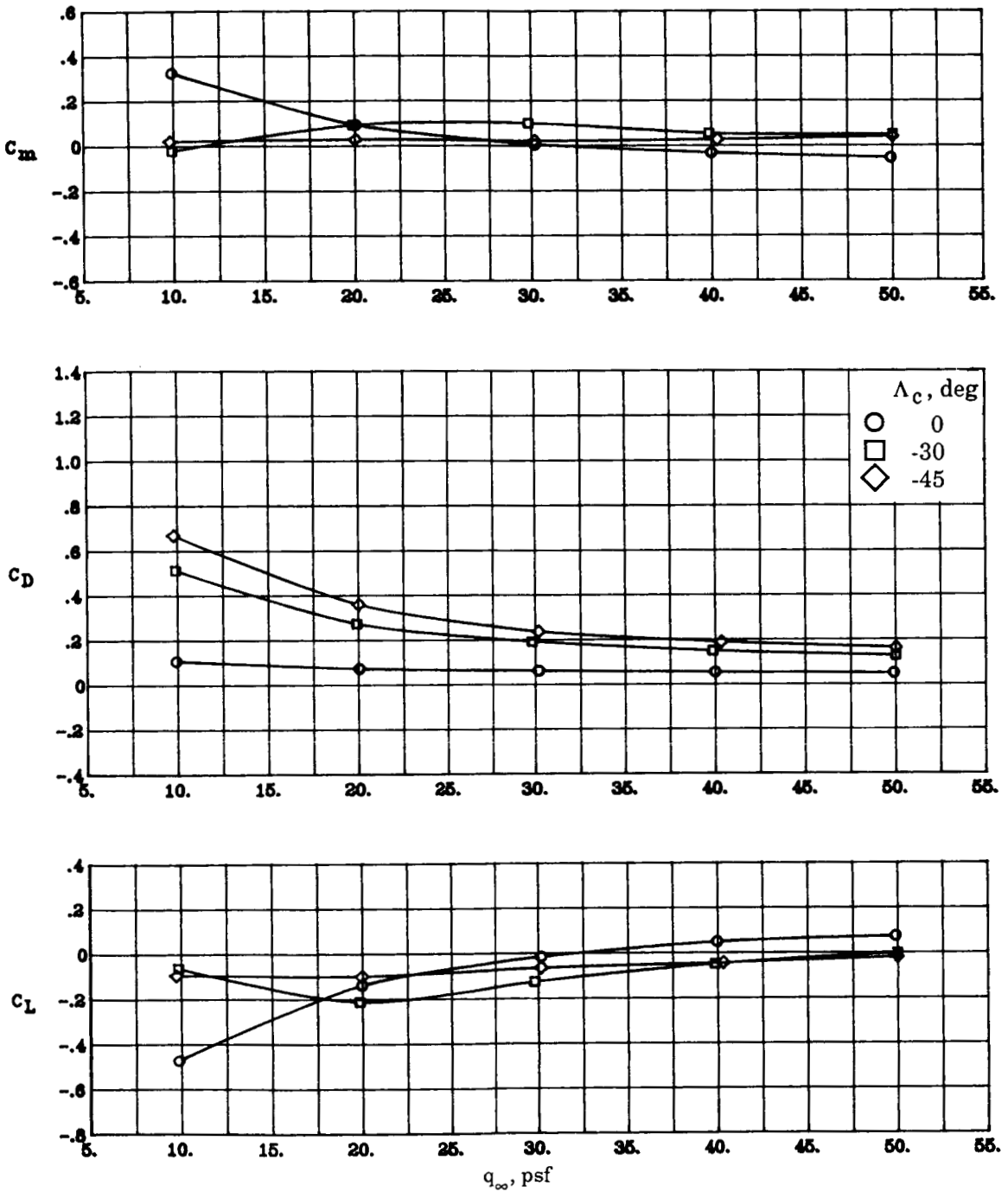


(g) NPR = 2.0; $\beta = 0°$; $\delta_f = 0°$.

Figure 5. Continued.

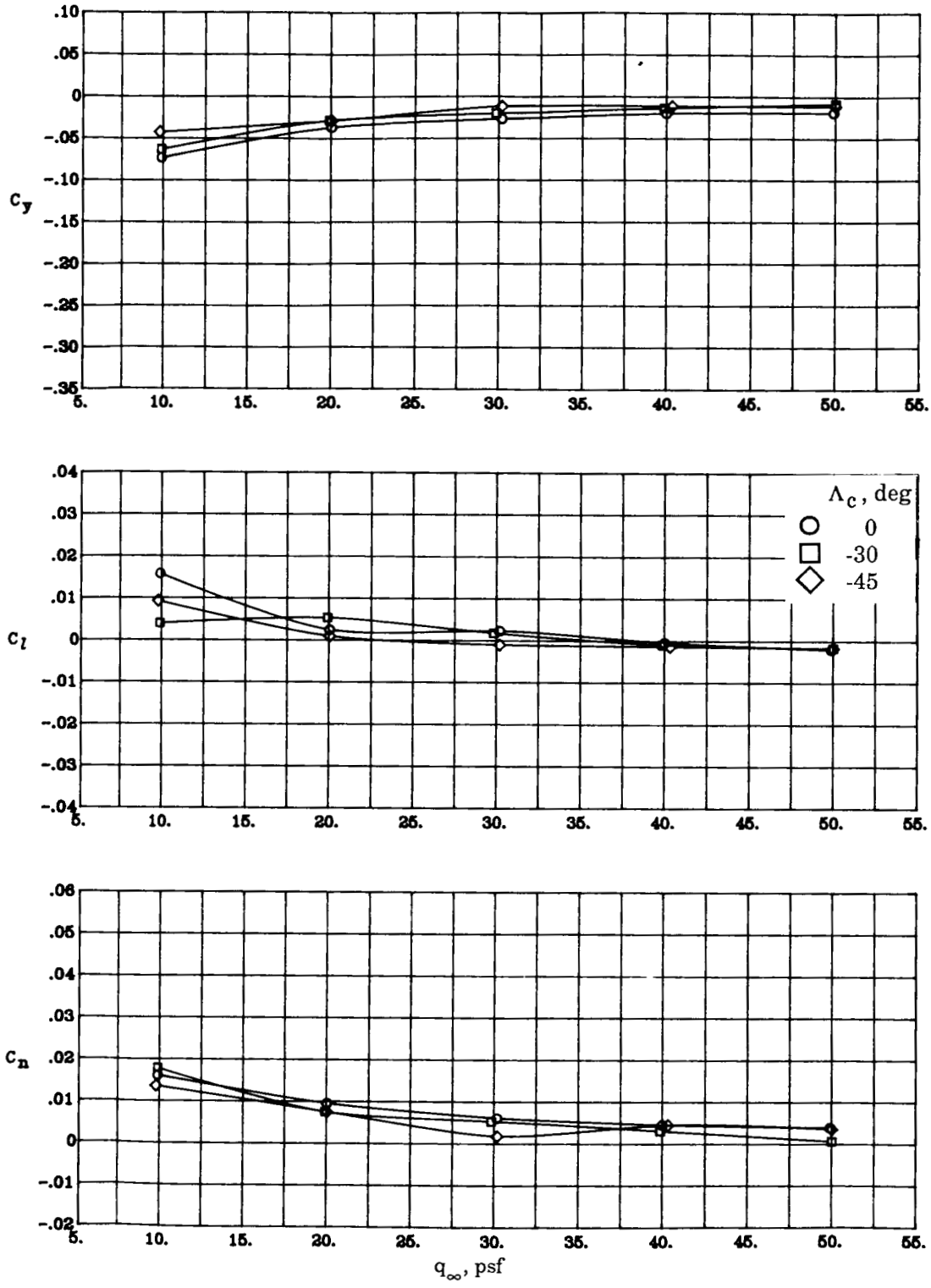


(g) Concluded.

Figure 5. Continued.

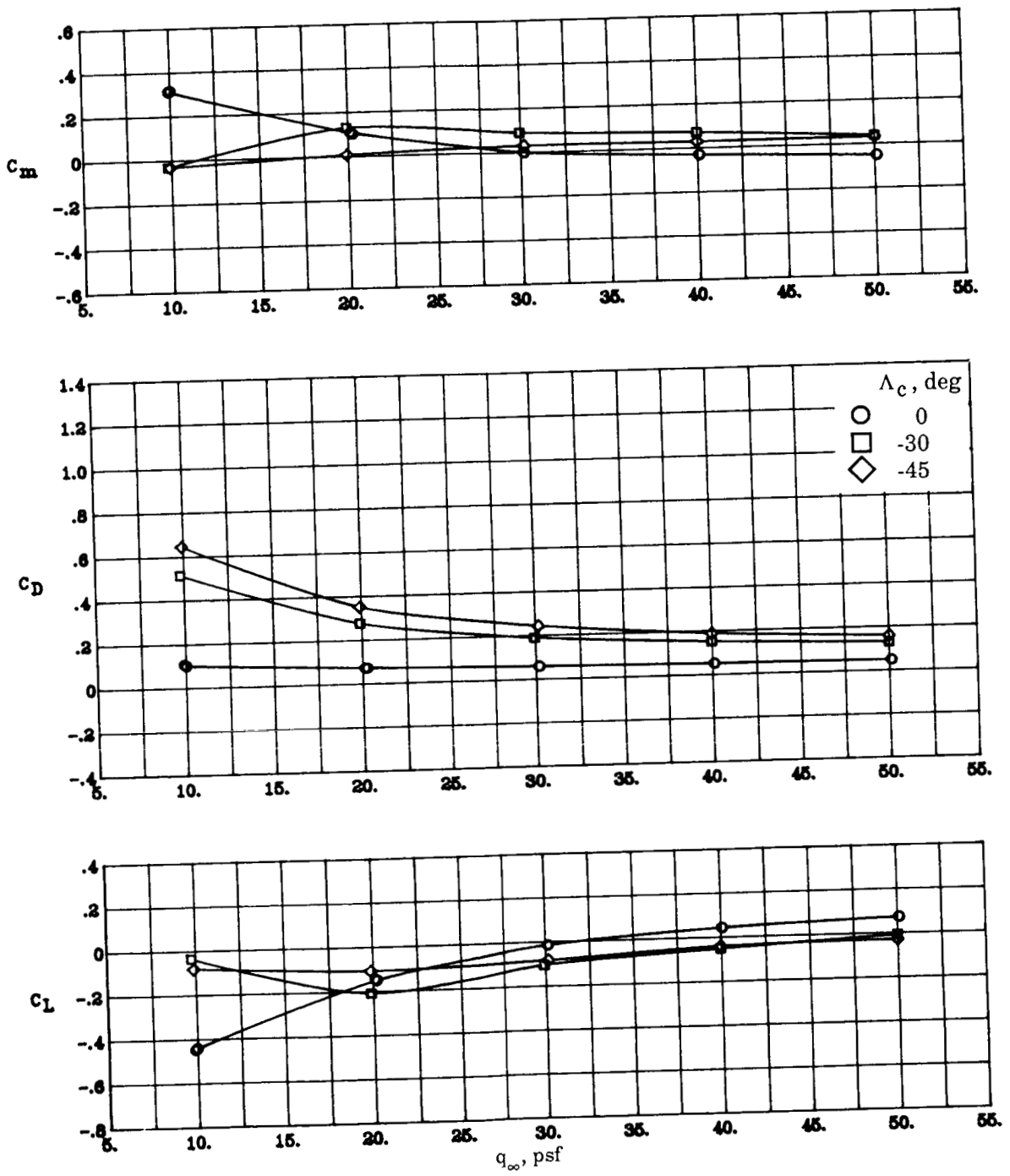


(h) NPR = 2.0; $\beta = 5°$; $\delta_f = 0°$.

Figure 5. Continued.

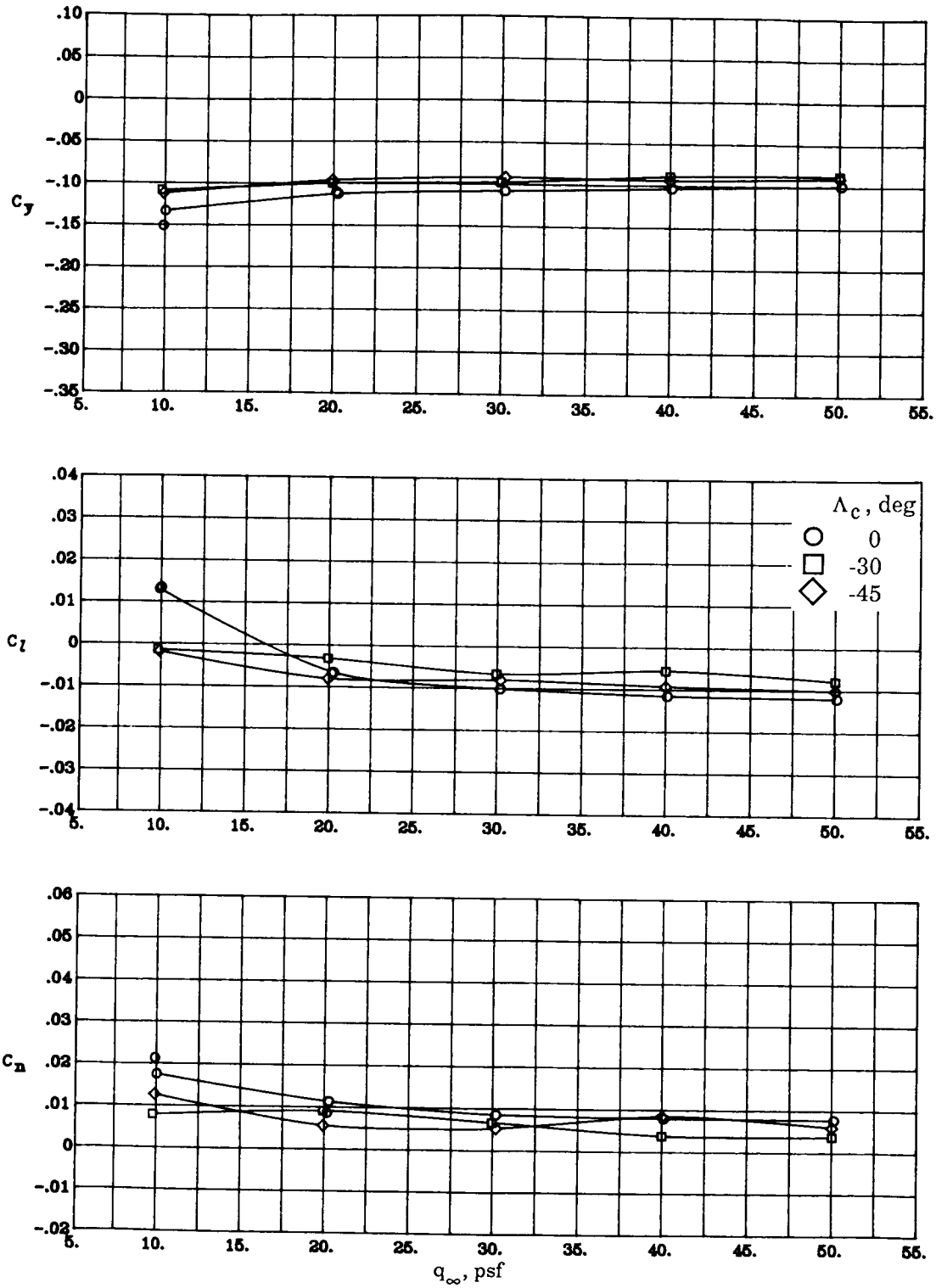


(h) Concluded.

Figure 5. Continued.

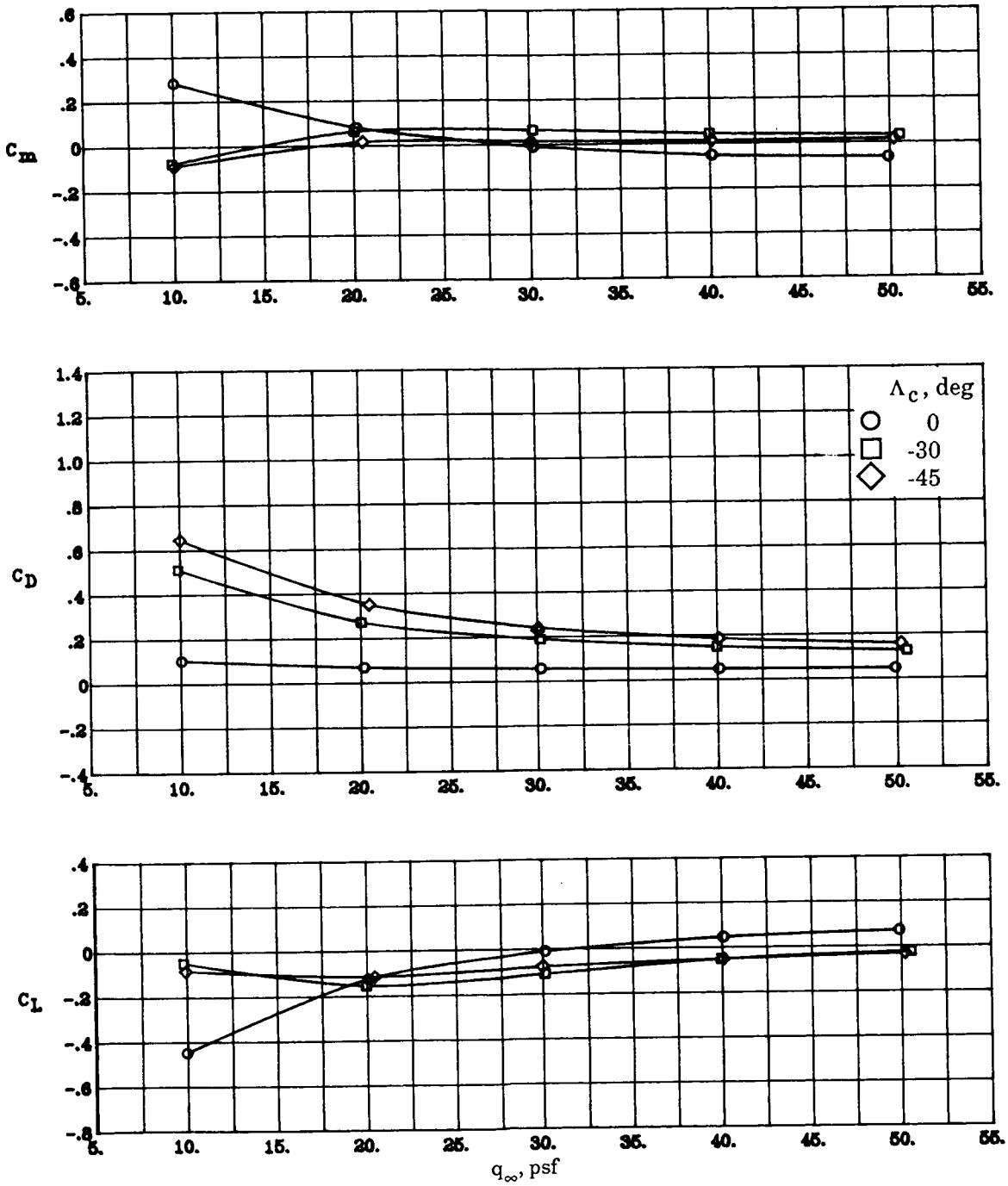


(i) NPR = 2.0; $\beta = 10°$; $\delta_f = 0°$.

Figure 5. Continued.

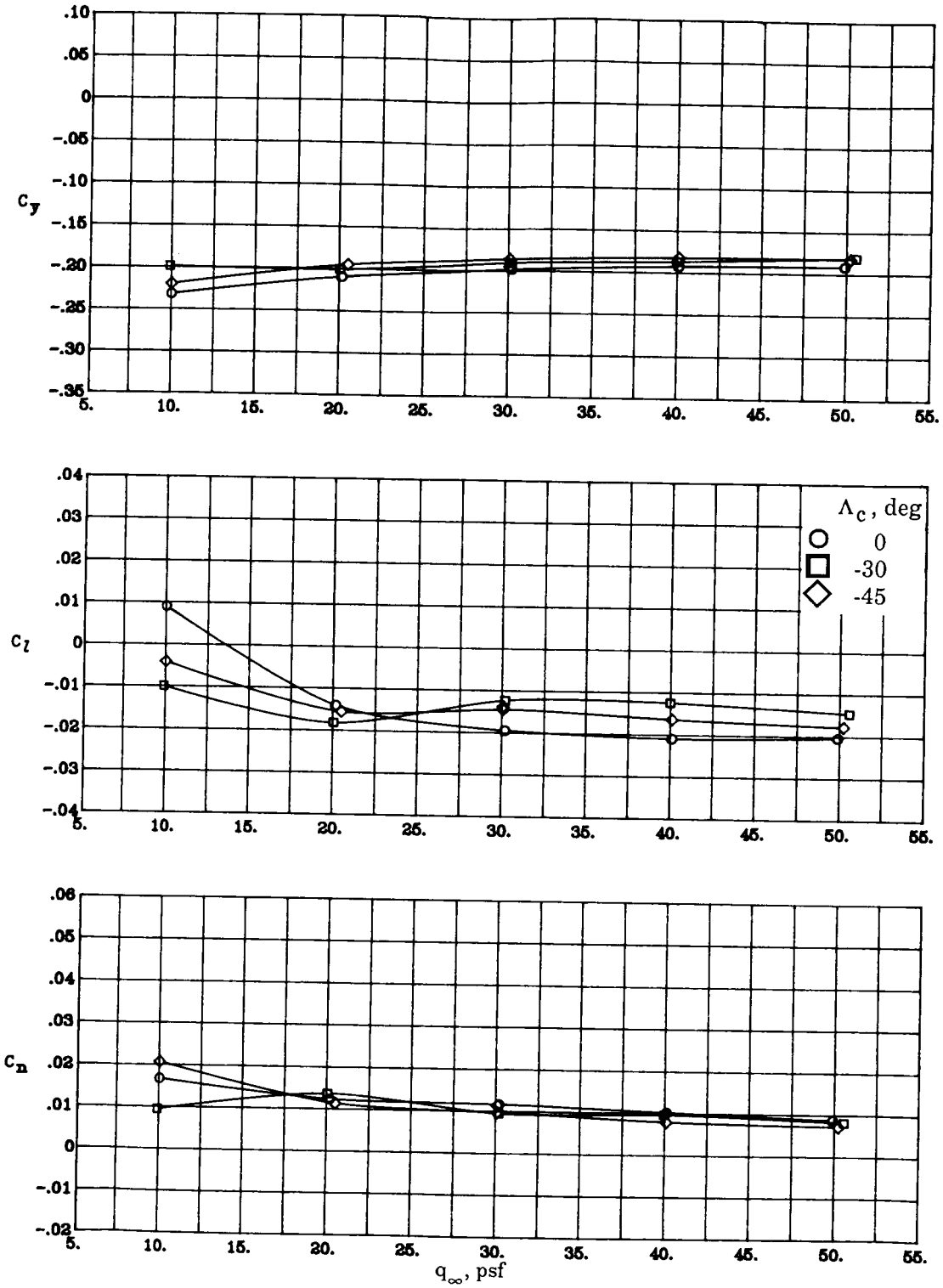


(i) Concluded.

Figure 5. Continued.

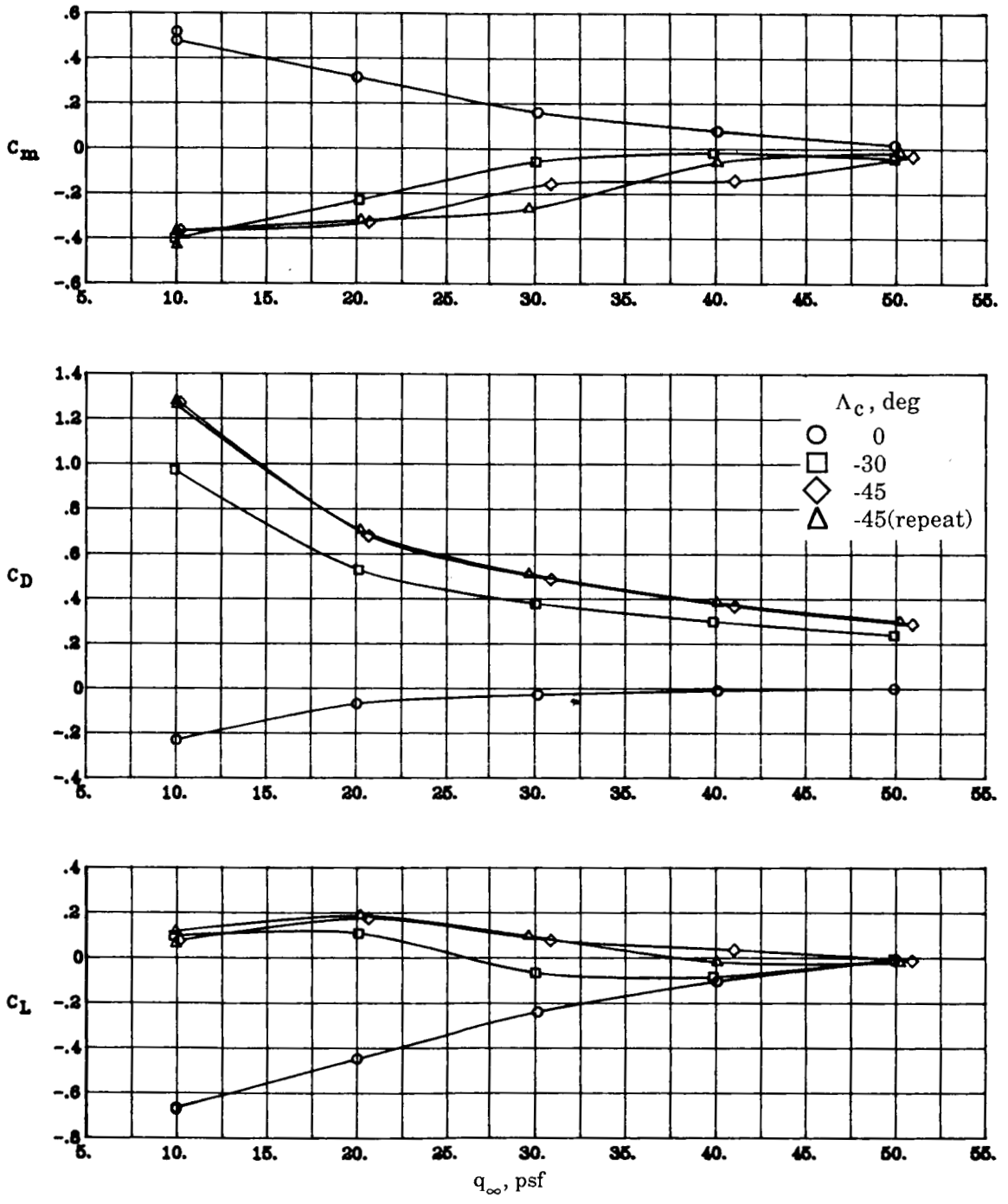


(j) NPR = 4.0; $\beta = 0°$; $\delta_f = 26°$.

Figure 5. Continued.

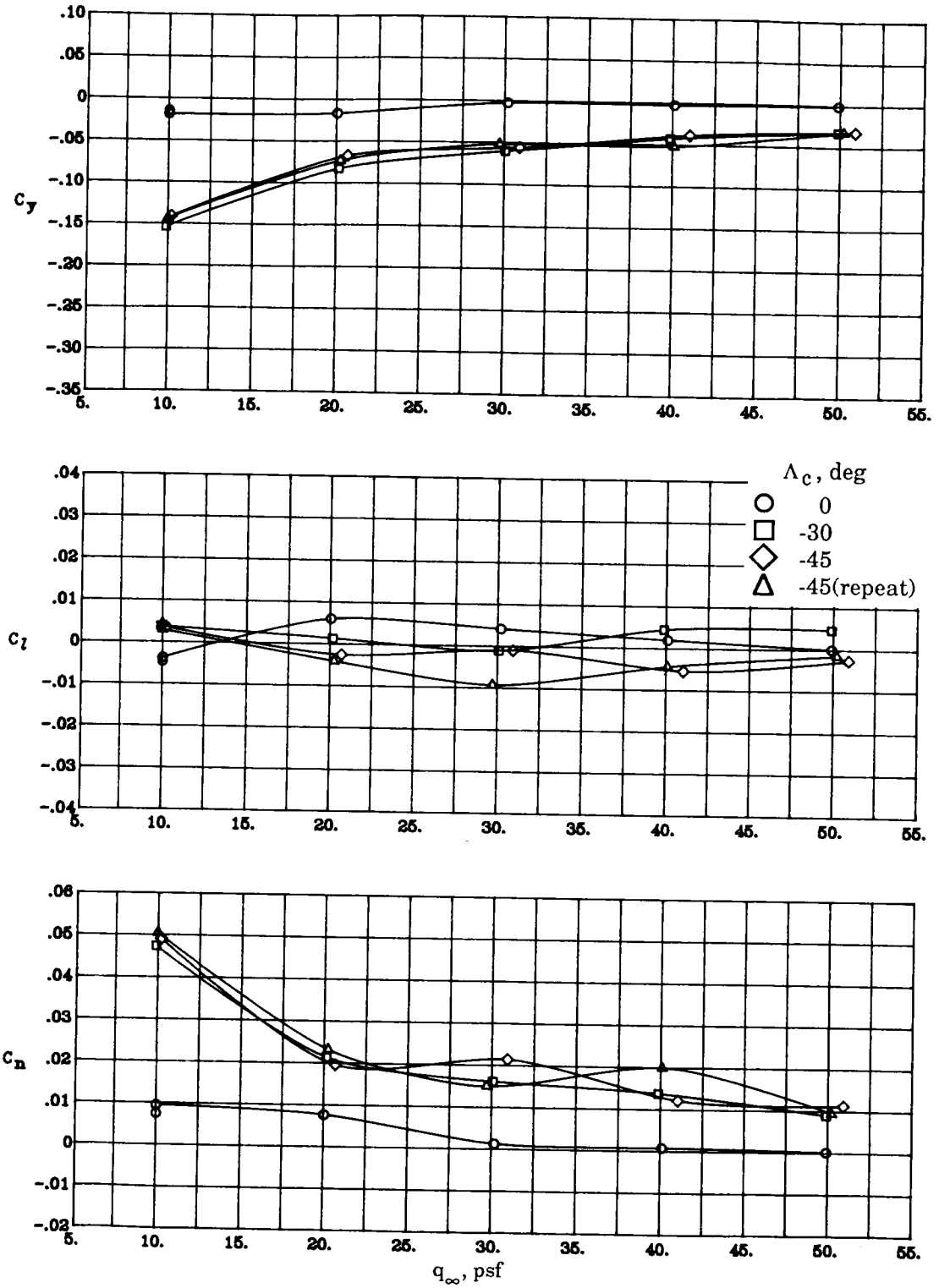


(j) Concluded.

Figure 5. Continued.

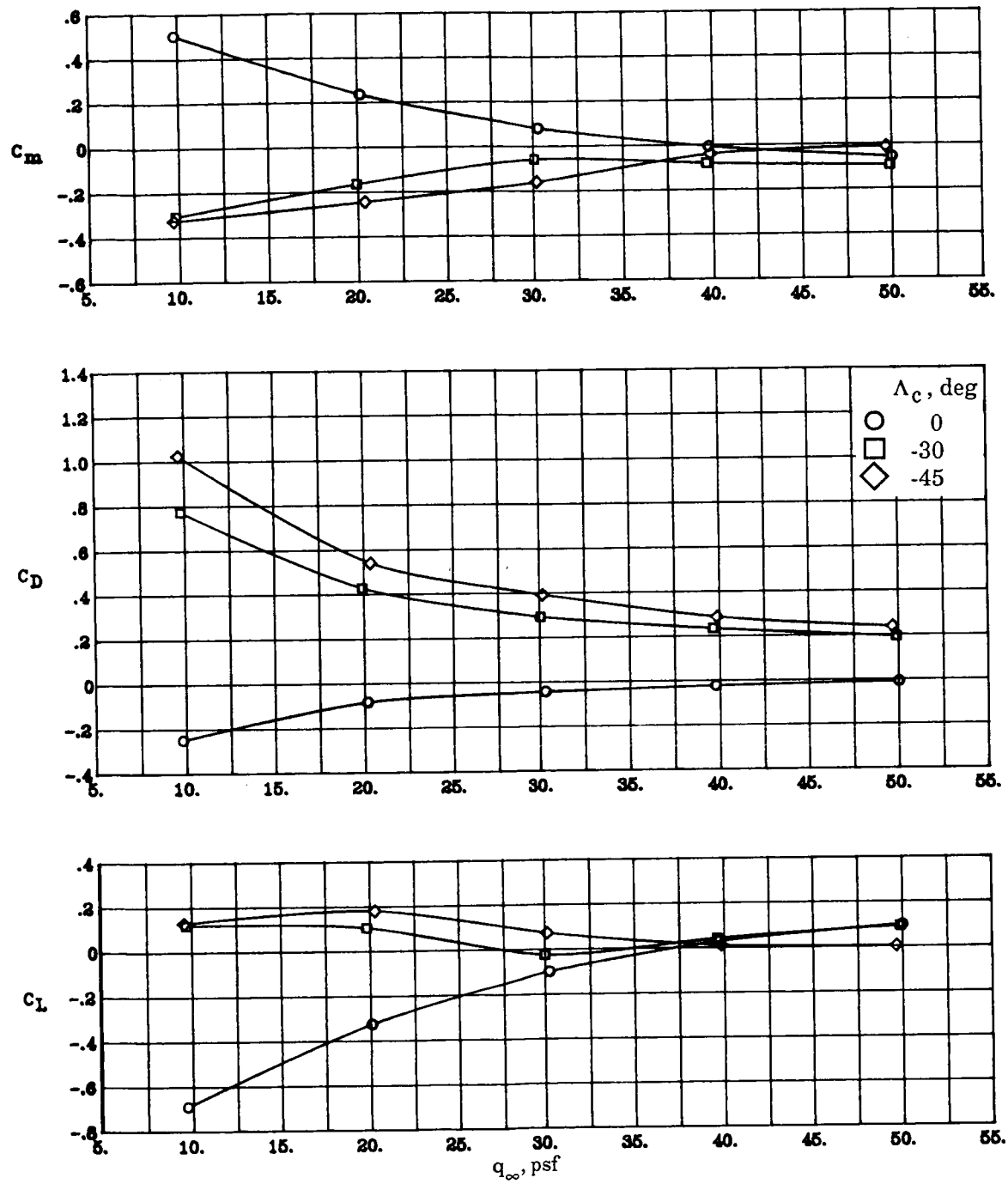


(k) NPR = 3.0; $\beta = 0°$; $\delta_f = 26°$.

Figure 5. Continued.

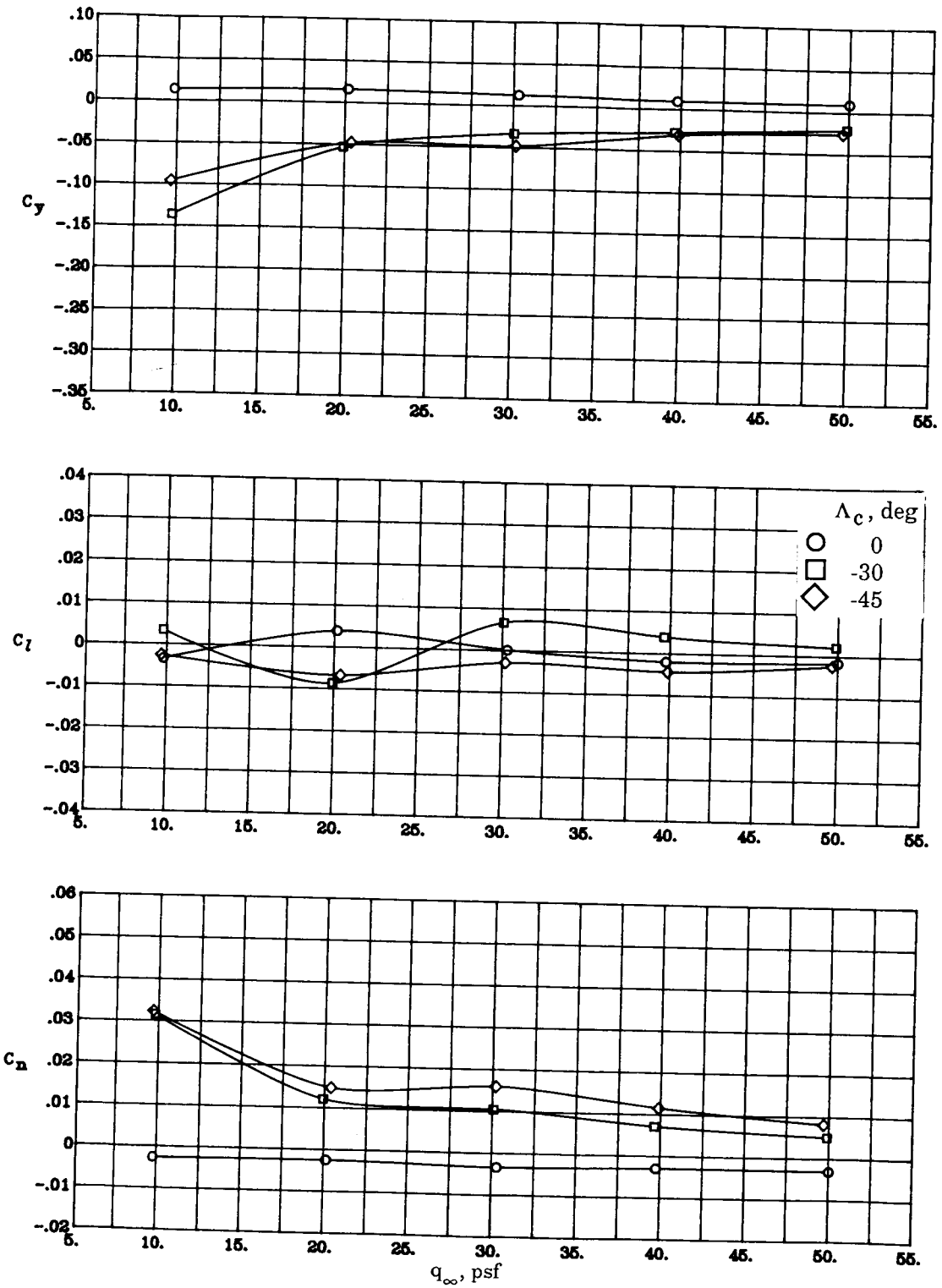


(k) Concluded.

Figure 5. Continued.

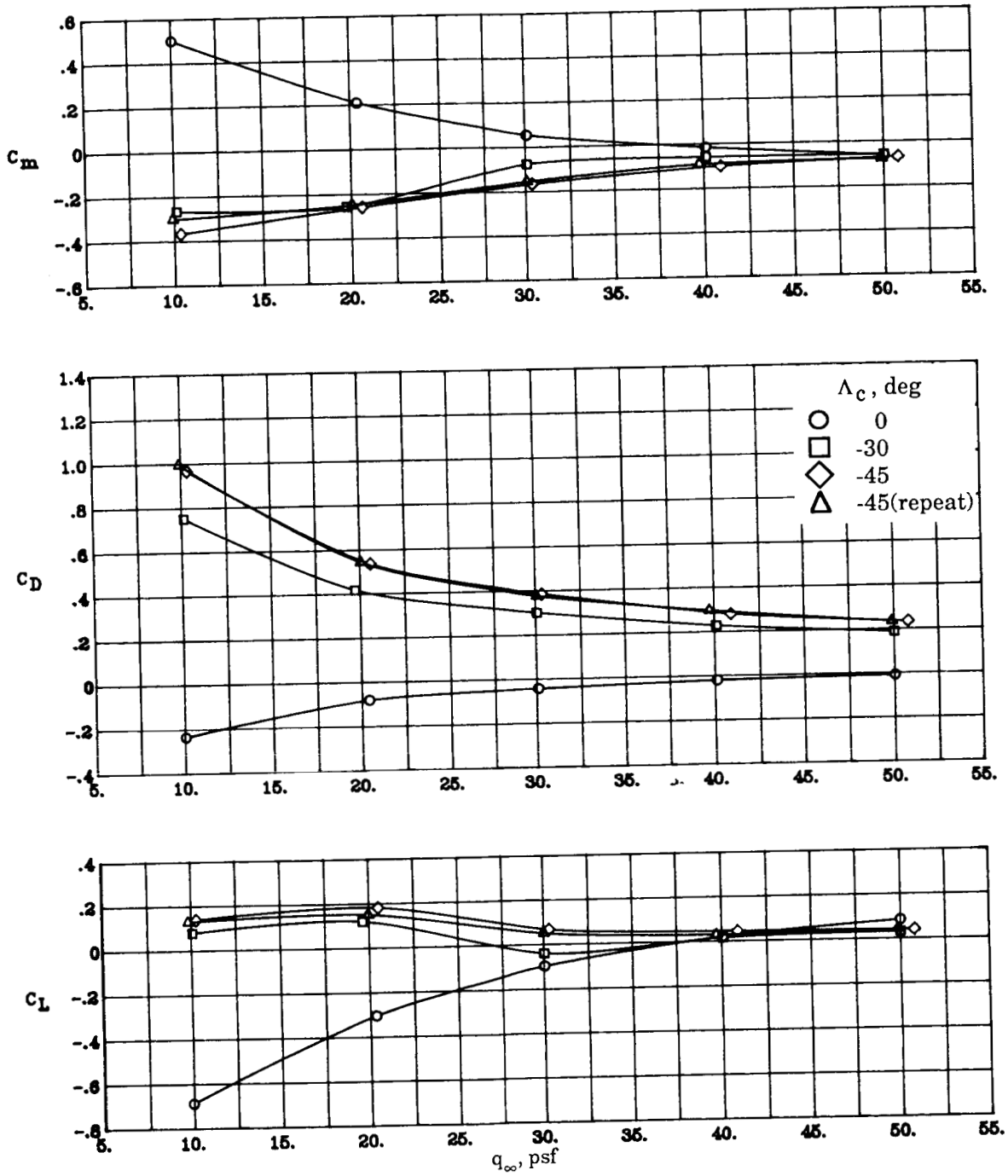


(l) NPR = 3.0; $\beta = 10°$; $\delta_f = 26°$.

Figure 5. Continued.

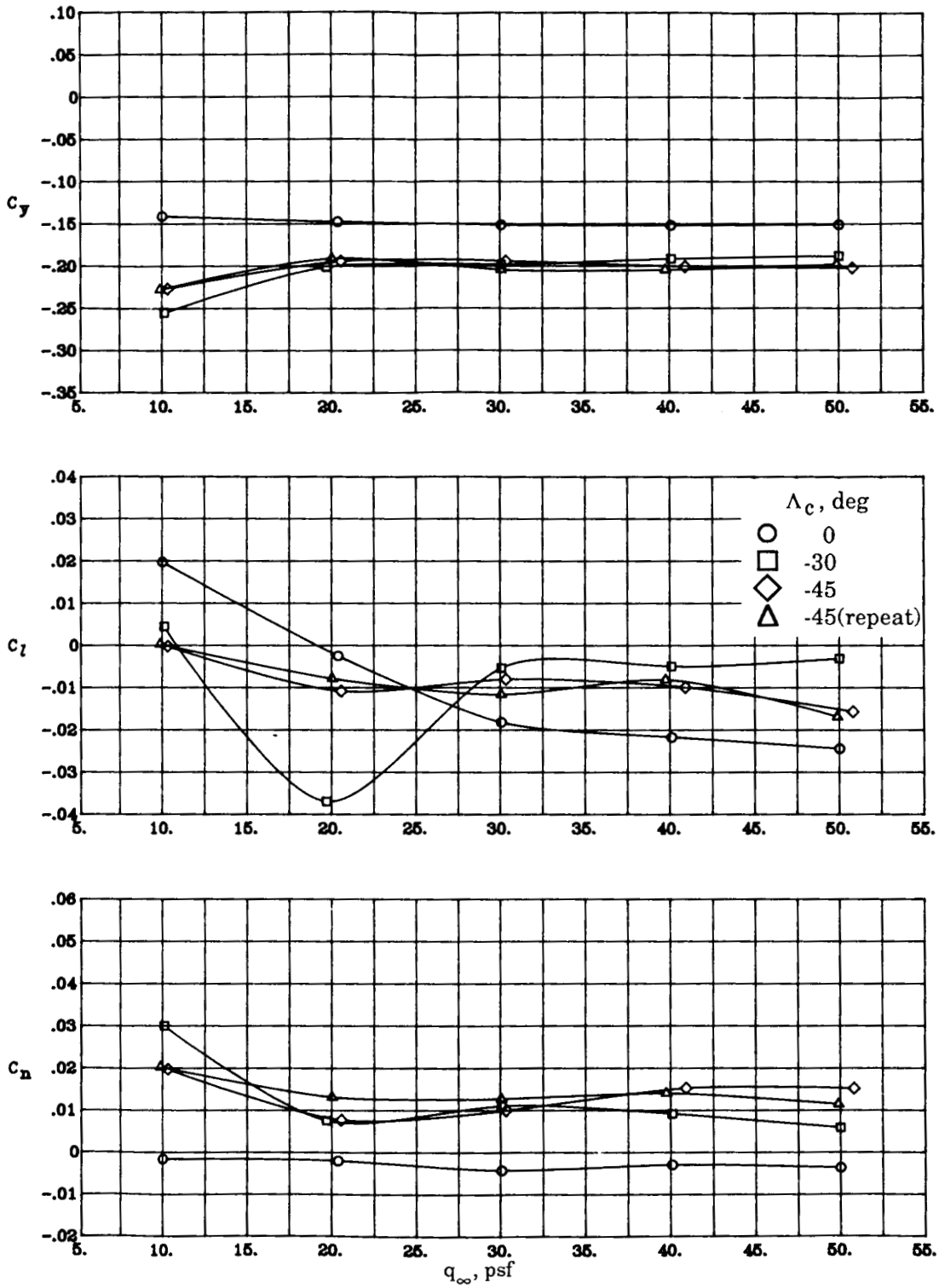


(l) Concluded.

Figure 5. Continued.

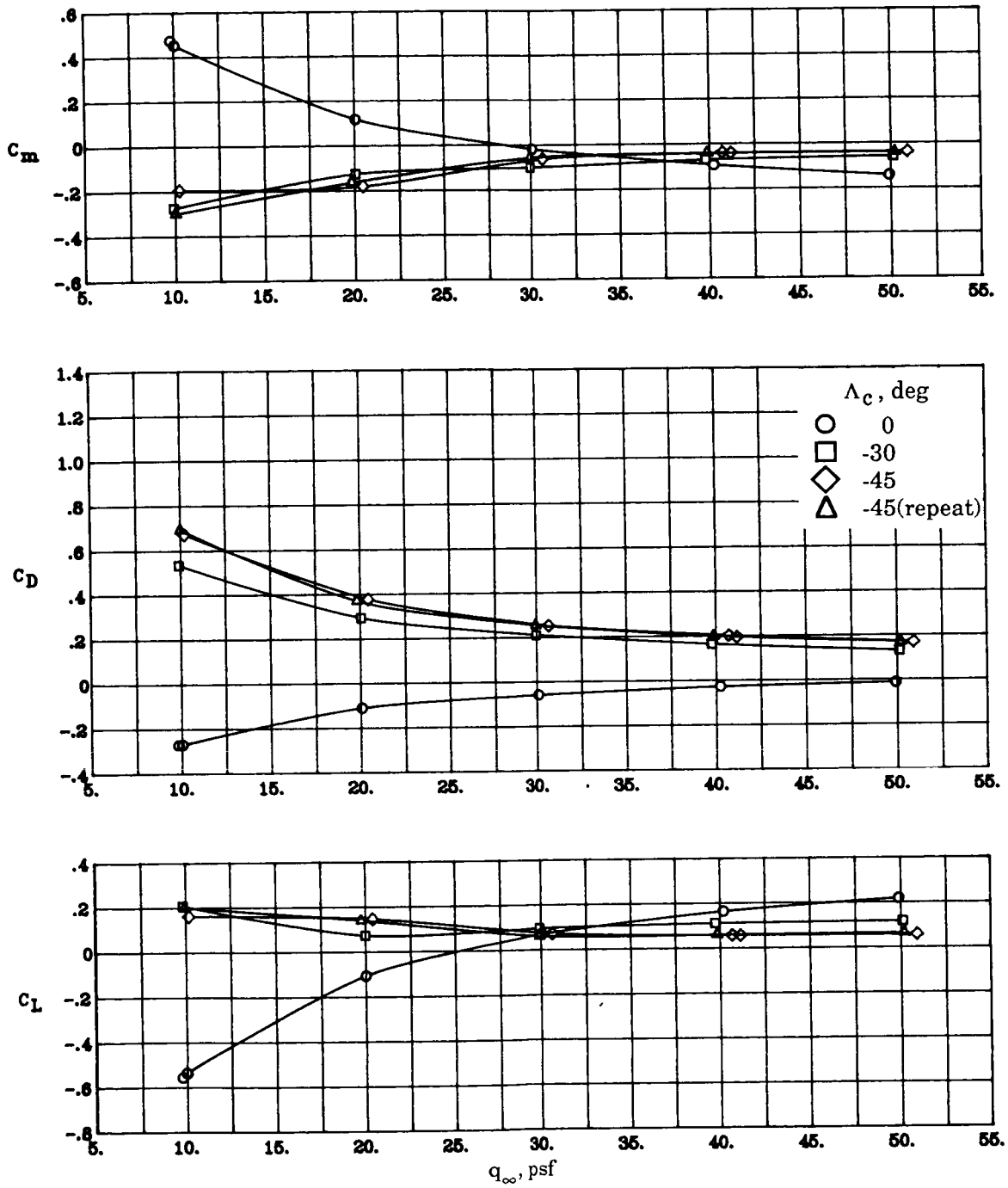


(m) NPR = 2.0; $\beta = 0°$; $\delta_f = 26°$.

Figure 5. Continued.

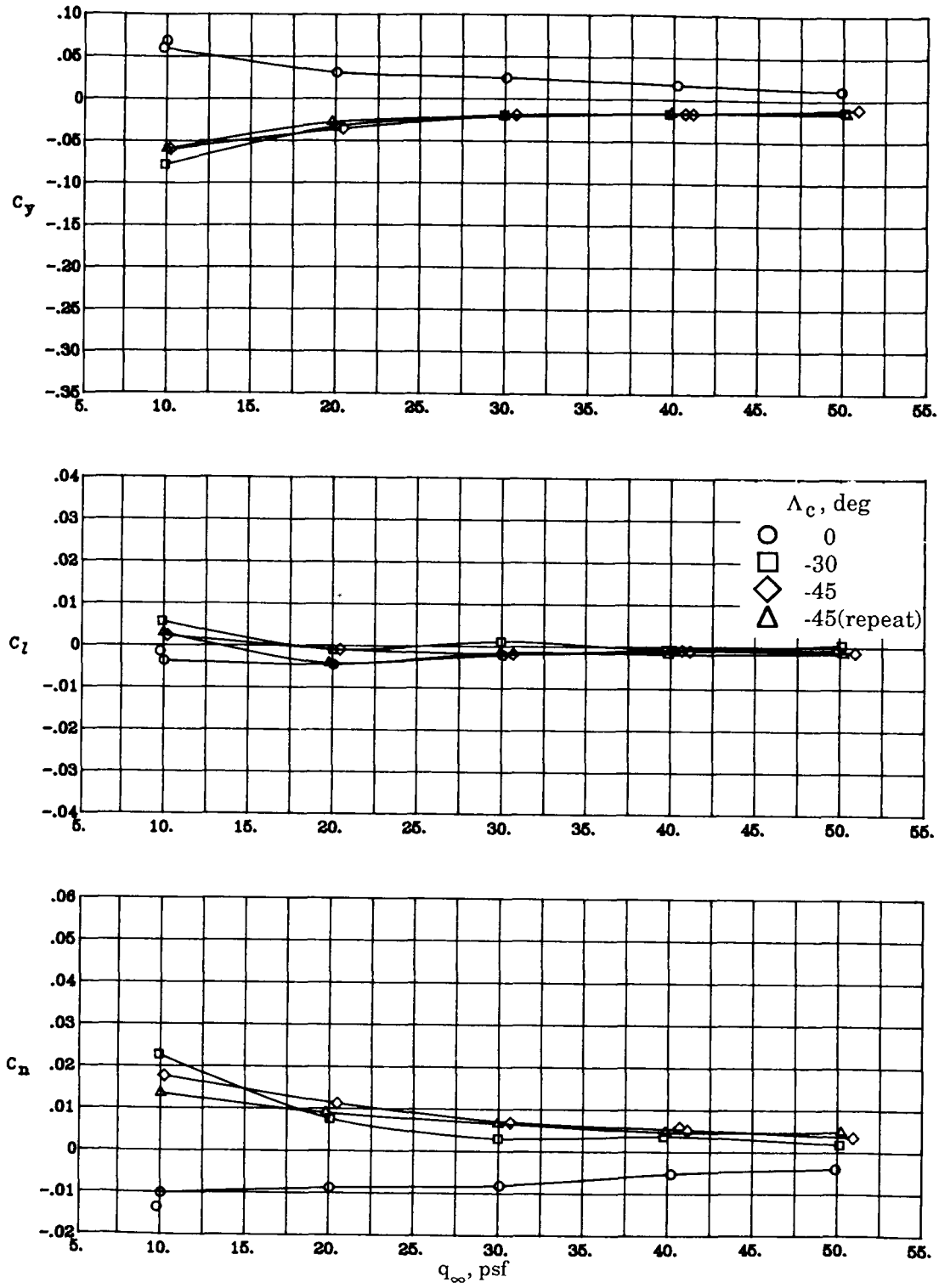


(m) Concluded.

Figure 5. Concluded.

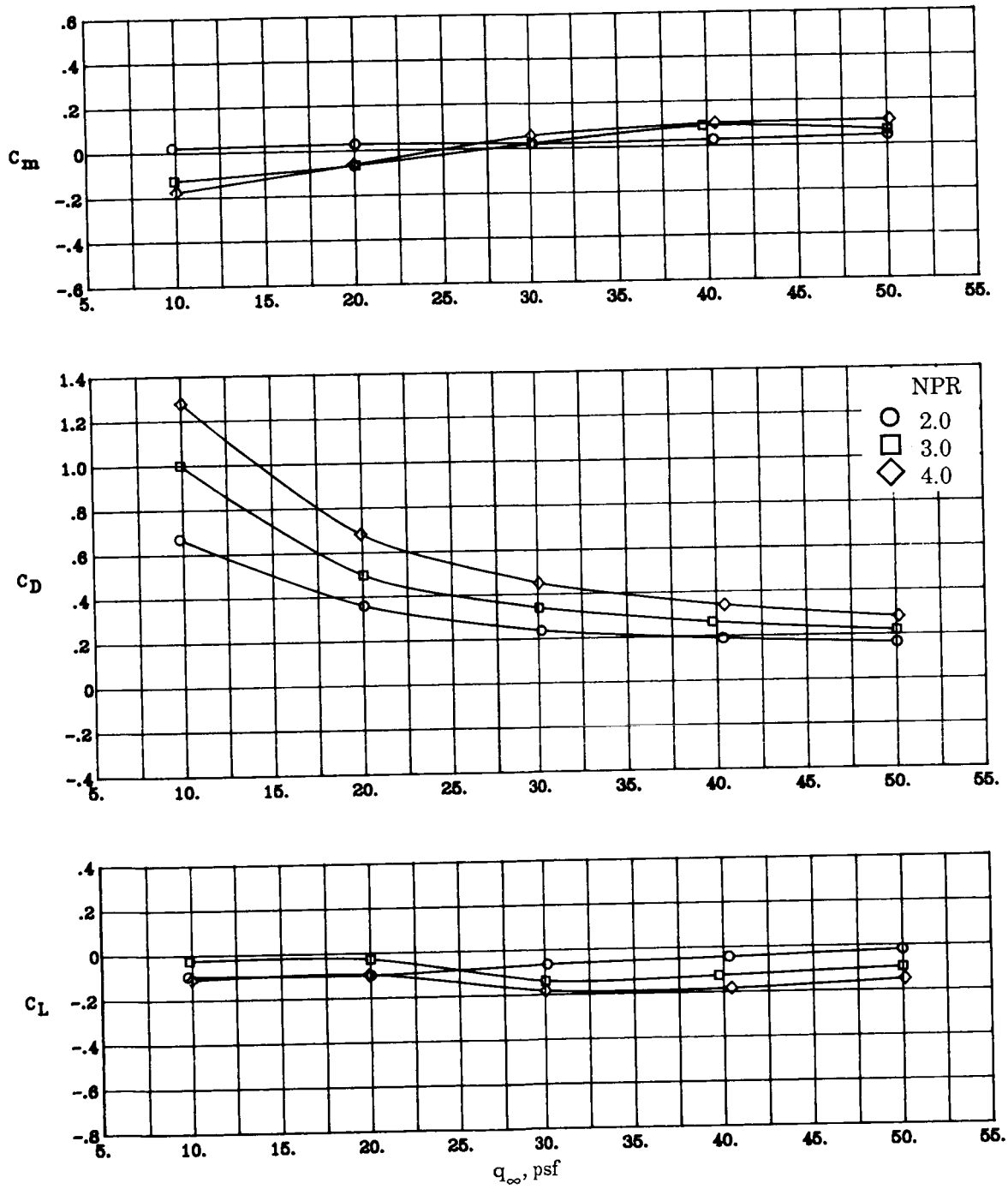


(a) $\Lambda_c = -45°$; $\beta = 0°$; $\delta_f = 0°$.

Figure 6. Effects of nozzle pressure ratio on aerodynamic characteristics.

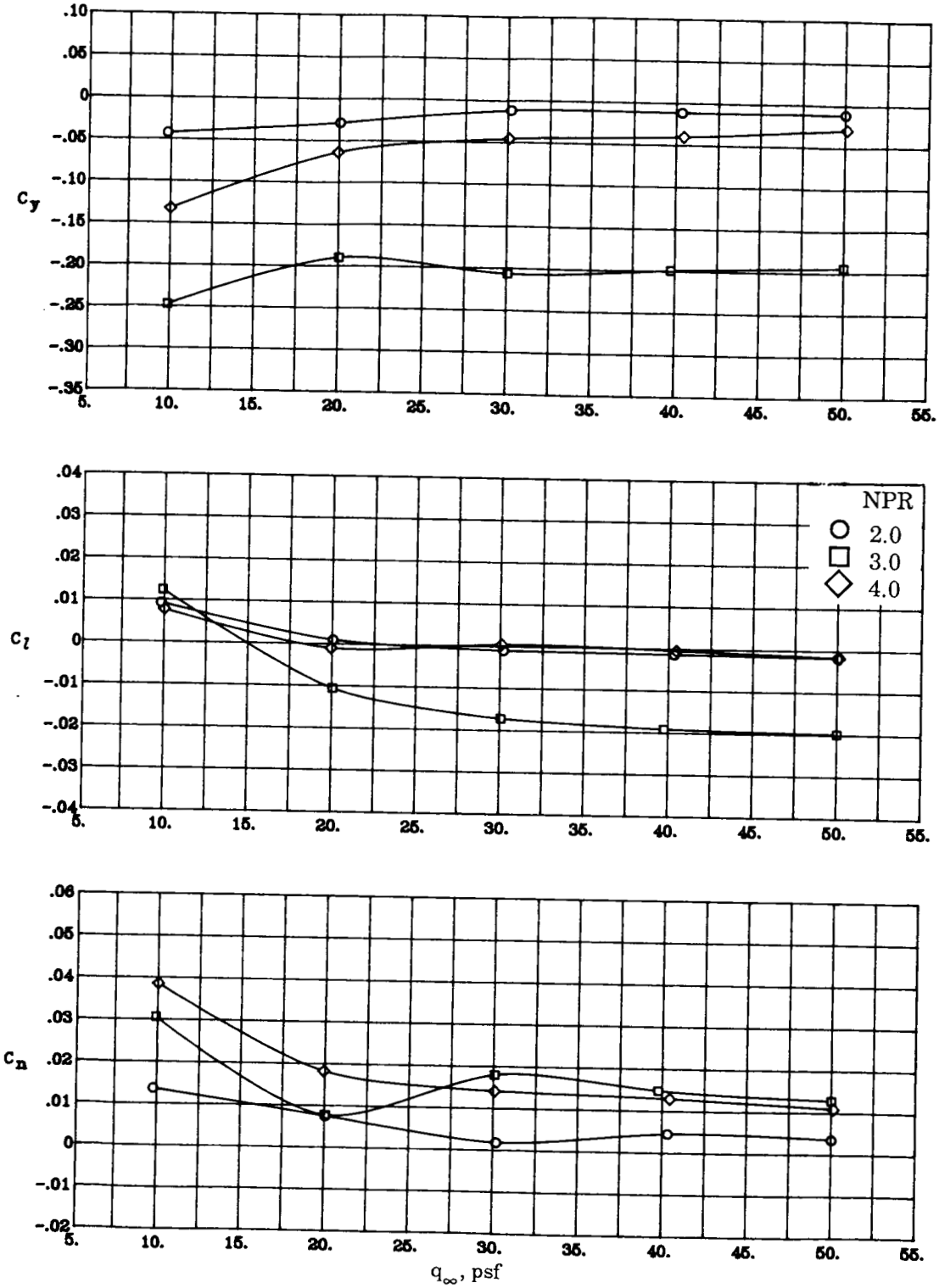


(a) Concluded.

Figure 6. Continued.

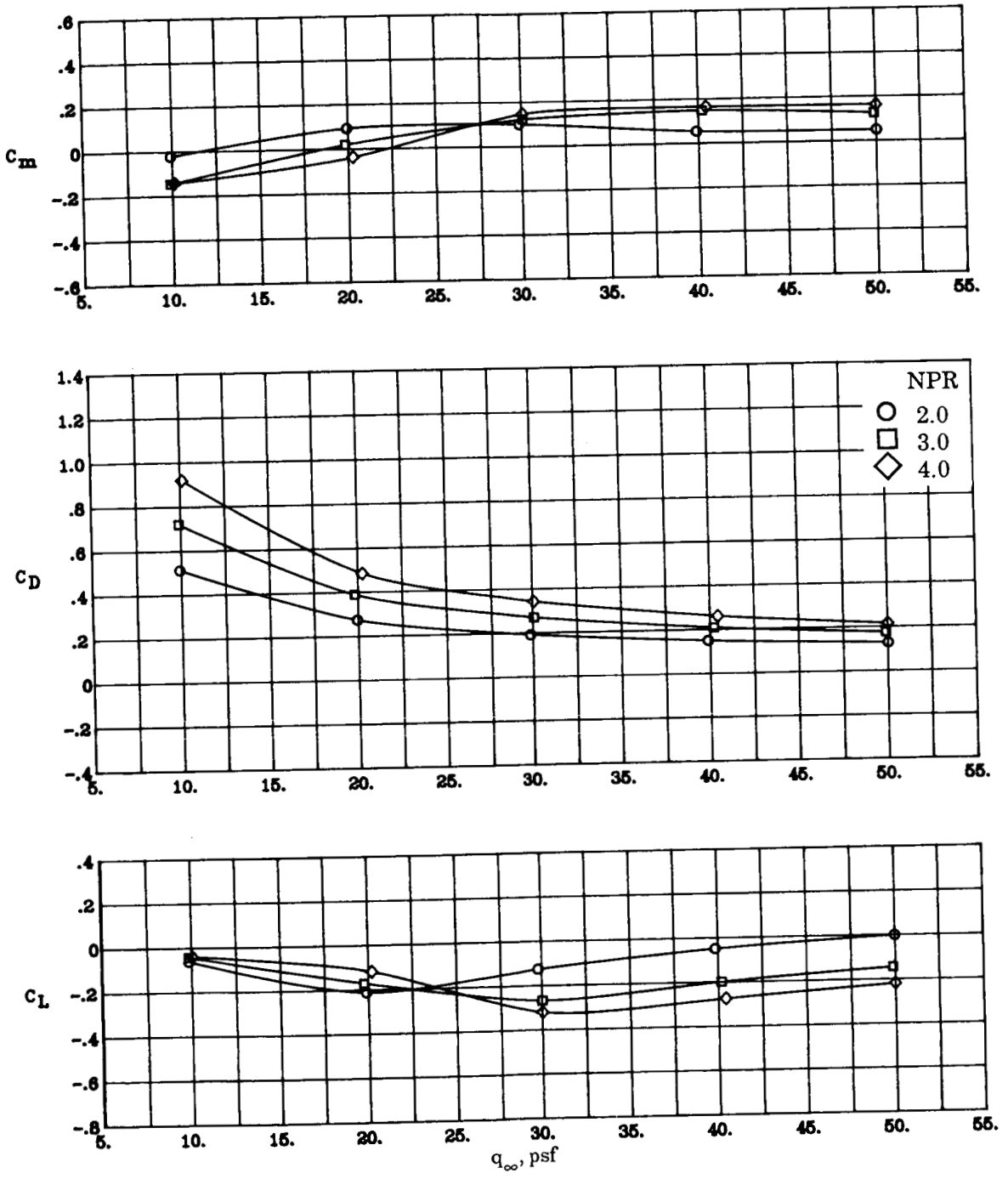


(b) $\Lambda_c = -30°$; $\beta = 0°$; $\delta_f = 0°$.

Figure 6. Continued.

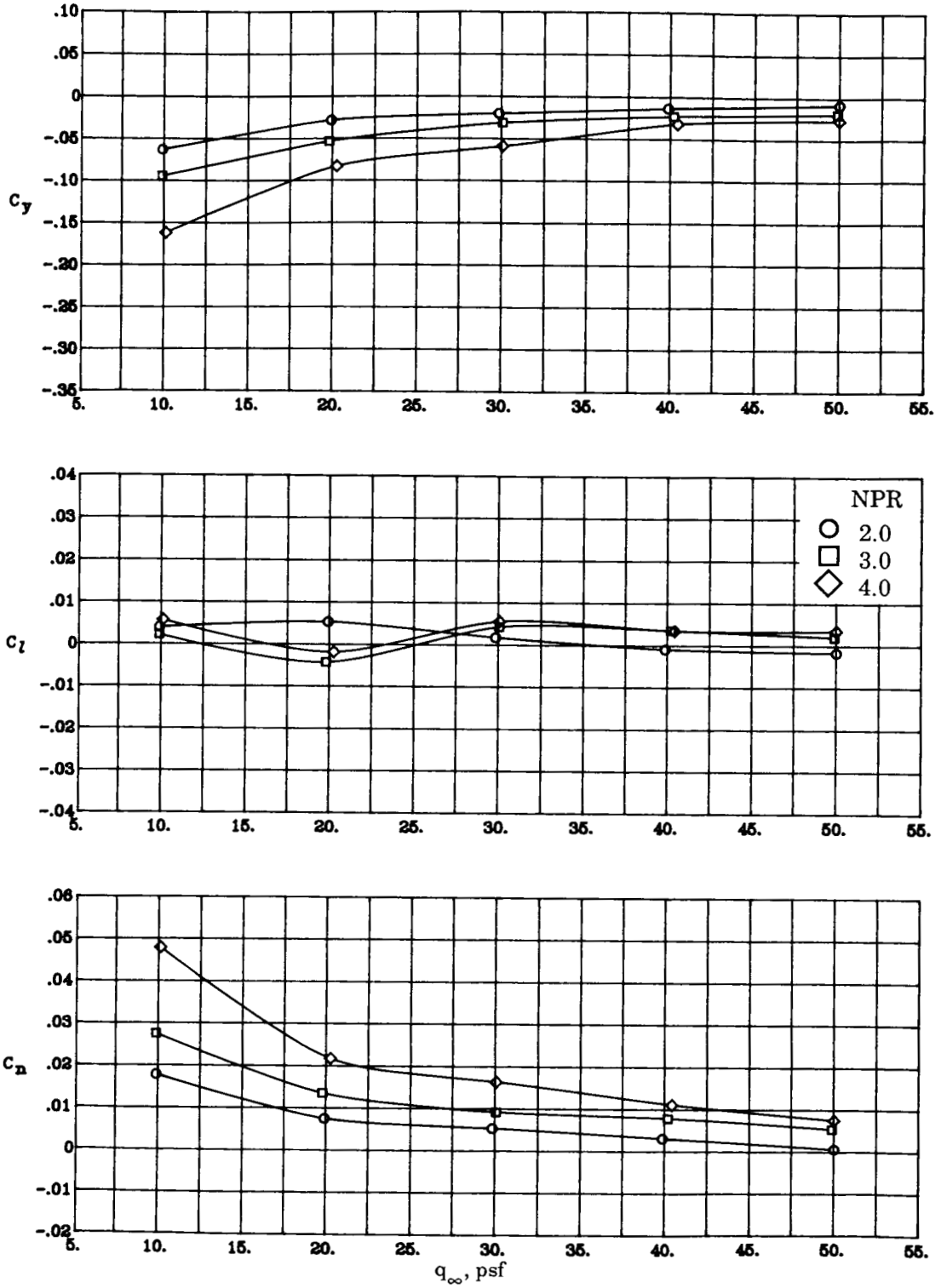


(b) Concluded.

Figure 6. Continued.

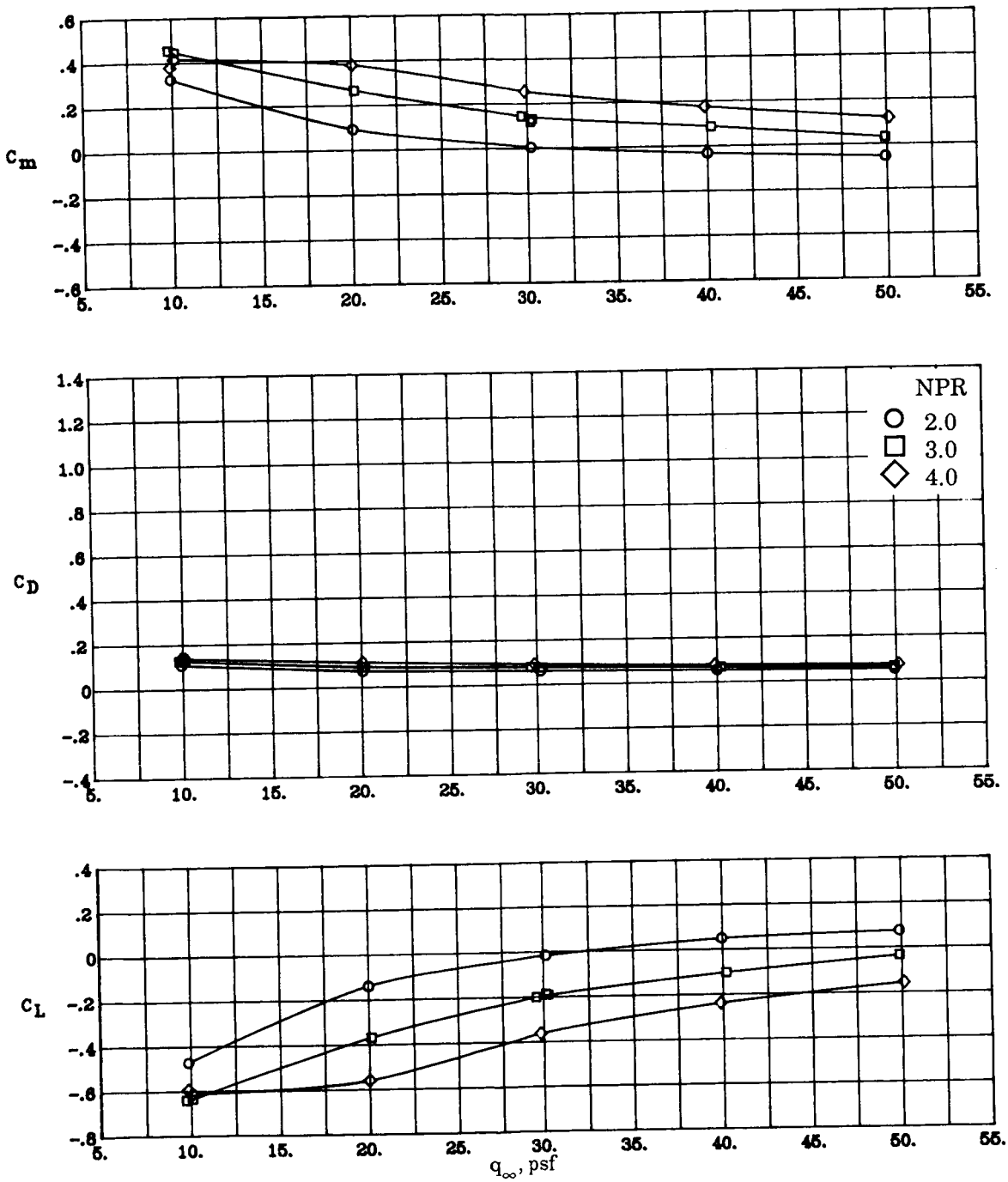


(c) $\Lambda_c = 0°$; $\beta = 0°$; $\delta_f = 0°$.

Figure 6. Continued.

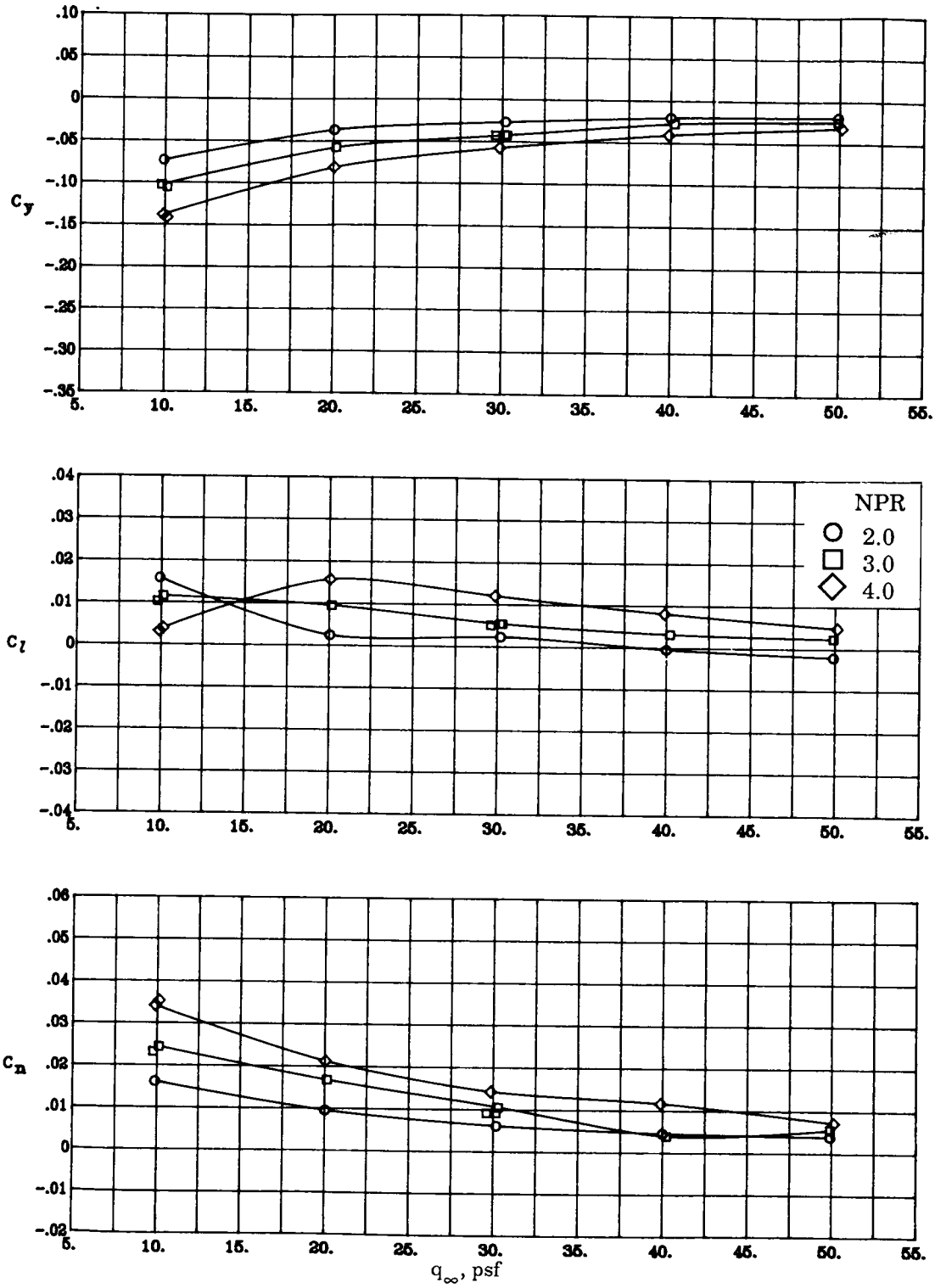


(c) Concluded.

Figure 6. Continued.

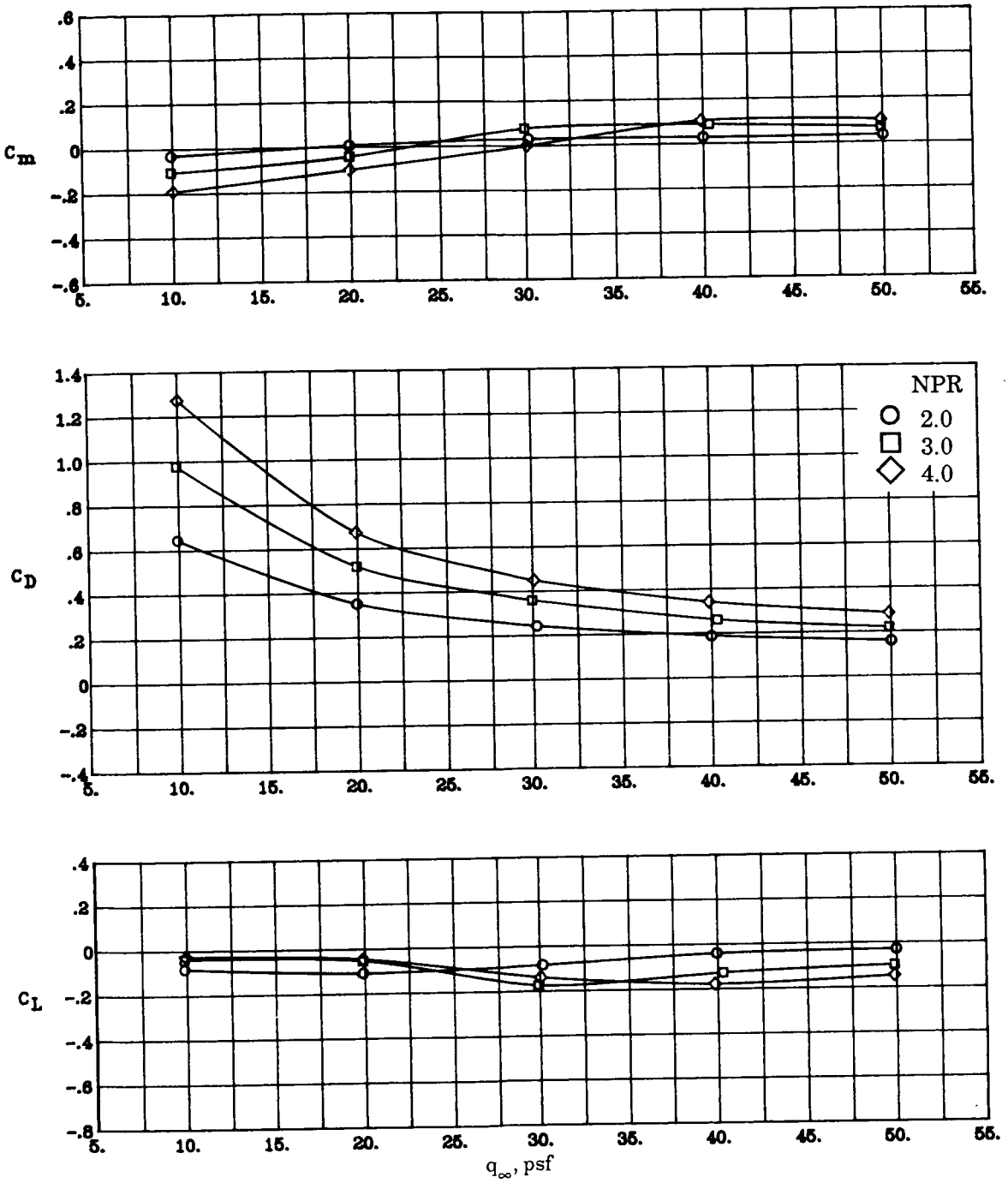


(d) $\Lambda_c = -45°$; $\beta = 5°$; $\delta_f = 0°$.

Figure 6. Continued.

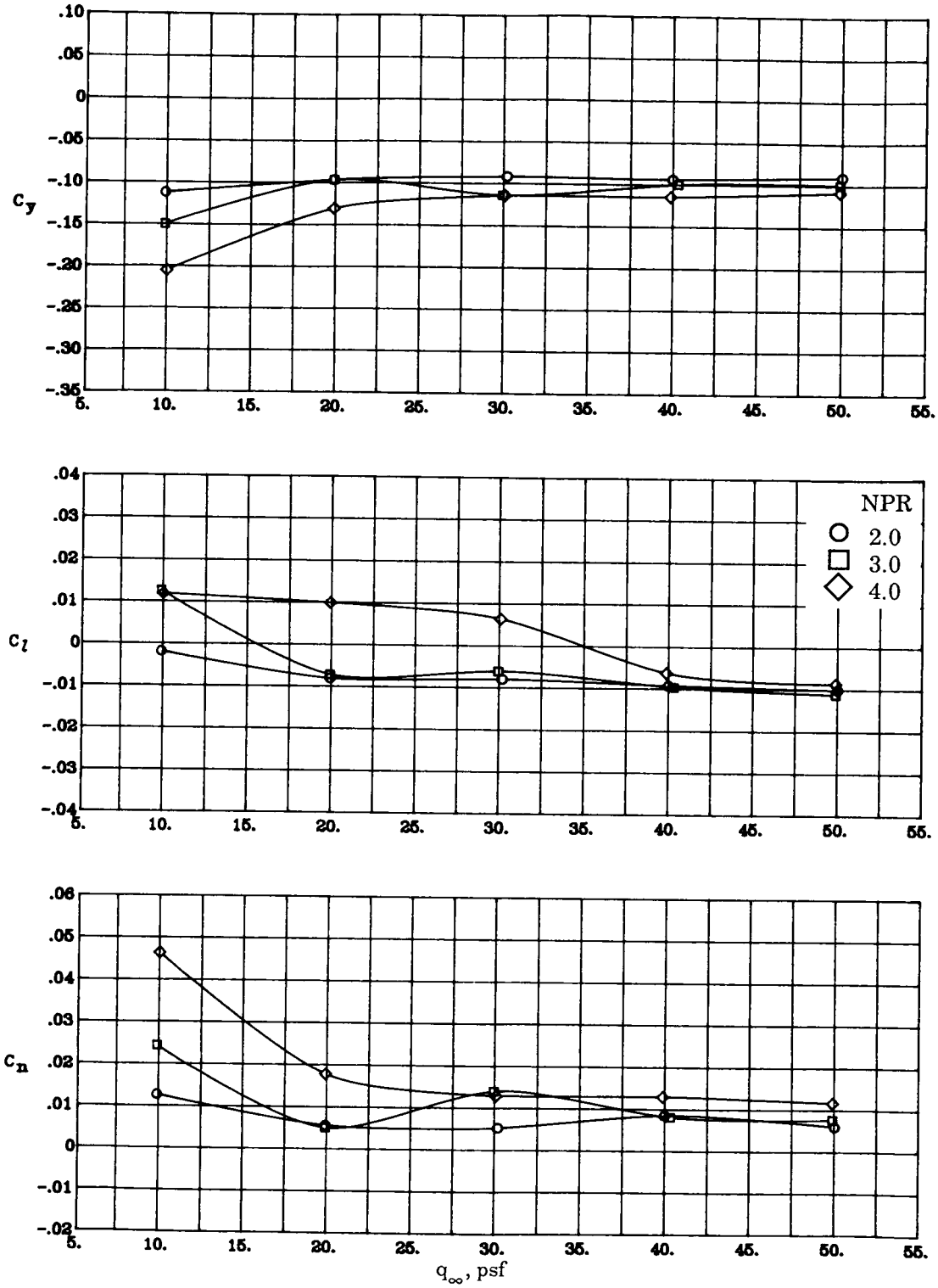


(d) Concluded.

Figure 6. Continued.

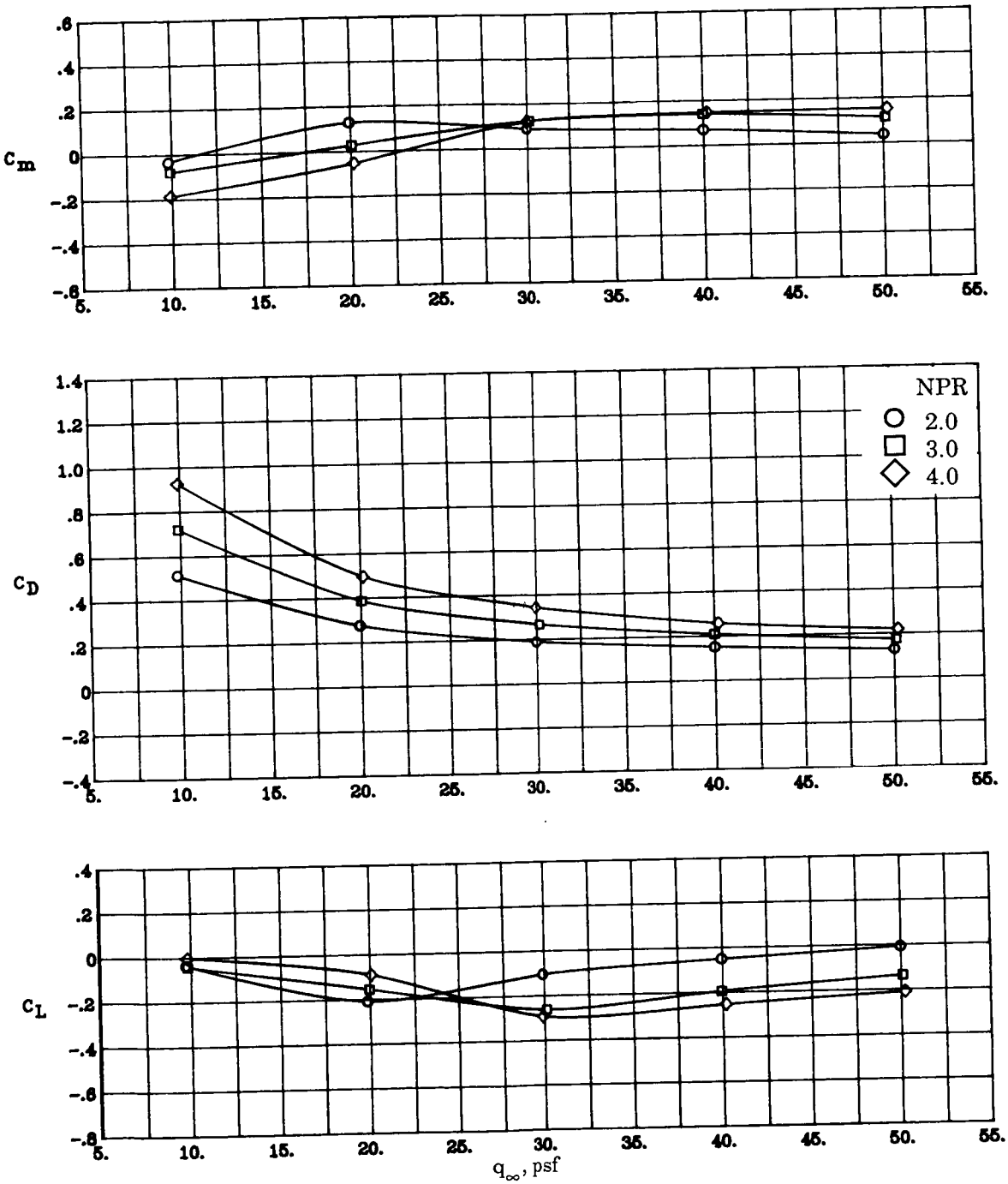


(e) $\Lambda_c = -30°$; $\beta = 5°$; $\delta_f = 0°$.

Figure 6. Continued.

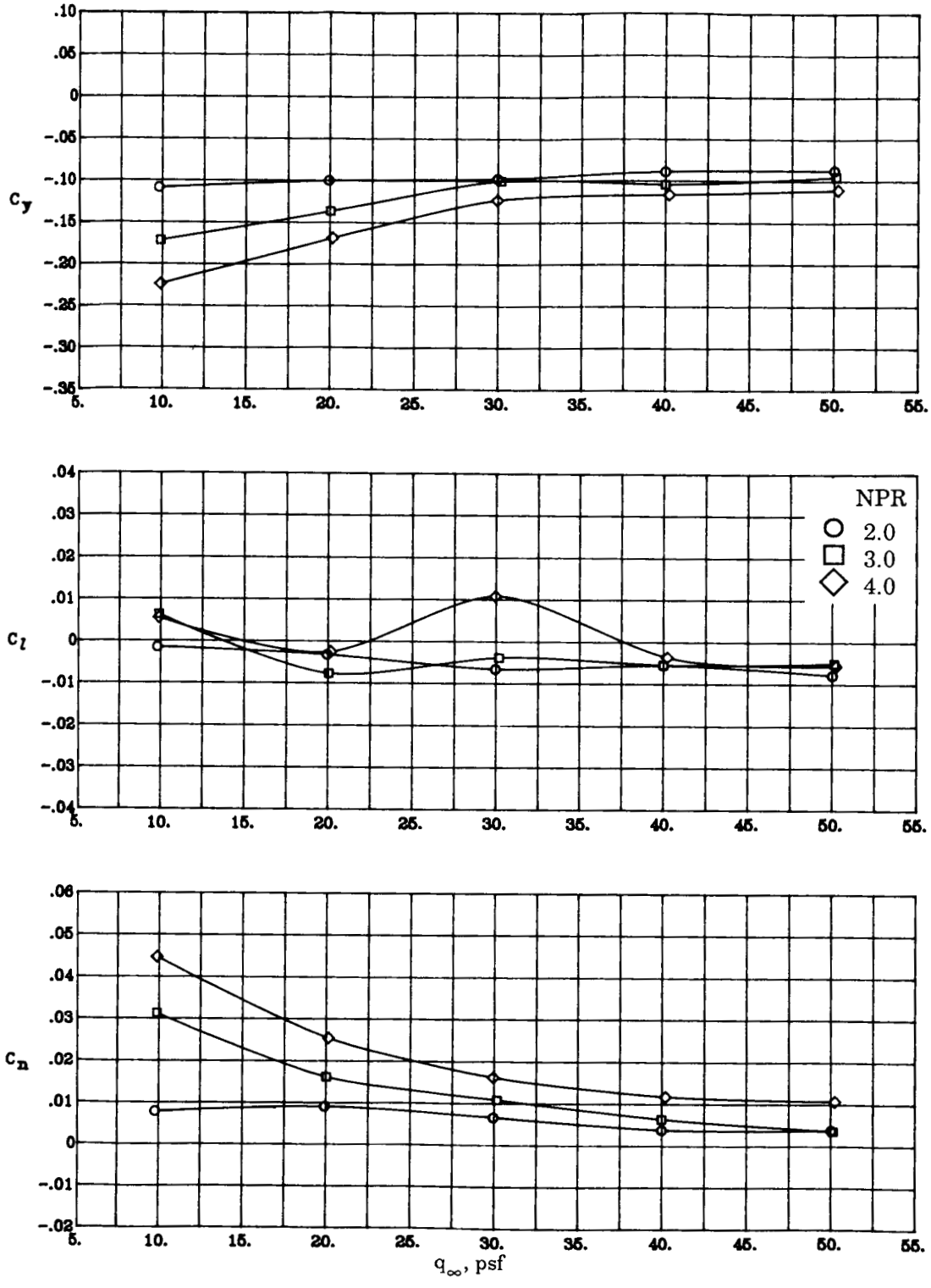


(e) Concluded.

Figure 6. Continued.

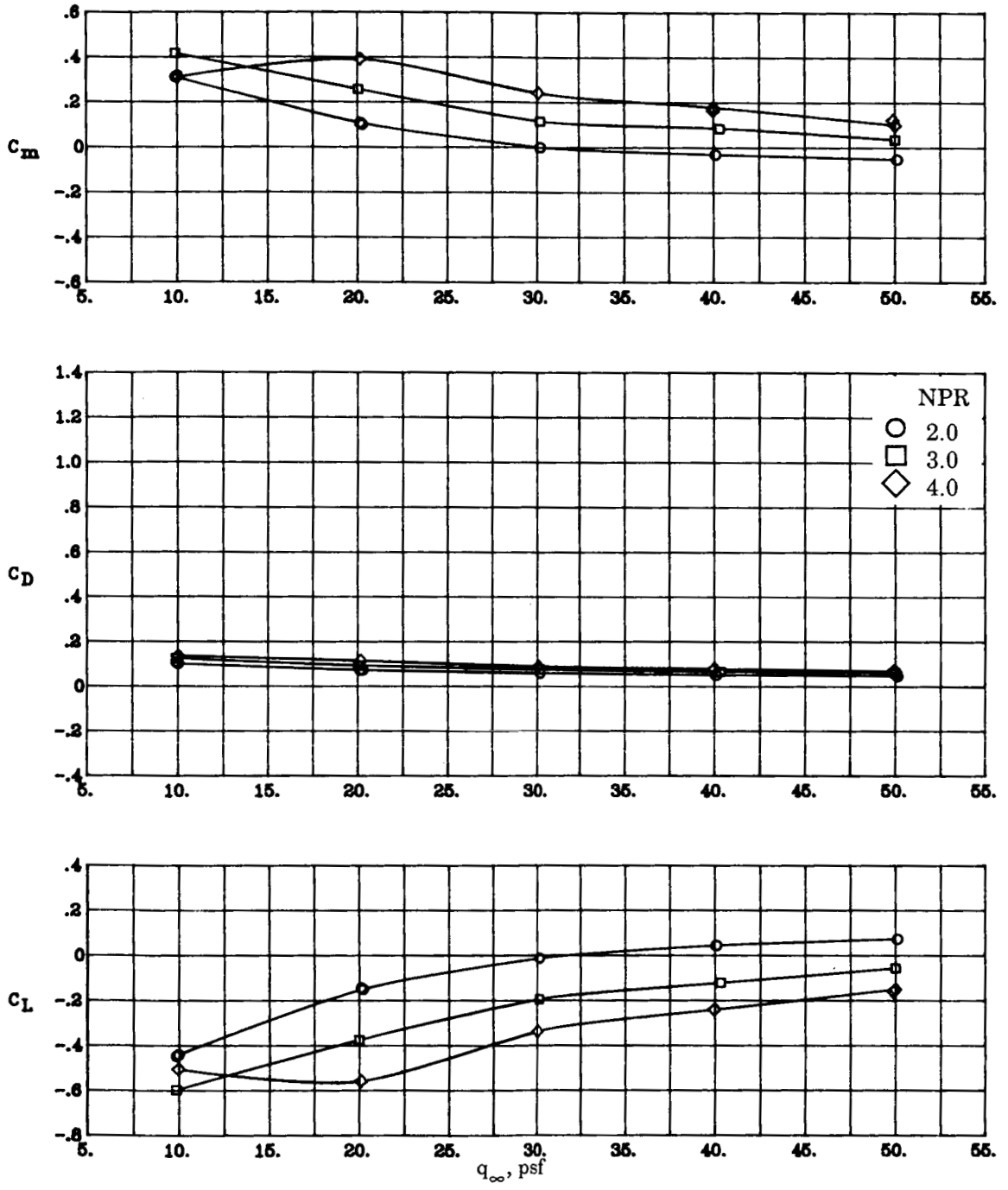


(f) $\Lambda_c = 0°$; $\beta = 5°$; $\delta_f = 0°$.

Figure 6. Continued.

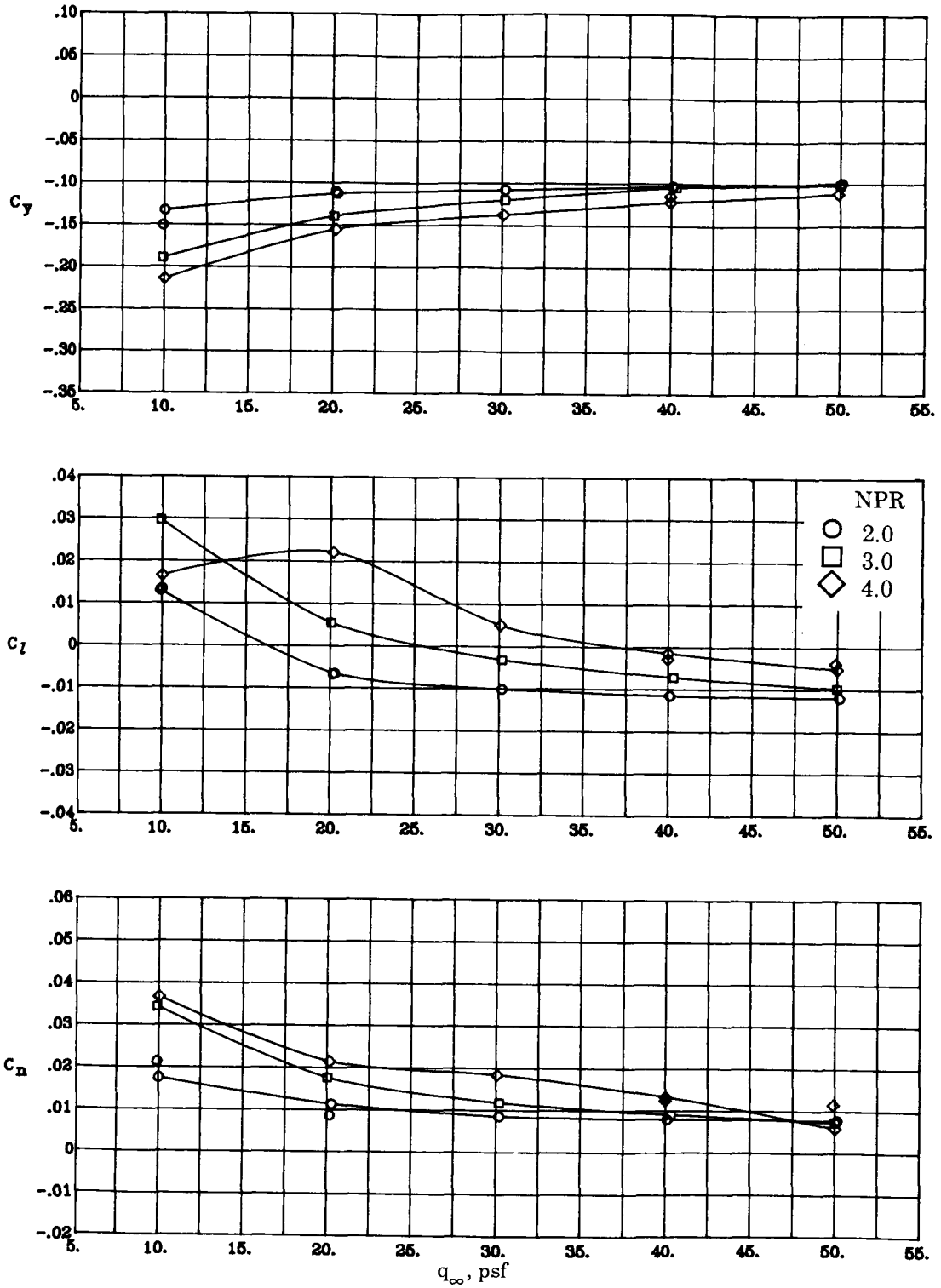


(f) Concluded.

Figure 6. Continued.

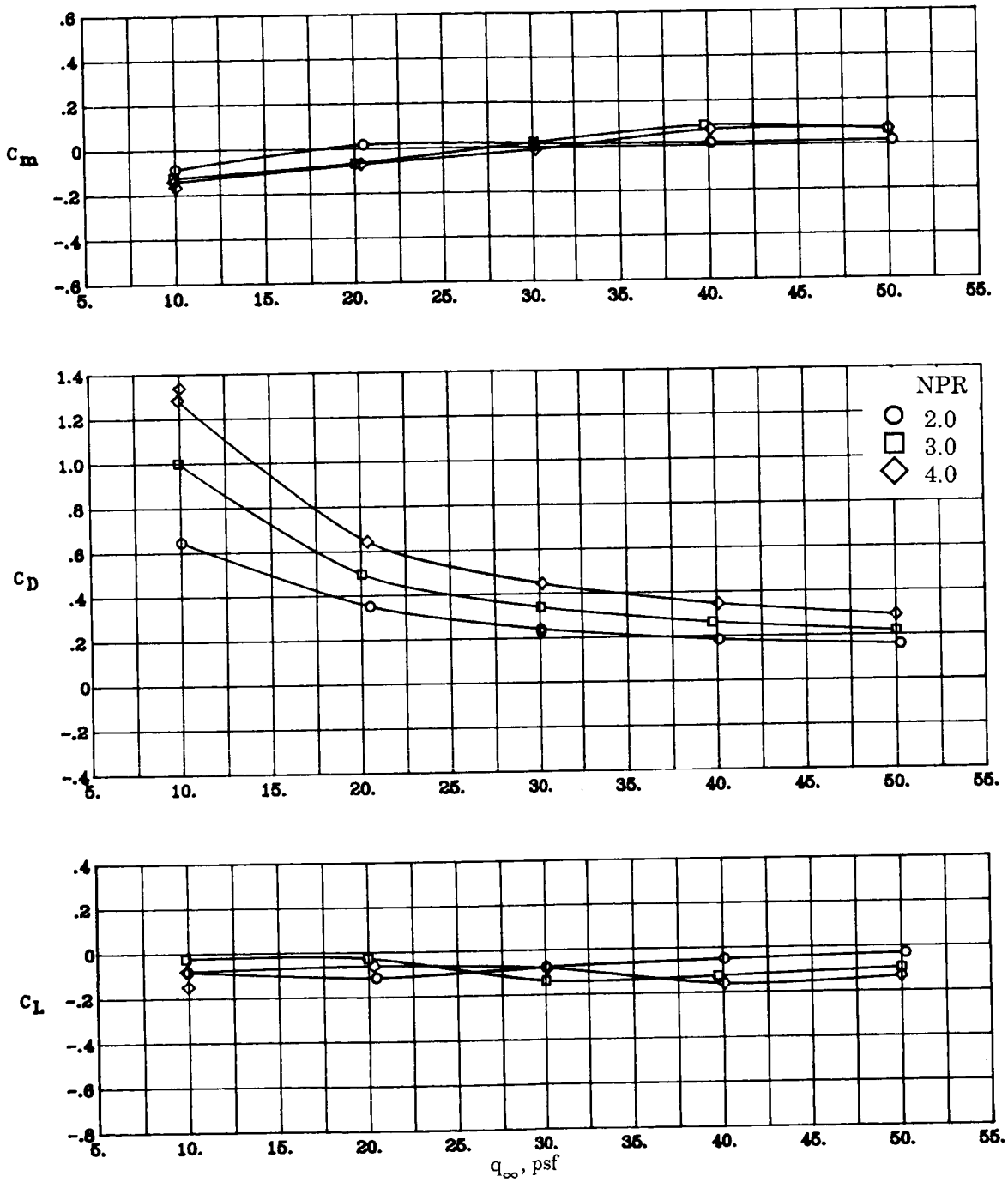


(g) $\Lambda_c = -45°$; $\beta = 10°$; $\delta_f = 0°$.

Figure 6. Continued.

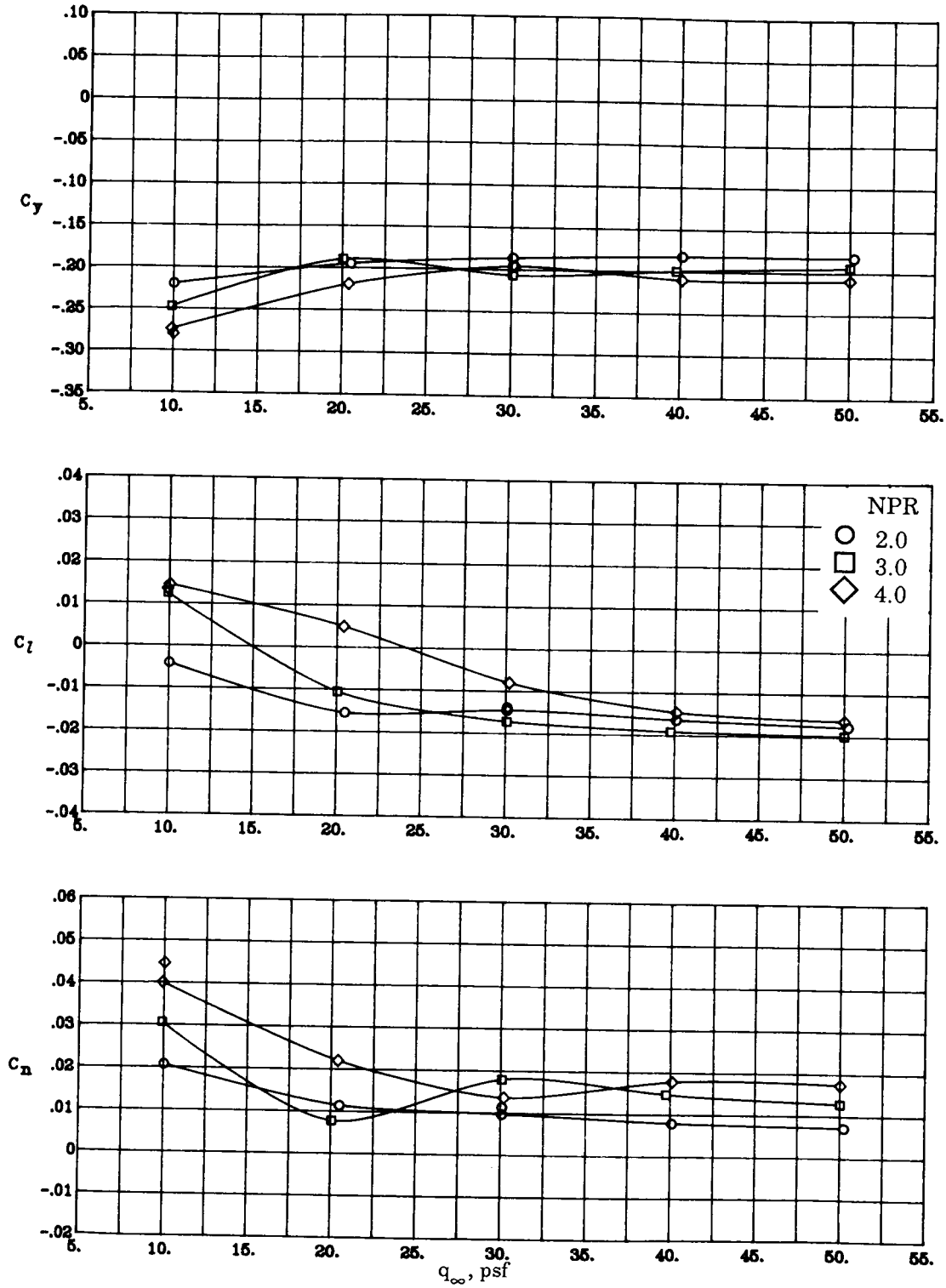


(g) Concluded.

Figure 6. Continued.

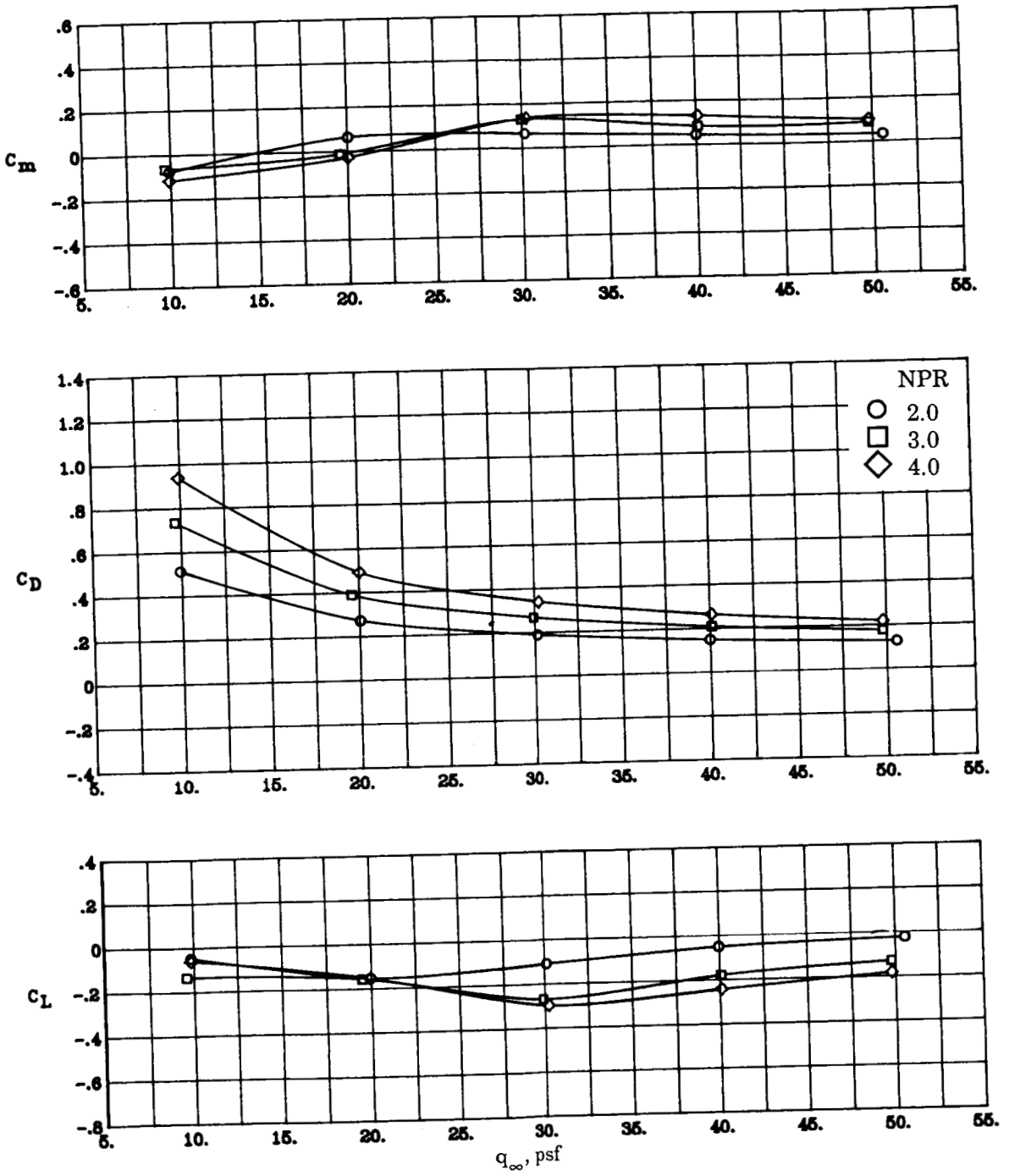


(h) $\Lambda_c = -30°$; $\beta = 10°$; $\delta_f = 0°$.

Figure 6. Continued.

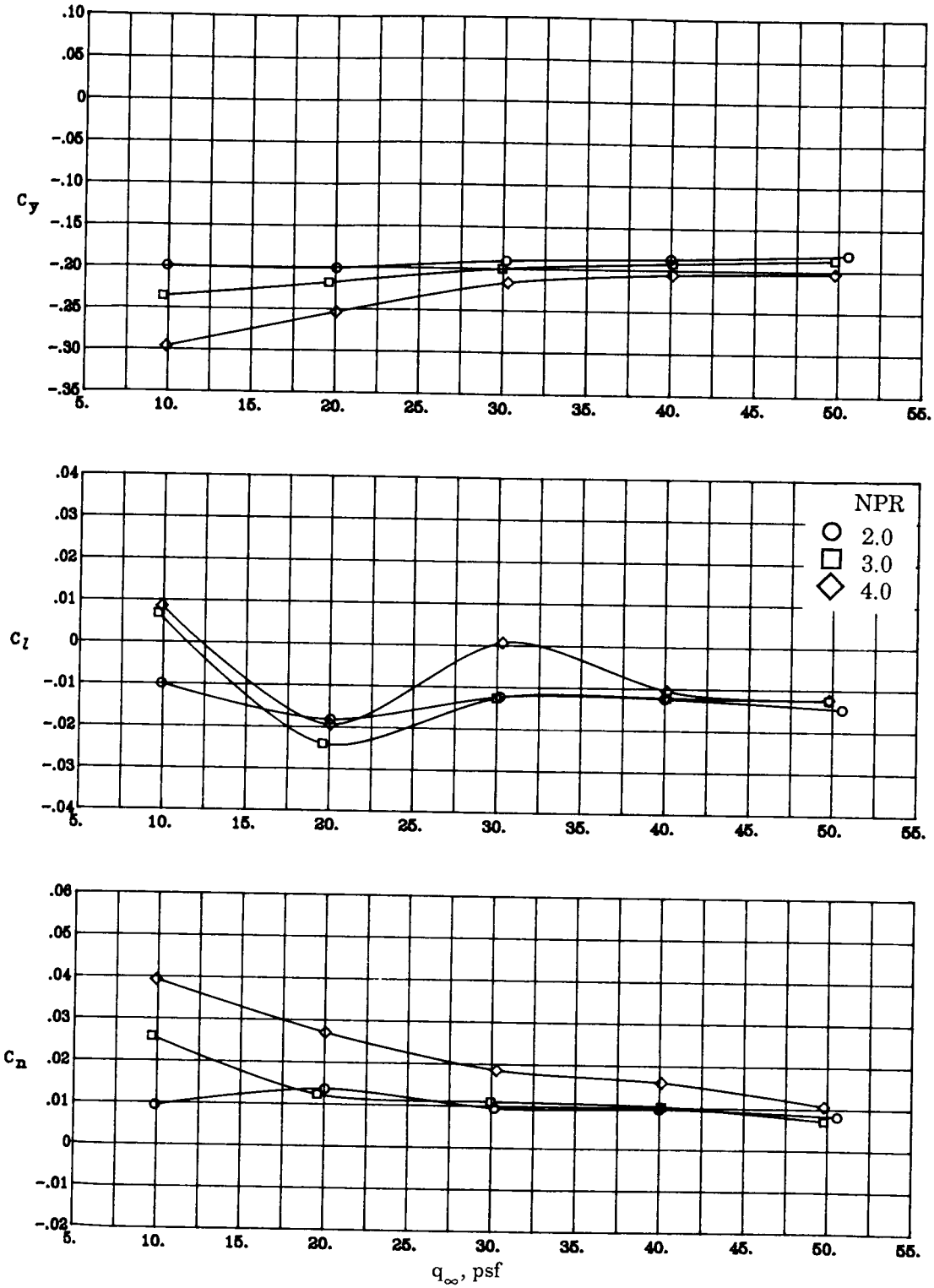


(h) Concluded.

Figure 6. Continued.

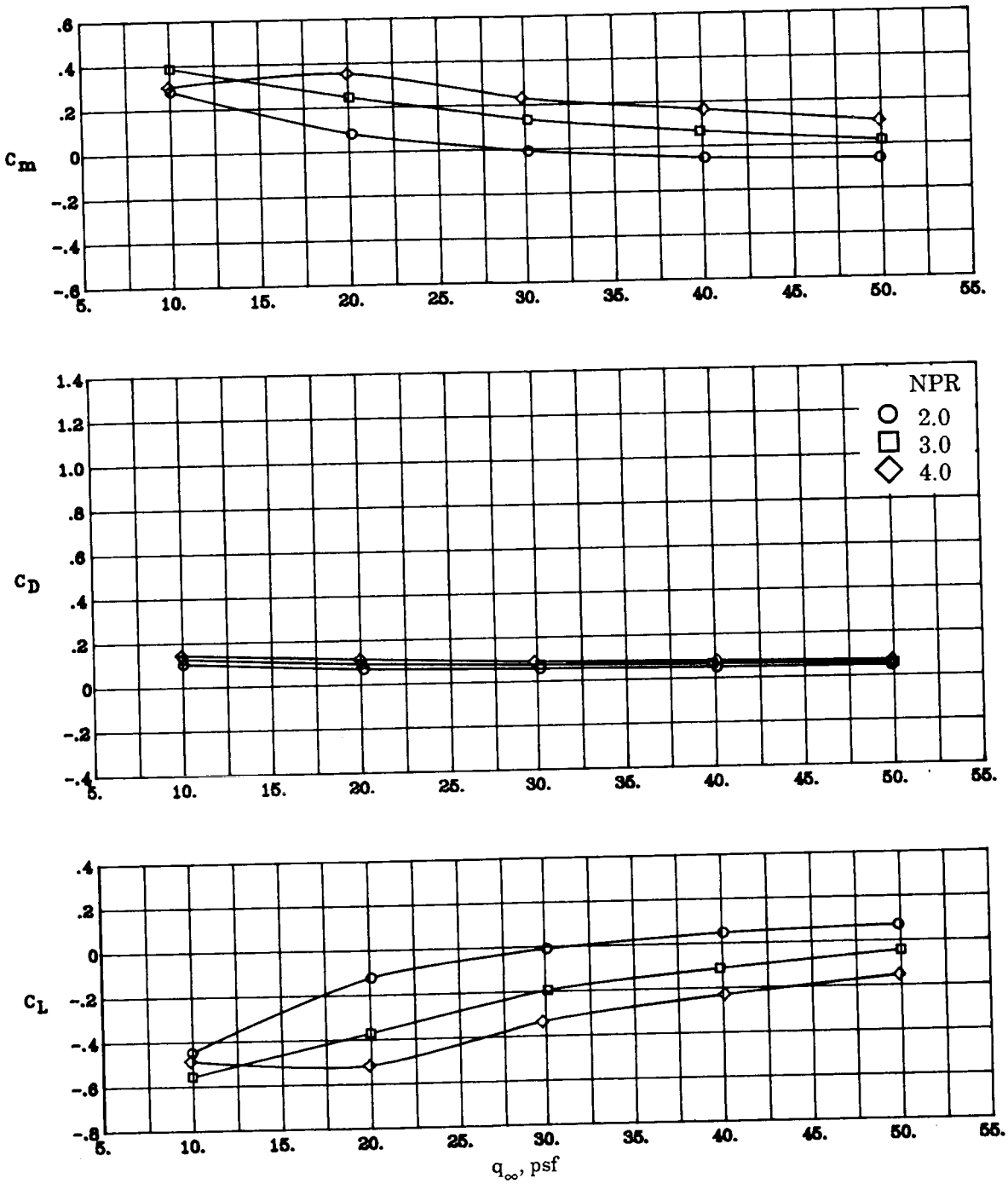


(i) $\Lambda_c = 0°$; $\beta = 10°$; $\delta_f = 0°$.

Figure 6. Continued.

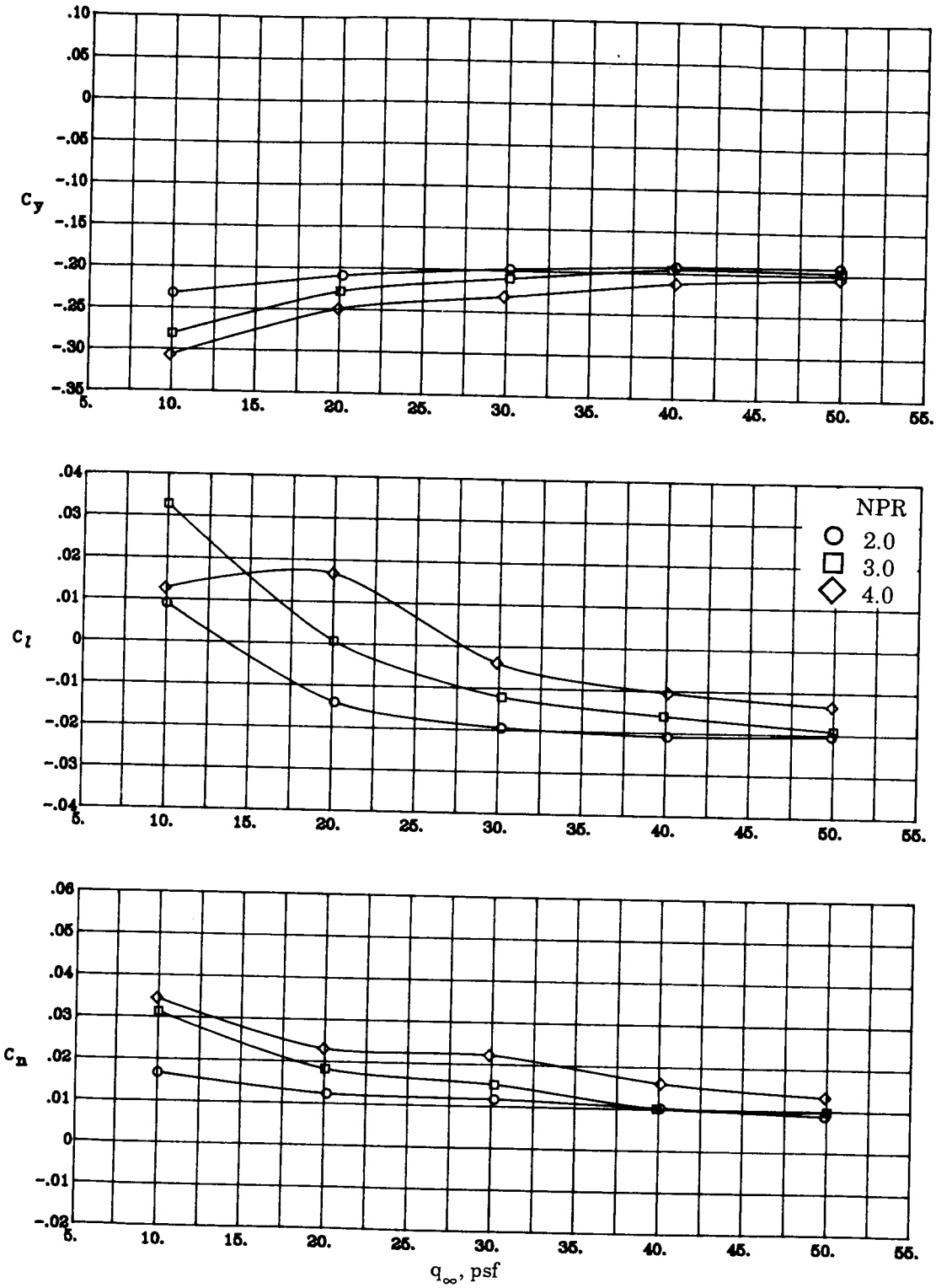


(i) Concluded.

Figure 6. Continued.

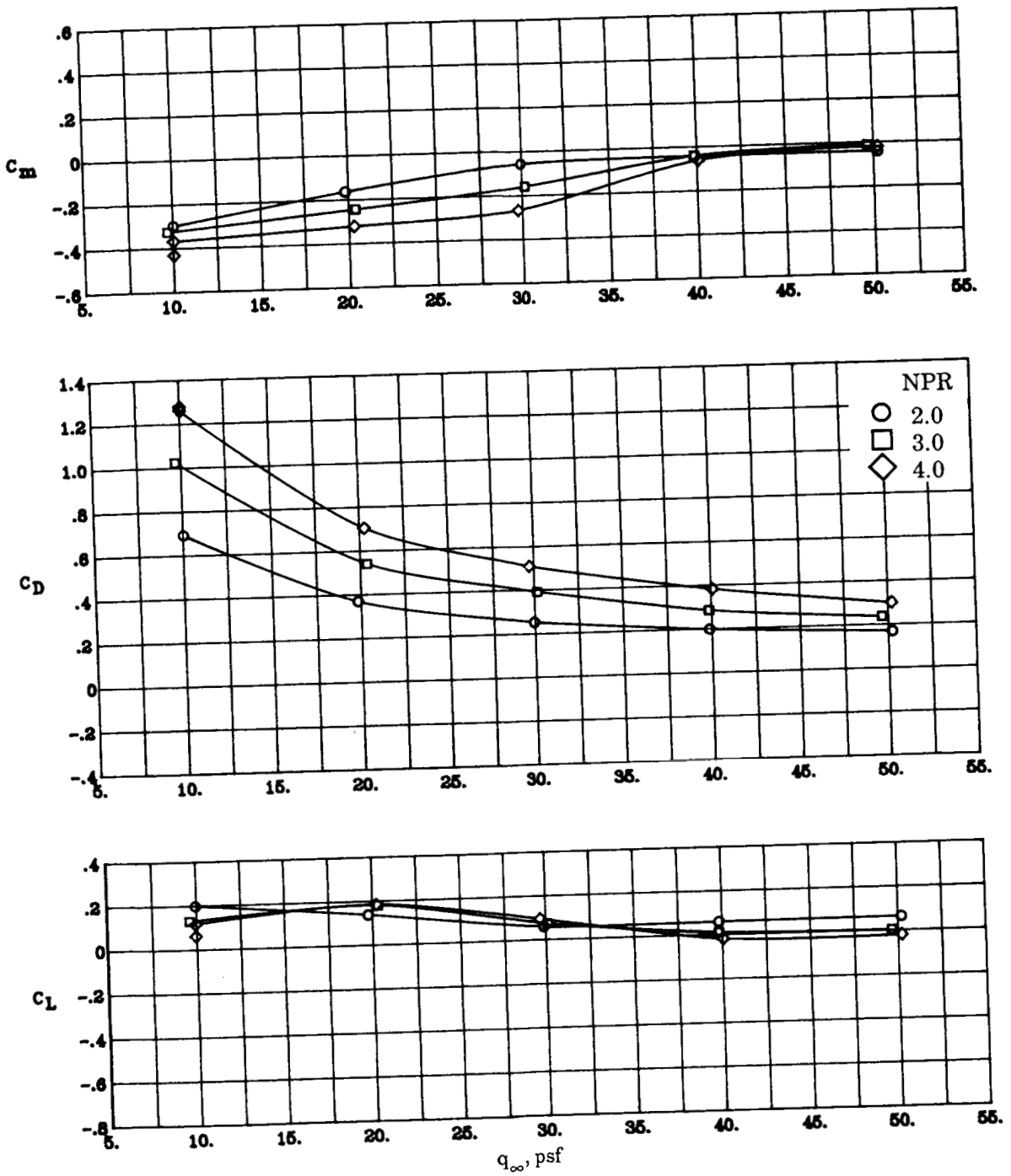


(j) $\Lambda_c = -45°$; $\beta = 0°$; $\delta_f = 26°$.

Figure 6. Continued.

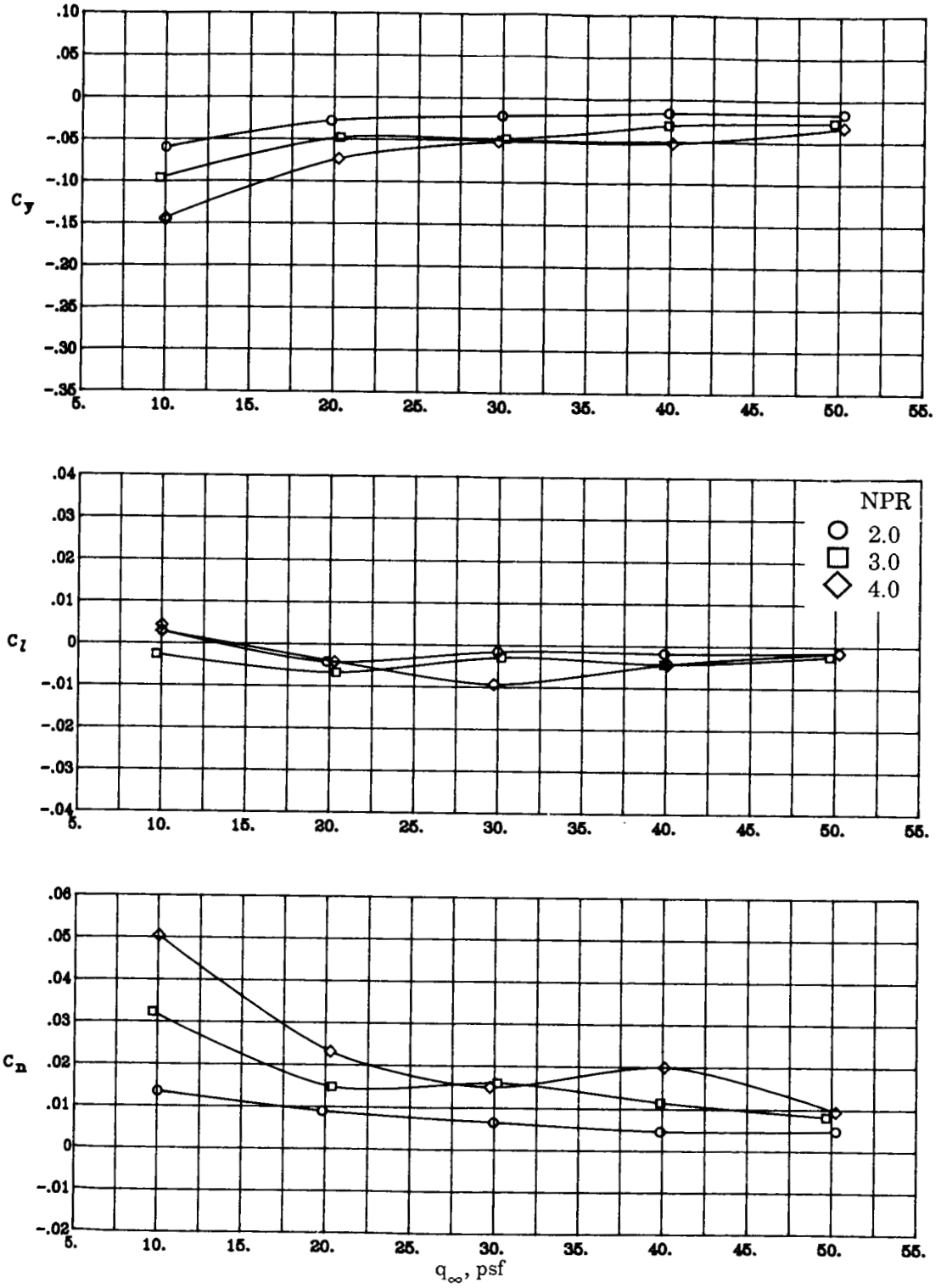


(j) Concluded.

Figure 6. Continued.

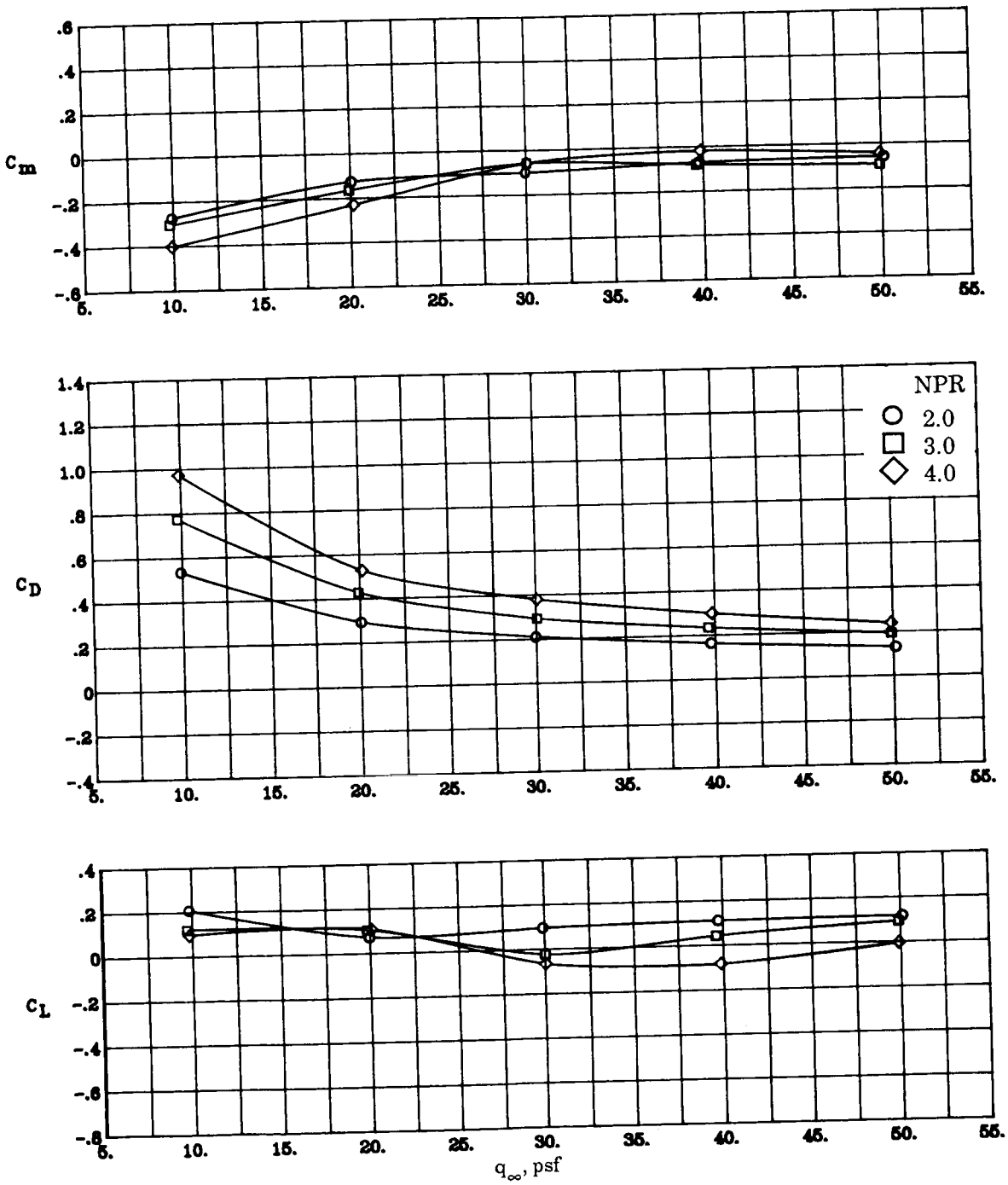


(k) $\Lambda_c = -30°$; $\beta = 0°$; $\delta_f = 26°$.

Figure 6. Continued.

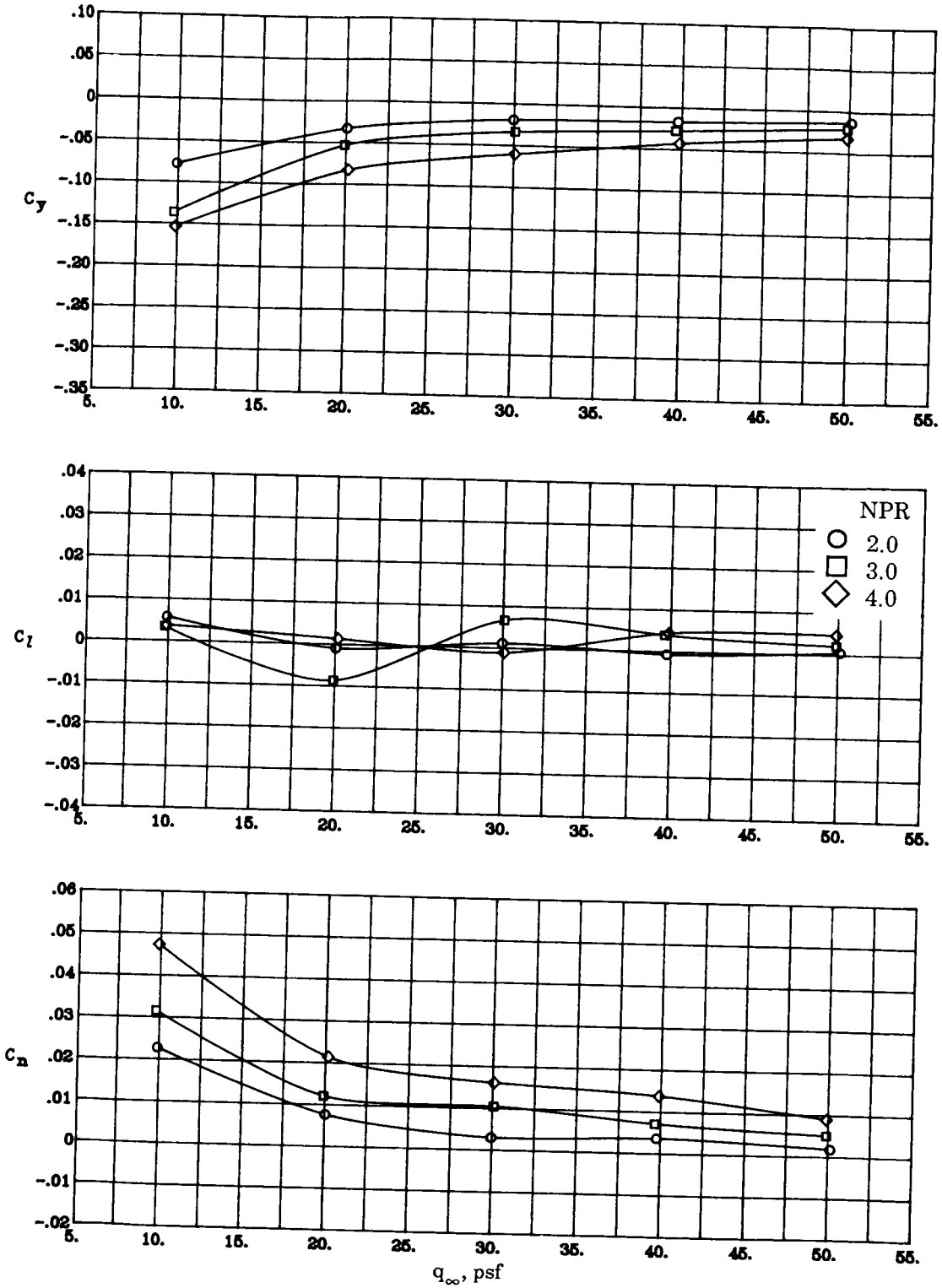


(k) Concluded.

Figure 6. Continued.

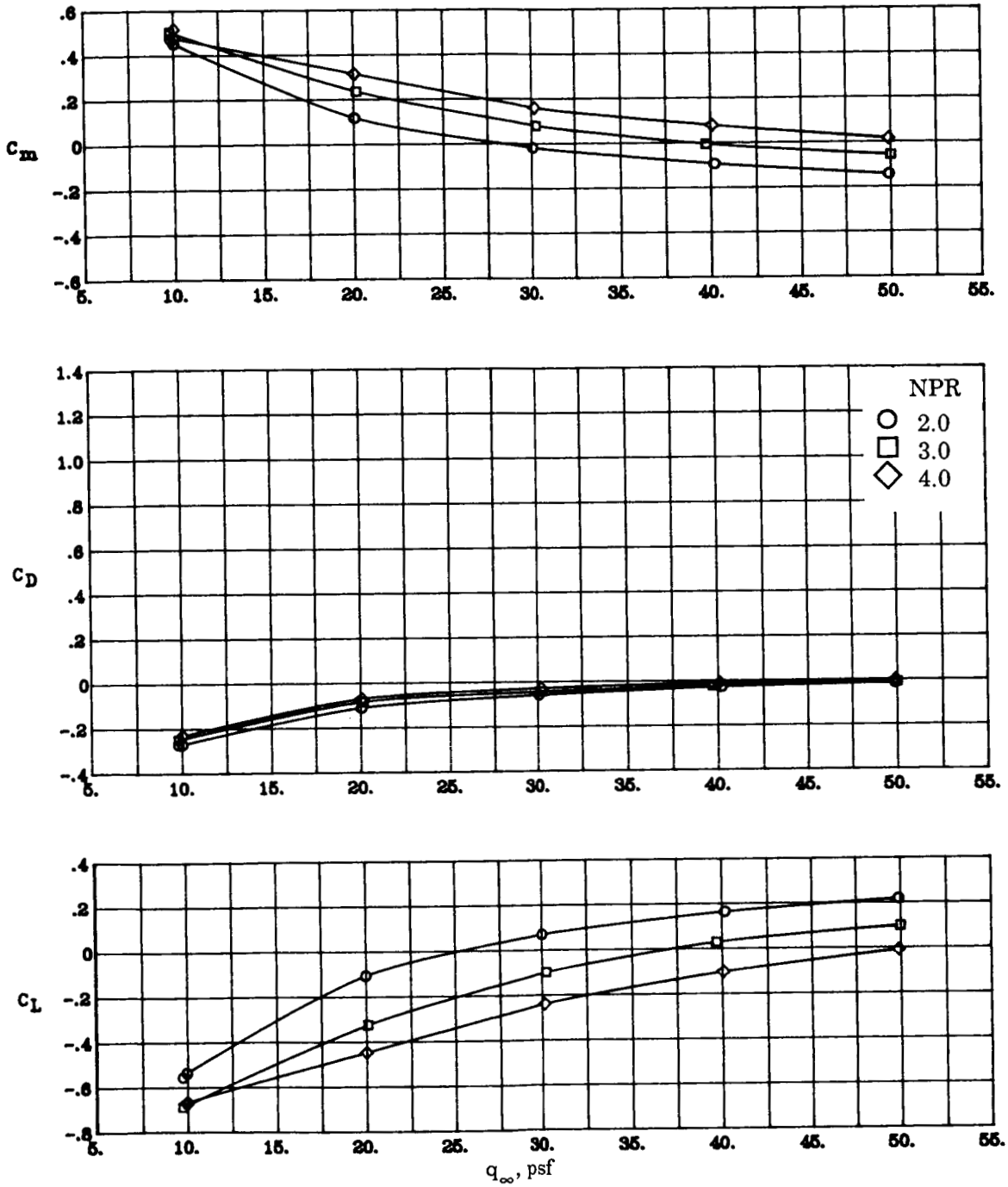


(l) $\Lambda_c = 0°$; $\beta = 0°$; $\delta_f = 26°$.

Figure 6. Continued.

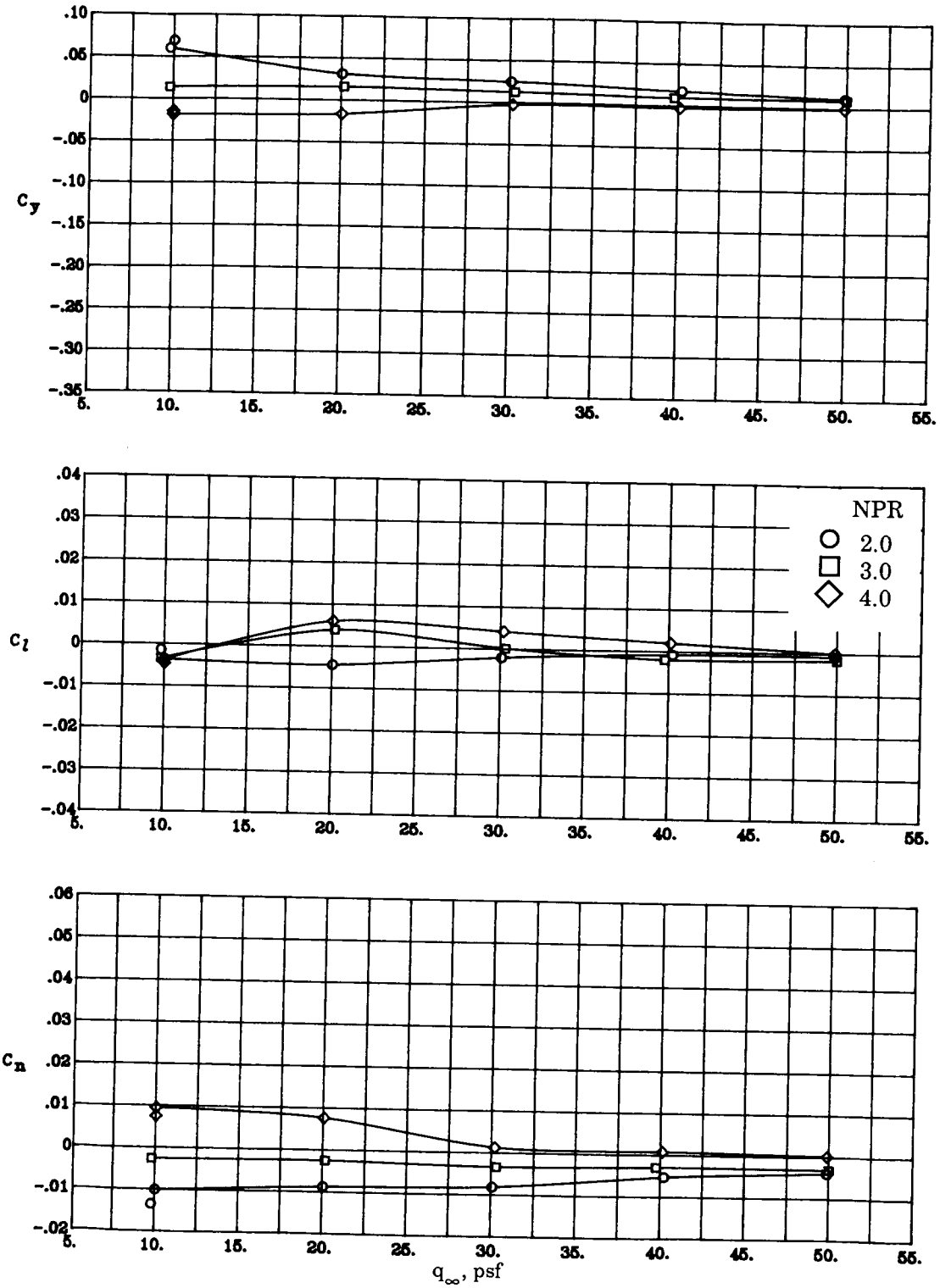


(l) Concluded.

Figure 6. Concluded.

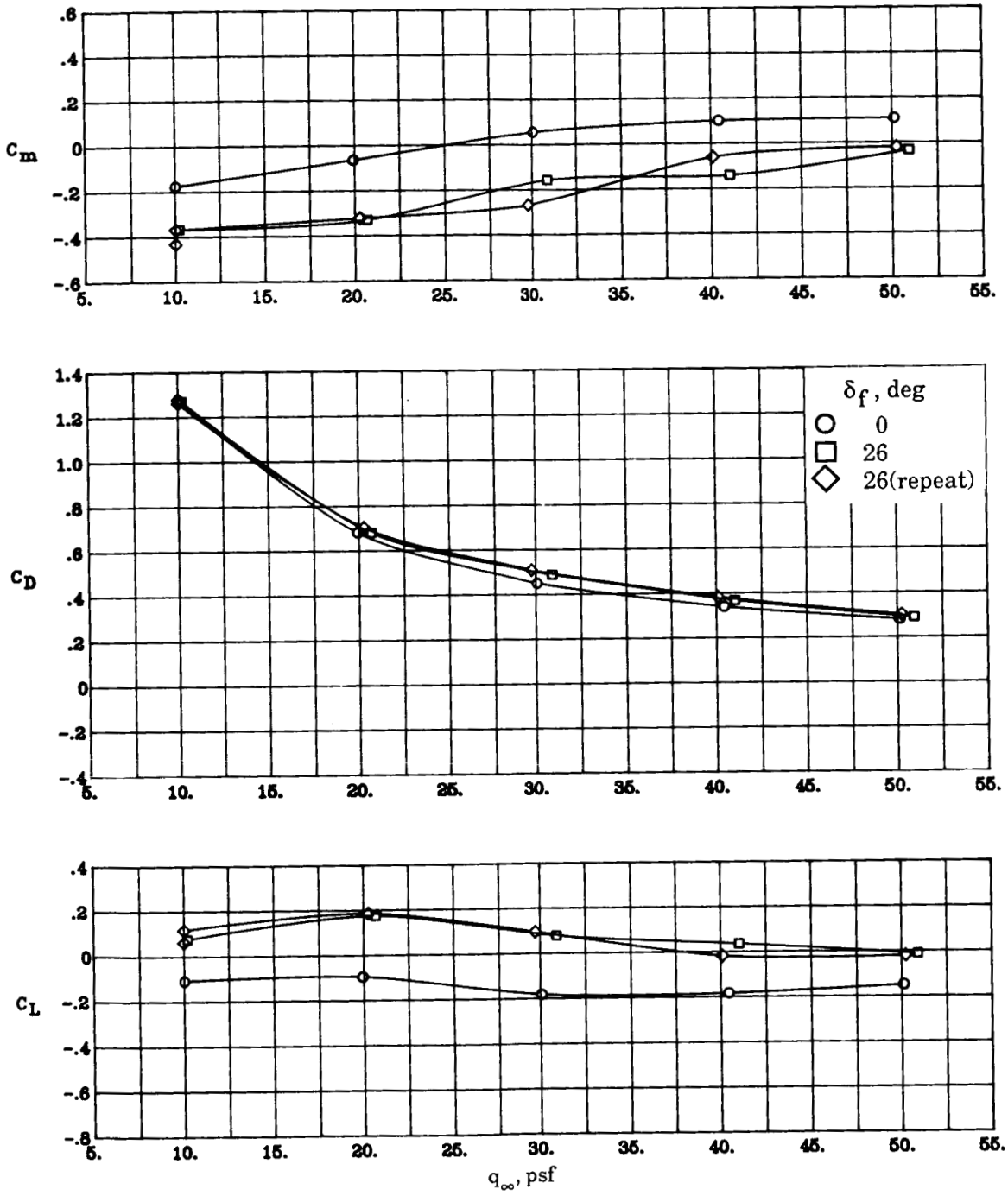


(a) $\Lambda_c = -45°$; NPR = 4.0; $\beta = 0°$.

Figure 7. Effects of flap deflection on aerodynamic characteristics.

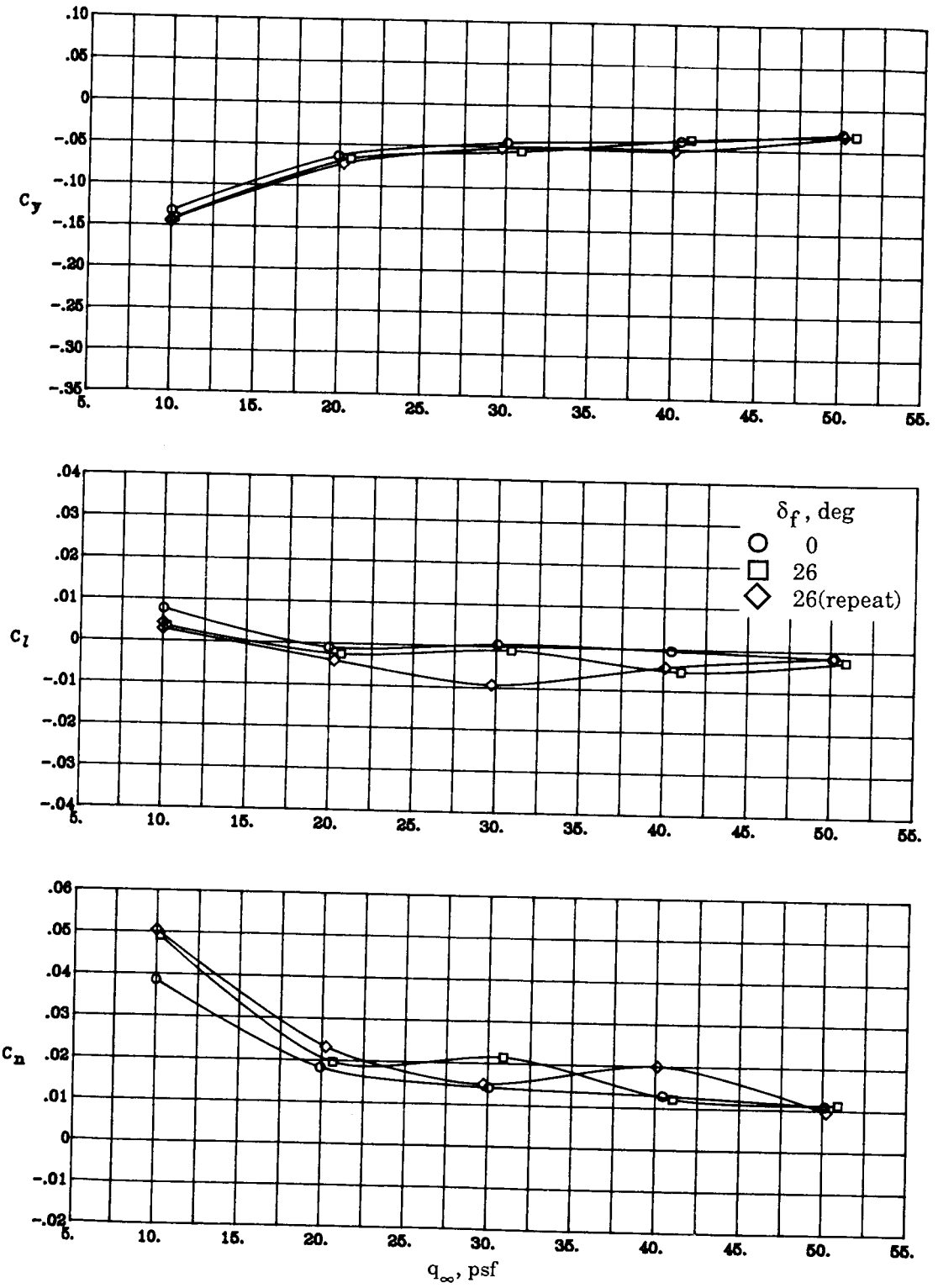


(a) Concluded.

Figure 7. Continued.

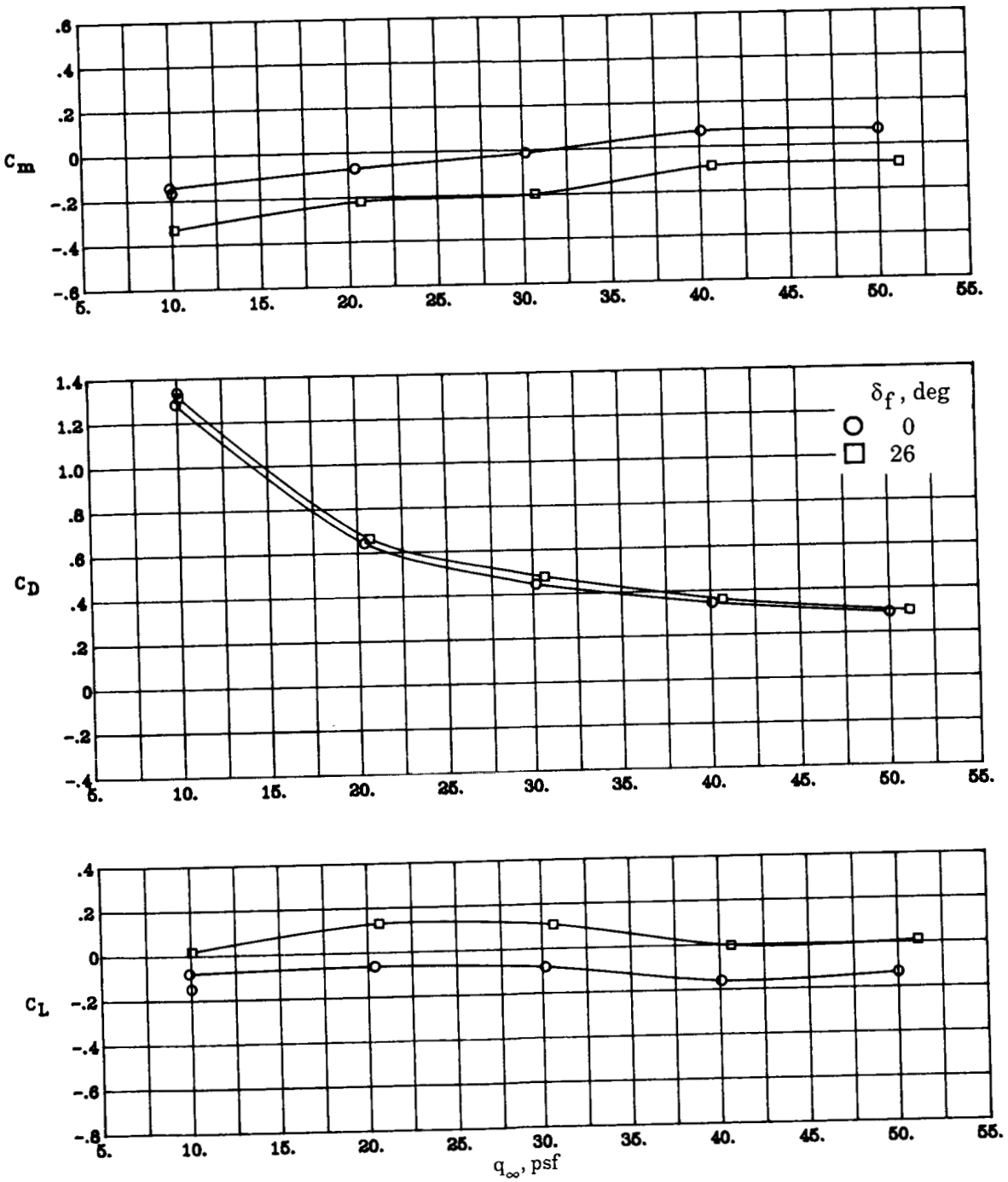


(b) $\Lambda_c = -45°$; NPR = 4.0; $\beta = 10°$.

Figure 7. Continued.

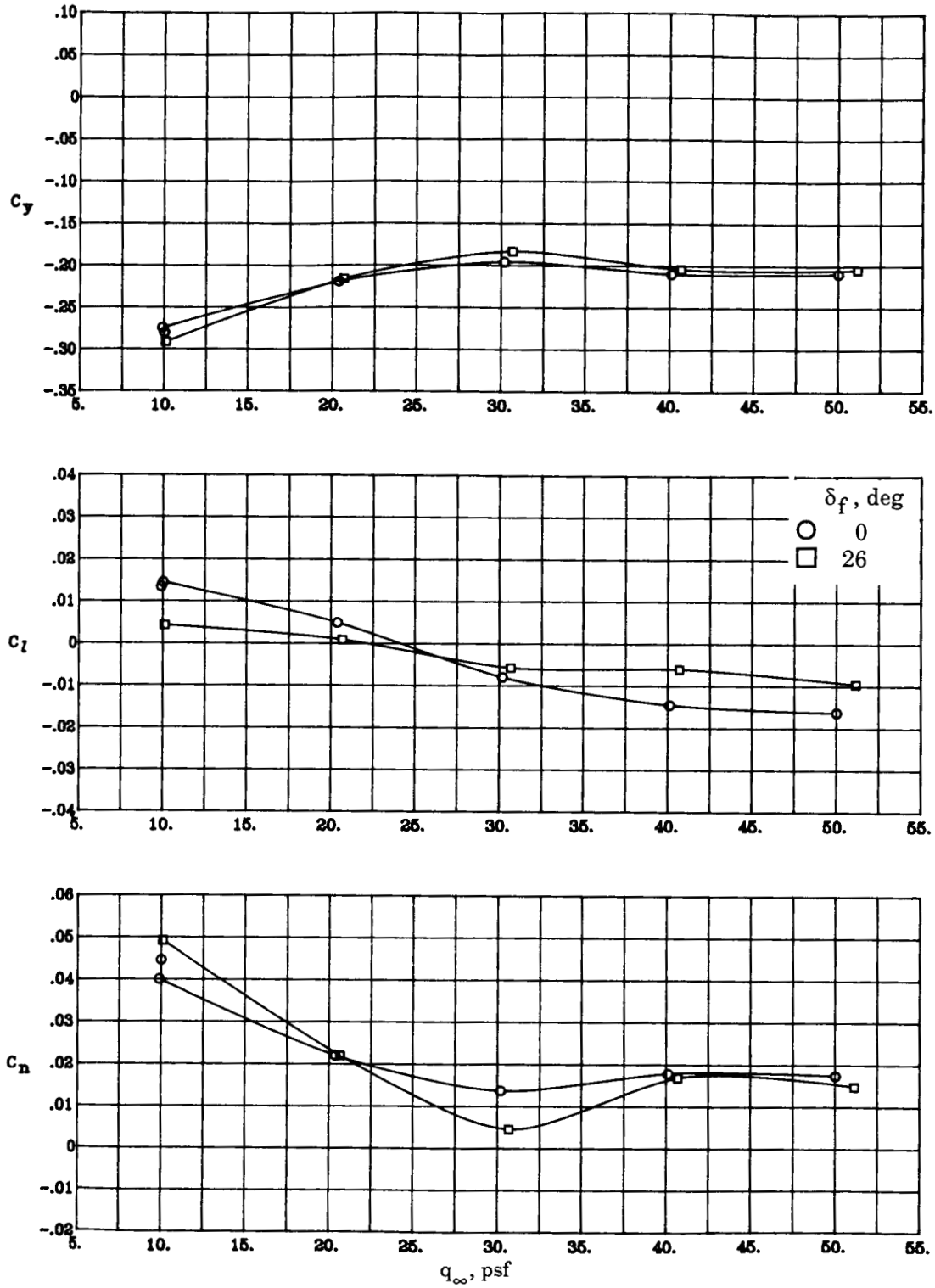


(b) Concluded.

Figure 7. Continued.

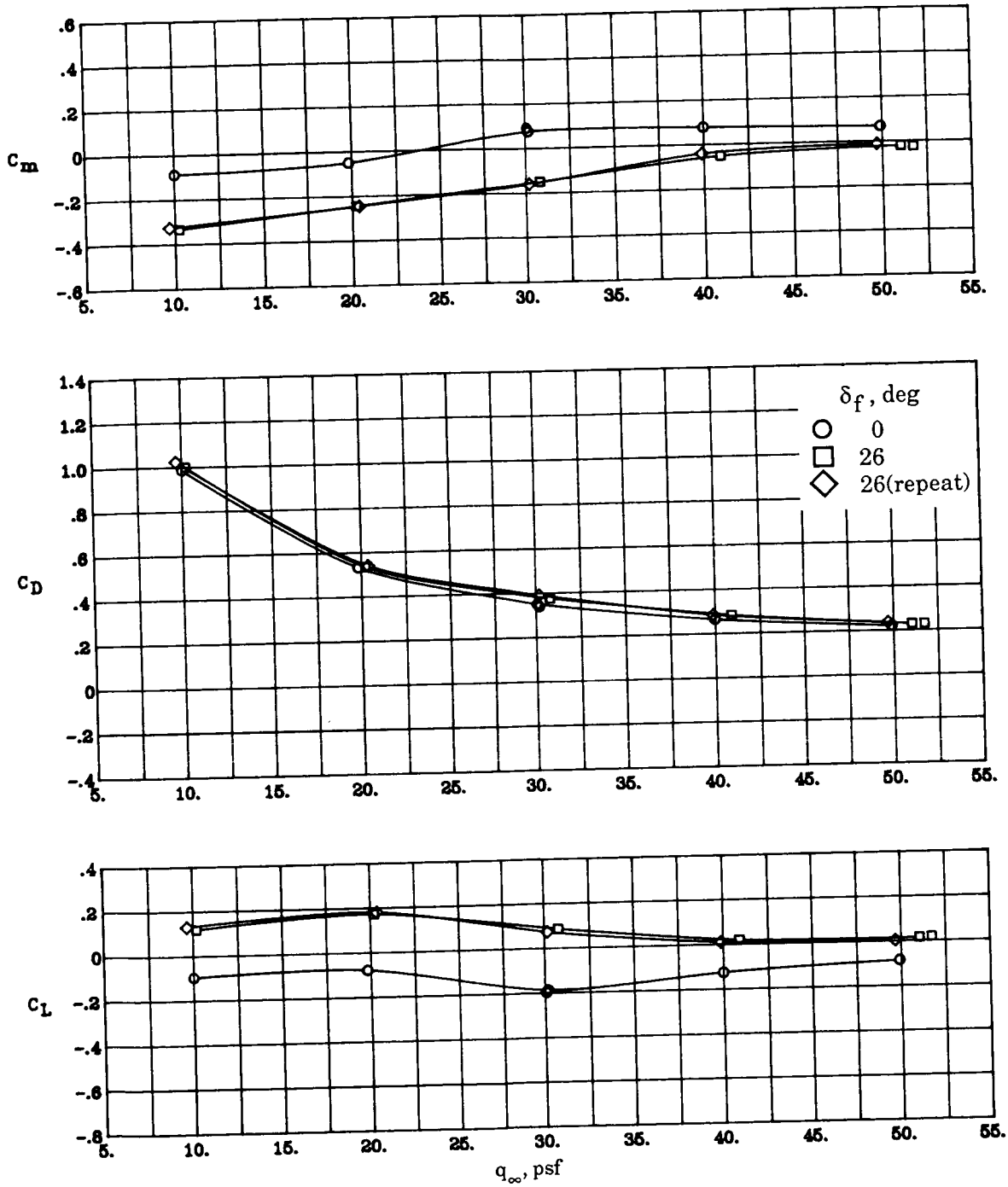


(c) $\Lambda_c = -45°$; NPR = 3.0; $\beta = 0°$.

Figure 7. Continued.

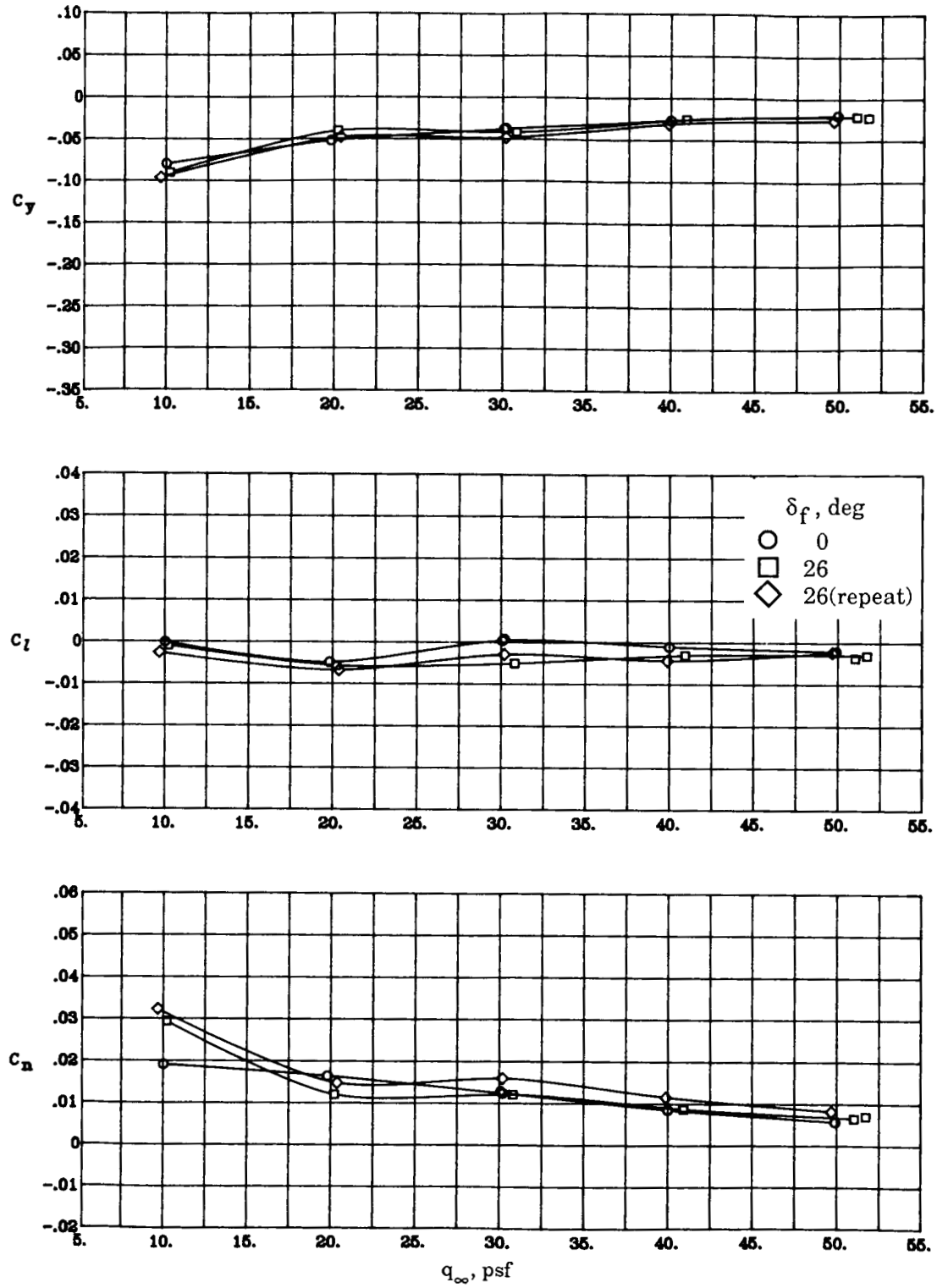


(c) Concluded.

Figure 7. Continued.

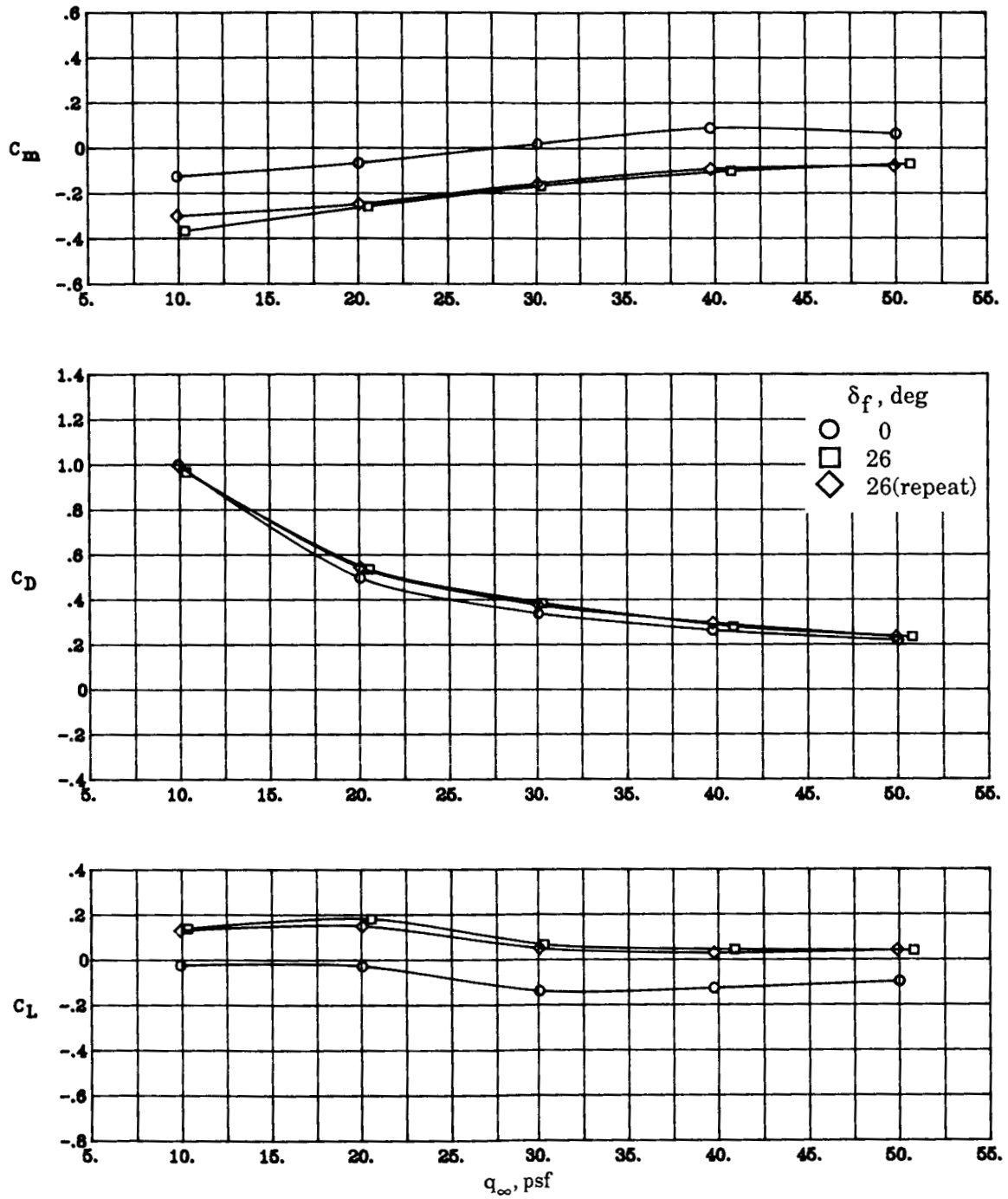


(d) $\Lambda_c = -45°$; NPR = 3.0; $\beta = 10°$.

Figure 7. Continued.

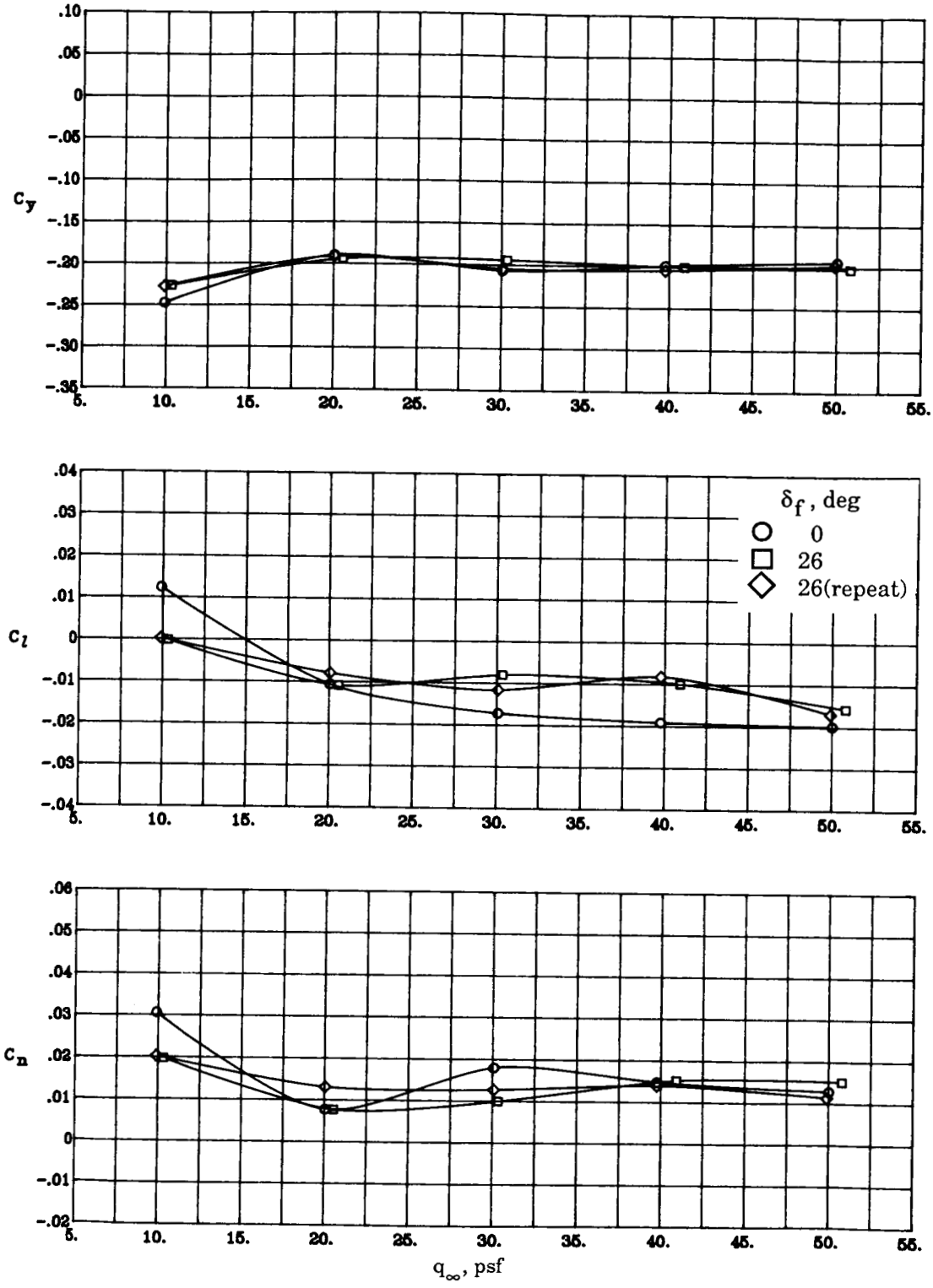


(d) Concluded.

Figure 7. Continued.

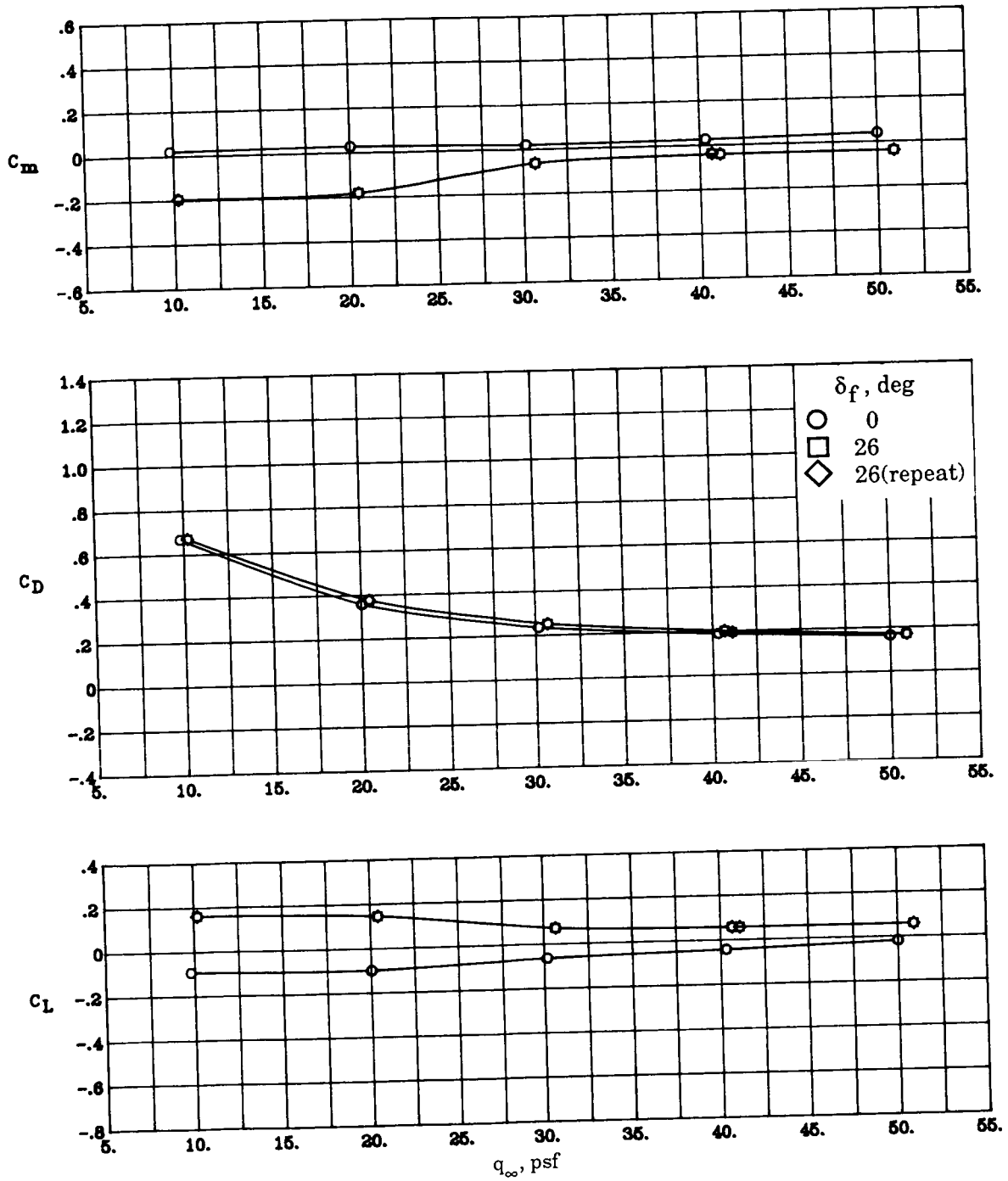


(e) $\Lambda_c = -45°$; NPR = 2.0; $\beta = 0°$.

Figure 7. Continued.

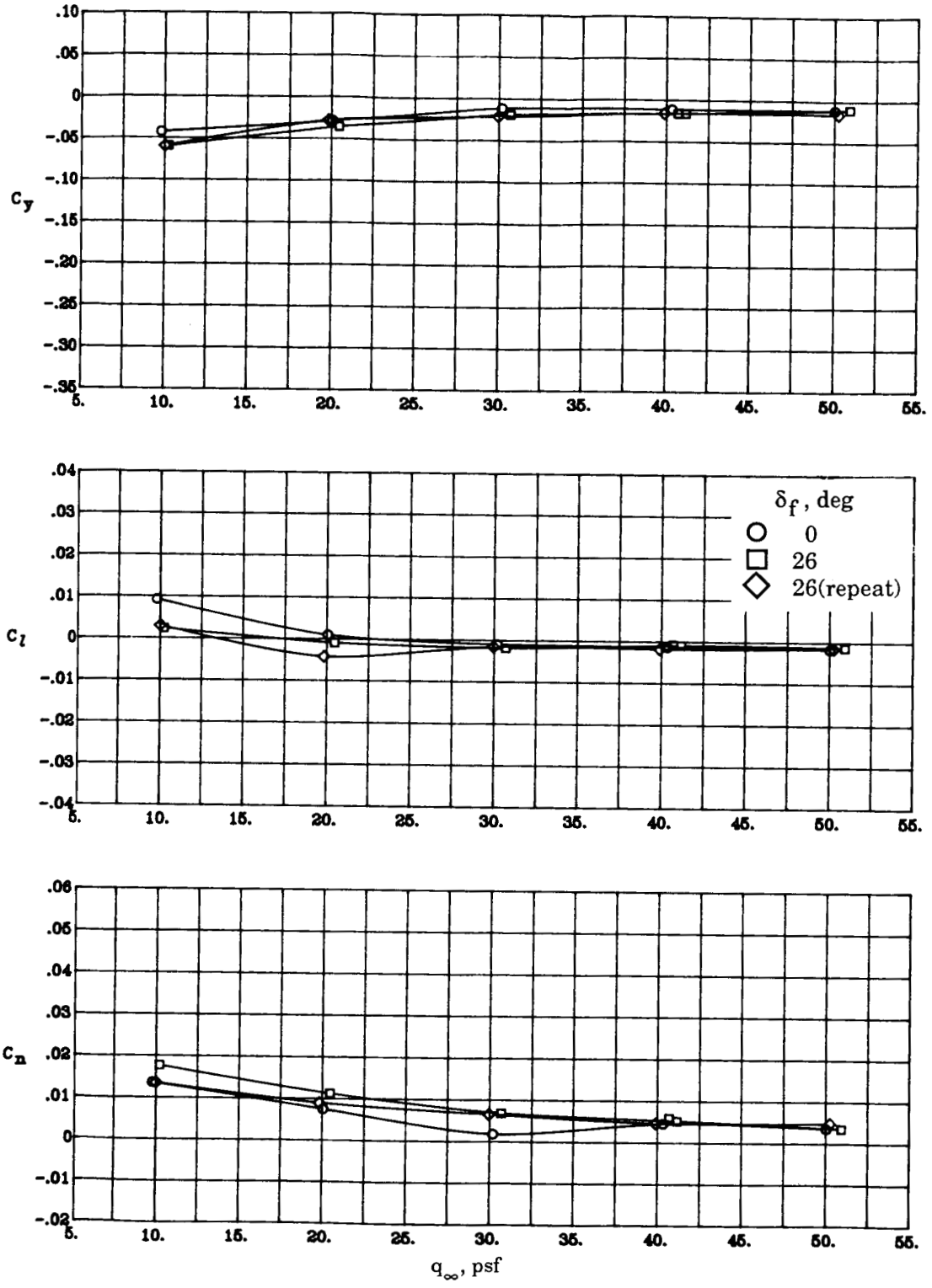


(e) Concluded.

Figure 7. Continued.

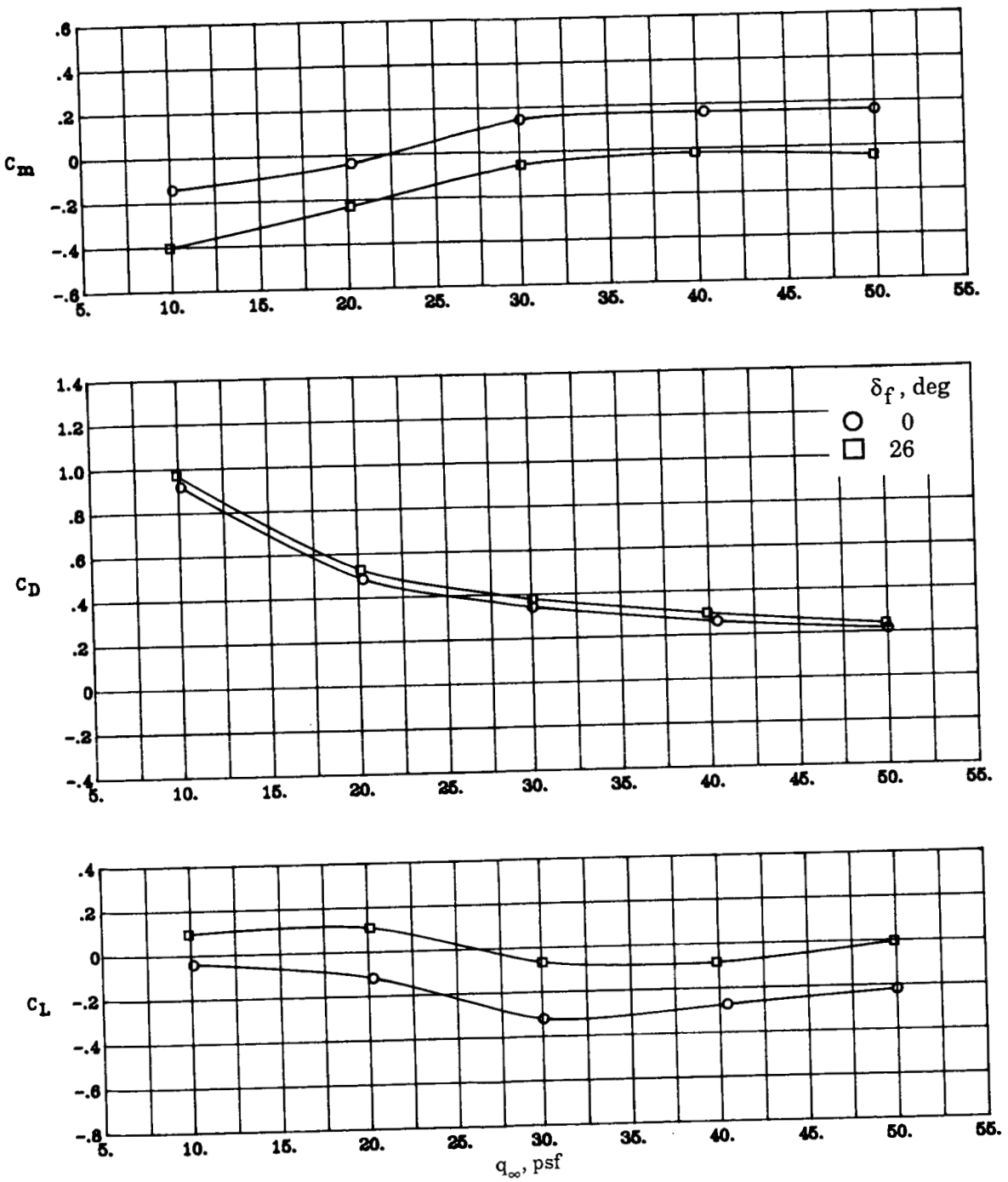


(f) $\Lambda_c = -30°$; NPR = 4.0; $\beta = 0°$.

Figure 7. Continued.

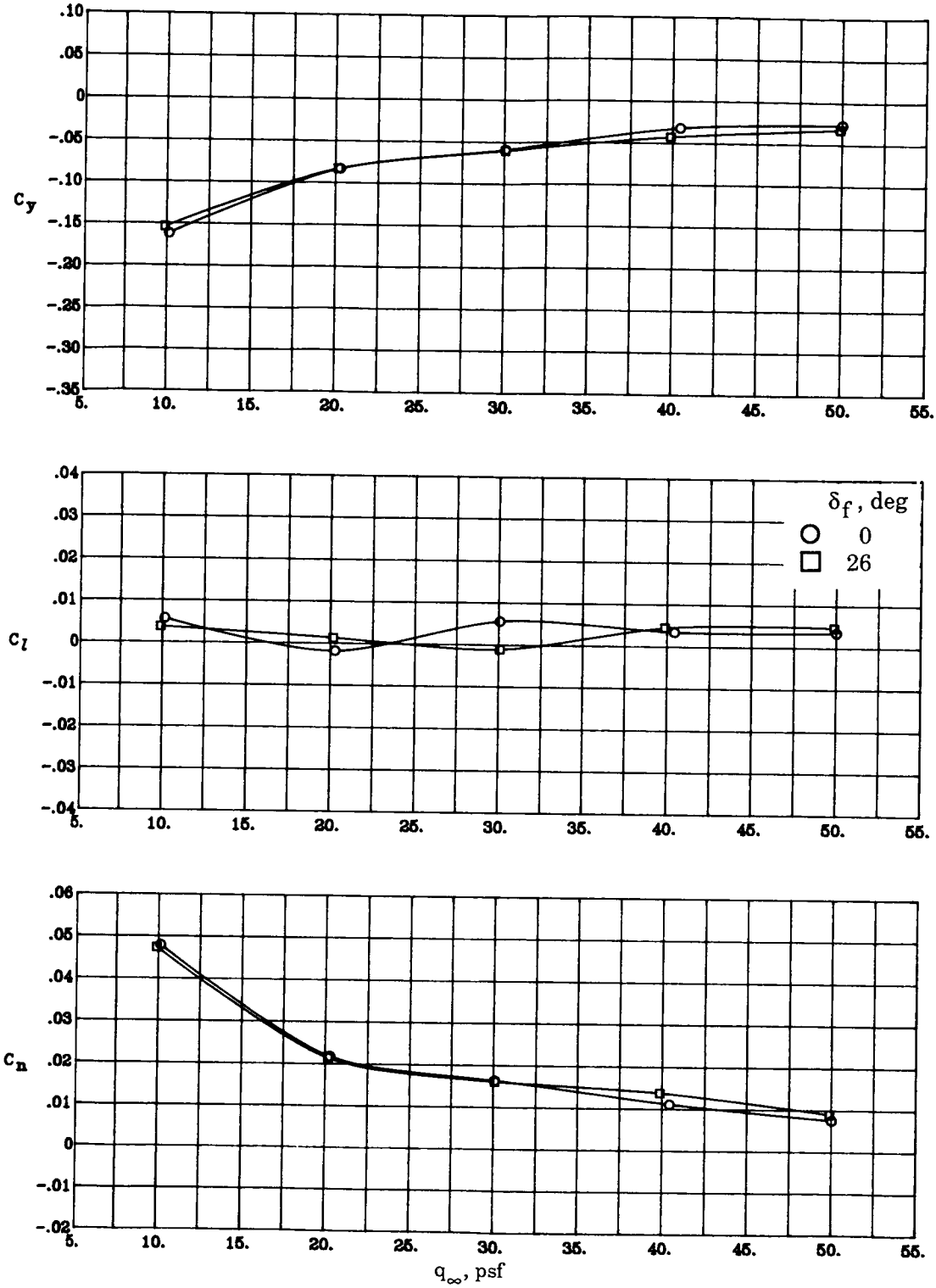


(f) Concluded.

Figure 7. Continued.

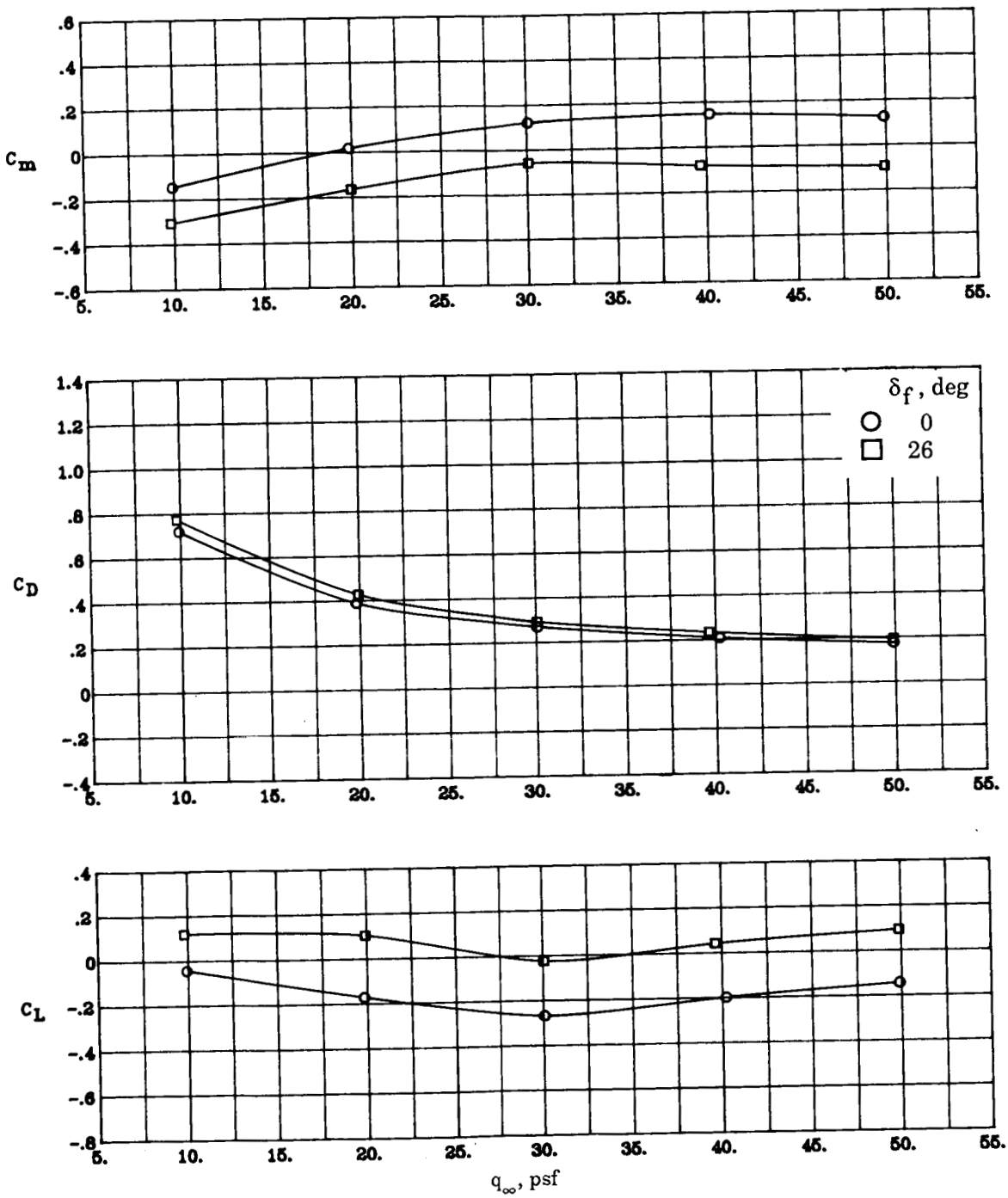


(g) $\Lambda_c = -30°$; NPR = 3.0; $\beta = 0°$.

Figure 7. Continued.

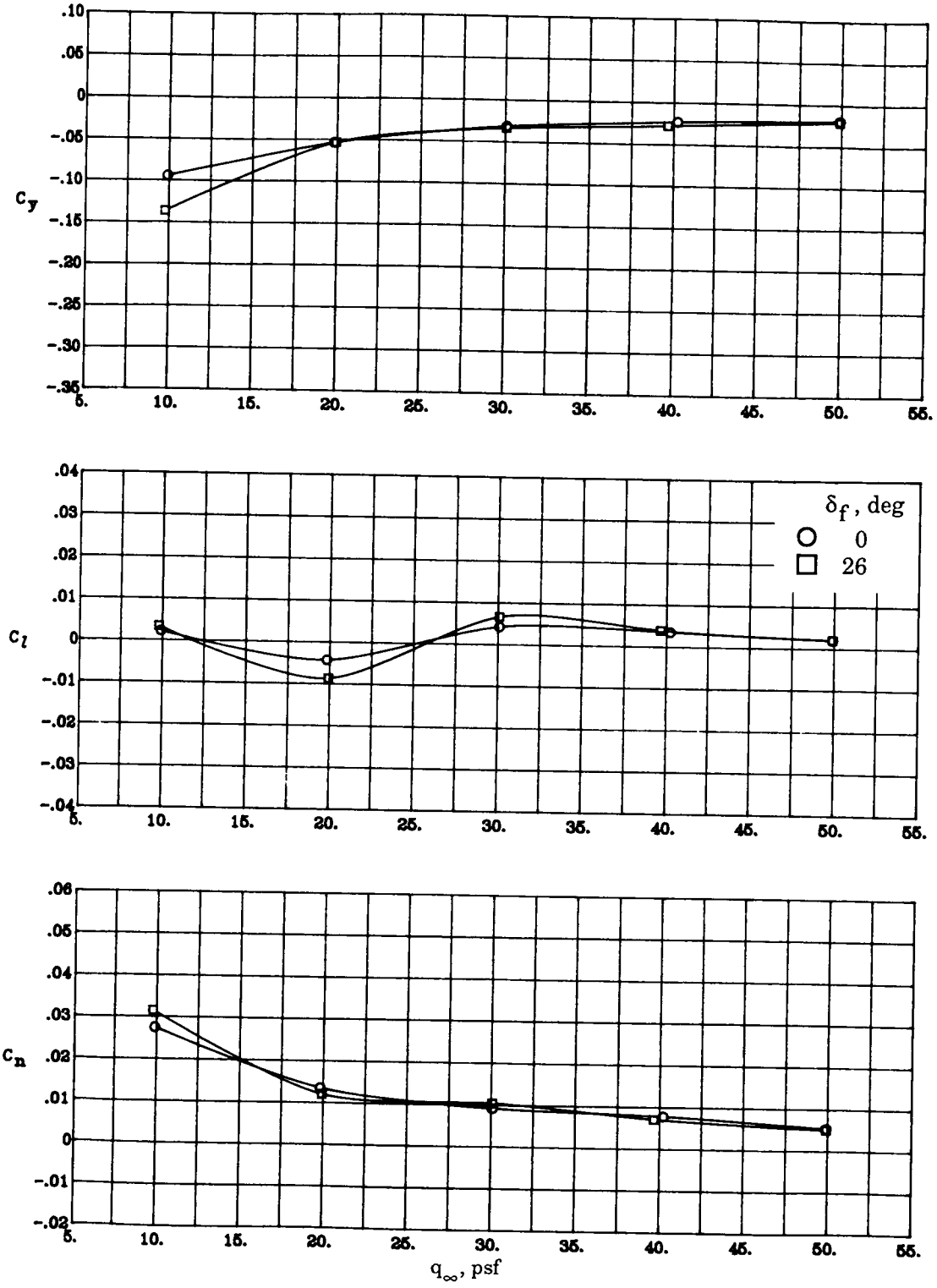


(g) Concluded.

Figure 7. Continued.

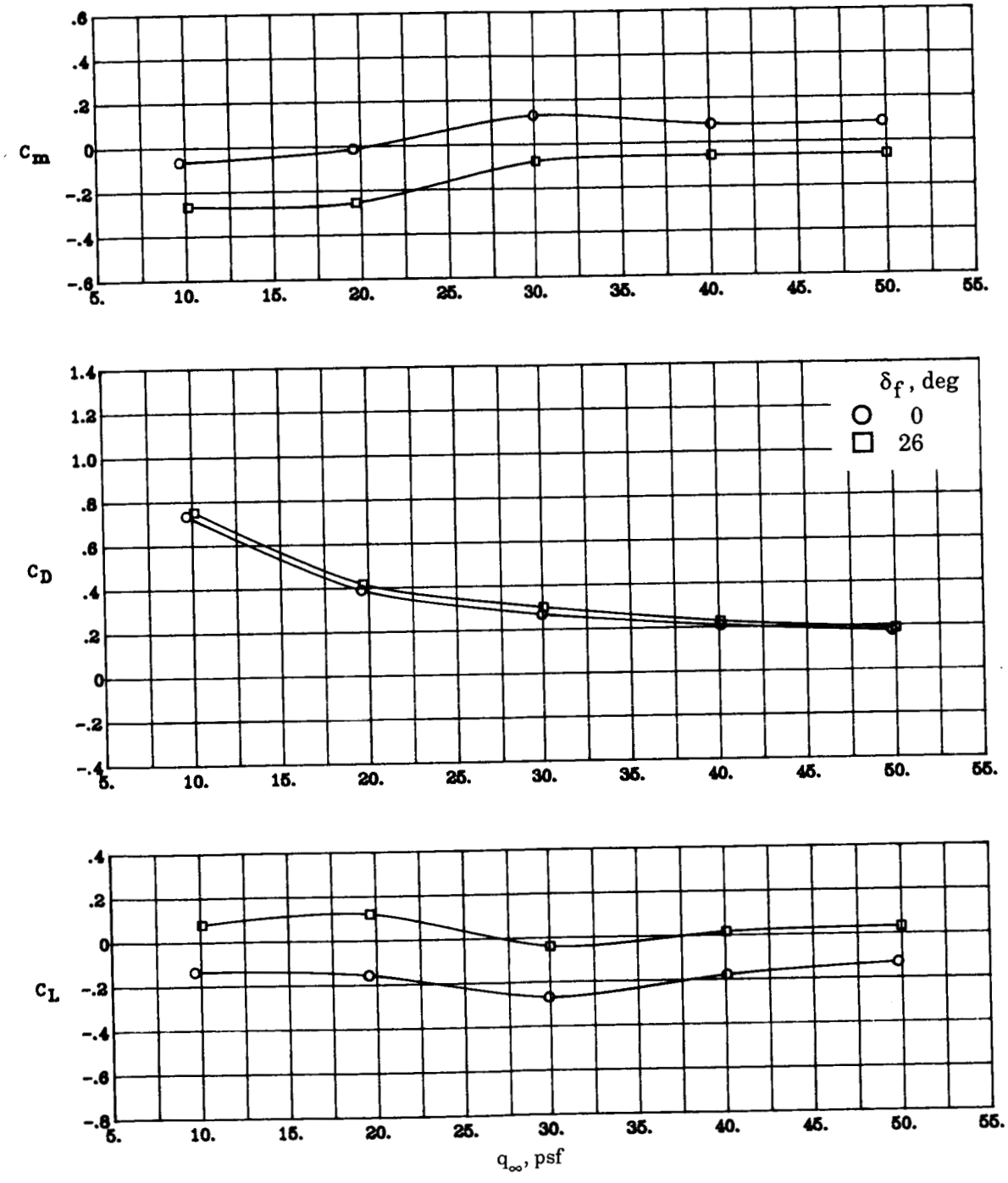


(h) $\Lambda_c = -30°$; NPR = 3.0; $\beta = 10°$.

Figure 7. Continued.

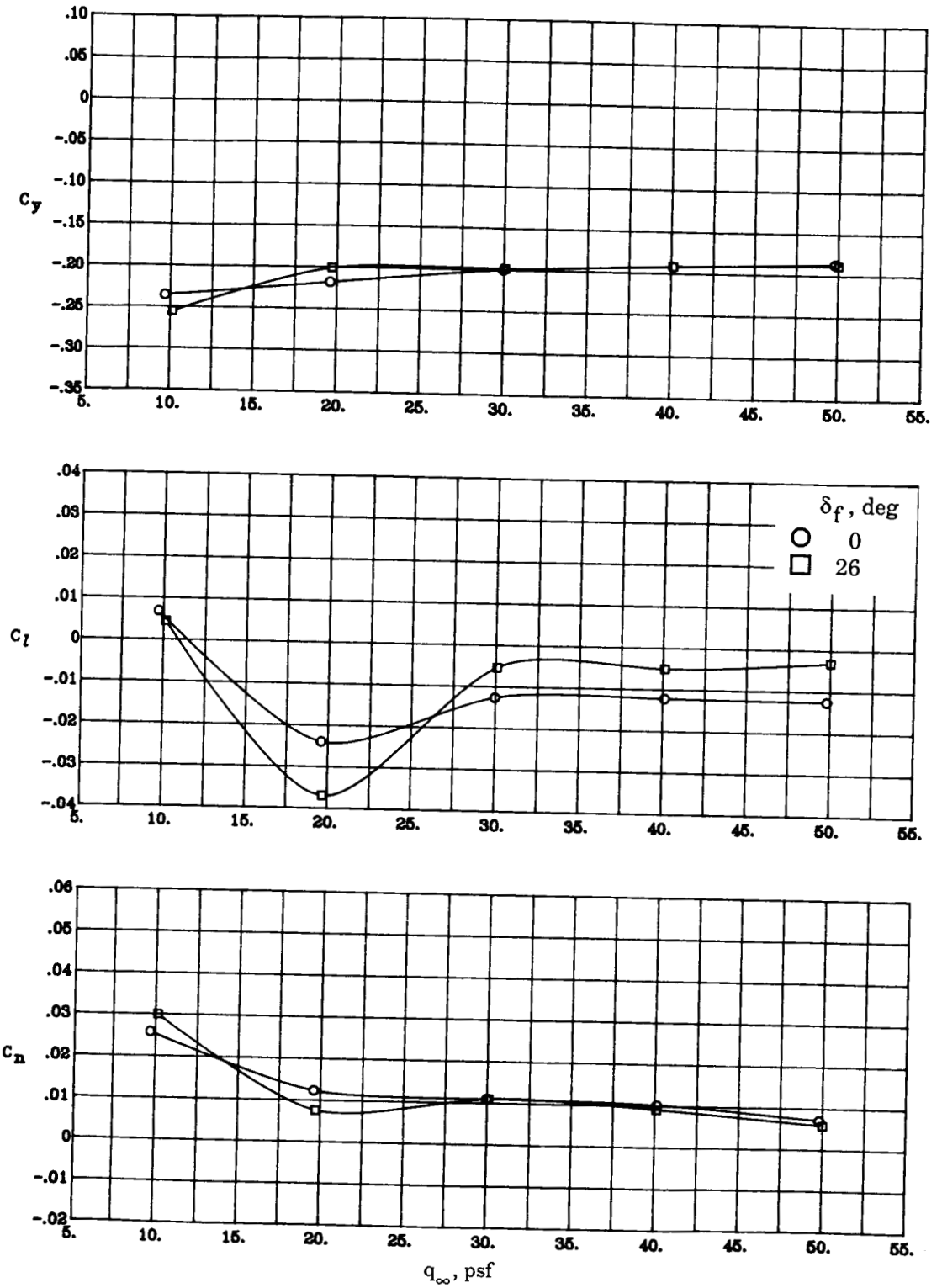


(h) Concluded.

Figure 7. Continued.

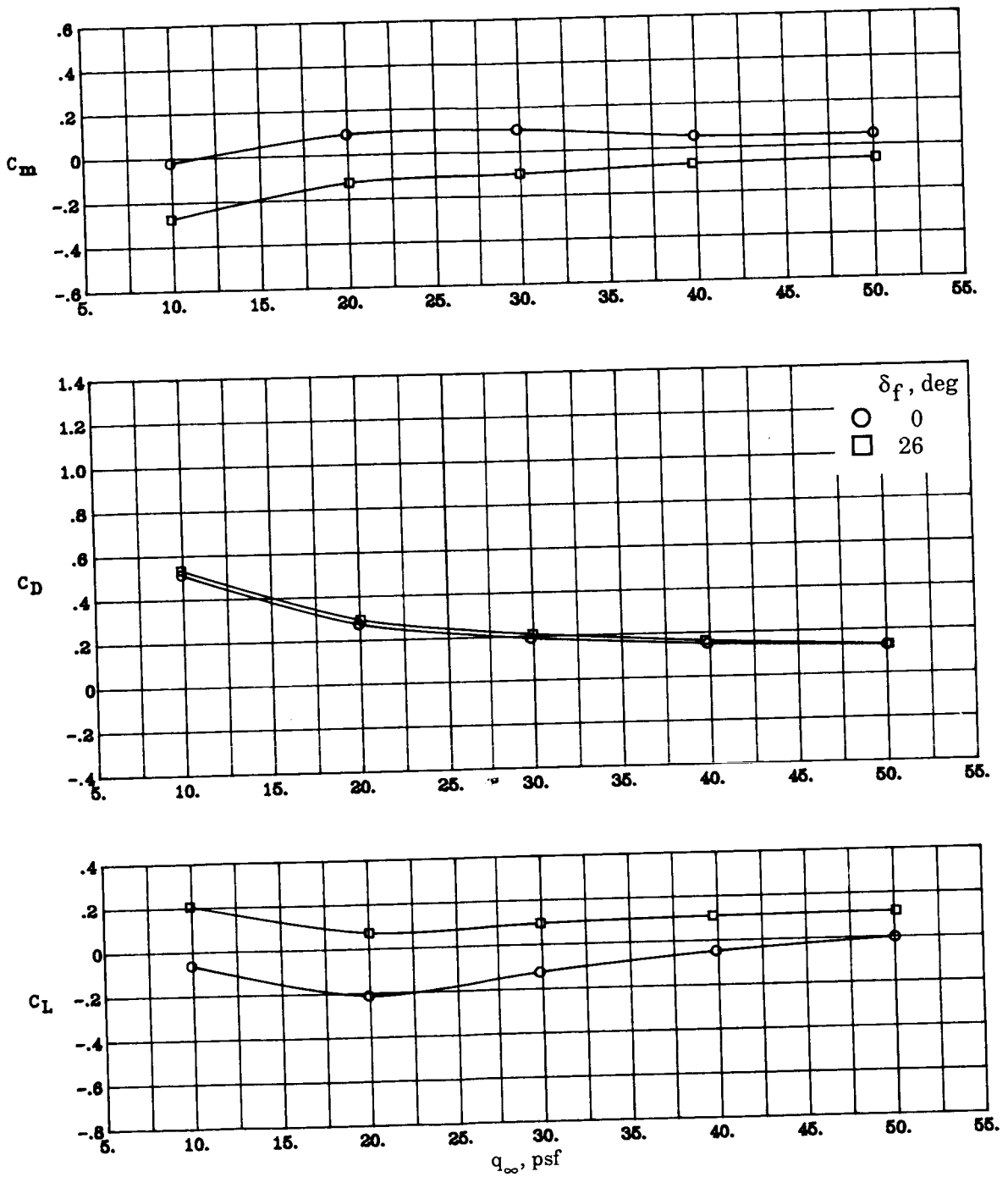


(i) $\Lambda_c = -30°$; NPR = 2.0; $\beta = 0°$.

Figure 7. Continued.

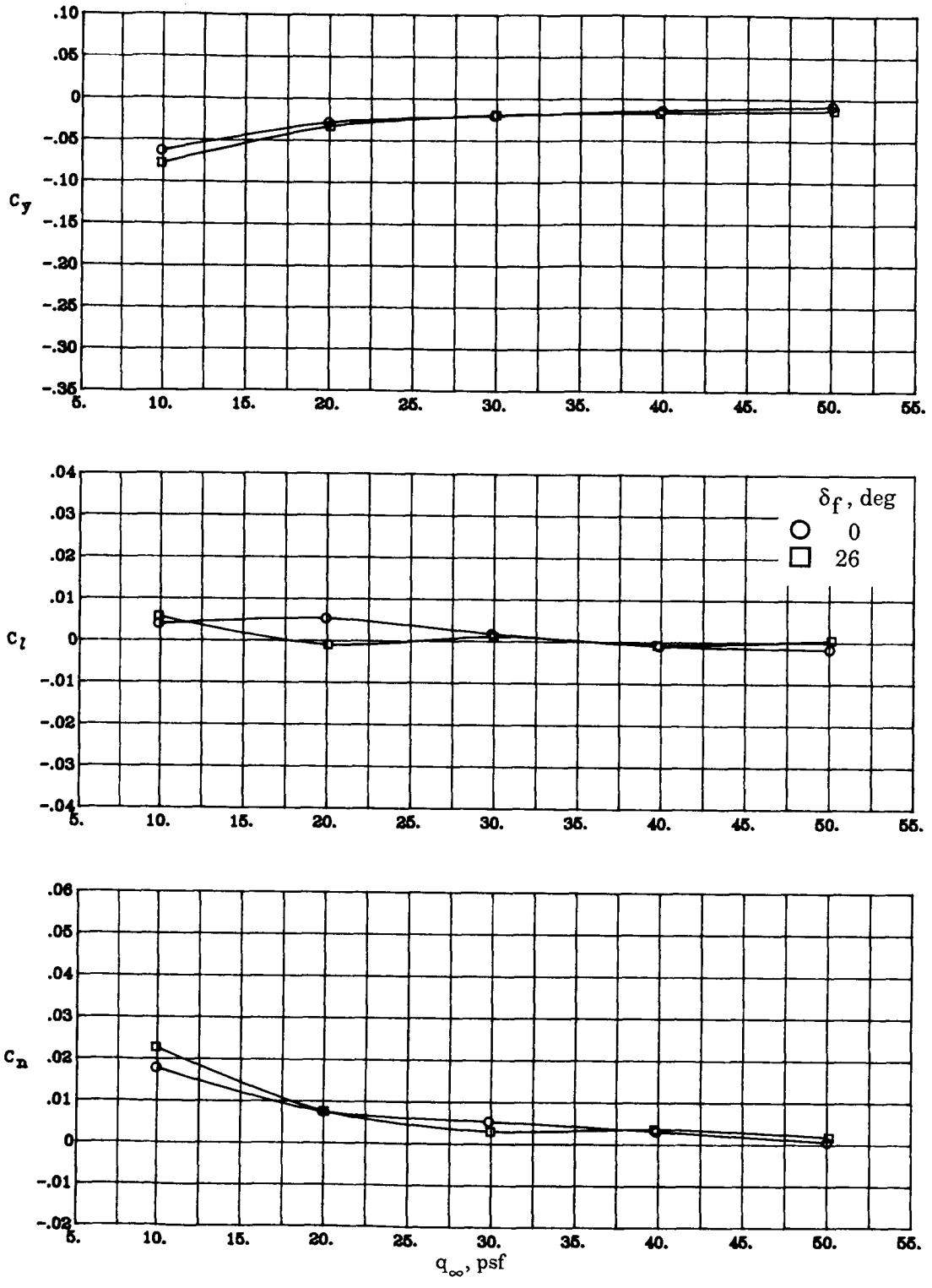


(i) Concluded.

Figure 7. Continued.

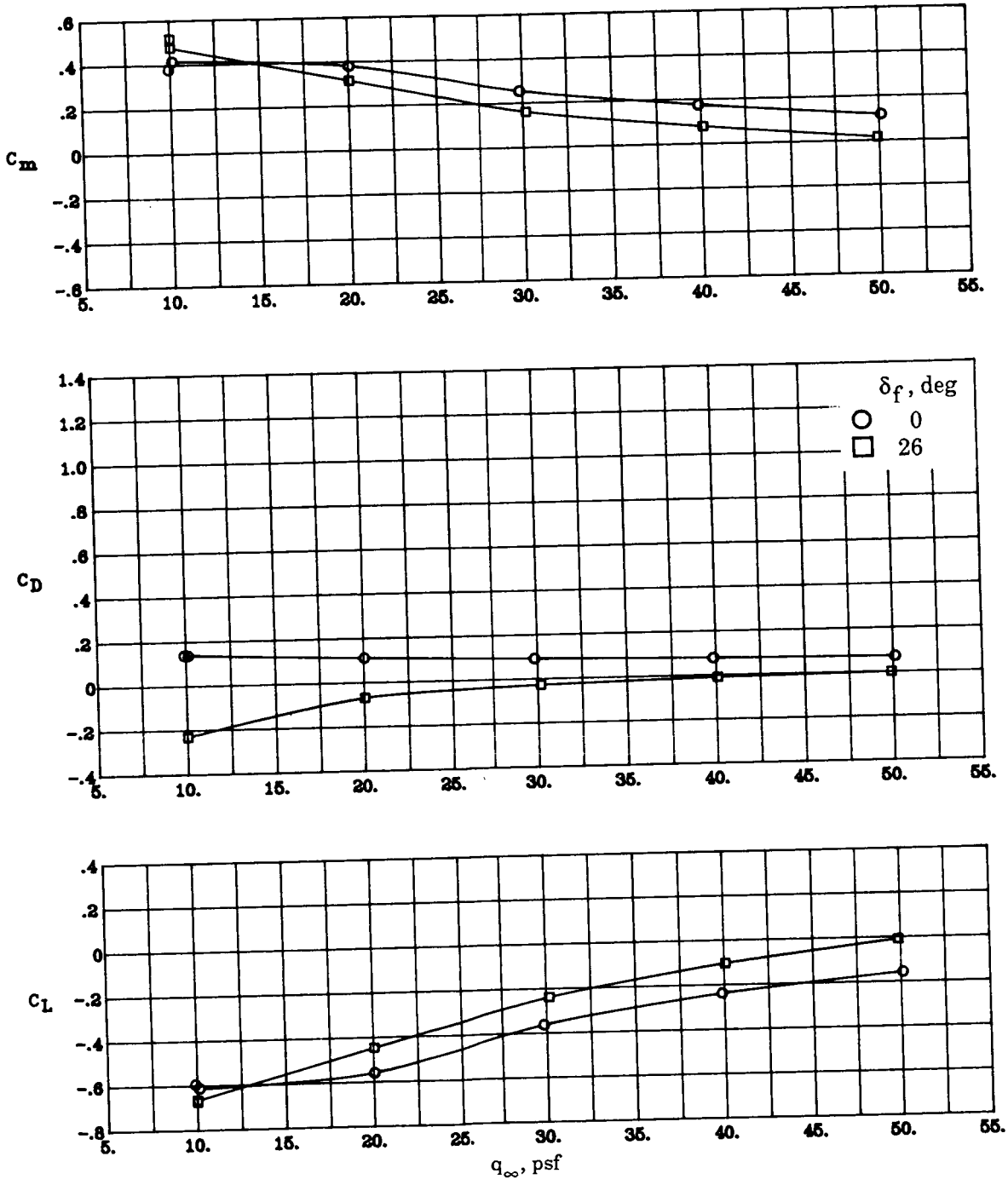


(j) $\Lambda_c = 0°$; NPR = 4.0; $\beta = 0°$.

Figure 7. Continued.

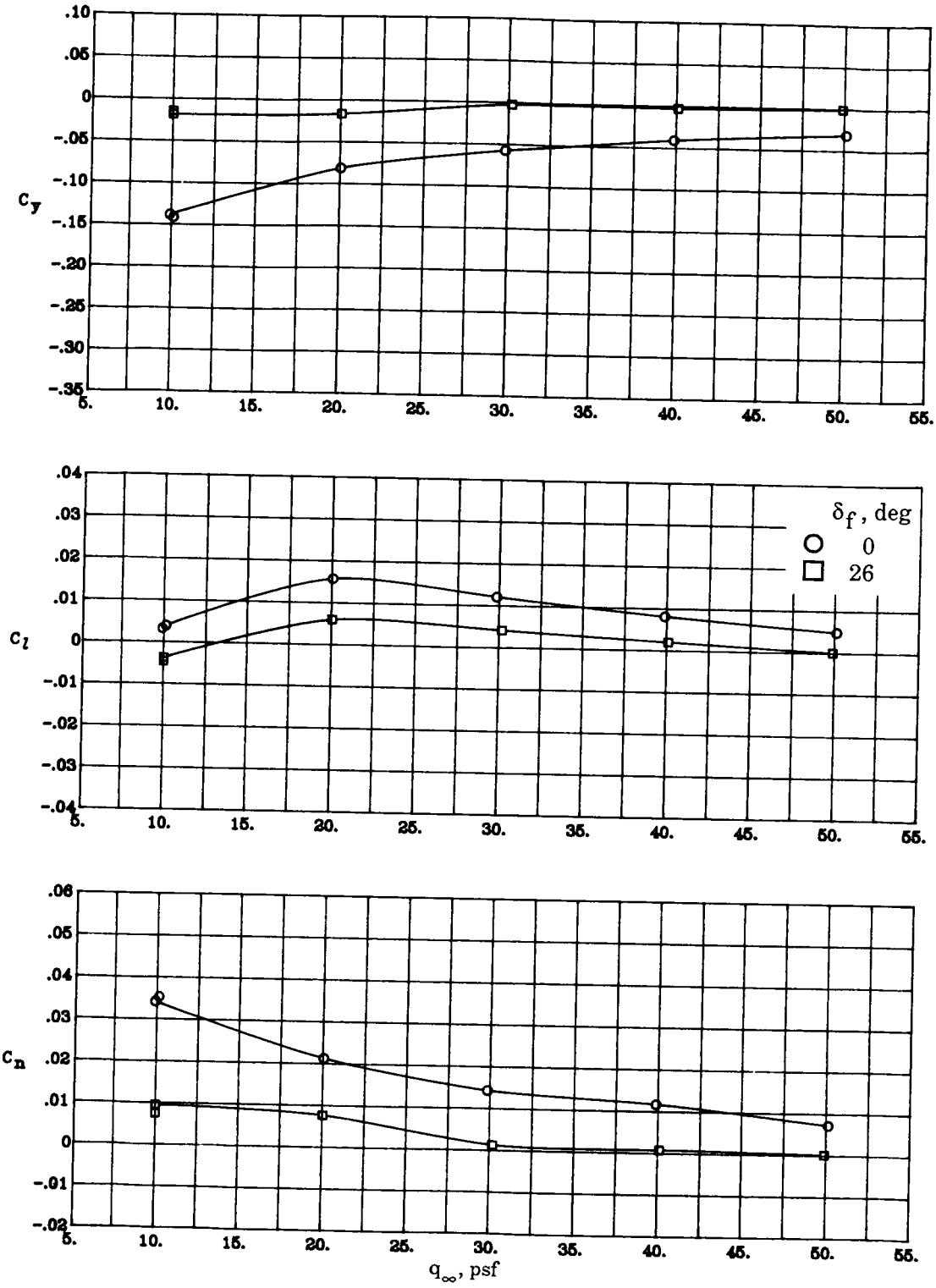


(j) Concluded.

Figure 7. Continued.

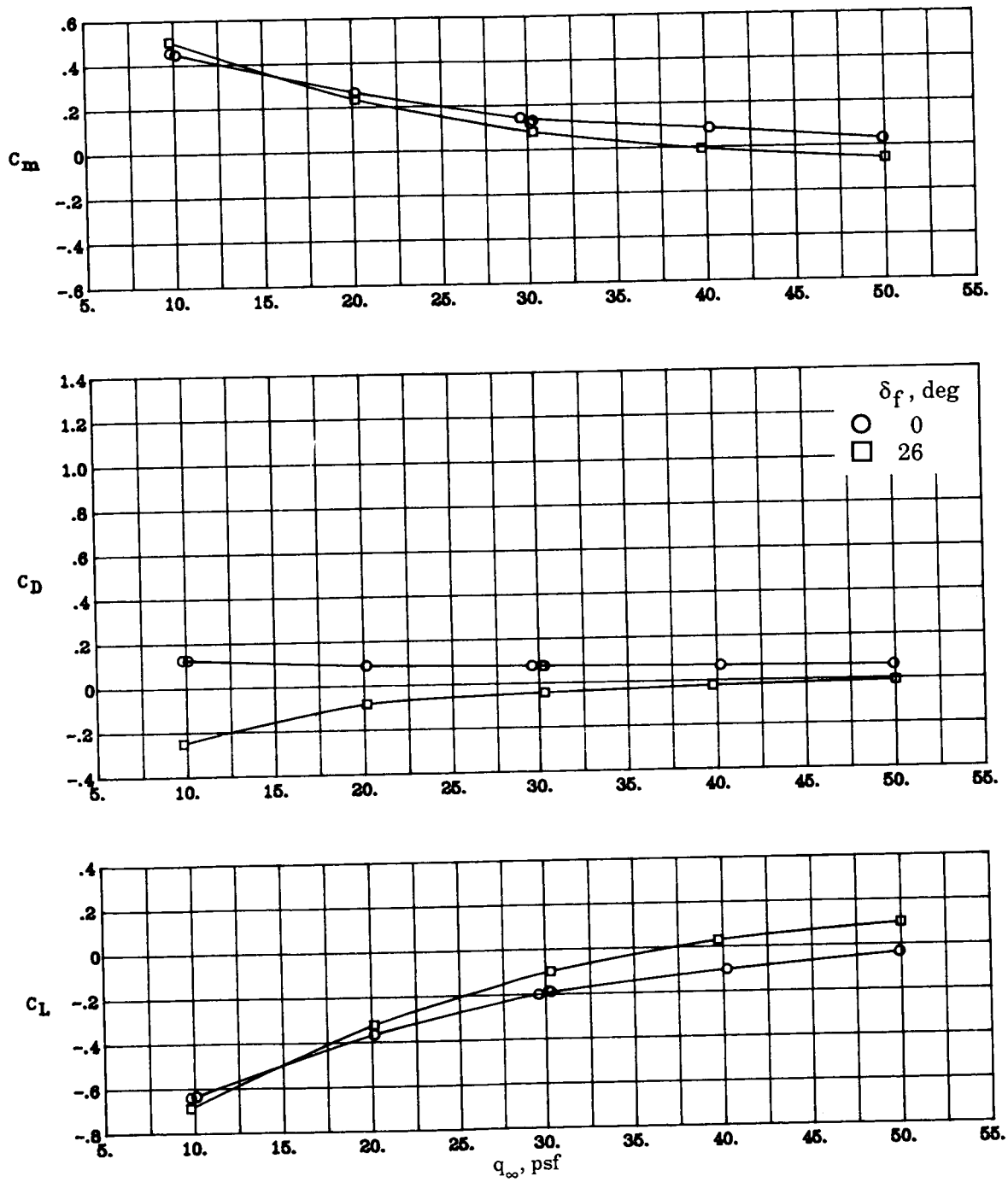


(k) $\Lambda_c = 0°$; NPR = 3.0; $\beta = 0°$.

Figure 7. Continued.

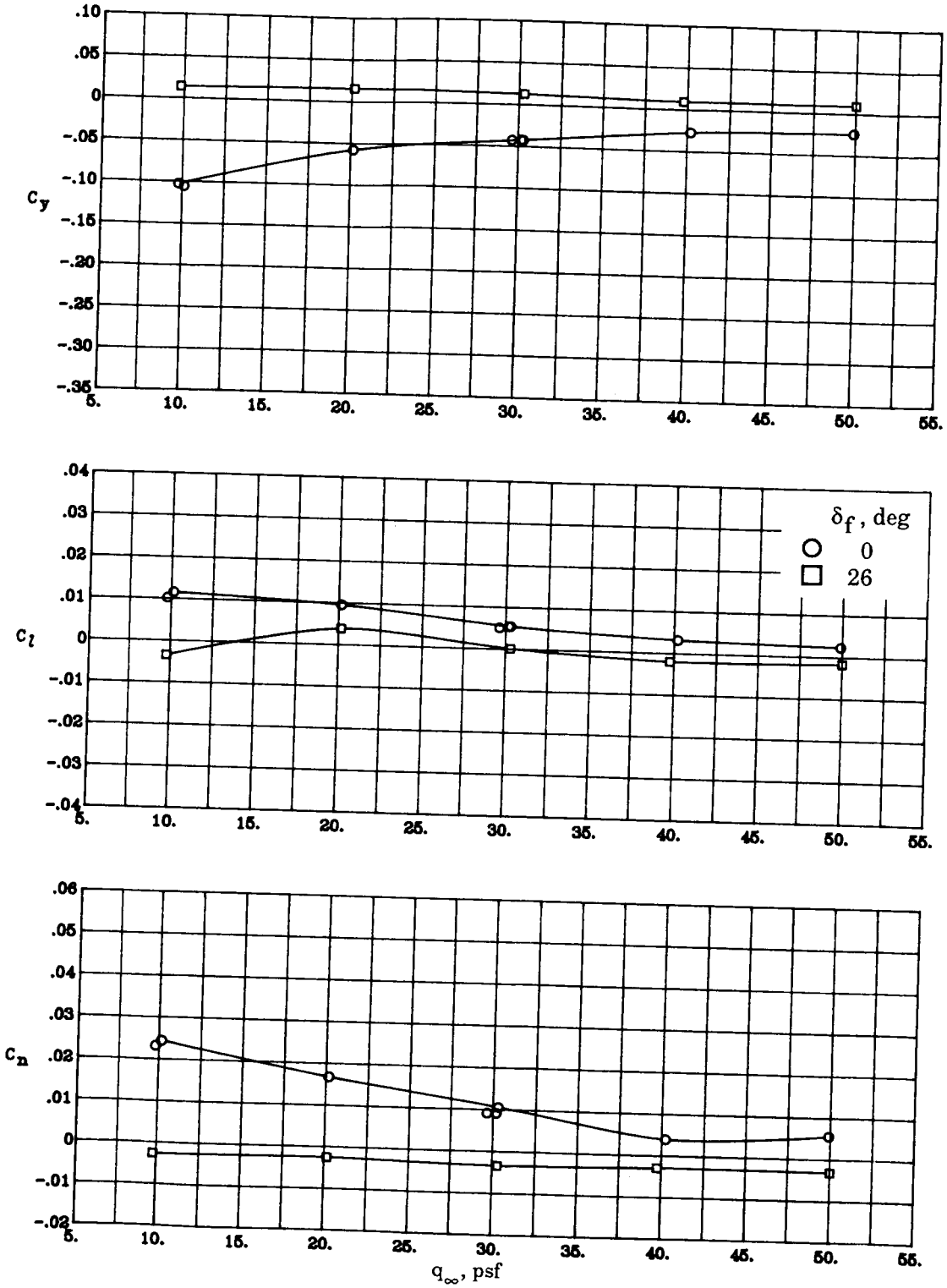


(k) Concluded.

Figure 7. Continued.

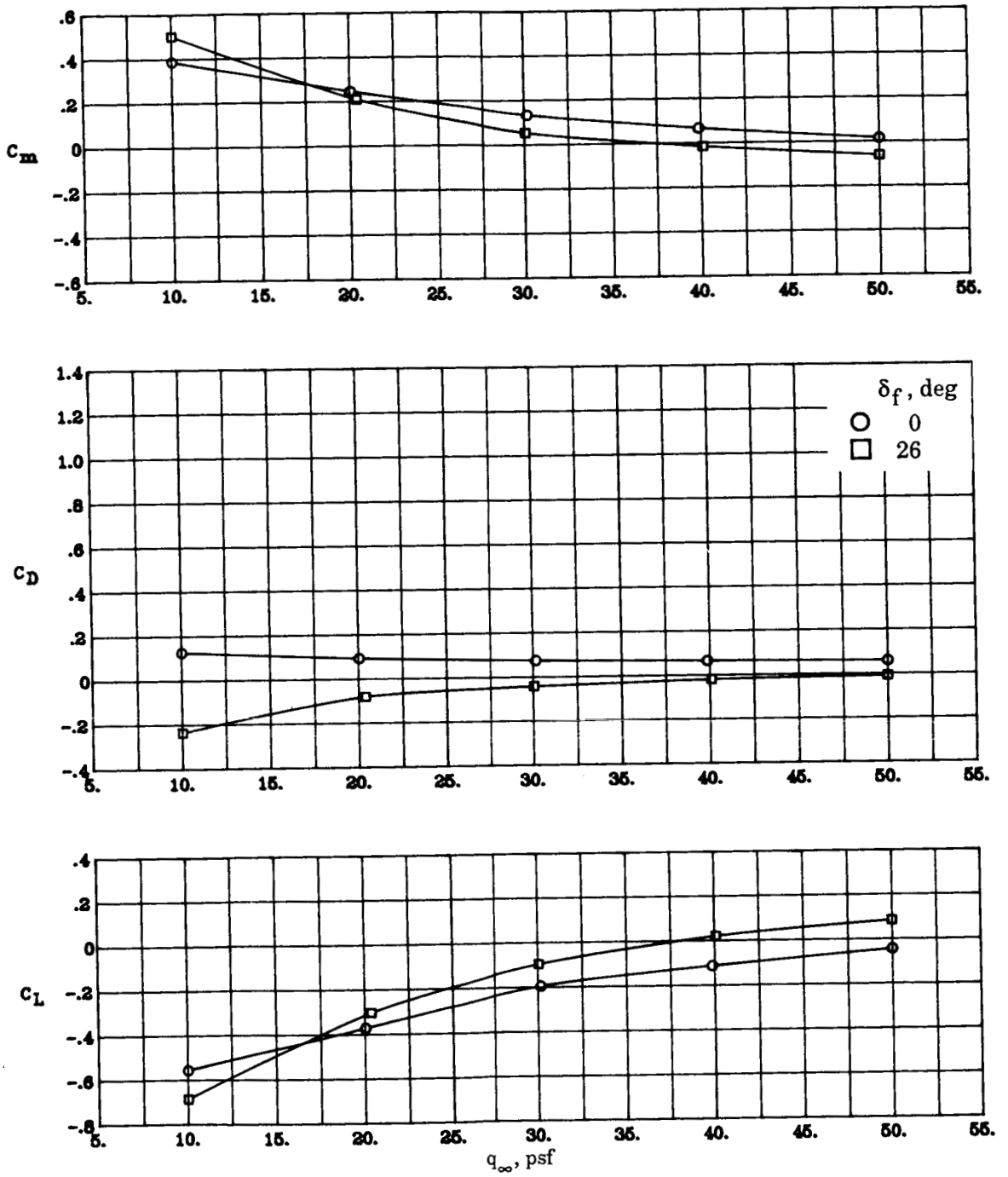


(l) $\Lambda_c = 0°$; NPR = 3.0; $\beta = 10°$.

Figure 7. Continued.

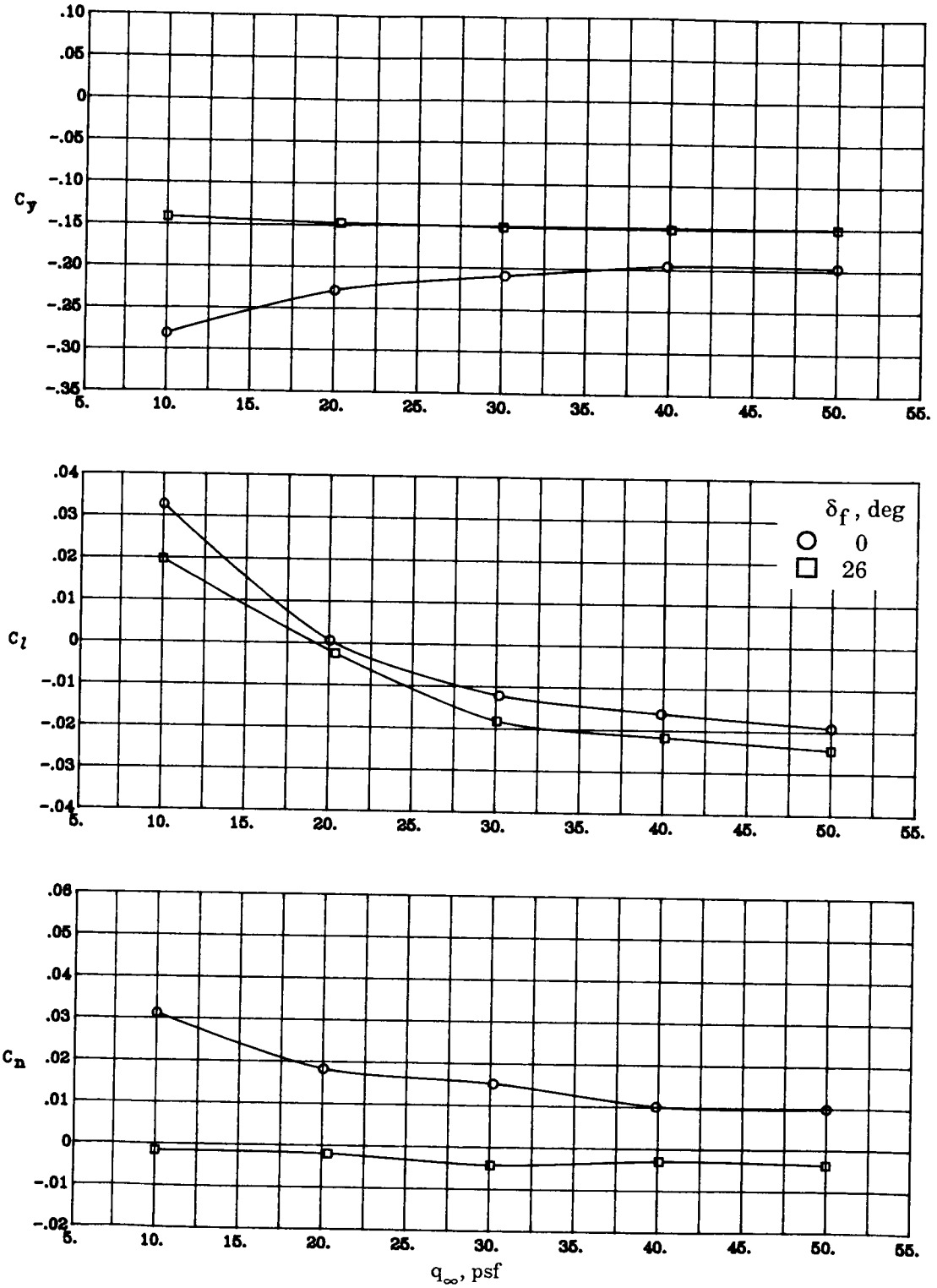


(l) Concluded.

Figure 7. Continued.



C-2

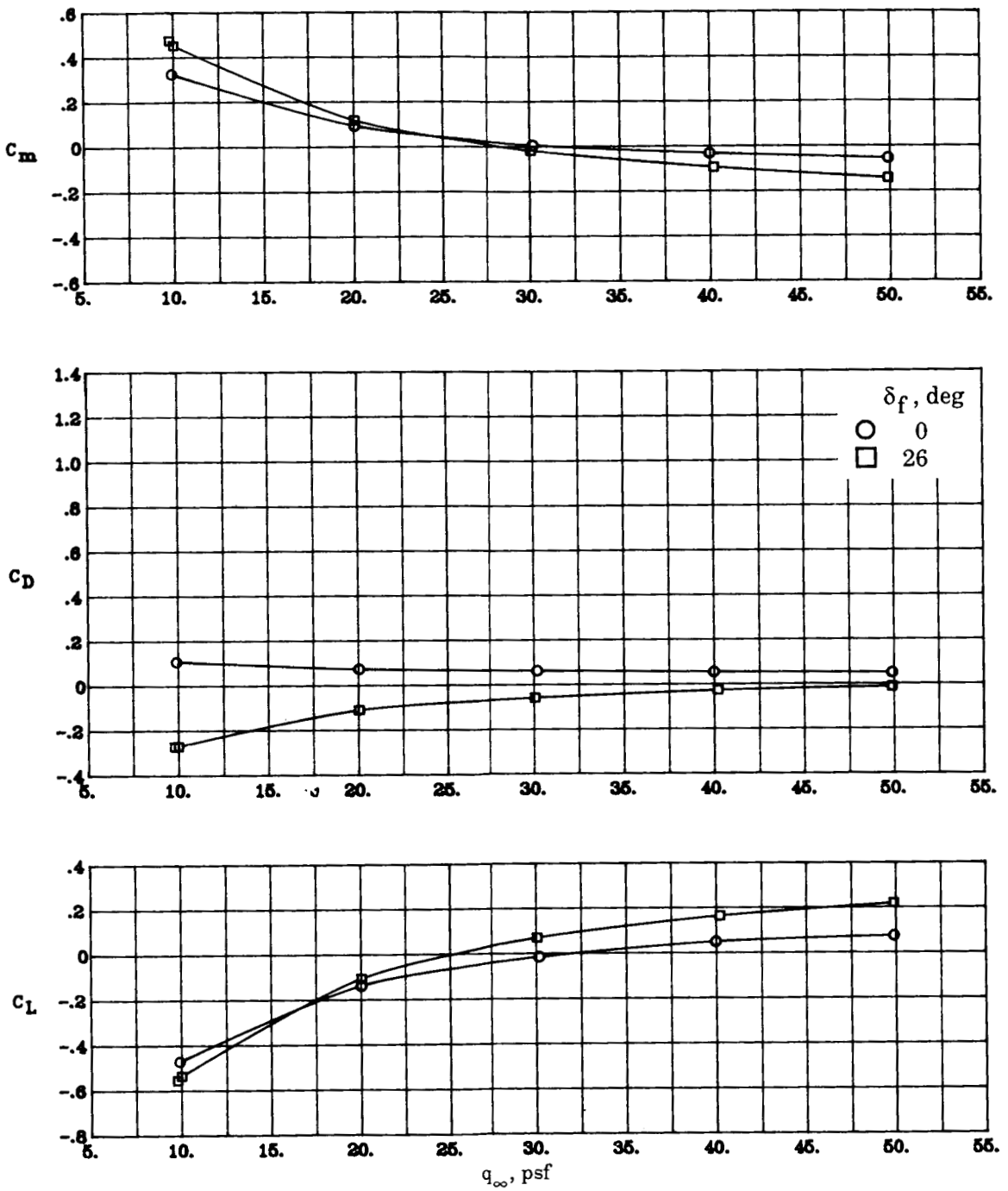


(m) $\Lambda_c = 0°$; NPR = 2.0; $\beta = 0°$.

Figure 7. Continued.

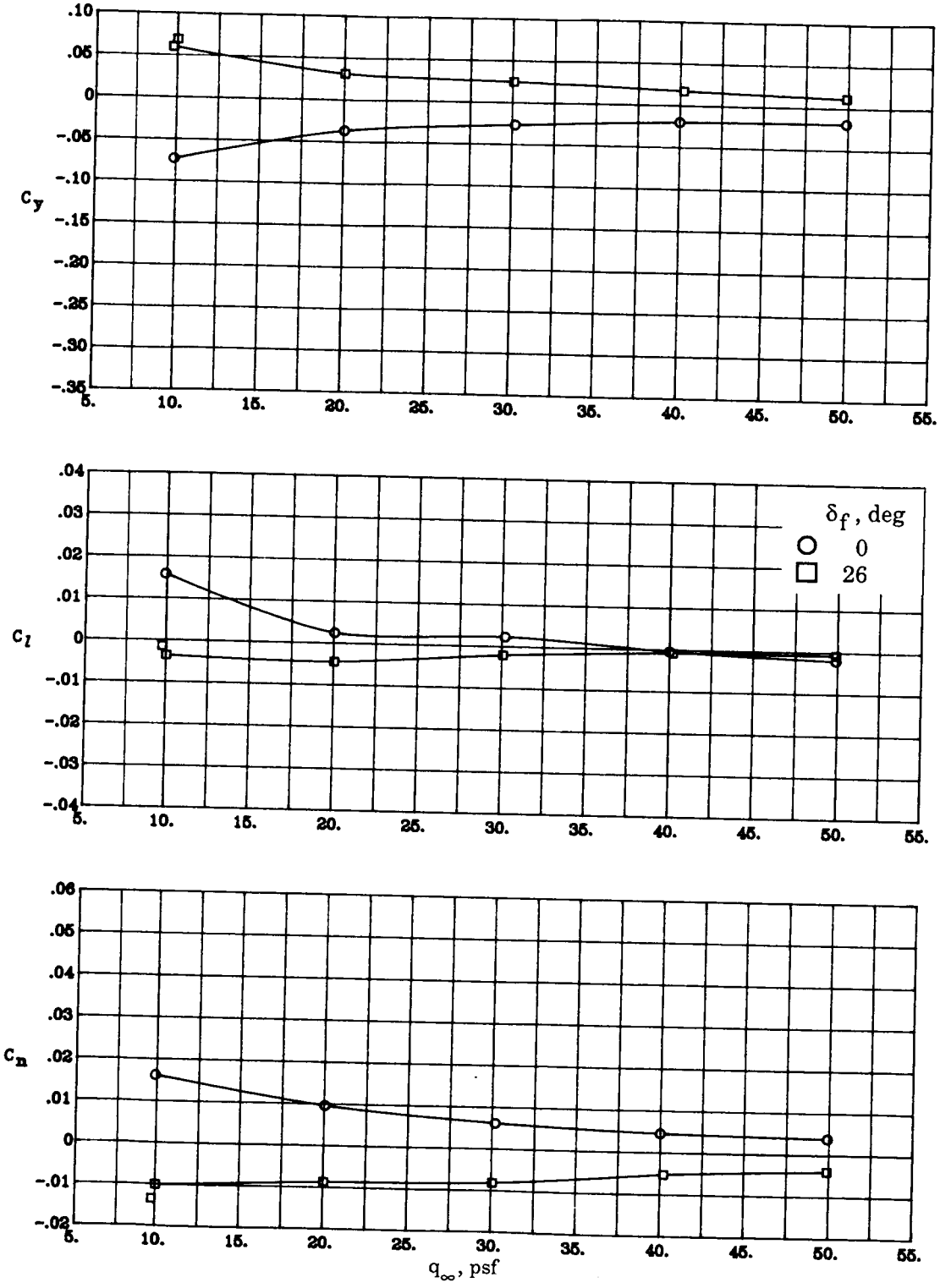


(m) Concluded.

Figure 7. Concluded.

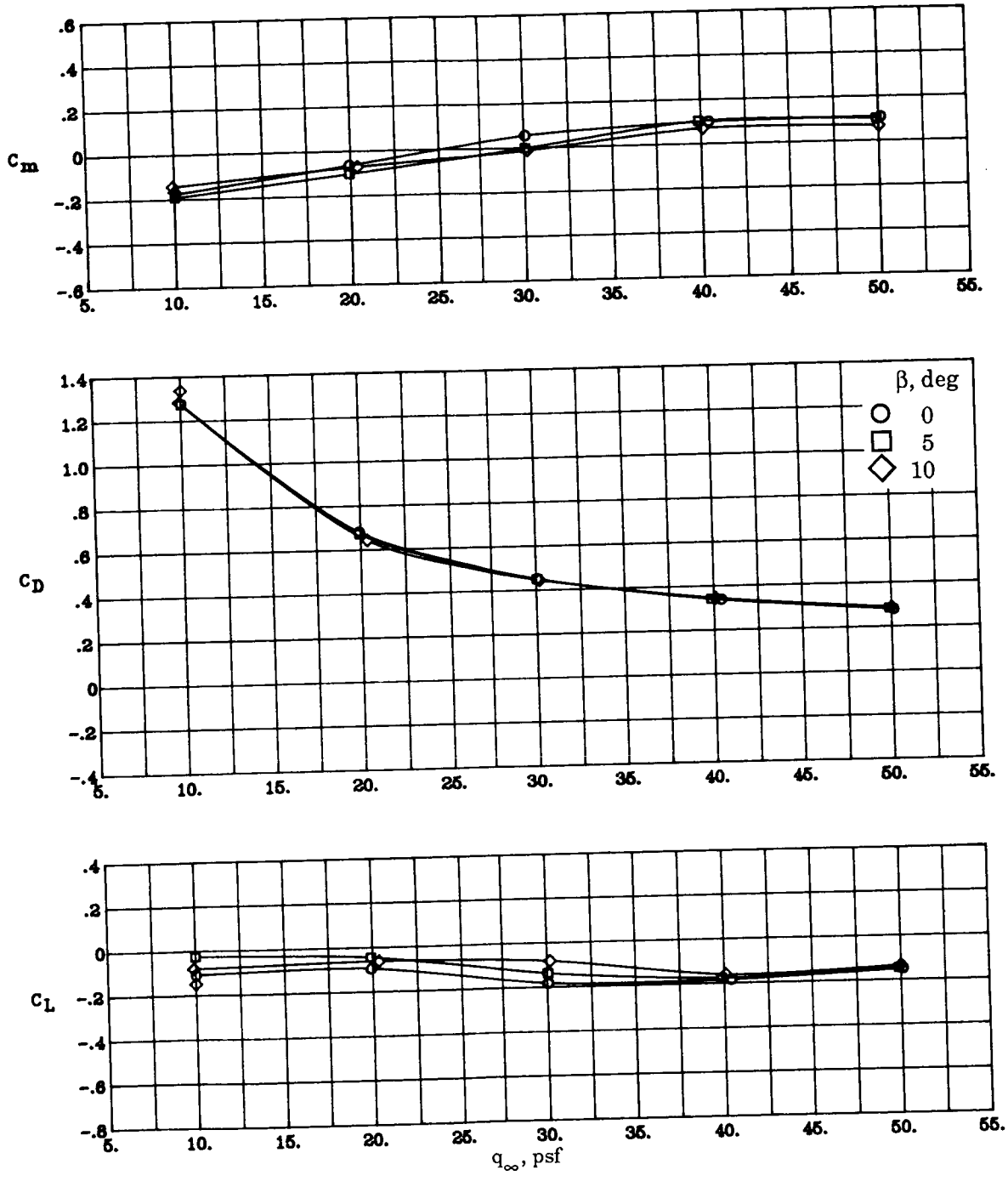


(a) $\Lambda_c = -45°$; NPR = 4.0; $\delta_f = 0°$.

Figure 8. Effects of sideslip angle on aerodynamic characteristics.

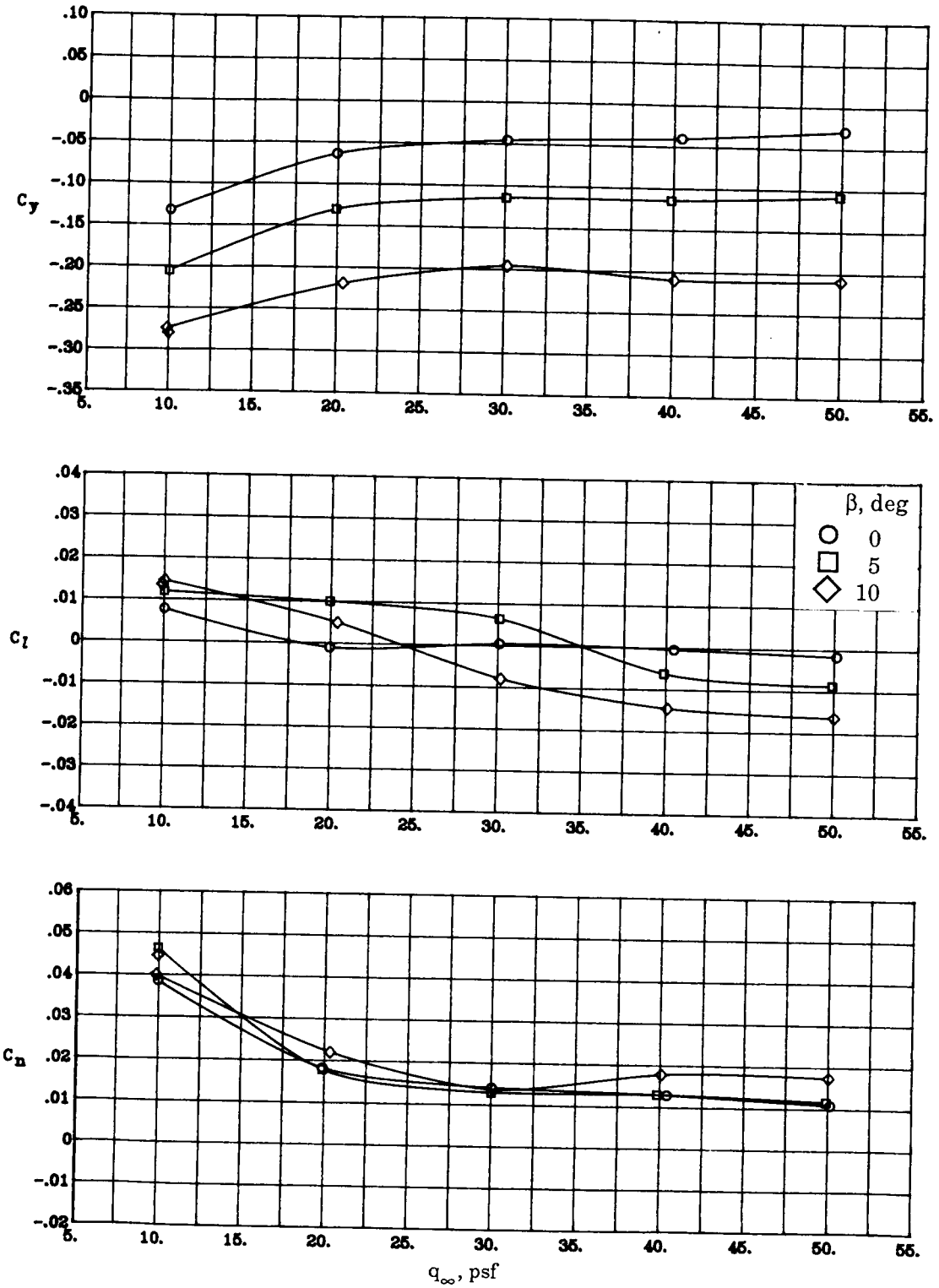


(a) Concluded.

Figure 8. Continued.

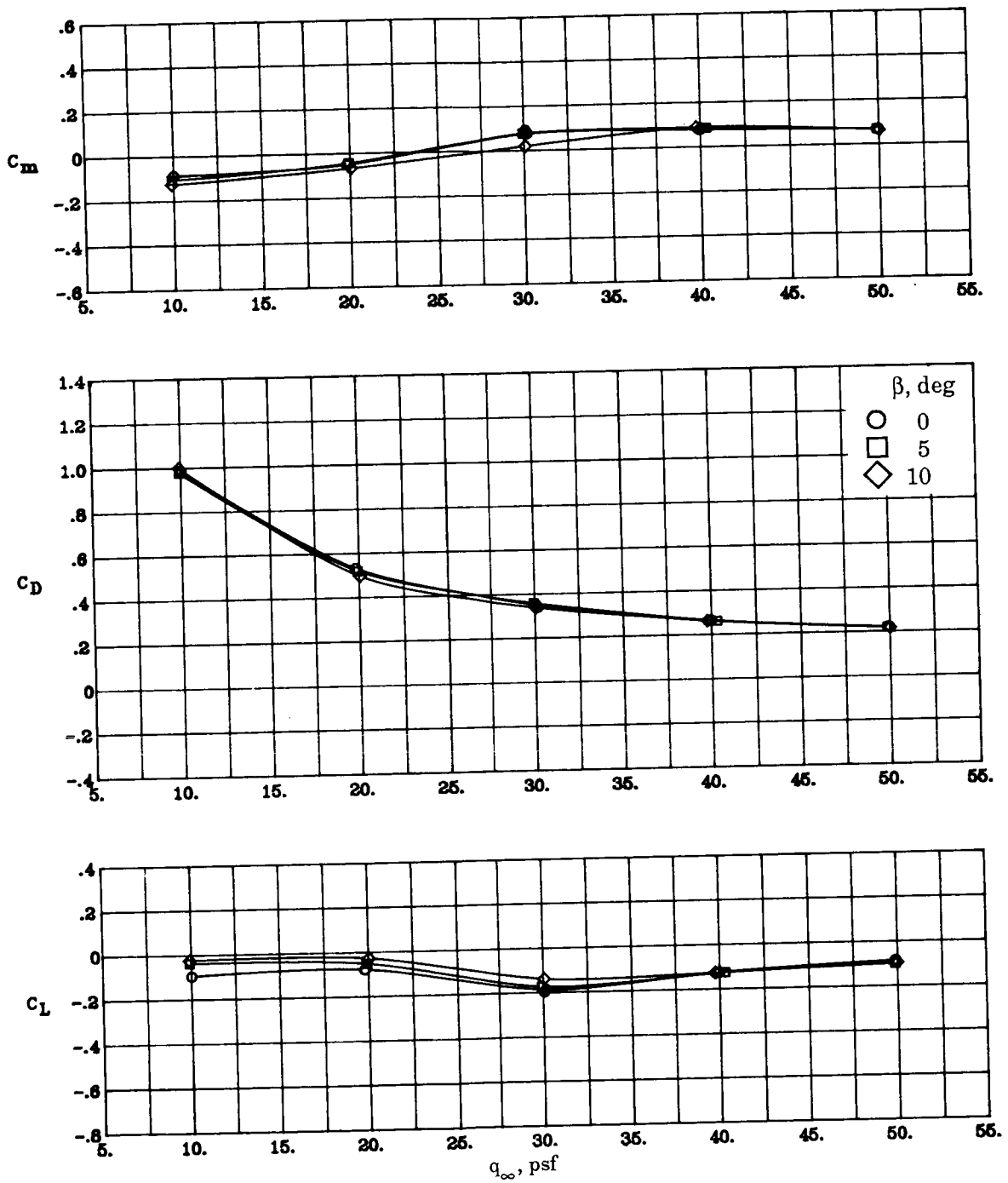


(b) $\Lambda_c = -45°$; NPR = 3.0; $\delta_f = 0°$.

Figure 8. Continued.

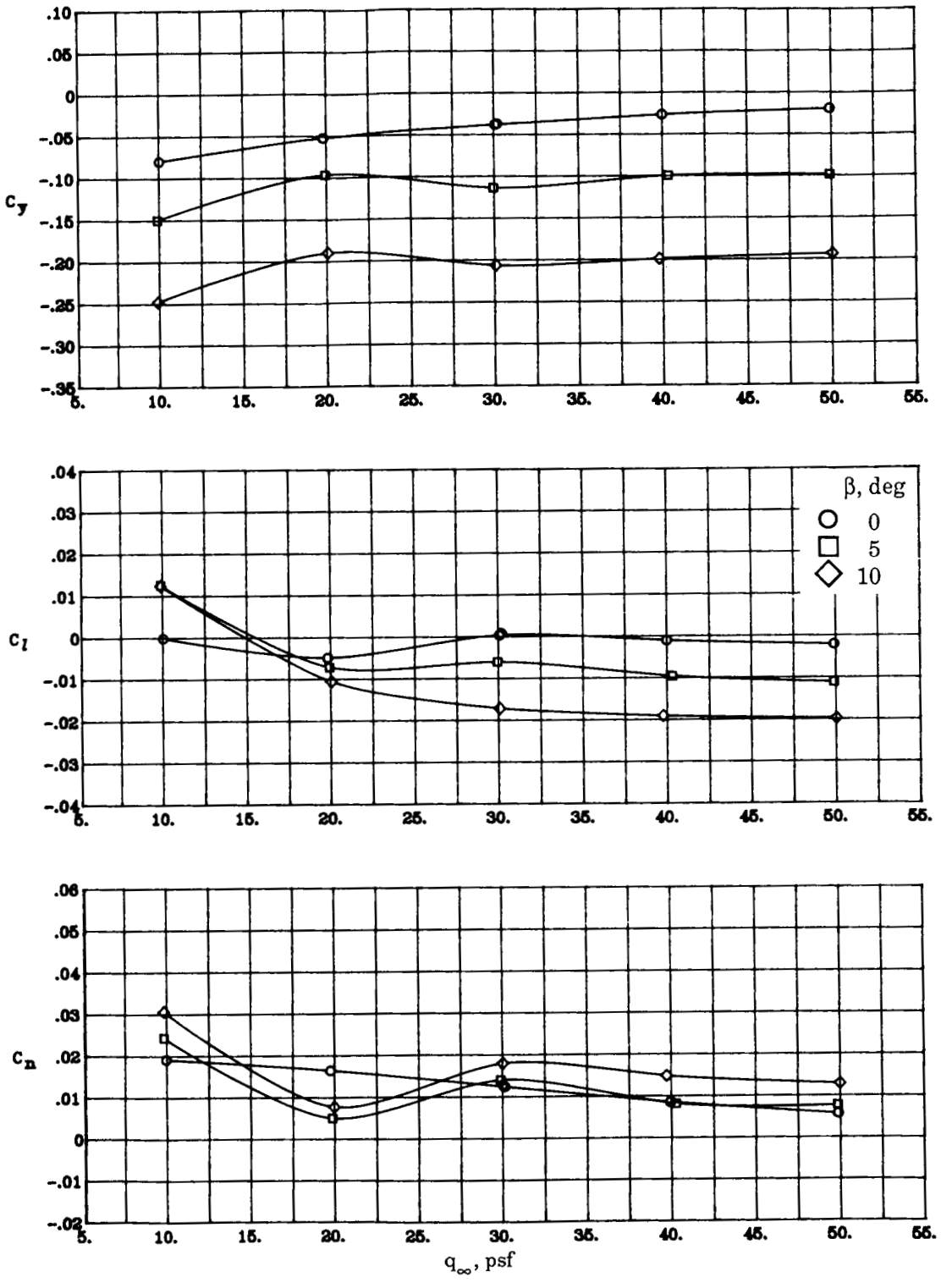


(b) Concluded.

Figure 8. Continued.

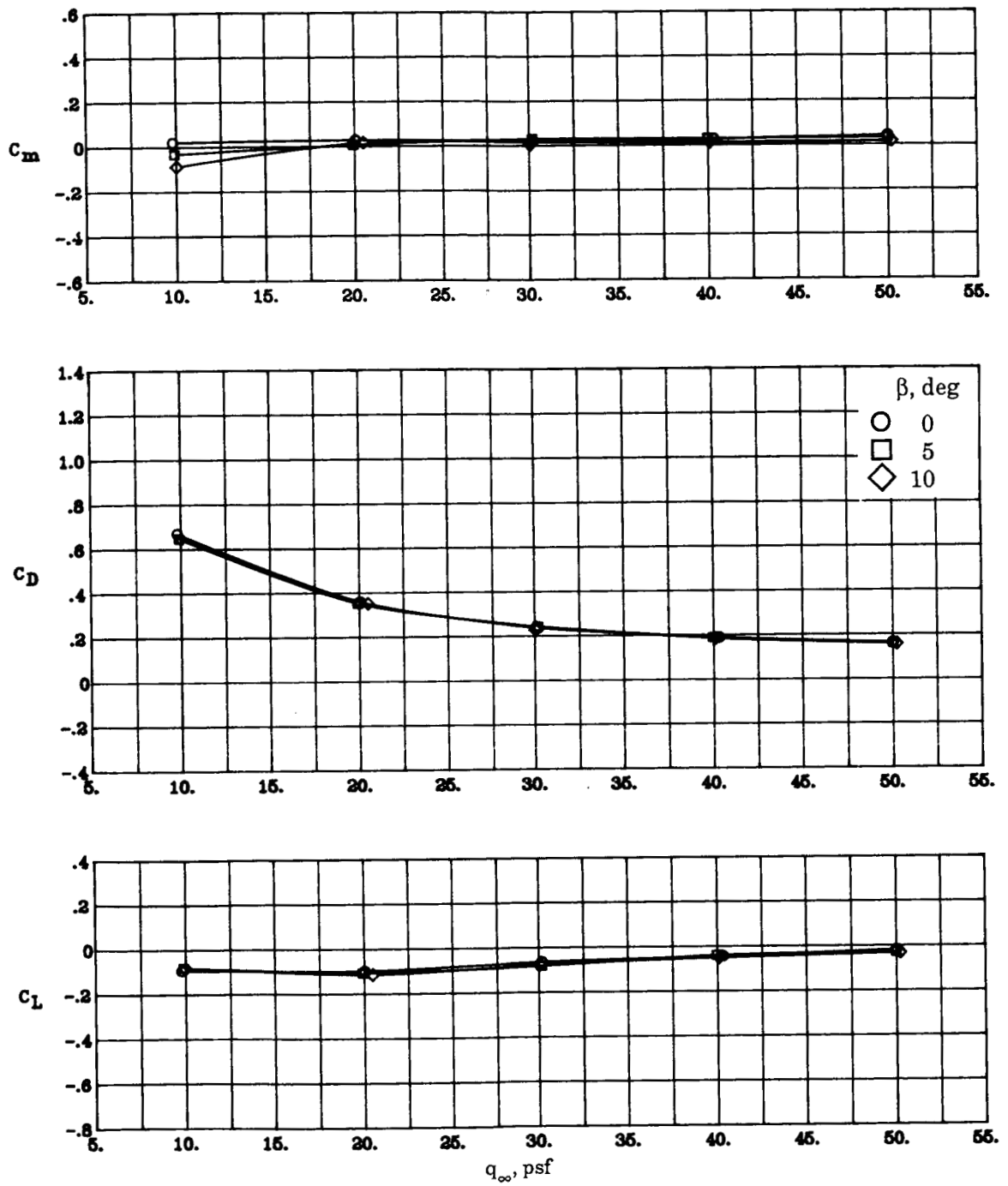


(c) $\Lambda_c = -45°$; NPR = 2.0; $\delta_f = 0°$.

Figure 8. Continued.

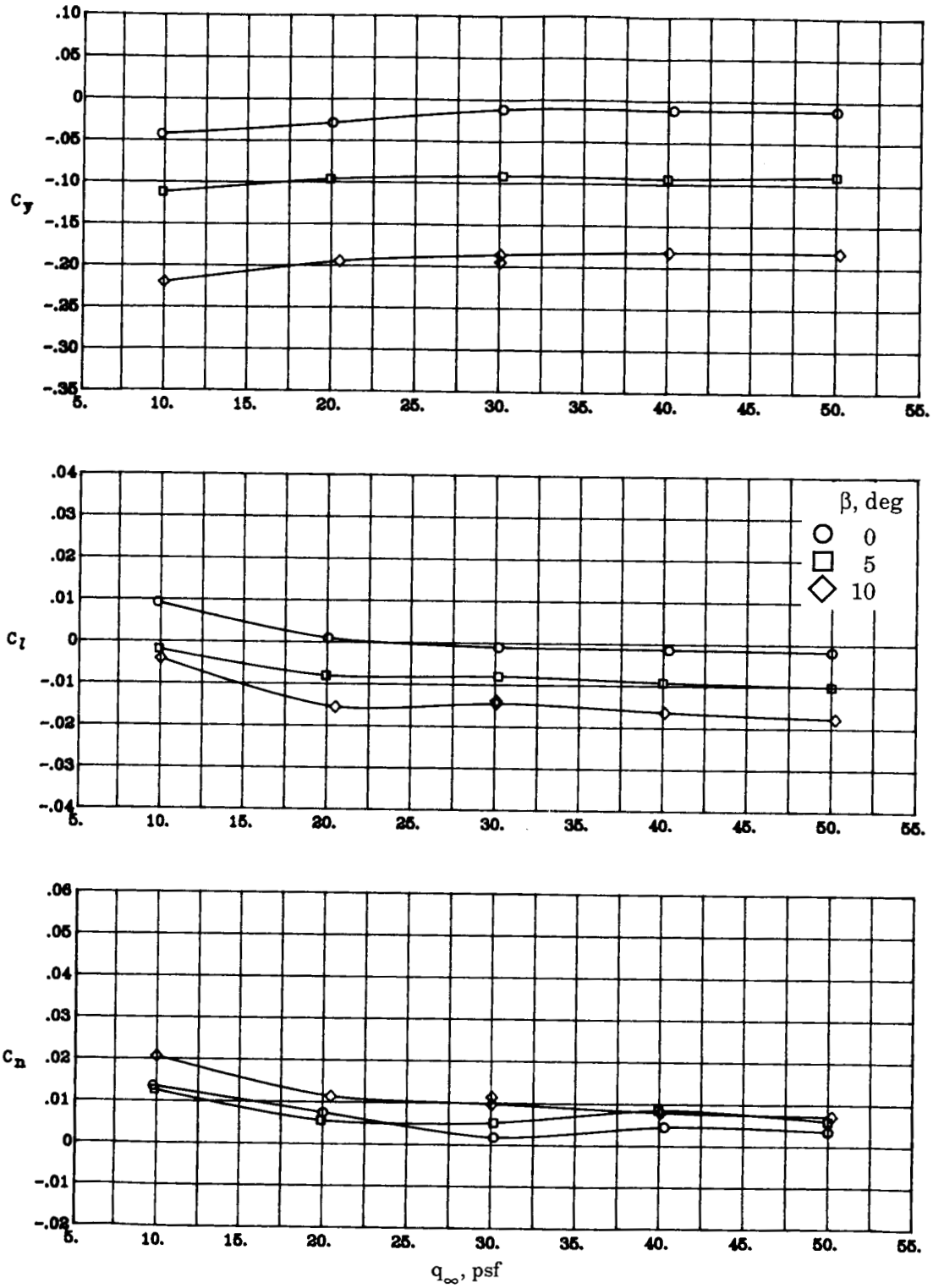


(c) Concluded.

Figure 8. Continued.

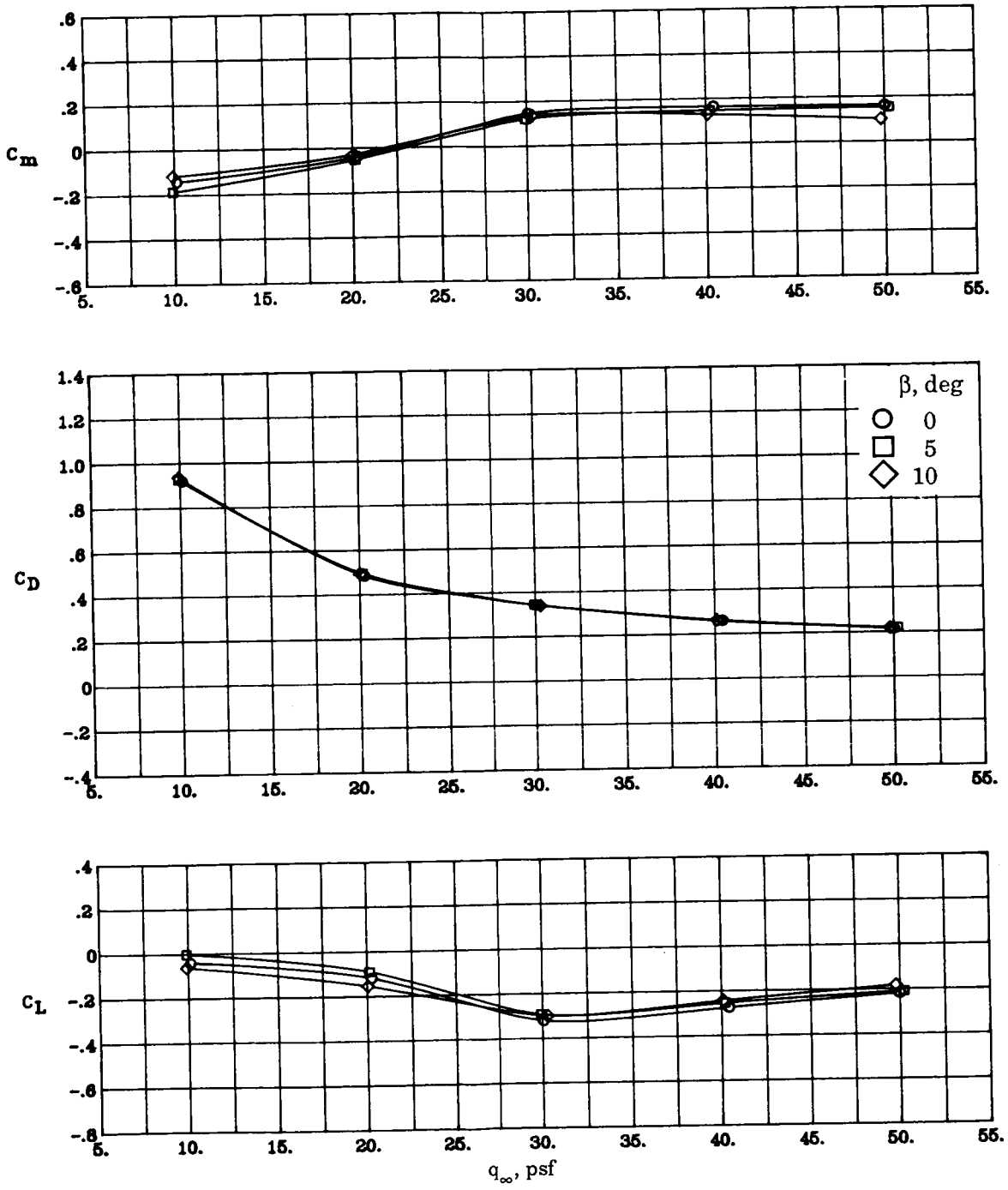


(d) $\Lambda_c = -30°$; NPR = 4.0; $\delta_f = 0°$.

Figure 8. Continued.

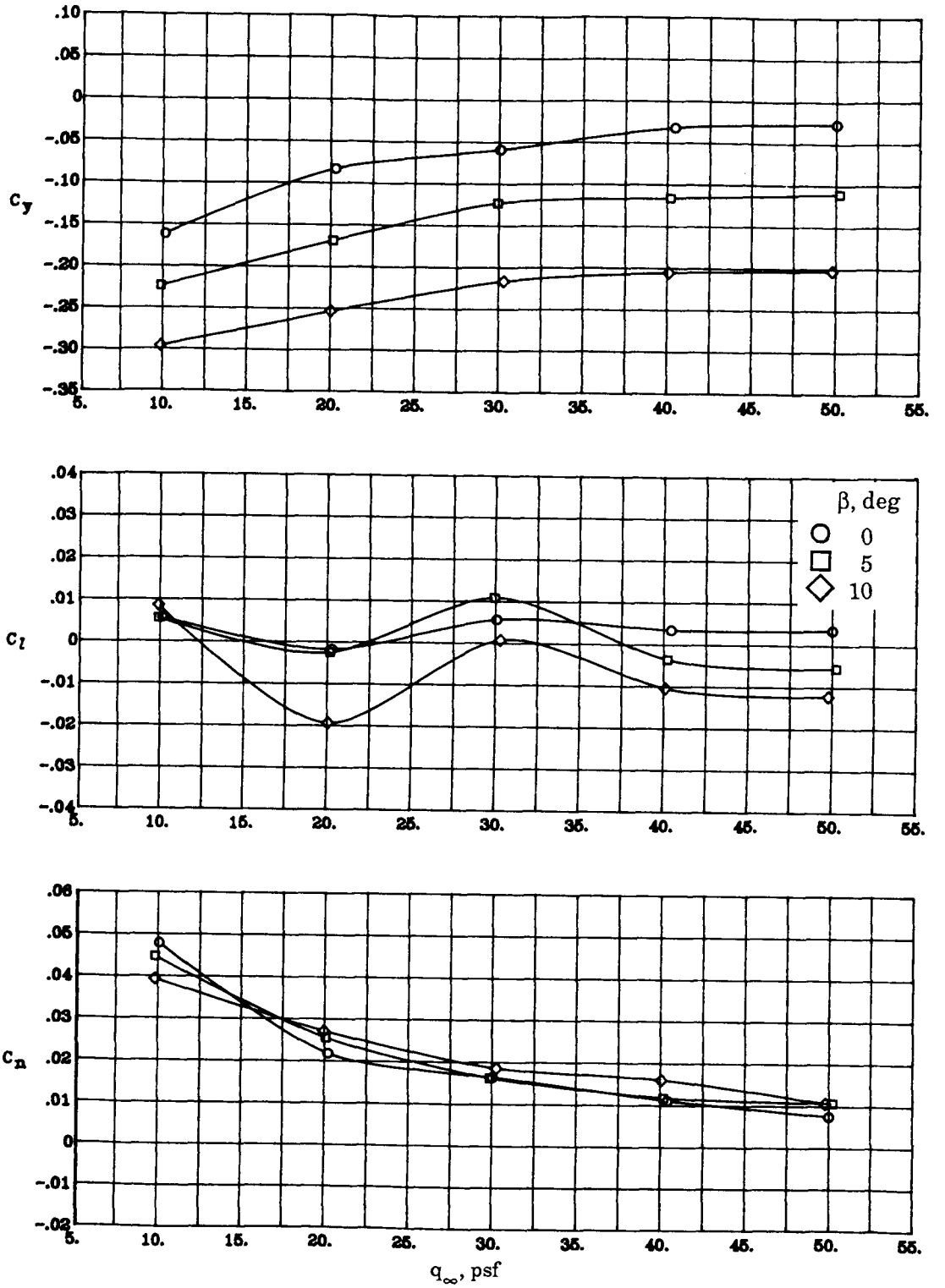


(d) Concluded.

Figure 8. Continued.

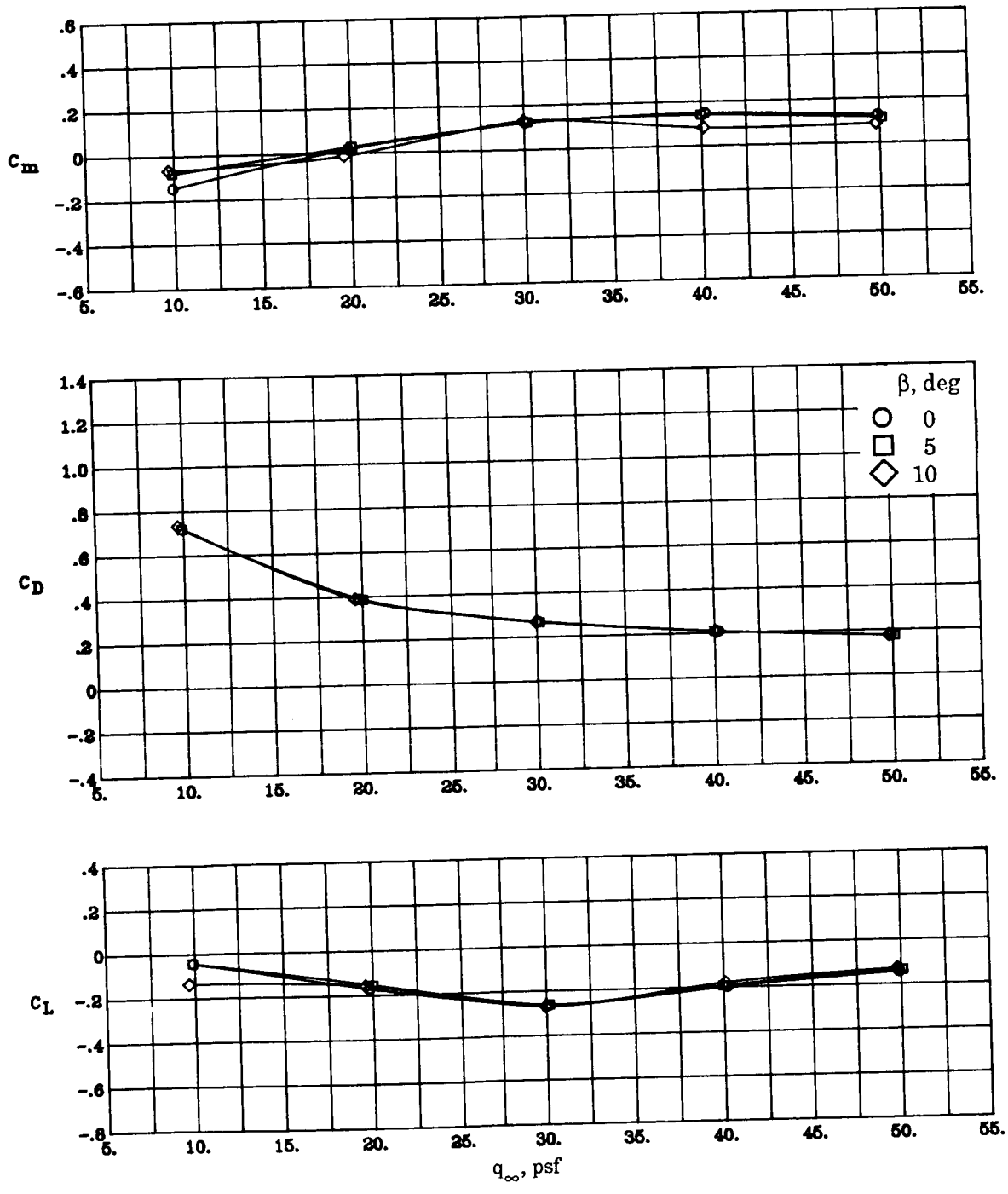


(e) $\Lambda_c = -30°$; NPR = 3.0; $\delta_f = 0°$.

Figure 8. Continued.

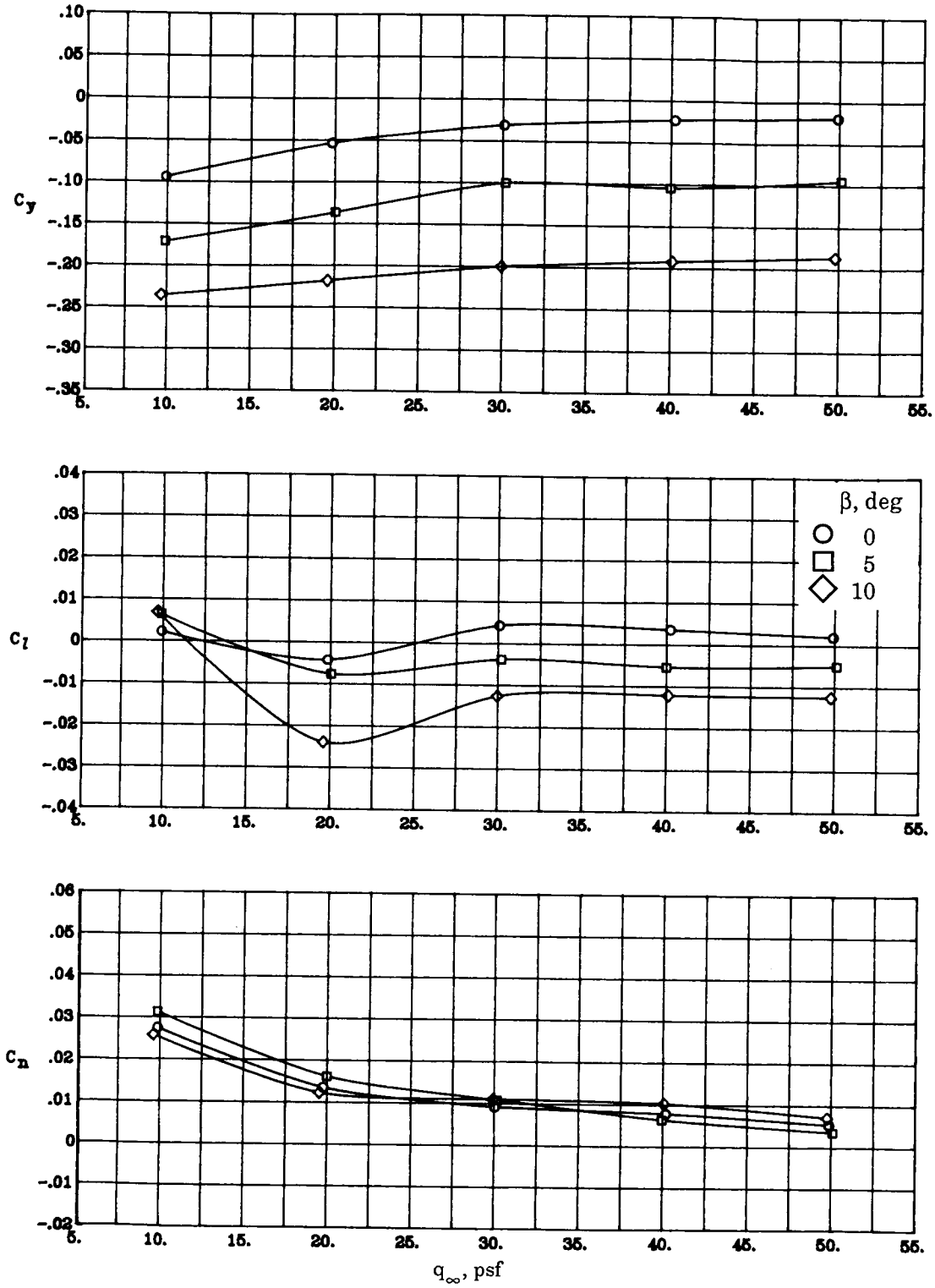


(e) Concluded.

Figure 8. Continued.

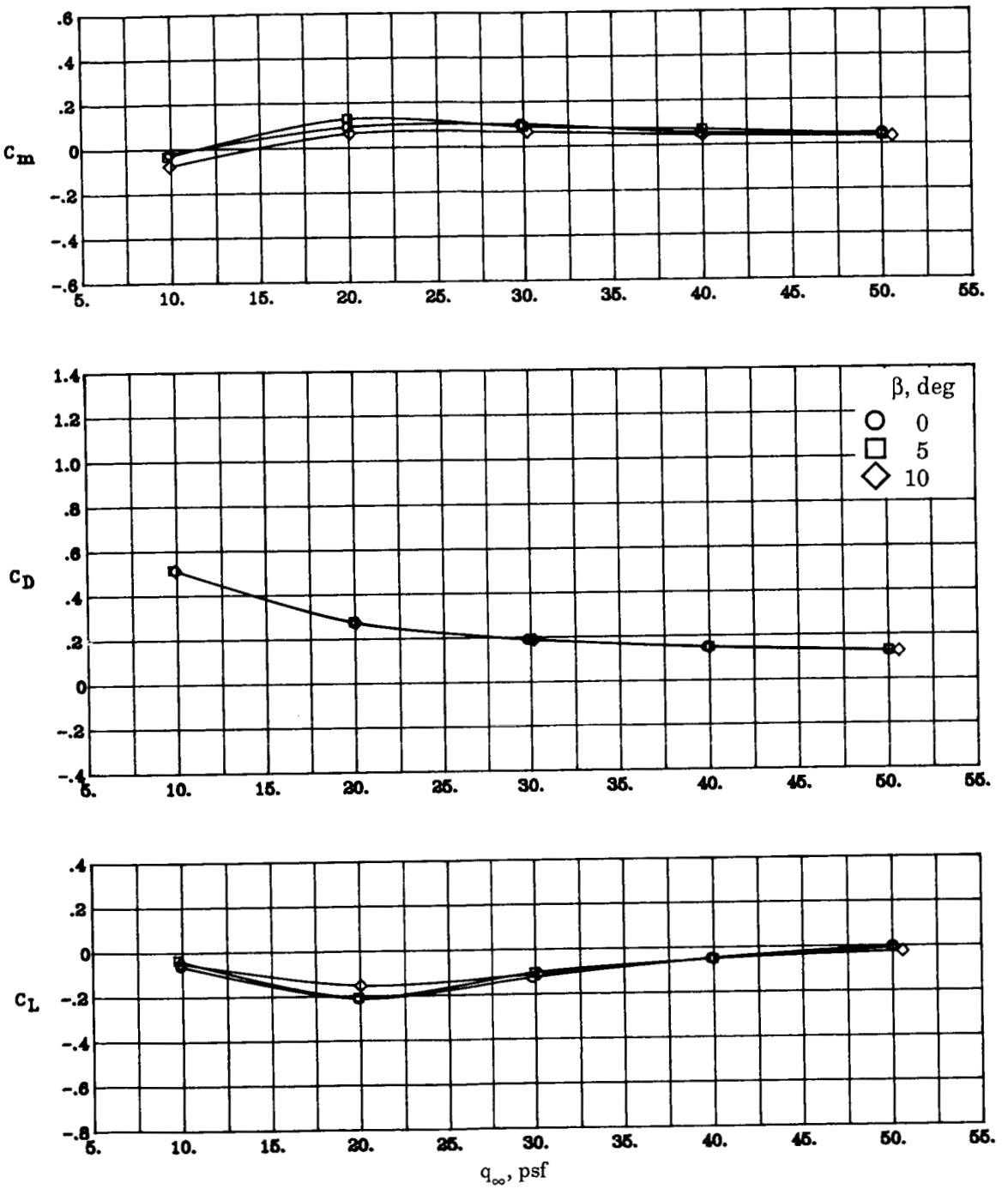


(f) $\Lambda_c = -30°$; NPR = 2.0; $\delta_f = 0°$.

Figure 8. Continued.

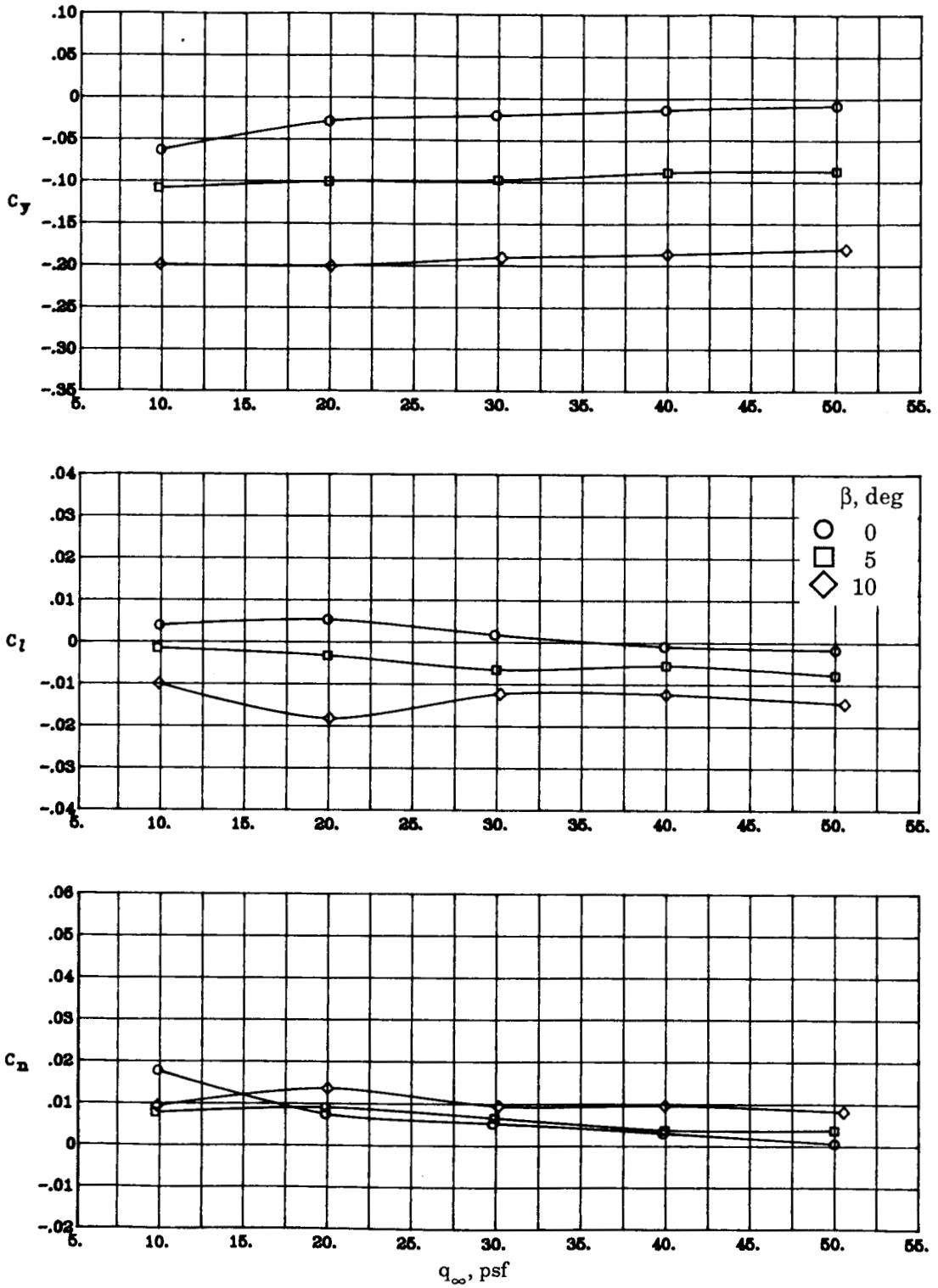


(f) Concluded.

Figure 8. Continued.

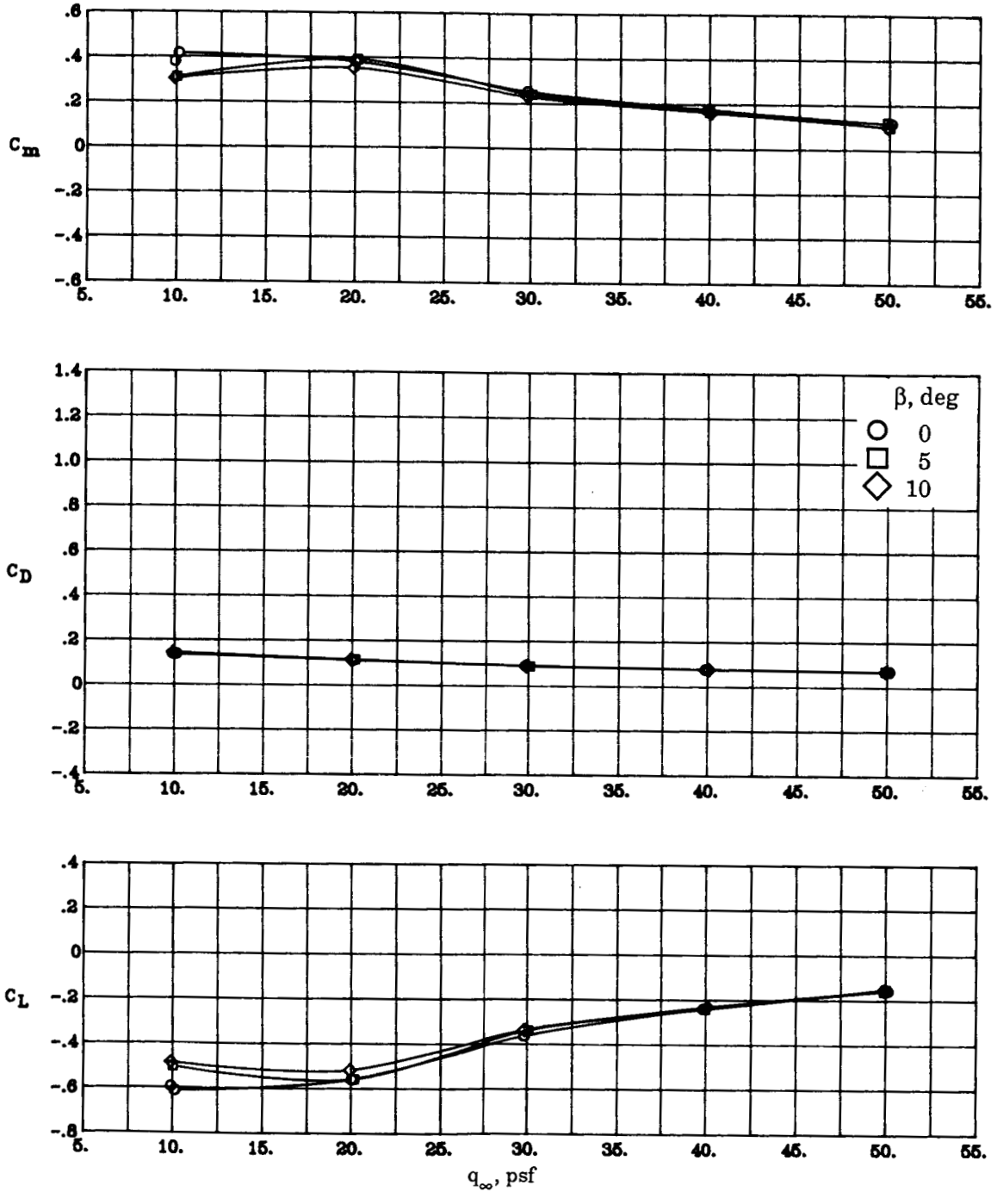


(g) $\Lambda_c = 0°$; NPR = 4.0; $\delta_f = 0°$.

Figure 8. Continued.

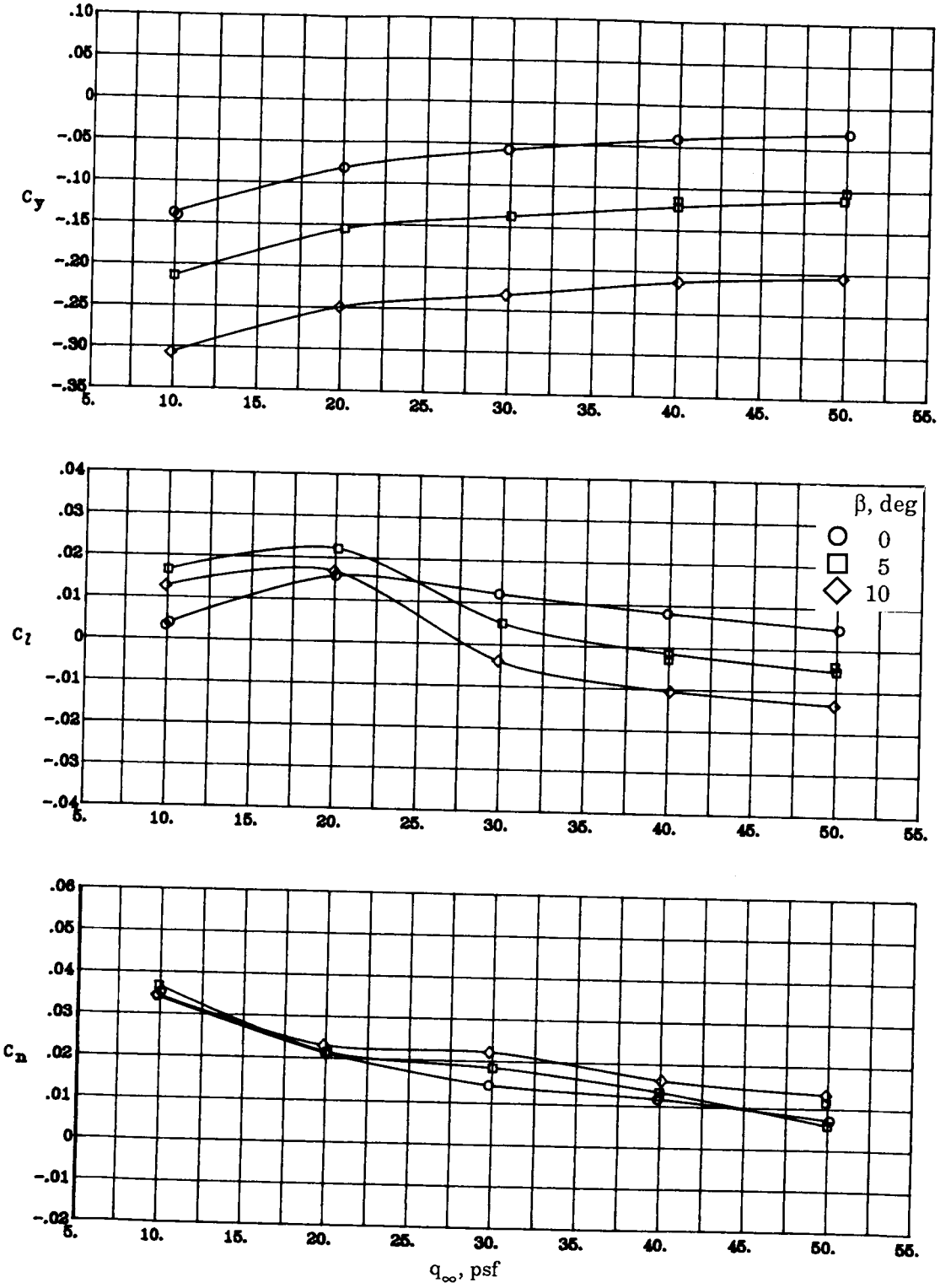


(g) Concluded.

Figure 8. Continued.

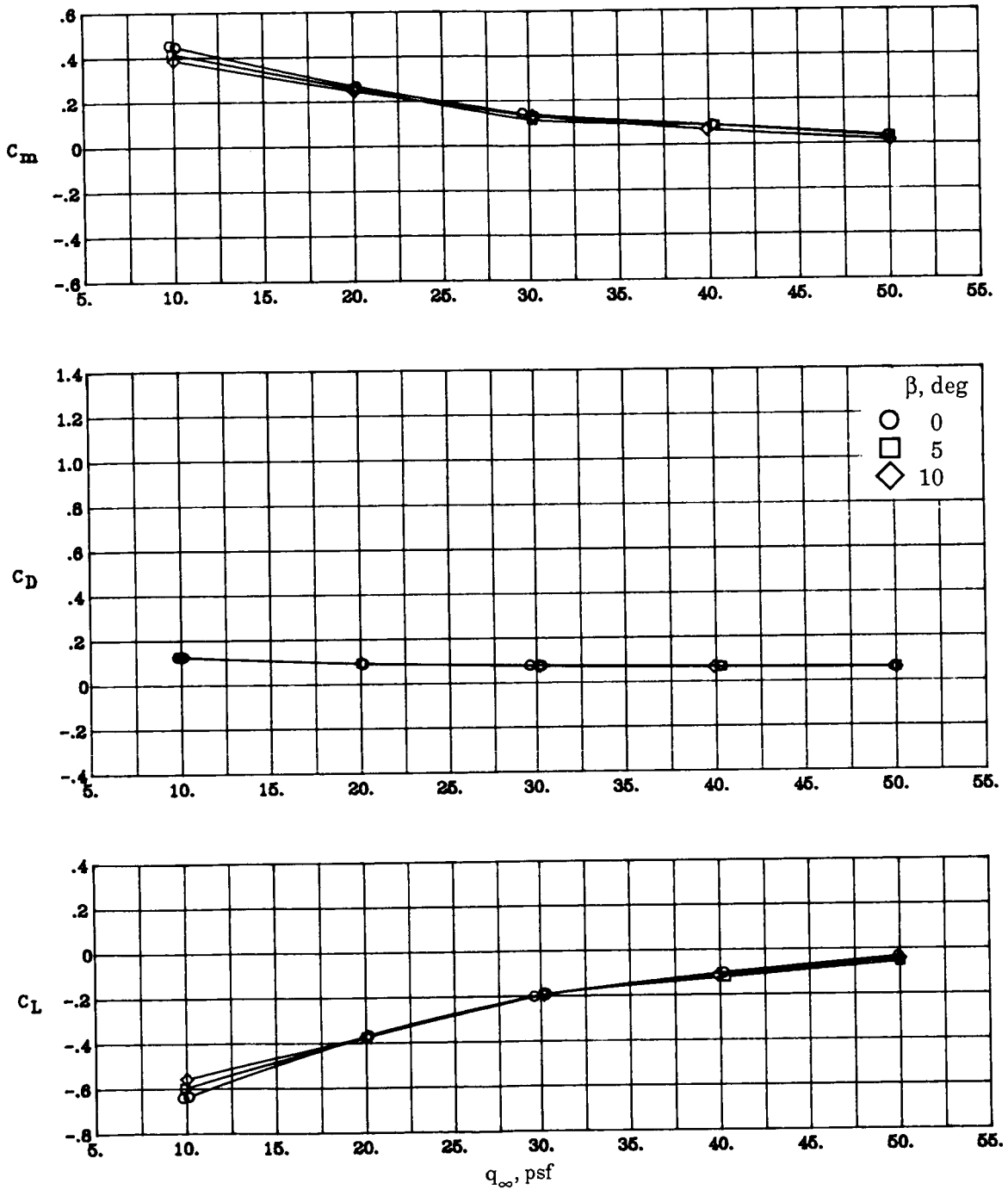


(h) $\Lambda_c = 0°$; NPR = 3.0; $\delta_f = 0°$.

Figure 8. Continued.

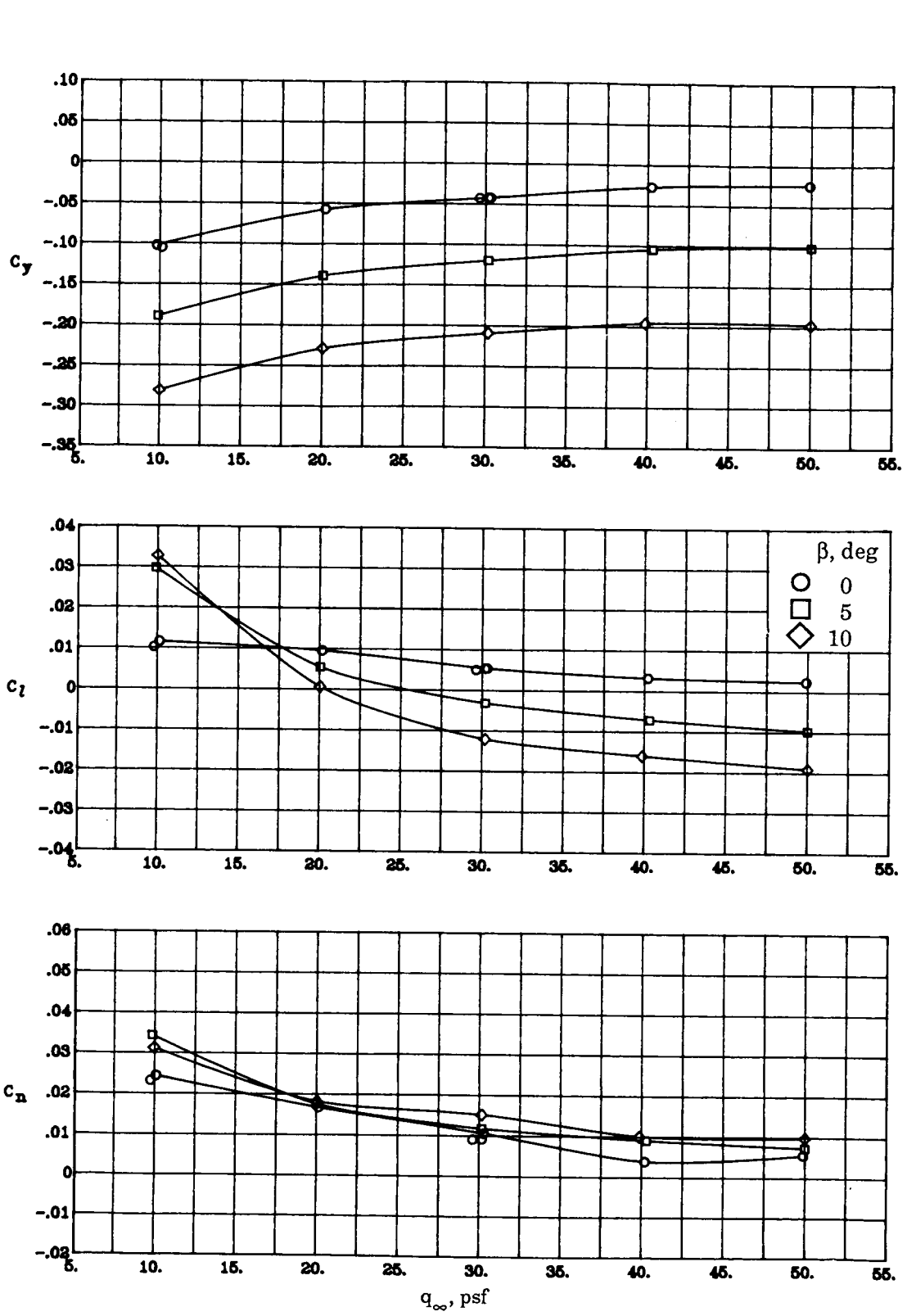


(h) Concluded.

Figure 8. Continued.

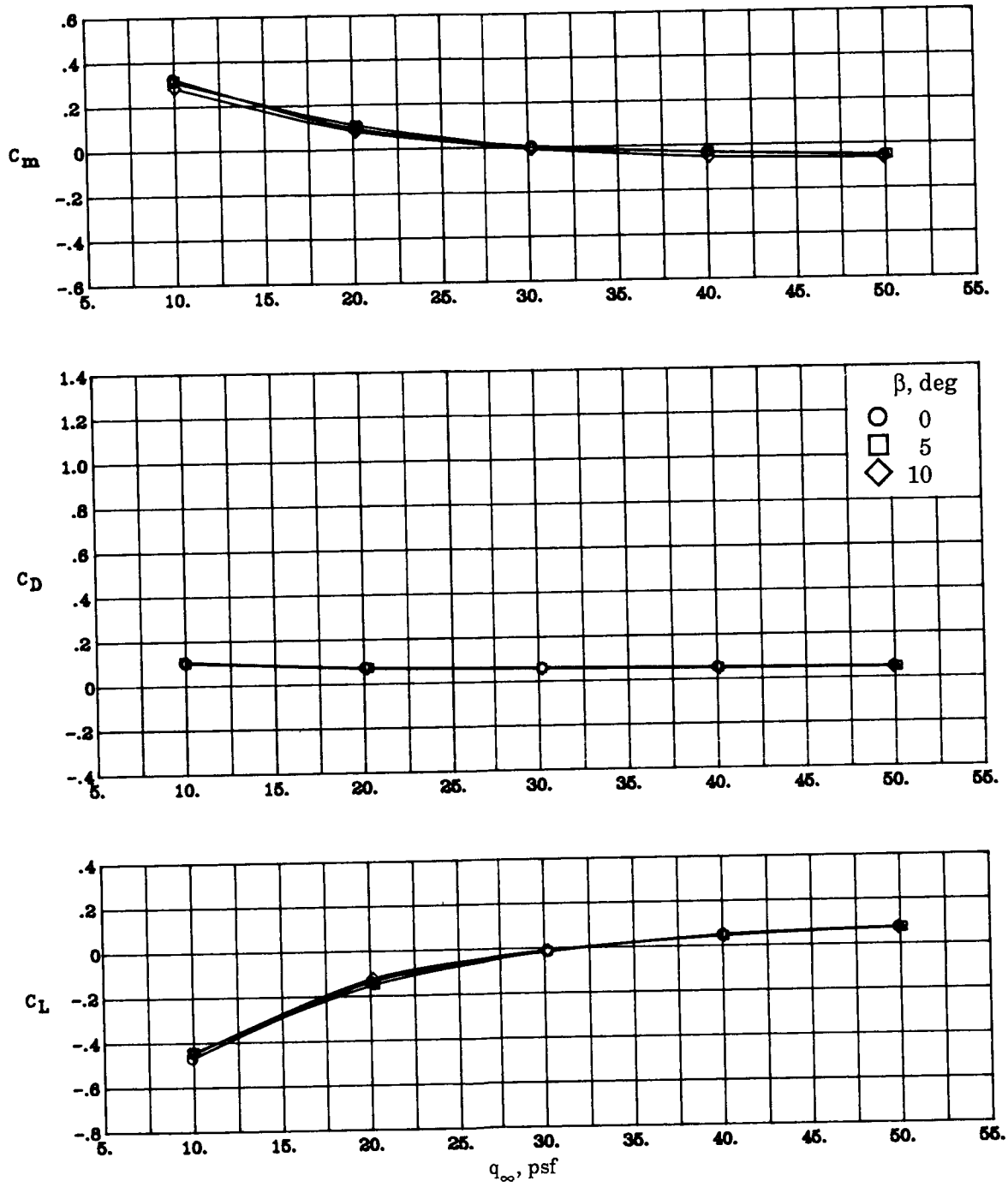


(i) $\Lambda_c = 0°$; NPR = 2.0; $\delta_f = 0°$.

Figure 8. Continued.

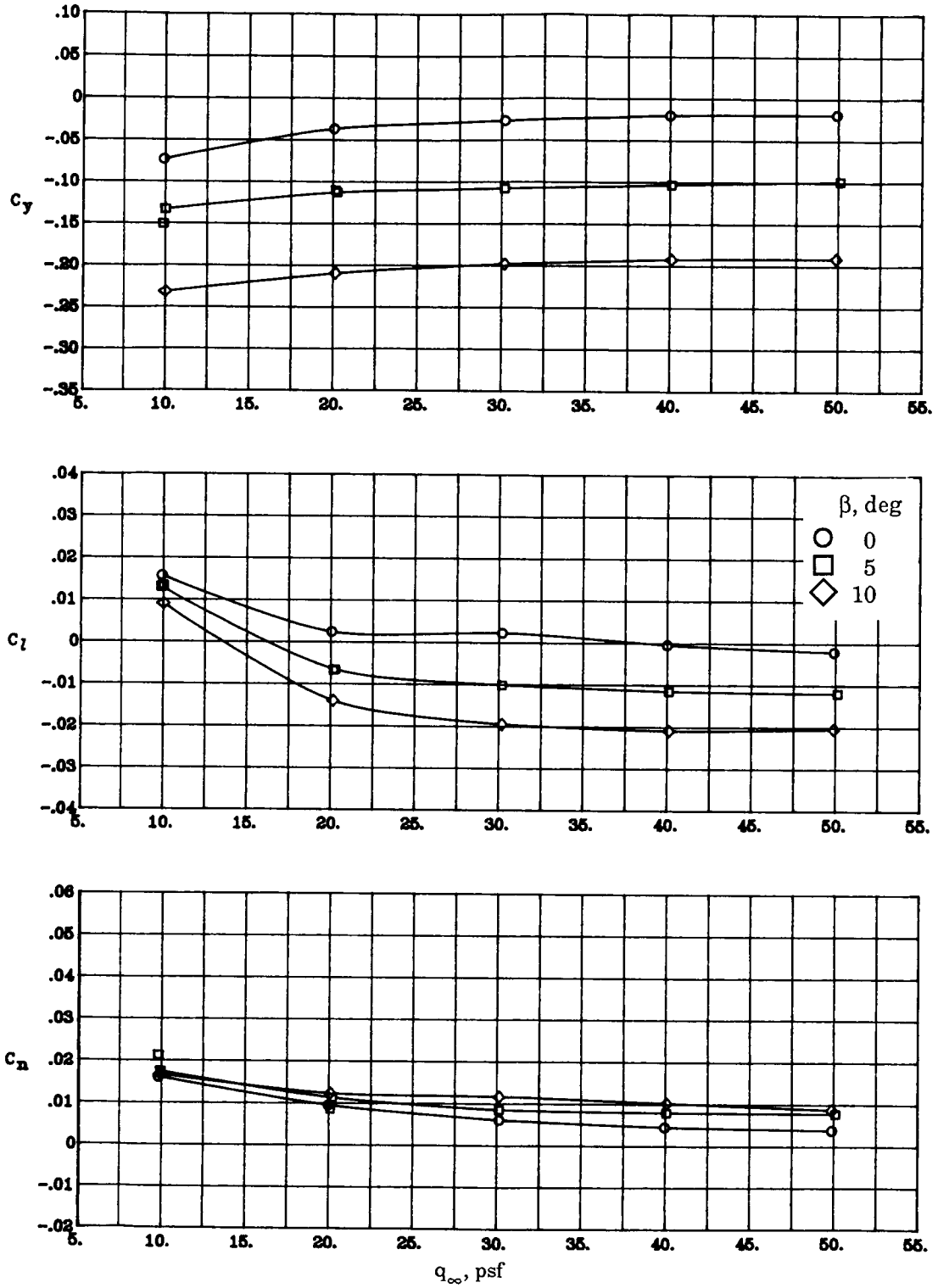


(i) Concluded.

Figure 8. Continued.

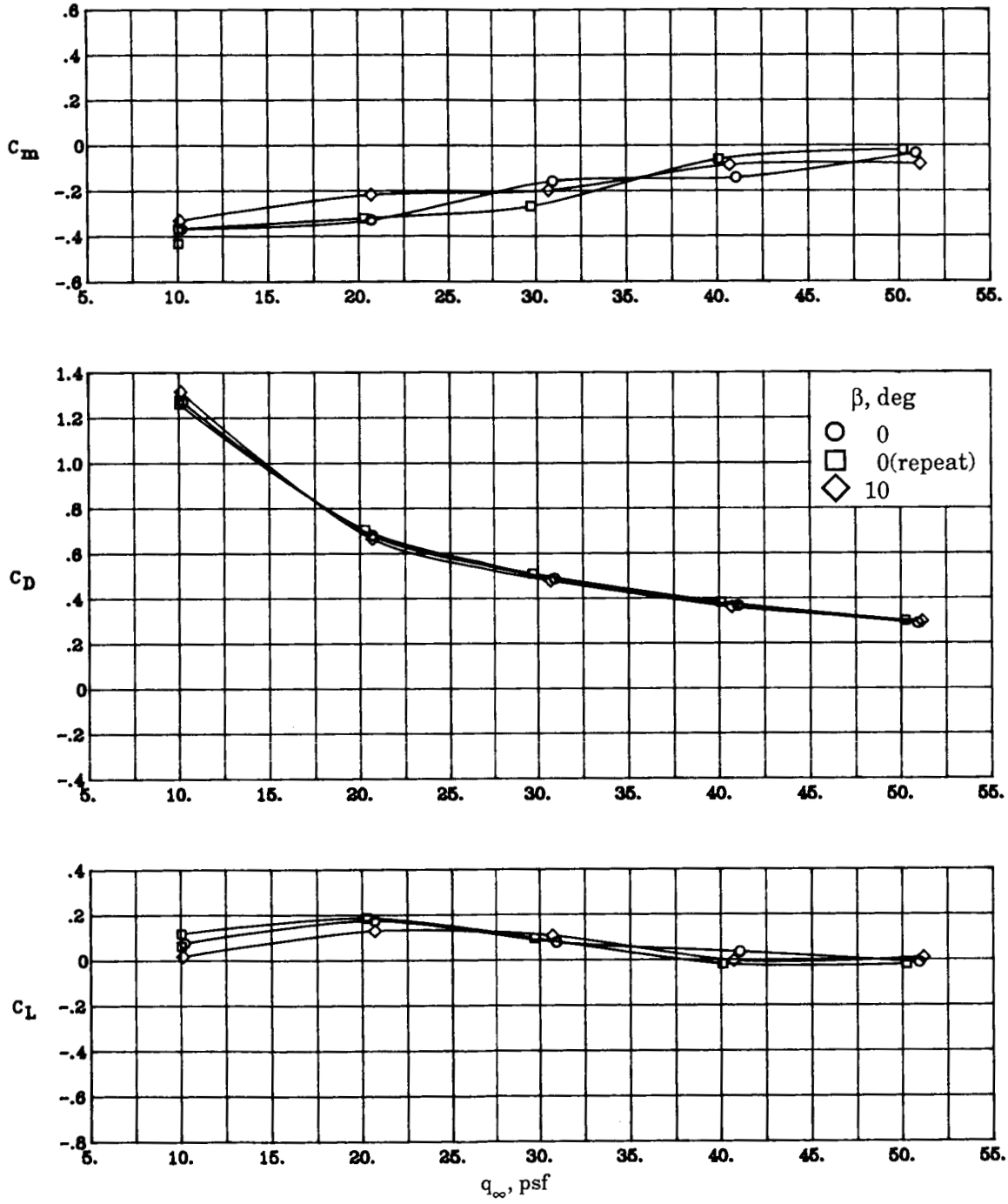


(j) $\Lambda_c = -45°$; NPR = 4.0; $\delta_f = 26°$.

Figure 8. Continued.

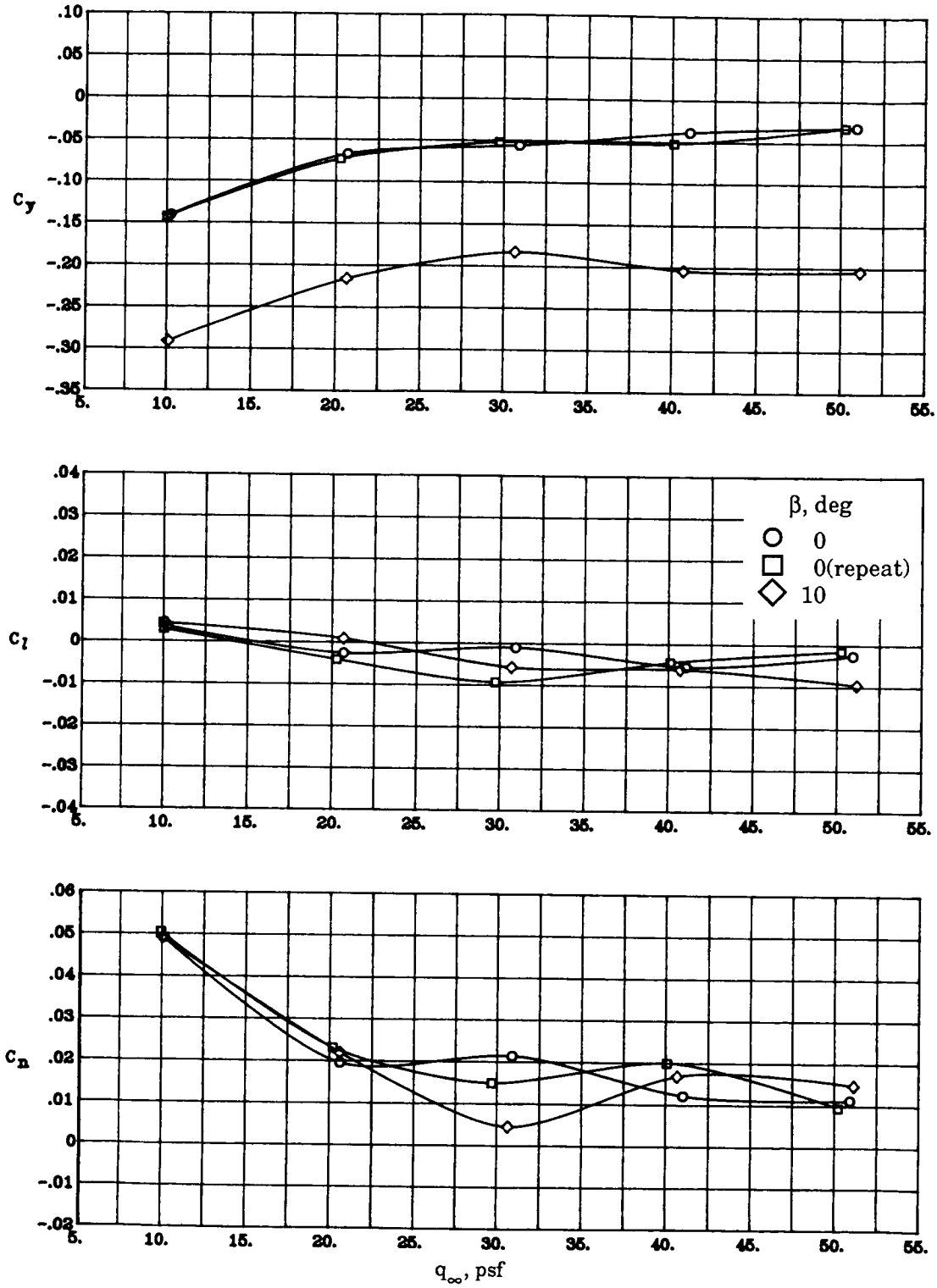


(j) Concluded.

Figure 8. Continued.

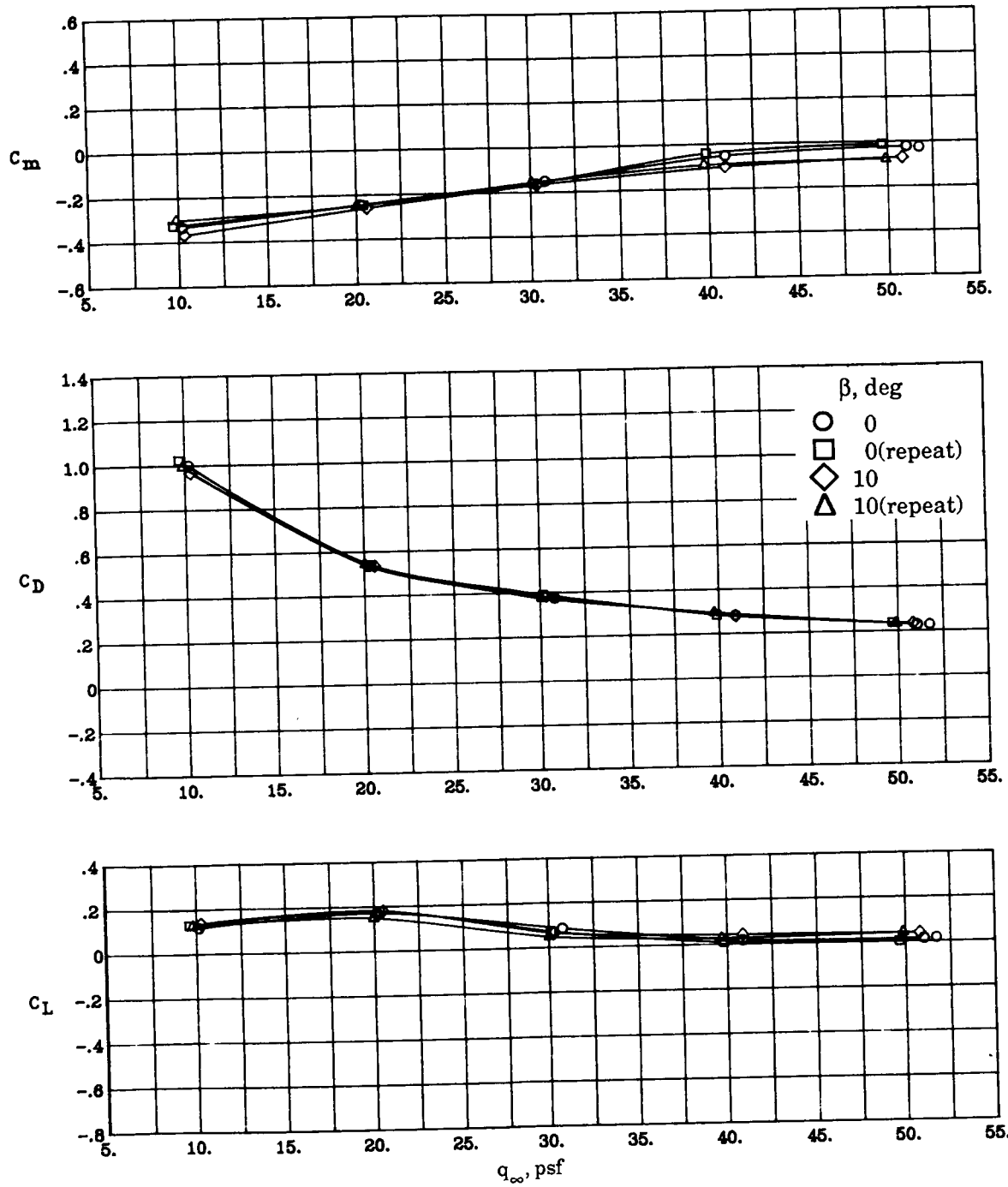


(k) $\Lambda_c = -45°$; NPR = 3.0; $\delta_f = 26°$.

Figure 8. Continued.

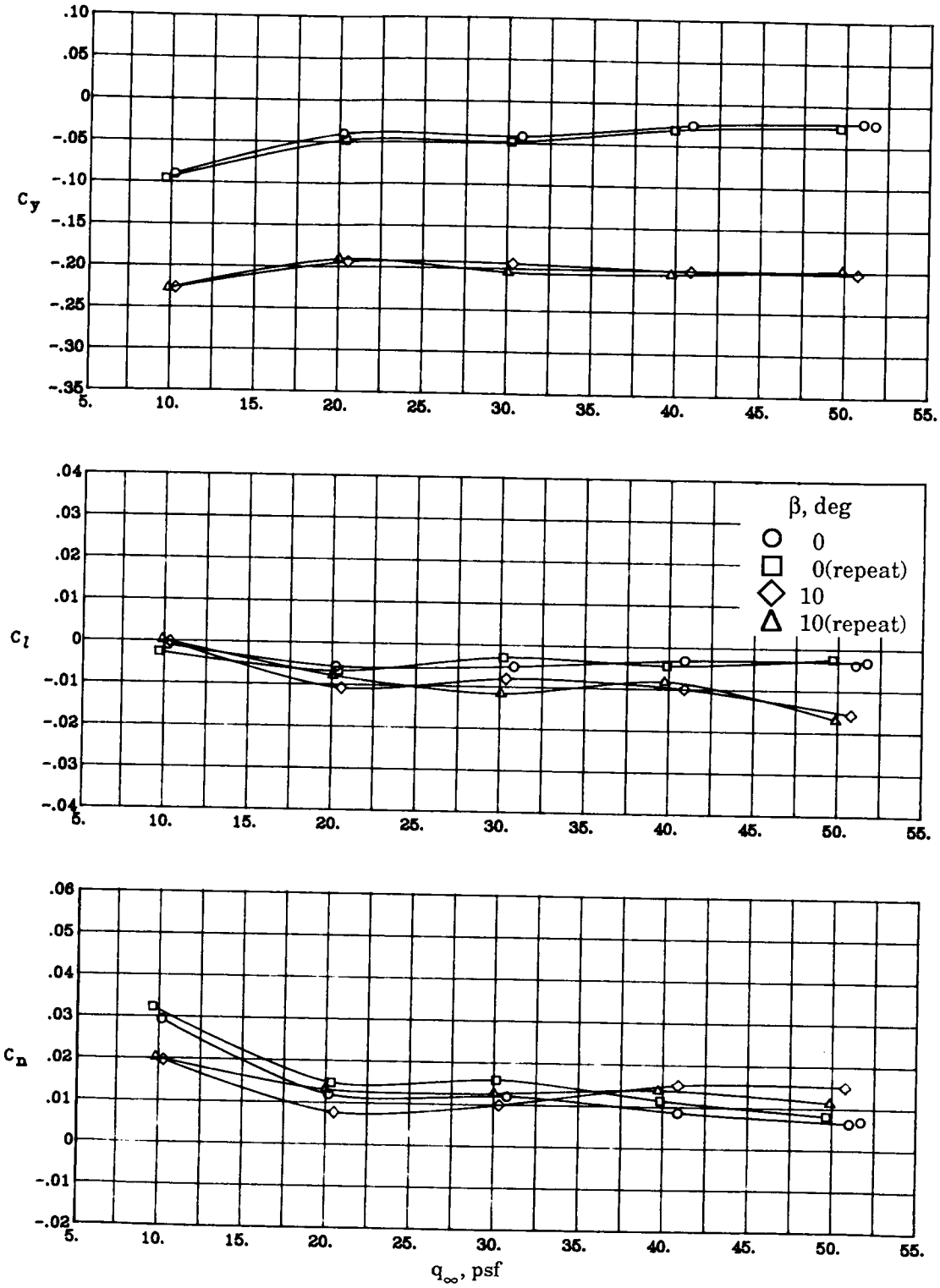


(k) Concluded.

Figure 8. Continued.

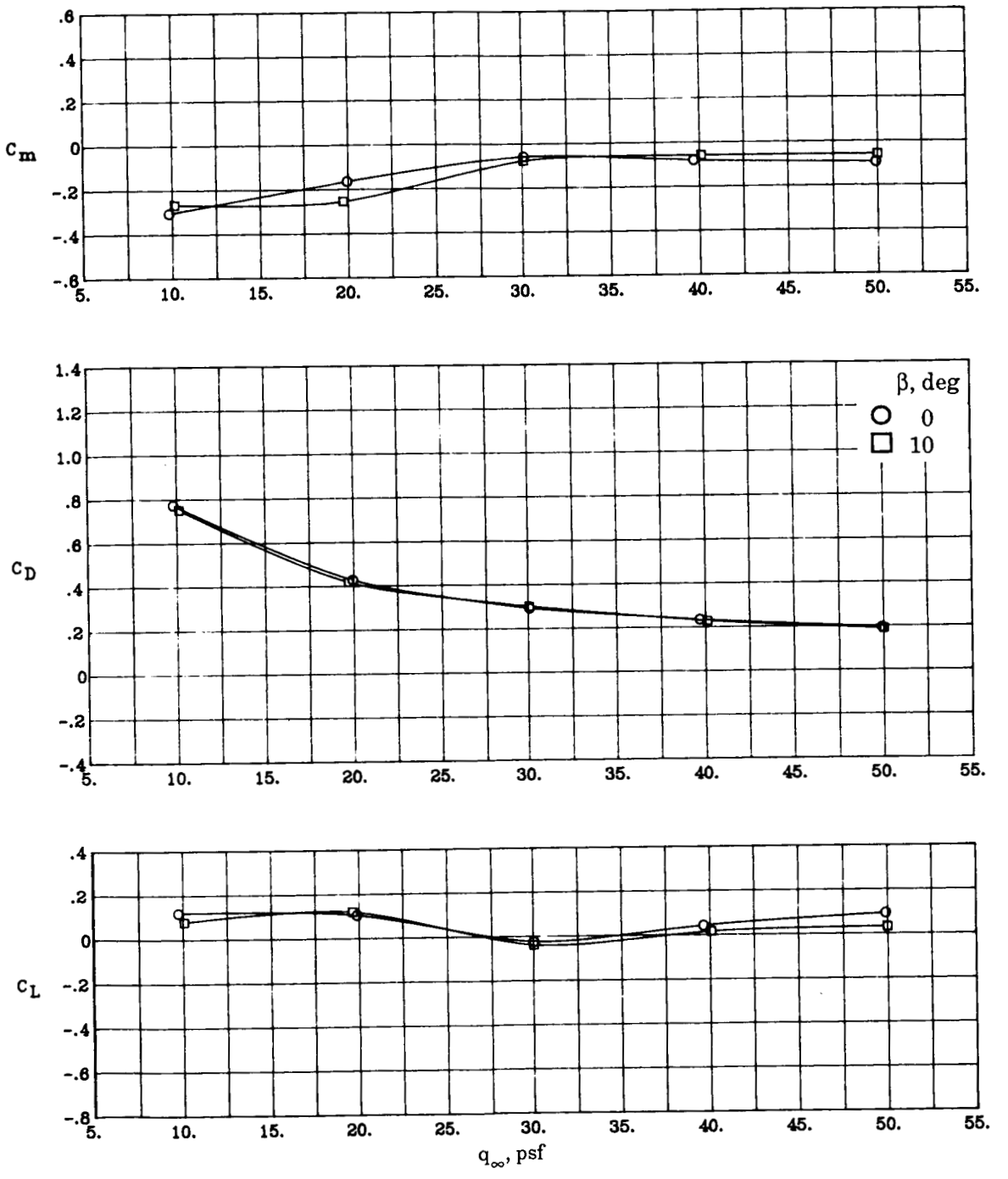


(l) $\Lambda_c = -30°$; NPR = 3.0; $\delta_f = 26°$.

Figure 8. Continued.

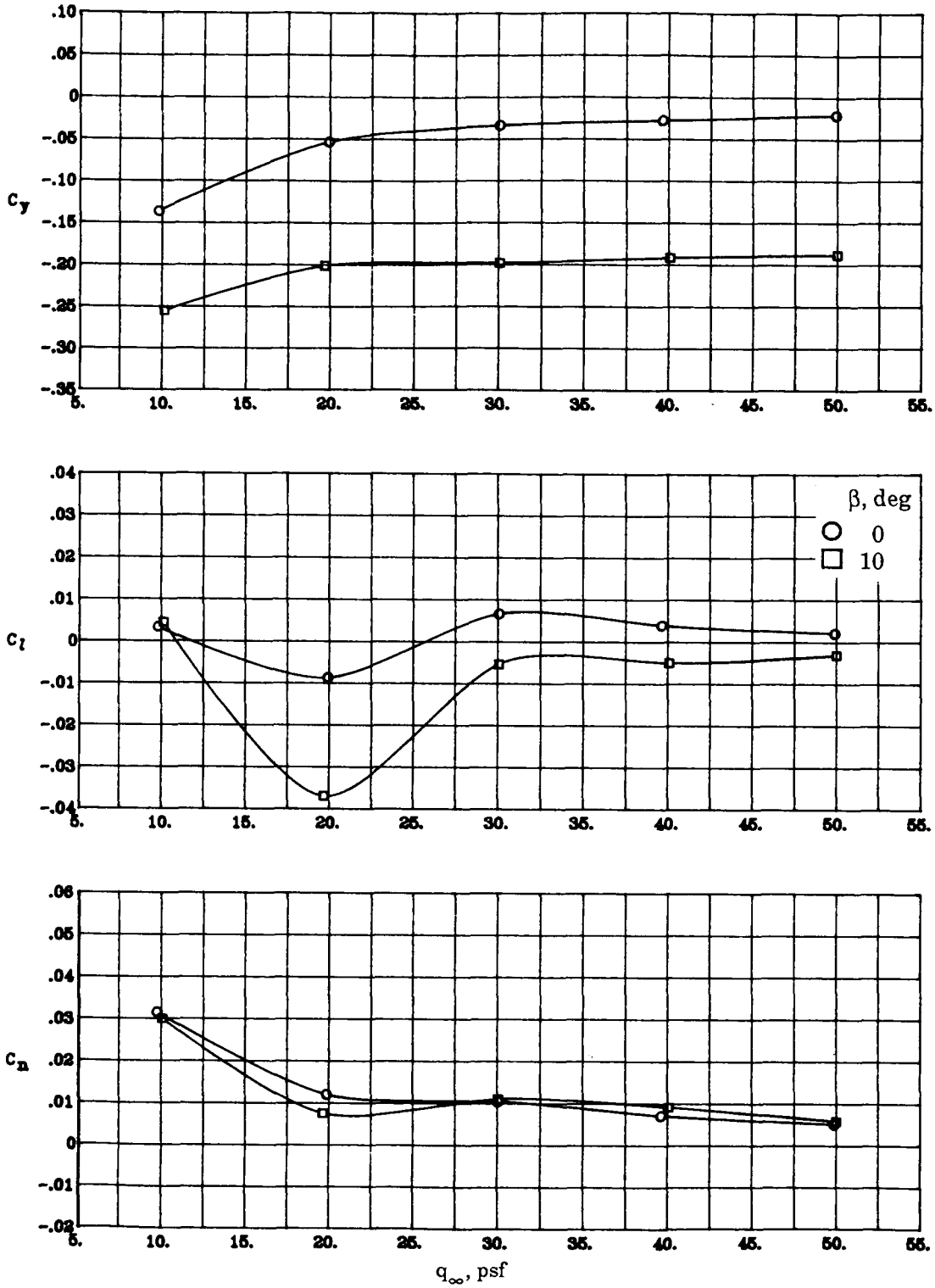


(l) Concluded.

Figure 8. Continued.

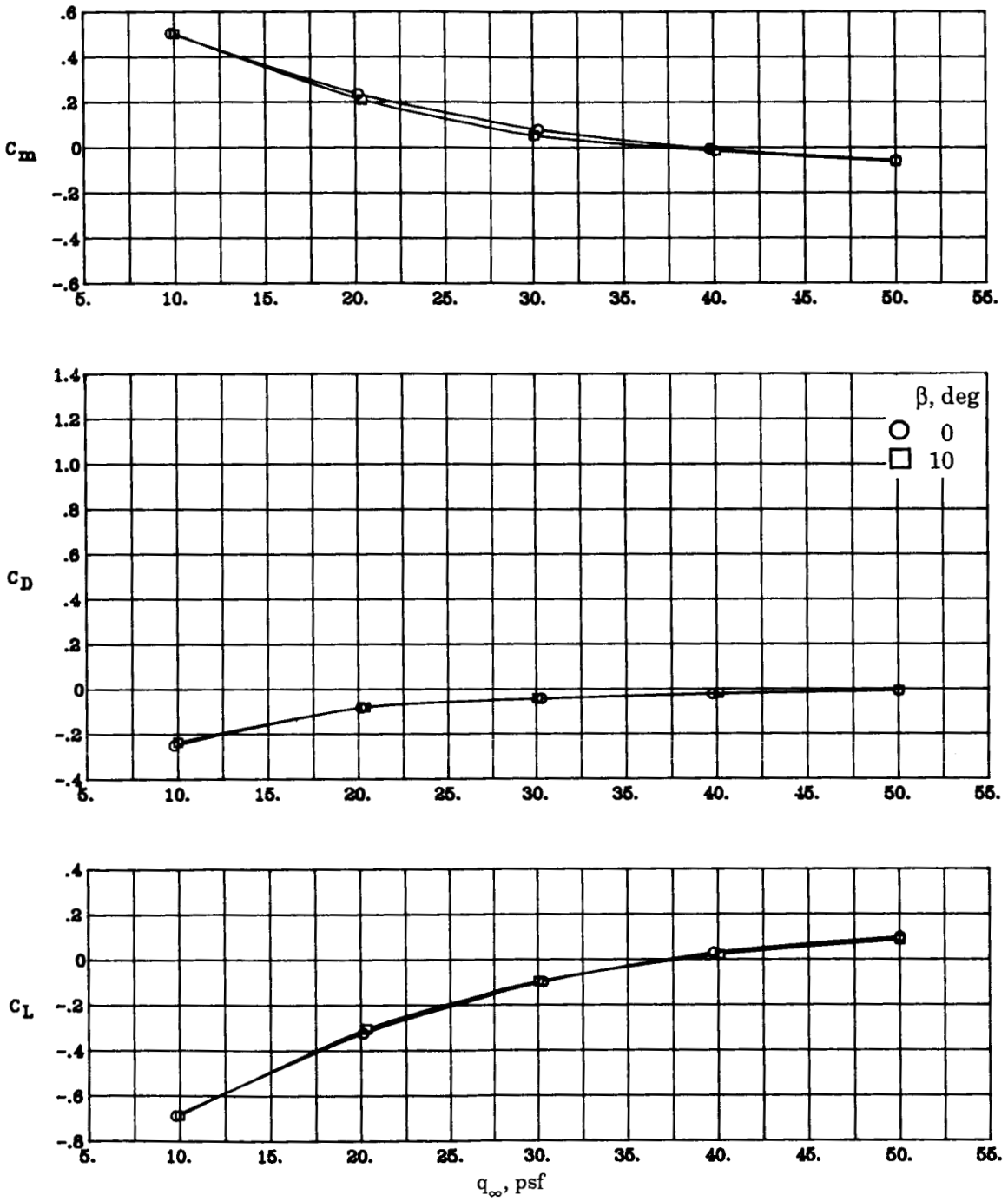


(m) $\Lambda_c = 0°$; NPR = 3.0; $\delta_f = 26°$.

Figure 8. Continued.

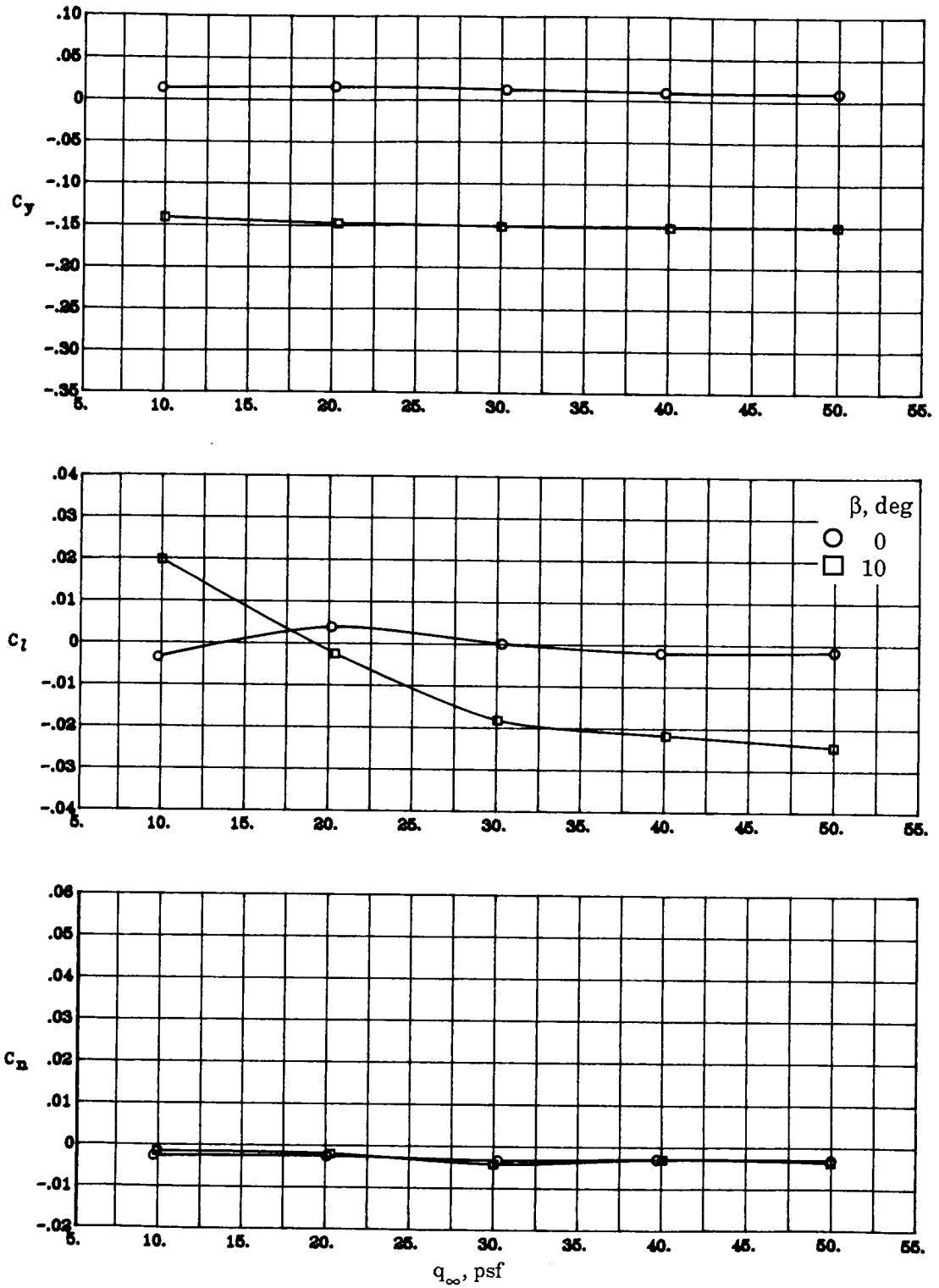


(m) Concluded.

Figure 8. Concluded.

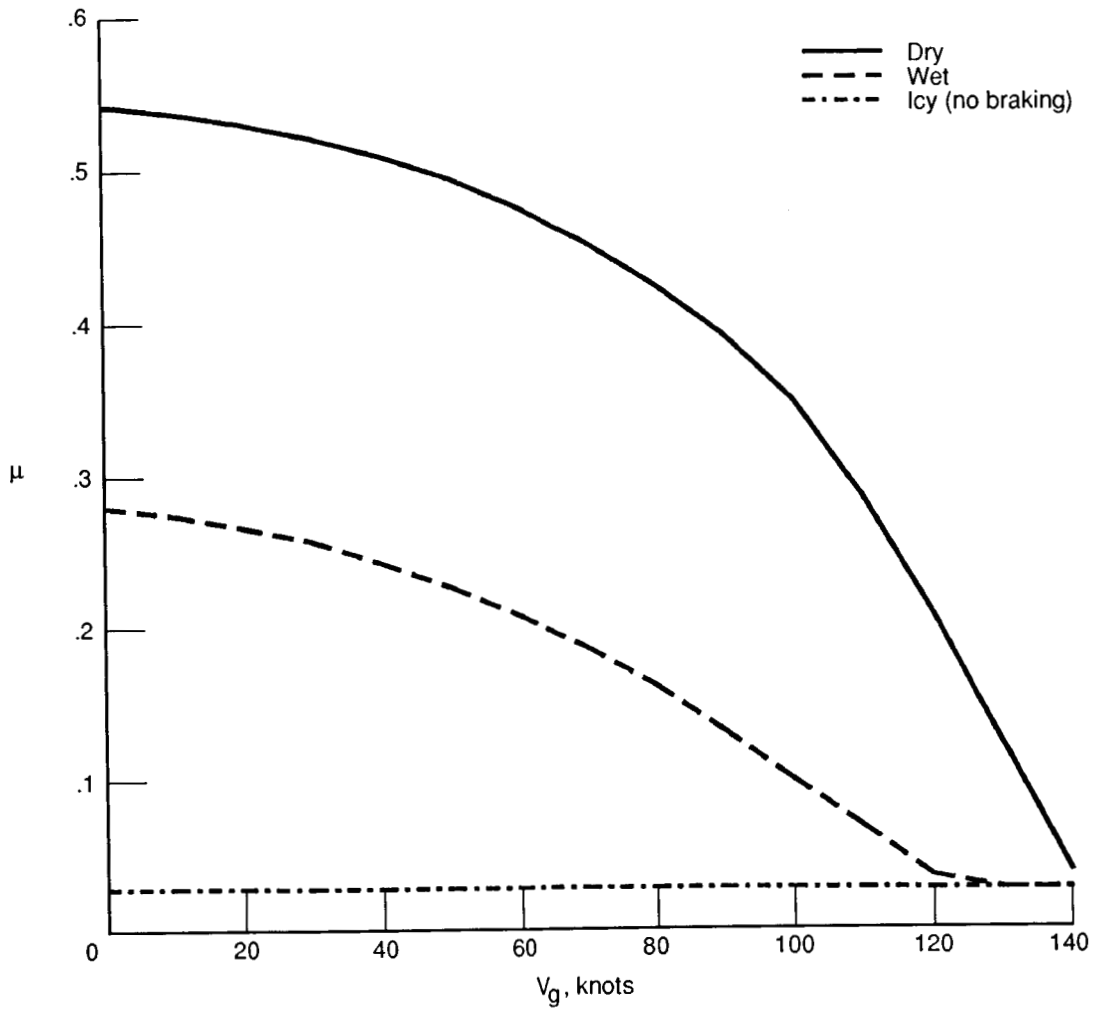


Figure 9. Effect of ground velocity on braking-friction coefficient for typical lightweight fighter aircraft with antiskid brakes.

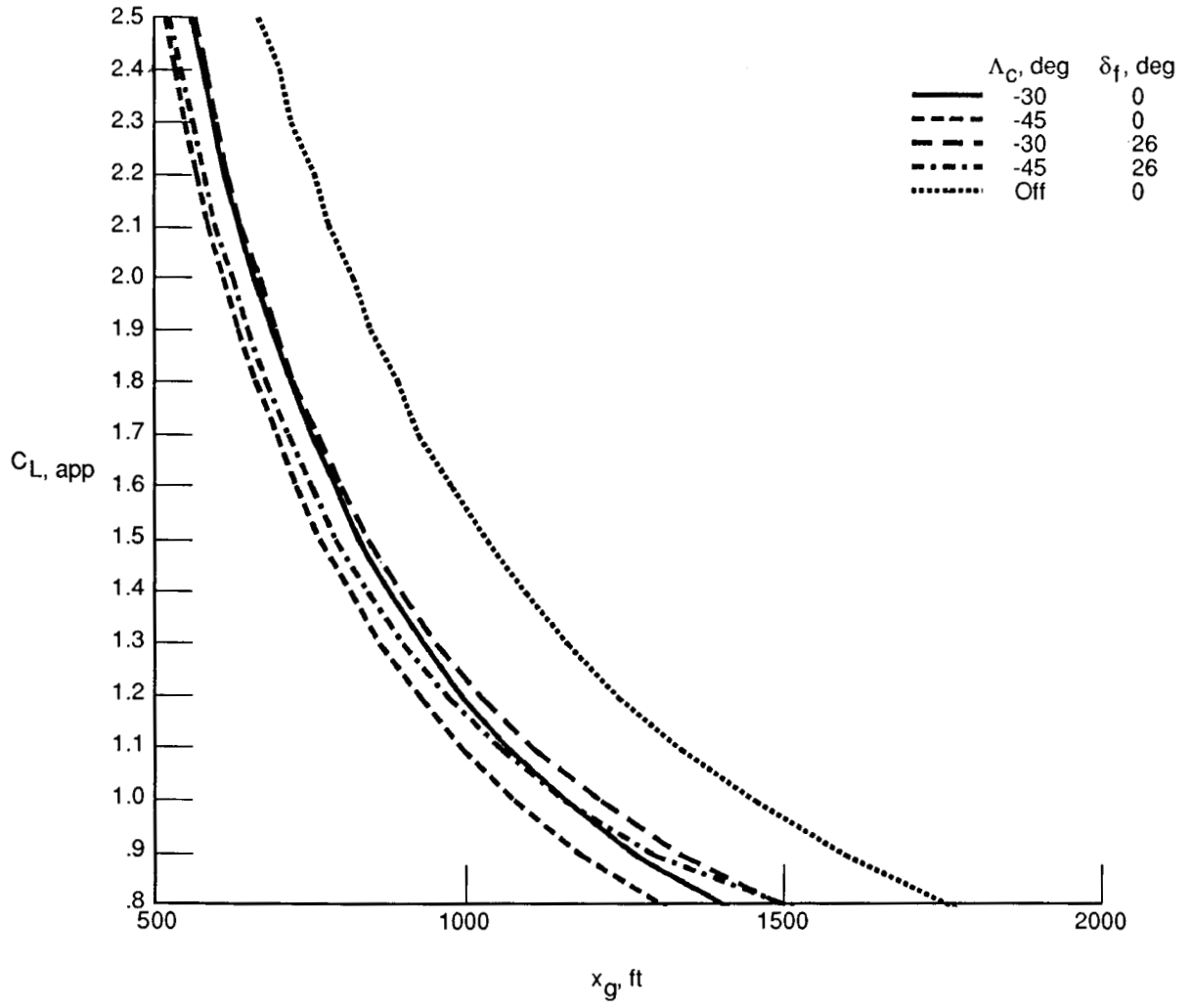


(a) Dry runway.

Figure 10. Predicted landing ground roll at various approach lift coefficients for different reverser and flap settings.

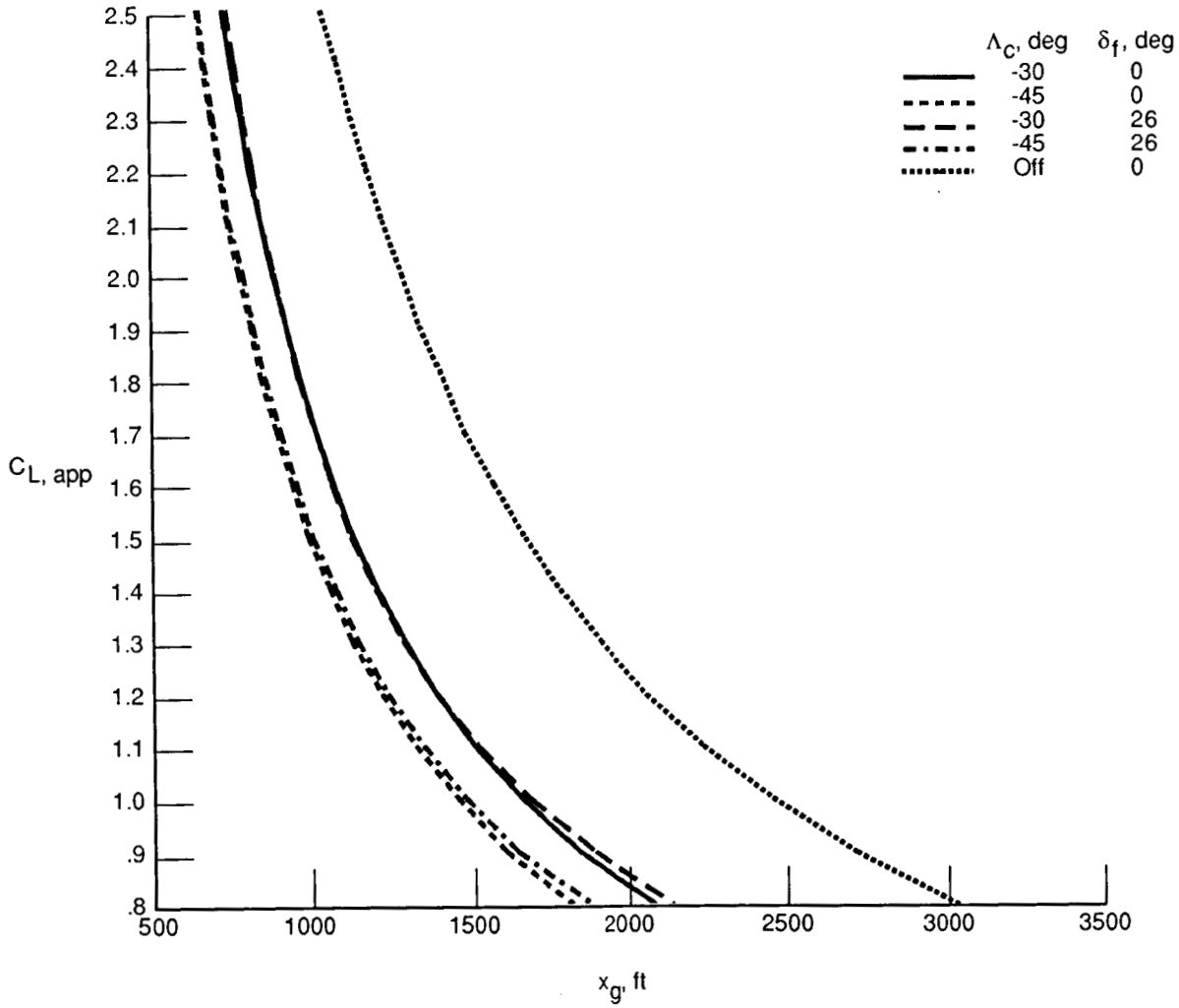


(b) Wet runway.

Figure 10. Continued.

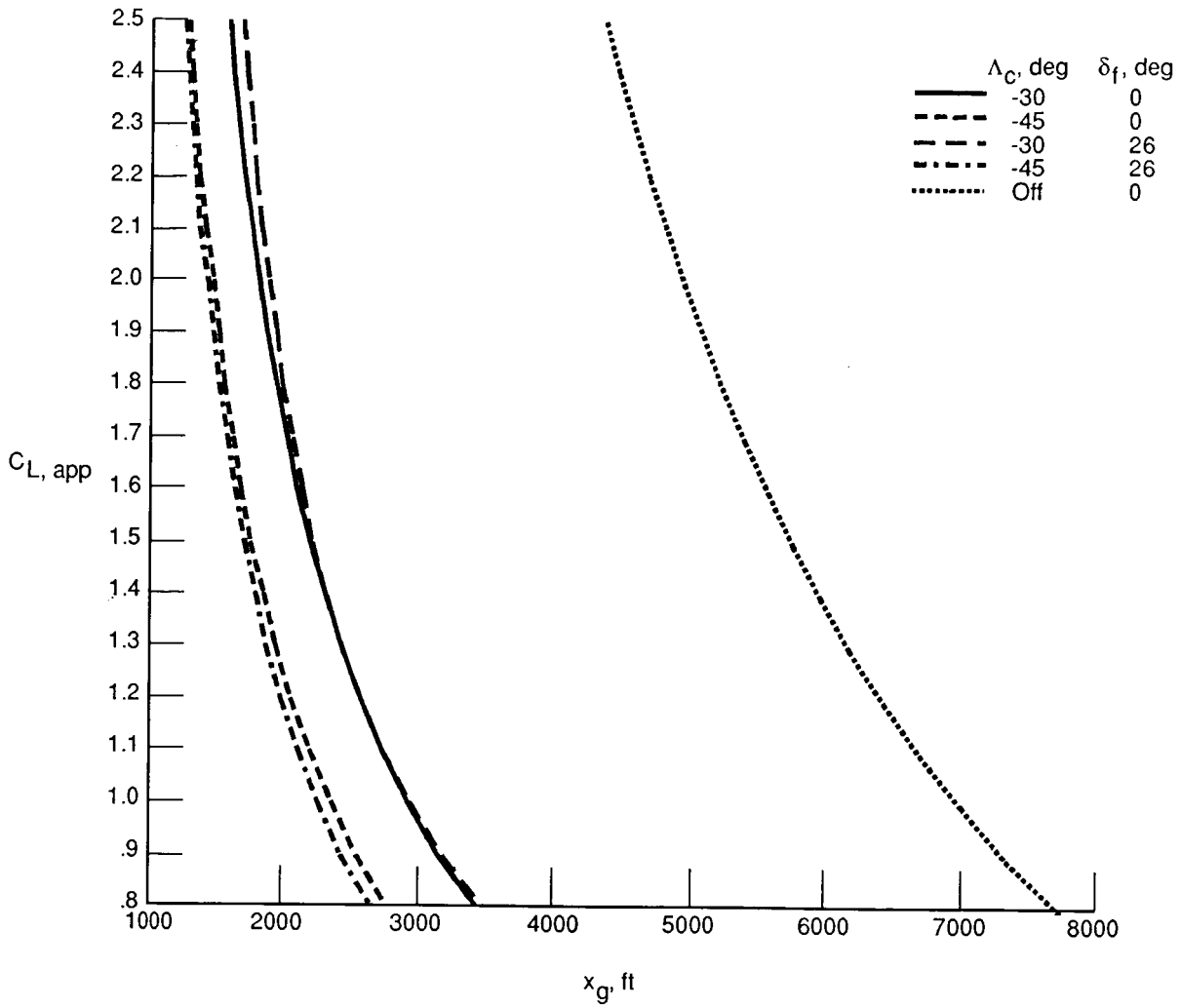


(c) Icy runway.

**Figure 10.** Concluded.

NASA
National Aeronautics and Space Administration

# Report Documentation Page

| 1. Report No. | 2. Government Accession No. | 3. Recipient's Catalog No. |
|---|---|---|
| NASA TP-2834 | | |

| 4. Title and Subtitle | 5. Report Date |
|---|---|
| Aerodynamics in Ground Effect and Predicted Landing Ground Roll of a Fighter Configuration With a Secondary-Nozzle Thrust Reverser | October 1988 |
| | 6. Performing Organization Code |
| 7. Author(s) | 8. Performing Organization Report No. |
| Daniel W. Banks | L-16435 |
| 9. Performing Organization Name and Address | 10. Work Unit No. |
| NASA Langley Research Center<br>Hampton, VA 23665-5225 | 505-61-71-02 |
| | 11. Contract or Grant No. |
| 12. Sponsoring Agency Name and Address | 13. Type of Report and Period Covered |
| National Aeronautics and Space Administration<br>Washington, DC 20546-0001 | Technical Paper |
| | 14. Sponsoring Agency Code |

15. Supplementary Notes

16. Abstract

An experimental investigation of the in-ground-effect aerodynamic characteristics and predicted landing-ground-roll performance of a wing-canard fighter configuration with a secondary-nozzle thrust reverser is discussed. These tests were conducted in the Langley 14- by 22-Foot Subsonic Wind Tunnel with a model equipped with a pneumatic jet for thrust simulation of nozzle pressure ratios up to 4.0. The model was tested in the landing roll-out configuration at approximately wheel touchdown height for decreasing dynamic pressures from 50 to 10 psf. Landing-ground-roll predictions of the configuration were calculated with the wind-tunnel results. Results indicate this thrust reverser is a viable concept, though it suffers from some of the same disadvantages as conventional thrust reversers.

| 17. Key Words (Suggested by Authors(s)) | 18. Distribution Statement |
|---|---|
| Thrust reverser<br>Cascade nozzle<br>Secondary nozzle<br>Short takeoff and landing<br>Landing ground roll | Unclassified–Unlimited<br><br>Subject Category 02 |

| 19. Security Classif.(of this report) | 20. Security Classif.(of this page) | 21. No. of Pages | 22. Price |
|---|---|---|---|
| Unclassified | Unclassified | 129 | A07 |



For sale by the National Technical Information Service, Springfield, Virginia 22161-2171